University Pablo de Olavide

Department of Physical, Chemical and
Natural Systems

Photoelectrochemistry of Nanocrystalline Semiconductor Metal Oxides in contact to Liquid Electrolytes: Photocatalytic and Photovoltaic Applications

Jesús Antonio Idígoras León

Supervisors:

Juan A. Anta

Thomas Berger

Seville, February 2015

University Pablo de Olavide

Department of Physical, Chemical and Natural Systems

Juan Antonio Anta, profesor titular vinculado al Departamento de Sistemas Físicos, Químicos y Naturales de la Universidad Pablo de Olavide.

Dr. Thomas Berger, vinculado al Departamento de Ciencia de Materiales y Física de la Universidad de Salzburgo

Certifican:

Que la presente memoria titulada **“Photoelectrochemistry of Nanocrystalline Semiconductor Metal Oxides in contact to Liquid Electrolytes: Photocatalytic and Photovoltaic Applications”** presentada por Jesús Antonio Idígoras León para la obtención del título de Doctor, ha sido realizada bajo nuestra dirección en el Departamento de Sistemas Físicos, Químicos y Naturales de la Universidad Pablo de Olavide, dentro del programa de Ciencia y Tecnología de Coloides e Interfases y cumple los requisitos para poder optar a la Mención Europea.

Juan A. Anta   Thomas Berger

Seville, February 2015

A mis padres y hermanos, por ayudarme en todo lo posible.

A Reyes y amigos, por su paciencia y apoyo.

As a result of the worldwide energy demand and the environmental impacts resulting from the use of fossil fuels, the search for sources of clean energy is steadily gaining importance. Since then, the scientific community has taken conscience of the energy-related challenges and has centred its efforts on taking advantage of renewable energy sources such as the sunlight. It has been known for a long time that light-induced processes at the interface between a semiconductor and an electrolyte can be exploited for the conversion of light in other forms of energy. As a consequence these systems have been extensively studied by chemists, physicists and material scientists. At present, the use of architectures based on nanomaterials has received a lot of attention as they constitute versatile and low-cost systems capable of capturing, storing and converting solar energy in chemical energy and electric power.

Mesoporous semiconductor electrodes comprise complex systems whose physicochemical properties depend not only on the nature of the nanocrystals, but also on the interaction between the crystalline building units forming the thin film. The mesoporous structure assures a high internal surface area. Furthermore, its complexity increases under relevant working conditions, such as in the presence of a surrounding gas or liquid phase. An understanding of how to systematically manipulate these interfaces and the interfacial processes that take place between the semiconductor and surrounding phase is a prerequisite for the optimization of emerging technologies and applications such as batteries, environmental remediation, sensors and solar cells, among others.

In applications such as photocatalysis and photovoltaics, special attention is paid to the relationship between the microscopic properties of the semiconductor thin film (electronic properties, crystal structure, particle size and shape) and the macroscopic performance of the photocatalyst and the solar cell, respectively. For this reason, in this thesis a fundamental study of the photocatalytic and photovoltaic properties of semiconductors such as TiO_2 and ZnO is performed to address the impact of the semiconductor/electrolyte interface on charge transfer processes and on the undesired charge recombination.

Charge recombination occurs by different ways in photocatalytic and photovoltaic applications. In the first case, recombination takes place between electrons and holes, which are generated upon light absorption in the semiconductor. On the other hand, in solar cells based on the semiconductor/electrolyte interface (as it is the case of a Dye-Sensitized Solar Cell), the recombination takes place between photoinjected electrons in the semiconductor and oxidized species present in the electrolyte. This represents the main route of efficiency-loss in such devices and constitutes a critical factor influencing the open-circuit voltage of the solar cell.

In relation to electron recombination processes, two research lines have been pursued in this thesis:

- A procedure entailing electron accumulation in the semiconductor film has been shown to reduce the recombination in photocatalytic and photovoltaic applications. This charge transfer reductive doping has been carried out in situ by means of a cathodic polarization of the respective electrodes in acidic solution. A negative Fermi level shift in the semiconductor has been achieved alternatively by external polarization or by accumulation of photogenerated charge carriers upon UV exposure. In both cases, comparable performance changes of the mesoporous films were observed. The influence of thin film structure and morphology on the extent of the beneficial effect of electrochemical doping has been addressed.

- For photovoltaic applications a study of electron recombination based on the chemical nature of the electrolyte has been performed. The effects on the kinetics of recombination using different electrolyte compositions and dyes have been discussed. In this context, we have analyzed how properties such as polarity and the presence of certain additives modify critically the recombination rate. Derived from the conclusions of this study, we propose a strategy to achieve a compromise between stability and low recombination by using blends of organic solvents and room temperature ionic liquids as electrolytes.

Recombination takes place in the solar cell on a very specific time scale, in the order of 0.001 - 1 seconds. However, there are other processes that also depend on the electrolyte nature, that also limit the efficiency of the solar cells and that occur on much shorter time scales. This is the case of electron injection from dye molecules and dye regeneration. In this thesis we present a global analysis of all these processes involving a combination of experimental techniques that include transient absorption spectroscopy, fluorescence decay and electrochemical techniques such as impedance spectroscopy. We take advantage of this global analysis to show for the first time the fundamental limitation that is associated with ZnO electrodes when they are used as photoanodes to separate charge at the metal-oxide/electrolyte interface. The behaviour of this oxide is also tested with different electrolyte formulations and state-of-the art molecular dyes.

Contributions to the Scientific Community

The most relevant publications resulting from this thesis are:

- **Modification of Mesoporous TiO_2 Films by Electrochemical Doping: Impact on Photoelectrocatalytic and Photovoltaic Performance.**
  J. Idígoras, T. Berger and J.A. Anta.
  Journal of Physical Chemistry C, **2013**, 117(4), 1561-1570.

- **The Redox Pair Chemical Environment Influence on the Recombination Loss in Dye-Sensitized Solar Cells.**
  J. Idígoras, L. Pellejà, E. Palomares and J.A. Anta.
  Journal of Physical Chemistry C, **2014**, 118(8), 3878-3889.

- **Control of Recombination Rate by Changing the Polarity of the Electrolyte in Dye-Sensitized Solar Cells.**
  J. Idígoras, R. Tena-Zaera and J.A. Anta.
  Physical Chemistry Chemical Physics, **2014**, 16, 21513-21523.

- **The Impact of the Electrical Nature of the Metal-Oxide on the Performance in Dye-Sensitized Solar Cells: New Look at Old Paradigms.**
  J. Idígoras, G. Burdzinski, J. Karolczak, J. Kubicki, G. Oskam, J.A. Anta and M. Ziolek.
  Journal of Physical Chemistry C, **2015**, accepted.

- **In Situ Self-Doping of mesoporous TiO_2 films.**
  J. Idígoras, T. Berger and J.A. Anta.
  Manuscript in preparation, **2015.**

- **Photovoltaic performance of ZnO photoanodes with novel purely organic D-π-A dyes.**
  J. Idígoras, R. Demadrille and J.A. Anta.
  Manuscript in preparation, **2015.**

Other publications closely related to this thesis are listed below:

- **ZnO-based Dye Solar Cell with pure Ionic-Liquid Electrolyte and Organic Sensitizer: the Relevance of the Dye–Oxide Interaction in an Ionic-Liquid medium.**
  E. Guillén, **J. Idígoras**, T. Berger, J.A. Anta, C. Fernández-Lorenzo, R. Alcántara, J. Navas, and J. Martín-Calleja.
  Physical Chemistry Chemical Physics, **2011,** 13, 207-213.

- **Direct Estimation of the Electron Diffusion Length in Dye-Sensitized Solar Cells.**
  J. Navas, E. Guillén, R. Alcántara, C. Fernández-Lorenzo, J. Martín-Calleja, G. Oskam, **J. Idígoras**, T. Berger and J.A. Anta.
  Journal of Physical Chemistry Letters, **2011**, 2, 1045-1050.

- **Charge Collection Properties of Dye-Sensitized Solar Cells based on 1-Dimensional TiO_2 Porous Nanostructures and Ionic Liquid Electrolytes.**
  L. González-García, **J. Idígoras**, A.R. González-Elipe, A. Barranco and J.A. Anta.
  Journal of Photochemistry and Photobiology A: Chemistry, **2012**, 241, 58-66.

- **A Continuity Equation for the Simulation of the Current–Voltage Curve and the Time-Dependent Properties of Dye-Sensitized Solar Cells.**
  J.A. Anta, **J. Idígoras**, E. Guillén, J. Villanueva-Cab, H.J. Mandujano-Ramírez, G.Oskam, L. Pellejà and E. Palomares.
  Physical Chemistry Chemical Physics, **2012**, 14, 10285-10299.

- **ZnO-ionic Liquid Hybrid Films: Electrochemical Synthesis and Application in Dye-Sensitized Solar Cells.**
  E. Azaceta, **J. Idígoras**, J. Echeberria, A. Zukal, L. Kavan, O. Miguel, H.J. Grande, J.A. Anta and R. Tena-Zaera.
  Journal of Materials Chemistry A, **2013**, 1, 10173-10183.

- **ZnO/ZnO Core–Shell Nanowire Array Electrodes: Blocking of Recombination and Impressive Enhancement of Photovoltage in Dye-Sensitized Solar Cells.**
  E. Guillén, E. Azaceta, A. Vega-Poot, **J. Idígoras**, J. Echeberria, J.A. Anta and R. Tena-Zaera.
  Journal of Physical Chemistry C, **2013,** 117, 13365-13373.

- **Influence of Dye Chemistry and Electrolyte solution on Interfacial Processes at Nanostructured ZnO in Dye-Sensitized Solar Cells.**
  N.M. Gómez-Ortíz, **J. Idígoras**, E. Guillén, A. Hernández, A. Sastre-Santos, F. Fernández-Lázaro, J.A. Anta and G. Oskam.
  Journal of Photochemistry and Photobiology A: Chemistry, **2013**, 264, 26-33.

- **Highly efficient flexible cathodes for dye sensitized solar cells to complement Pt@TCO coatings.**
  J. Idígoras, E, Guillén, F.J. Ramos, J.A. Anta, M. Nazeeruddin and S. Ahmad.
  Journal of Materials Chemistry A, 2014, 2, 3175-3181.

- **Mechanisms of Electron Transport and Recombination in ZnO Nanostructures for Dye-Sensitized Solar Cells.**
  A. Vega-Poot, M. Macías-Montero, **J. Idígoras**, A. Borrás, A. Barranco, A.R. Gonzalez-Elipe, F.I. Lizama-Tzec, G. Oskam and Juan A. Anta.
  ChemPhysChem, **2014**, 15(6), 1088-109.

- **Comparison of TiO_2 and ZnO Solar Cells Sensitized with an Indoline Dye: Time-Resolved Laser Spectroscopy Studies of Partial Charge Separation Processes.**
  J. Sobús, G. Burdzinski, J. Karolczak, **J. Idígoras,** J.A. Anta and M. Ziolek.
  Langmuir, **2014**, 30(9), 2505-2512.

- **Ion Transport in Electrolytes for Dye-Sensitized Solar Cells: A Combined Experimental and Theoretical Study.**
  J.M. Vicent-Luna, **J. Idígoras**, S. Hamad, S. Calero, Sofia and J.A. Anta.
  Journal of Physical Chemistry C, **2014**, 118(49), 28448-28455.

- **Indoline Dye-Sensitized Solar Cells: Initial Charge Separation in different Photoanode Nanostructures and the details of Electron Injection Process.**
  M. Ziolek, J. Sobús, G. Burdzinski, J. Karolczak, **J. Idígoras,** J.A. Anta, R. Tena-Zaera and G. Oskam.
  Manuscript in preparation, **2014.**

Chapter 1: Physicochemical properties of the metal oxide/electrolyte interface.

Chapter 2: The semiconductor-electrolyte junction: Photocatalytic applications.

Chapter 3: The semiconductor-electrolyte junction: Photovoltaic applications.

Chapter 4: Experimental: Characterization techniques and preparation of devices.

Chapter 6: Electrochemical hydrogen-doping: Impact on photoelectrocatalytic and photovoltaic applications.

Chapter 7: The influence of the chemical environment of the redox pair on the recombination loss in Dye-Sensitized Solar Cells.

Chapter 8: Control of recombination rate by changing the polarity of the electrolyte in Dye-Sensitized Solar Cells.

Chapter 1:

Physicochemical properties of the metal oxide/electrolyte interface

1. The interaction semiconductor-electrolyte.

The study of the semiconductor/electrolyte interface has both fundamental and practical incentives. Approaches to gain a fundamental understanding of this interface result from both electrochemistry and solid-state physics perspectives and have proven to be equally fruitful. This knowledge background in turn impacts in many technologies, including microelectronics, environmental remediation, sensors, solar cells and energy storage. To facilitate a self-contained description, well-established aspects related to the semiconductor and its energy band model, redox couples in solution and the electrostatics at the semiconductor/electrolyte interface will be introduced.

1.1. Semiconductors.

Semiconductors are materials that may behave either like a conductor or like an insulator depending on diverse factors, as for example the electric or magnetic field, the pressure, the incident radiation, or the temperature. The main distinction between these kinds of materials is rather arbitrary and depends on the magnitude of the energy band gap (E_g) between the filled valence band (VB) and the empty conduction band (CB) (**Figure 1.1**). Unlike molecular systems, characterized by discrete molecular orbital energy levels, semiconductor energy levels form broad energy bands, where the charge carriers can be delocalized.

In semiconductors the energy band gap is typically in the range of 1 - 4 eV. The width of the band gap determines the conductivity of the material as well as its optical response. In contrast to semiconductors, metals are characterized by a high density of electronic states at energies just above the Fermi level. Electrons at the Fermi level can be thermally excited to these empty states giving rise to the high electrical conductivity of metals. In *intrinsic semiconductors* high excitation energies are necessary to overcome the band gap and to promote electrons from the valence band to the conduction band leaving behind electron holes. Both negative and positive charge carriers can contribute to the electrical conductivity.

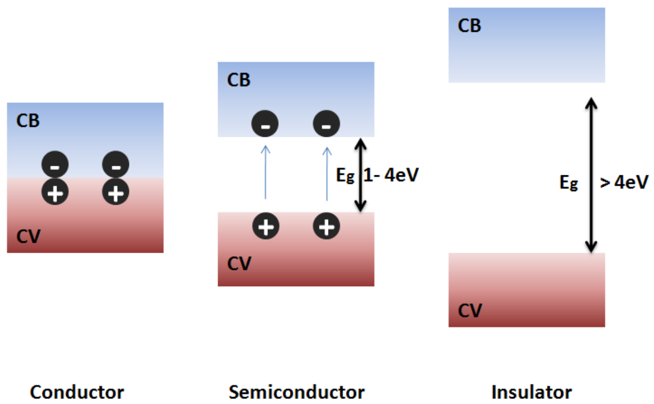

Figure 1.1: Electronic band structure of conductors, semiconductors and insulators.

For high density electron ensembles such as valence electrons in metals, Fermi-Dirac statistics is applicable. In a thermodynamic sense, the Fermi level, E_F is defined as the electrochemical potential of electrons in a particular phase. At 0K, all electronic energy levels below E_F are occupied and those above E_F are empty. At finite temperatures, it can be shown that when the Fermi level lies in a broad distribution of states, it corresponds to the particular energy level where the probability of finding an electron is ½.[1]

Bearing in mind this concept, the number of electrons in the conduction band (n_c) can be derived from the density of states function $N_c(E)$ of electrons in the conduction band and from the probability of occupation at a certain energy $f(E)$,[2]

$$n_c = \int_{-\infty}^{+\infty} N_c(E)\, f(E) dE \qquad (1.1)$$

which is given by the Fermi-Dirac distribution function,

$$f(E) = \frac{1}{1 + \exp\left(\frac{E_c - E_F}{k_B T}\right)} \qquad (1.2)$$

Here k_B is the Boltzmann constant and T is the absolute temperature. For a situation for which E_c-E_F >>k_BT (non-degenerate semiconductor), where E_c is the lower energy of the conduction band, the Fermi-Dirac distribution can be approximated by Boltzmann statistics. In this case, it is possible to relate the Fermi level to the concentration of electrons in the conduction band by the following expression,[3]

$$n_c = N_c \exp\left(-\frac{E_c - E_F}{k_B T}\right) \qquad (1.3)$$

where N_c is the density of states at the conduction band edge. A similar approximation can be used to describe holes in the valence band edge. The concentration of holes is then given by

$$p_v = N_v \exp\left(+\frac{E_v - E_F}{k_B T}\right) \qquad (1.4)$$

where E_v is the upper energy edge of the valence band and N_v is the density of states function of holes in the valence band. In the absence of light excitation $n_c = p_v$, and then the intrinsic concentration of charge carriers n_i (electron and holes) is equal to n^2_i.

$$n_c p_v = N_c N_v \exp\left(\frac{E_v - E_c}{k_B T}\right) = N_c N_v \exp\left(\frac{-E_g}{k_B T}\right) = n_i^2 \qquad (1.5)$$

where the energy of the band gap E_g is recovered. The preceding case refers to a semiconductor in its *intrinsic state*. The Fermi level in that case lies approximately in the middle of the energy band gap. This simply reflects the fact that the probability of electron occupancy is very high in the VB and very low in the CB and does not imply an occupiable energy level at the Fermi level itself.

In the case of *extrinsic semiconductors*, the number of charge carriers depends on the dopant concentration in the material. In this case, the condition $n_c = p_v = n_i$ does not hold. The introduction of donor or acceptor species of electrons in the semiconductor can alter perceptibly its electronic structure and consequently its Fermi level. This is shown in **Figure 1.2** for the case of silicon. Most of the times, doping is carried out by the introduction of atoms with a higher or a lower number of valence electrons, giving rise to a *n-type* or *p-type* semiconductor, respectively. Consequently, majority charge carriers are electrons in the first case and holes in the second case.

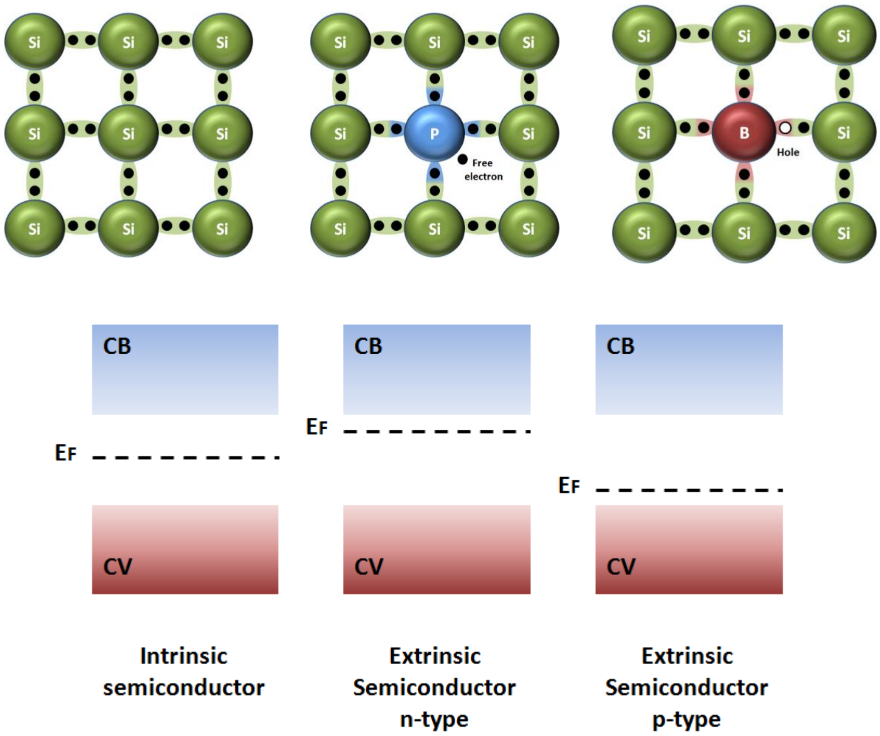

Figure 1.2: Schematic representation and energetic band structure in different types of semiconductor.

1.2. Redox couples in solution: Energetic description.

The half-reaction of a generic redox couple can be written as[4,5]

$$Ox + ze^- \leftrightarrow Red \qquad (1.6)$$

where z is the number of interchanged electrons. In electrochemistry, the tendency of a redox couple to get oxidized or reduced is determined by the *redox potential* (E_{redox}), measurable by electrochemical methods. The electrochemical potential of electrons in a redox electrolyte is given by the Nernst equation. For an ideal system for which activities can be approximated by concentrations, this reads[4,5]

$$E_{redox} = E^o_{redox} + \frac{RT}{zF}\ln\left[\frac{c_{ox}}{c_{red}}\right] \qquad (1.7)$$

where R is the ideal gas constant, F is the Faraday's constant and c_{ox} and c_{red} are the molar concentrations of the oxidized and the reduced species, respectively.

A model giving a molecular interpretation of electron transfer reactions was provided by Marcus.[6,7] According to his interpretation an instantaneous electron transfer would lead to a new state whose free energy is not at its minimum due to the fact that electronic transitions occur very rapidly and the subsequent arrangement of solvent molecules depends on the charge distribution. The change of the charge distribution upon electron transfer would thus lead to a polarization of the surroundings (due to both orientation and displacement polarization of solvent molecules). This determines the Gibbs free energy of activation via the so-called *reorganization energy* (λ).

Considering a single one-electron transfer to an acceptor ($Ox + e^- \leftrightarrow Red$), the free energy change (ΔG) can be described for both the oxidized and the reduced species as a function of the atomic positions and the number of transferred electrons. Marcus described this function by a parabola (which can be interpreted as the potential energy of a harmonic oscillator). The minimum of this parabola corresponds to the equilibrium configuration of each species with respect to its surrounding. In the original Marcus picture (**Figure 1.3**), the reaction coordinate represents the number of transferred electron, varying from x = 0 (zero transferred charge → Ox) to x = 1 (full charge transferred → Red). Hence, when the electron is transferred from oxidized to reduced species, the electron should reach, for fixed atomic positions the free energy landscape of the acceptor species. In this picture, the reorganization energy (λ) is the free energy difference between the two energy landscapes at fixed atomic positions.

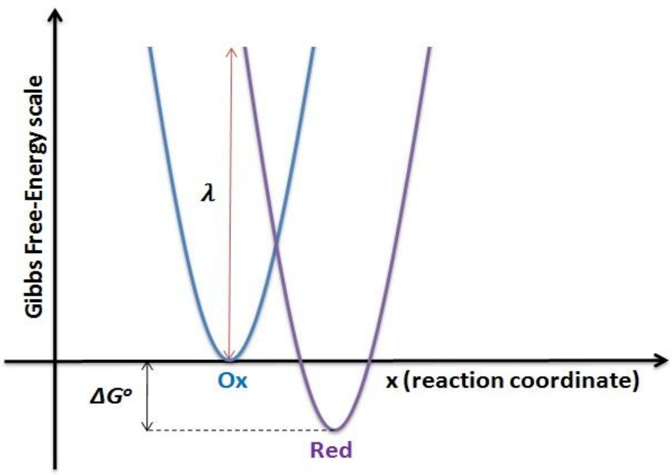

Figure 1.3: In this picture, the vertical axis represents the Gibbs free energy (ΔG^o) and the horizontal axis the "coordinate of reaction". The parabola of the left represents the potential energy for the oxidized species before charge transferred (initial state) and the parabola of the right represents the energy for the reduced species after charge transferred (final state).

A very simple calculation taking into account the equations for the two parabolas for oxidized and reduced species[5] establishes that the reaction rate constant (k) is described by a gaussian centred at λ with standard deviation $(2\lambda k_B T)^{½}$

$$k = k_0 \exp\left(-\frac{(\Delta G + \lambda)^2}{4\lambda k_B T}\right) \qquad (1.8)$$

where k_0 is a prefactor. In Marcus's model two contributions to the reorganization energy are considered: (1) *outersphere*, due to the interaction between the redox species and the surrounding solvent molecules and, (2) *innersphere,* which arises from the breaking and formation of chemical bonds upon the charge transfer process.[7,8]

1.3. The semiconductor-electrolyte interface.

At this point it is important to unify definitions and units as two different scientific communities use different conventions to refer to the same physical magnitude, that is, the chemical potential. The semiconductor solid-state physics community has adopted the electron energy in vacuum as reference for this, whereas electrochemists have traditionally used the Normal Hydrogen Electrode scale (NHE). As mentioned in the previous section, in solid state physics, the electrochemical potential of electrons is the *Fermi level*. Both descriptions are related via the following equation[10,11]

$$E_F = -qE_{redox}\,(NHE) - 4.5eV \qquad (1.9)$$

where q is the elementary charge and E_{redox}(NHE) is the equilibrium potential of the redox couple with respect to the normal hydrogen electrode in volts.[4,12] It is important to note that the energy scale (in eV) and the potential scale (in V) have different signs.

When a semiconductor is brought in contact with an electrolyte containing electrochemically active species, an equilibration of chemical potential takes place as a consequence of double layer formation and electron transfer between the semiconductor and the active species present in the solution.[9] In fact, the electron transfer will occur if the Fermi level in the semiconductor is different to the equilibrium redox potential of electrolyte. As it will be described in the following section, for a given redox potential of the electrolyte, the electron transfer from semiconductor to oxidized species or, in the opposite case, from the reduced species to the semiconductor depends on the position of the Fermi level in the latter (n-type or p-type). In any case, this process leads to a equilibrarion of Fermi levels across the semiconductor/electrolyte interface.

To determine the energy levels of the reduced and oxidized species present in the electrolyte their interactions with the surrounding solvent molecules have to be taken into account. We can use here the Marcus model presented before. Upon electron transfer from oxidized to reduced species, the solvent will respond to the change in charge distribution due to the presence of extra negative charge. Therefore, the negative poles of solvent molecules will orient toward the solution. The free energy difference between both species is given by

$$E_{ox} - E_{red} = 2\lambda \qquad (1.10)$$

For simplicity, the reorganization energy (λ) of the molecules is considered to be equal for both oxidized and reduced species.

To define a distribution function of acceptor or donor states in the electrolyte Gerischer[9] utilized Marcus' ideas. The probability of finding the oxidized and reduced species at an energy E for the electron transfer is given by the following equation

$$P(E) = k_{r0}\sqrt{\frac{k_B T}{4\pi\lambda}}\exp\left(\frac{-(E-E_{redox})^2}{4\lambda k_B T}\right) \qquad (1.11)$$

where k_{r0} is a prefactor and E_{redox} is the equilibrium free energy of the redox pair (defined by Nernst equation, **Equation 1.8**).

As shown in **Figure 1.4** and according to **Equation 1.11**, the reorganization energy determines the energetic overlap between the electronic states of the semiconductor and the acceptor (oxidized species) and donor (reduced species) states in the electrolyte. Therefore, in electrolytes with high reorganization energy, high probabilities of electron transfer for a given energy E are found. The effect of reorganization energy on the kinetics of charge transfer will be discussed in this thesis by means of a study for Dye-Sensitized Solar Cells presented in **Chapters 7** and **8**

According to **Equation 1.10**,

$$E_{ox} = E_{redox} + \lambda \qquad (1.12)$$

$$E_{red} = E_{redox} - \lambda \qquad (1.13)$$

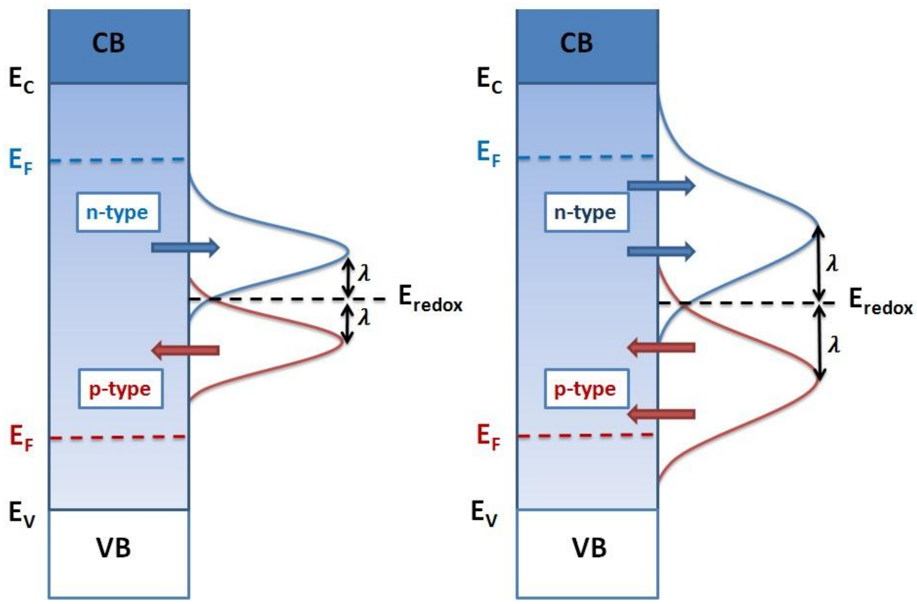

Figure 1.4: Illustration of the effect of the reorganization energy on the probability of charge transfer at a given energy E across the semiconductor/electrolyte interface.

1.3.1. Single-crystal electrodes.

A single-crystal semiconductor electrode in contact with a redox pair in an electrolyte behaves similarly to a metal-semiconductor junction forming a Schottky barrier.[3] For instance, when placing n-type doped single-crystal semiconductor electrodes in contact with an electrolyte containing a redox pair electron transfer will take place from the semiconductor to electron acceptor species in the electrolyte. For this electron transfer the Fermi level of the electrons in the semiconductor is higher than the equilibrium redox potential in solution. As a consequence the oxidized species will be reduced.

$$(Ox + e^{-} \rightarrow Red)$$

Upon electron transfer a depletion layer is generated in the semiconductor. This means that the concentration of the majority charge carriers, the electrons, becomes locally reduced in the vicinity of the interface. A depletion layer is characterized by a space charge layer width (W) and a voltage drop (V_{SC}) between the surface and the bulk of the semiconductor (**Figure 1.5**). To maintain the positive charge in the semiconductor is compensated on the electrolyte side of the interface by the accumulation of anions. In the case of a p-type semiconductor, the opposite situation takes place, and an accumulation layer of electrons is formed upon electron transfer to the semiconductor. In any case, the Poisson-Boltzmann equation is the element that determines the distribution of charges in the depletion layer. The solution of this equation is a classic calculation that yields for the space charge layer (W)[10]

$$W = \left(\frac{2\, \epsilon\epsilon_0\, V_{sc}}{q\, N_D}\right)^{1/2} \qquad (1.14)$$

The space charge layer depends on the dielectric constant of the semiconductor (ϵ), the vacuum permittivity (ϵ_0), the elementary electron charge (q) and the concentration of electron donor centres (N_D) or acceptor centres (for a p-type semiconductor).

Different models have been proposed to describe the charge distribution on the electrolyte side of the interface. The Stern model considers two contributions to the potential drop at the electrical double layer:

- In the Helmholtz-Perrin layer ($\Delta\phi_H$), known as *surface charge*, counter-ions are arranged at a fixed distance (0.4-0.6 nm) from the surface of electrode. This layer acts as a capacitor.[13]
- In the Gouy-Chapman layer, the ions are attracted to the surface charge via electrostatic forces. This *diffuse layer* is made of free ions that move in the fluid under the influence of electric interactions and thermal motion. This model also involves the solution of the Poisson-Boltzmann equation.

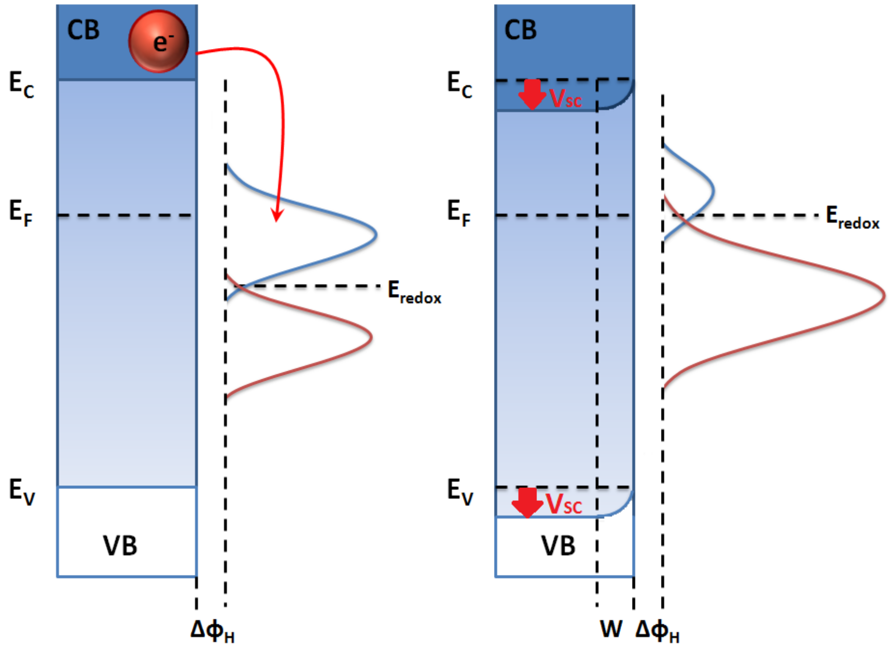

Figure 1.5: Electronic structure of a n-type semiconductor and a redox couple before (left) and after (right) electron transfer.

Up to here external electrode polarization has not been considered as a possibility to address the Fermi level position at the semiconductor/electrolyte interface. Importantly, in a case where the semiconductor bands are pinned at the interface (band pinning) the application of an external potential can induce a Fermi level shift with respect to the bands near the interface. This shift can be interpreted as band bending near the surface, as shown in **Figure 1.5**. At a characteristic potential (flat band potential, V_{fb}) the semiconductor bands are not bent but flat. Depending on the applied potential and on the curvature of band bending (depletion or accumulation layer), it is possible to modify the direction of electron transfer from/to the semiconductor, reducing or oxidizing the redox couple.

$$V_{sc} = V - V_{fb} \qquad (1.15)$$

Two conditions have to be fulfilled for interfacial charge transfer to take place:

- The Fermi levels involved must occupy the suitable positions. For an electron transfer from the semiconductor to the redox pair the Fermi level in the semiconductor must lie at more negative potential than that of the redox potential in solution (E_{redox}). That this a condition is fulfilled depends on the intrinsic nature of the system or on the applied potential.
- The process must be kinetically favourable. This condition implies an energetic overlap between electronic states in the semiconductor (electron donors) and electron acceptors in solution.

If these conditions are fulfilled, charge transfer across semiconductor/electrolyte interface can take place via two mechanisms:[14]

- Isoenergetic transfer: The electron transfer takes place between levels with the same energy. According to this mechanism, the rate of charge transfer will depend on the concentration of the electron donor states, the concentration of acceptor species at the semiconductor surface and on the probability of the overlap between energy levels.
- Transfer via localized or surface states: The surface states are energetically located in the band gap. These states can act like centres of recombination or charge transfer to the redox pair.

1.3.2. Nanocrystalline electrodes.

The concepts previously analyzed are strictly valid for single-crystal electrodes. For mesoporous, nanoparticulate films additional aspects have to be taken into account. These systems consist of a mesoporous three-dimensional network with particles with a size in the range of nanometres. Its main features are the following ones:

- They possess a high internal surface area in contact with the electrolyte. This introduces surface defects, so that the concentration of localized states per unit volume is much higher than to single-crystal electrodes.
- In nanocrystalline systems the concept of depletion or accumulation layers, band bending or flat-band potential is generally not applicable because the size of these nanoparticles is usually lower than the space charge layer within the semiconductor nanoparticles[15] (**Figure 1.6**).
- Band bending is typically absent in nanocrystalline TiO_2 electrodes studied in this thesis. This oxide has, furthermore, a high dielectric constant and a low doping level. According to **Equation 1.14**, this makes the depletion layer thickness even larger. However, this is not the case for ZnO-based electrodes, also studied in this thesis. ZnO has a lower dielectric constant and it can be highly doped, as for instance ZnO powders obtained in aqueous media and by hydrothermal methods.

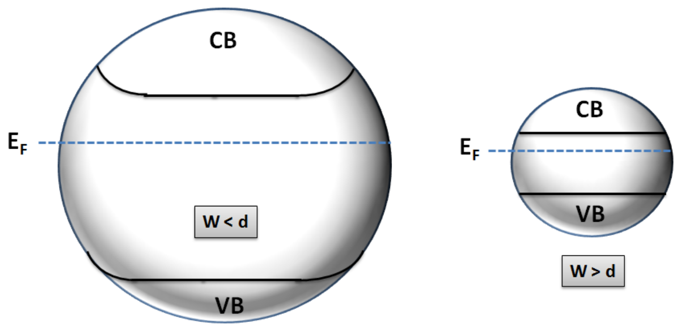

Figure 1.6: Band structure of differently sized nanoparticles. *W* and *d* refer to the space charge layer thickness and the nanoparticle size respectively.

As mentioned above, in the dark, electrons in the semiconductor are in equilibrium with the electrolyte if there is a suitable redox couple present in it and the charge transfer is possible. As a consequence, at equilibrium and in the dark, the Fermi level in the semiconductor equals the thermodynamic redox potential defined by the Nernst equation. However, under illumination with an energy higher than the band gap energy of the semiconductor, an electron-hole pair is generated. Under this condition, the electrical properties of the system will not be determined by the position of the Fermi level in the dark, but by the new chemical potentials of the charge carriers under illumination: the *quasi-Fermi* level of electrons ($_nE_F$) and the *quasi-Fermi* level of holes ($_pE_F$).[16,17] In other words, in the dark the thermal balance establishes that $E_F = {}_nE_F = {}_pE_F$. , meanwhile under illumination the Fermi level splits into two *quasi-Fermi* levels given by

$$_nE_F = E_F + k_BT \ln\left(\frac{n + \Delta n}{n}\right) \qquad (1.16)$$

$$_pE_F = E_F + k_BT \ln\left(\frac{p + \Delta p}{p}\right) \qquad (1.17)$$

According to the nature of the semiconductor, the relative concentration of minority charge carriers will experience a considerable increase under illumination. Concretely, a n-type semiconductor under illumination will experience an increase of the hole relative concentration. Consequently, the quasi-Fermi level of holes will be much lower than the Fermi level in the dark, whereas the quasi-Fermi level of electrons will be very similar to the one in dark. For a p-type semiconductor, the behaviour will be opposite.

Therefore, under illumination, electrons in the oxide are no longer at equilibrium with the redox potential of the electrolyte and the electron density in the conduction band is modified until it rises to a steady-state value. The difference between the Fermi level in the dark and under illumination ($_nE_F$) defines the open-circuit photovoltage of the system[18] (**Figure 1.7** and **Equation 1.18**).

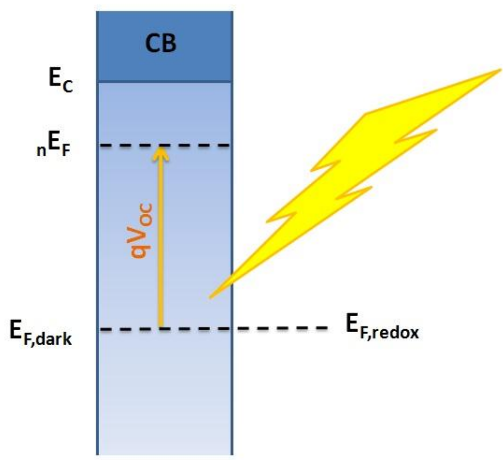

Figure 1.7: Energy diagram of a semiconductor in contact with an electrolyte at open-circuit conductions.

$$V_{OC} = {}_n E_F - E_{F,redox} = \frac{k_BT}{q} \ln\left(\frac{n_c}{n_c^0}\right) \qquad (1.18)$$

where n_c and n_c^0 is the concentration of electrons in the conduction band under illumination and in the dark, respectively (note that if $n_c = n_c^0$, the $V_{oc}= 0$). According to this equation, the free electron concentration can be defined in terms of the open-circuit voltage

$$n_c = n_c^0 \exp\left(\frac{qV_{OC}}{k_B T}\right) \qquad (1.19)$$

Upon illumination electron-hole pairs are generated in the nanocrystalline electrode. However, charge separation will not be supported by an internal electric field, as it is the case in single-crystal electrodes.[19,20] Apart from the small particle size[15] and the low doping level [21] mentioned above, we have to add that the nanoparticles are surrounded by an electrolyte with a high ionic strength. As a result, a space charge layer cannot be formed and the driving force for the transport of these charge carriers is its own concentration gradient between the different regions of the nanocrystalline network. In other words, transport of charge carriers of typical nanostructured metal-oxide electrodes takes place mainly by *diffusion*.[22,23]

2. Electron traps in nanoparticles electrodes.

Electron transport in nanostructured semiconductors, in contrast to bulk semiconductors, has peculiarities that arise from the presence of disorder in the material. The consequence of disorder in the electronic structure of the material is the appearance of localized states (**Figure 1.8**).[24,25] This is well-known since the classic works of Anderson and Mott on the existence of localized states and its implication in the occurrence of anomalous electron transport properties.[26,27] The breaking of the crystalline symmetry brings forward the appearance of defects in the lattice, either at grain boundaries or at interfaces. These defects create localized states for electrons and holes. We call these localized states "traps", because they act as electric potential wells that immobilize the charge carriers with respect to the extended states across which electric conduction takes place. [28,29]

The existence of an ensemble of traps in a disordered semiconductor is the manifestation of two types of disorder: *spatial* and *energetic*. The first is a consequence of the morphology of the material or the particular architecture of a semiconductor, and leads to the appearance of preferential directions of transport or to the occurrence of percolation limitations. The second determines how the energy of the traps is distributed in the energy spectrum of the electronic structure of the material. This is defined via an energy trap distribution or density of states $g(E)$,[30–33]

$$g(E) = \frac{\alpha N_t}{k_B T} \exp\left(\frac{-\alpha(E_c - E)}{k_B T}\right) \qquad (1.20)$$

where E_c is the energy of the transport level, N_t is the total trap density and α is a parameter that accounts for the average energy of the distribution of trap states below the transport level. Commonly, the trap parameter is related to the temperature via $\alpha = T/T_0$ where T_0 is the characteristic temperature of the distribution. A large value of T_0 with respect to T implies that the distribution is *deep*, with traps of energies much lower than the energy of the transport level. If T_0 is small, the distribution is shallow, and the energies of the traps lie closer to the transport level. In the first case, thermal release of electrons from the traps is difficult and transport is expected to be slow. The opposite situation takes place if T_0 is small. When T_0 is of the order of the ambient temperature T, thermal agitation is sufficient to excite electrons out of traps. In this case electron transport is not effectively limited by the presence of the traps. Obviously, the parameter that governs the degree of trapping for a given temperature and trap distribution is α. This parameter will hence play a central role in this thesis to describe capacitances and transport properties.

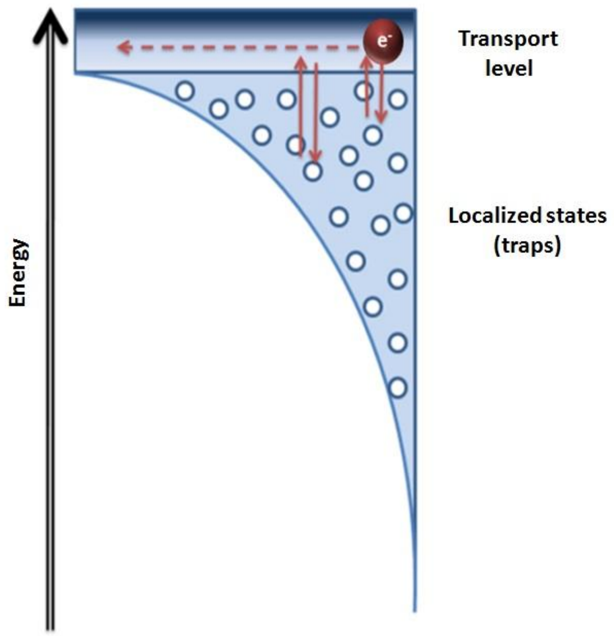

Figure 1.8: Schematic diagram of the multiple-trapping description of electron dynamic in mesoporous nanocrystalline electrode.

The electron transport in nanostructured semiconductors are influenced by this broad distribution of localized states or traps. Two main empirical observations are common. First, measured diffusion coefficients lie several orders of magnitude below bulk (single-crystal) values.[34,35] This is a consequence of the trapping-detrapping events. Electrons are trapped in these localized states and after thermal excitation they can jump again to the transport level (conduction band). The second observation is that diffusion coefficients and electron mobility are density-dependent,[23,30,36,37] with larger values found when the electron concentration is increased, either by illumination or by application of an external voltage. As the Fermi level rises, the rate of detrapping to the transport level is enhanced and the diffusion coefficient increases. Values of around 10^{-4}-10^{-6} cm^2/s are typically measured in nanostructured films of TiO_2, ZnO and SnO_2. These values are between 2 and 5 orders of magnitude below bulk values. The dependence of the electron diffusion coefficient on the electrochemical bias (either via an external voltage or induced by illumination) is a consequence of the *filling* of the trap distribution and the subsequent shift of the Fermi level.

2.1. The chemical capacitance: Electron accumulation in localized states.

The potential dependence of the stored charge defines a *chemical capacitance* of electron accumulation. The chemical capacitance C_μ is a thermodynamic quantity that reflects the capability of a system to accept or release additional carriers due to a change in the applied potential or illumination conditions. For free (conduction band) electrons, the chemical capacitance can be obtained by differentiating **Equation 1.19** with respect to Fermi level,

$$C_\mu^{CB} = q^2 \frac{\partial n_c}{\partial_n E_F} = \frac{N_c q^2}{k_B T} \exp\left(-\frac{(E_c - {}_nE_F)}{k_B T}\right) \qquad (1.21)$$

This equation defines the capacitance associated with delocalized states or transport states. However, most of the electrons in a nanostructured semiconductor are located in trap states. In the same way, the density of localized electrons in traps, n_t, can also be defined as a function of the quasi-Fermi level. The occupancy of the traps will be given by the product of the density of states (**Equation 1.20**) and the Fermi-Dirac function (**Equation 1.2**). At zero temperature the Fermi-Dirac distribution can be approximated by a step-function centred at the Fermi level. Consequently, the occupied trap density as a function of the quasi-Fermi level is given by

$$n_t = \int_{-\infty}^{+\infty} f(E)\, g(E) dE = \int_{-\infty}^{{}_nE_F} \frac{\alpha N_t}{k_B T} \exp\left(\frac{-\alpha(E_c - E)}{k_B T}\right) dE = N_t \exp\left(\frac{-\alpha(E_c - {}_nE_F)}{k_B T}\right) \qquad (1.22)$$

The chemical capacitance is determined by the accumulation of electrons in the trap distribution with respect to a variation of the Fermi level. By differentiating **Equation 1.22** with respect to the Fermi level potential one obtains

$$C_\mu^{traps} = \frac{\alpha N_t q^2}{k_B T} \exp\left(-\frac{\alpha(E_c - {}_nE_F)}{k_B T}\right) \qquad (1.23)$$

As the Fermi level is directly related to the applied voltage (see **Equation 1.20**), the capacitance can also be expressed as a function of voltage,

$$C_\mu^{traps} = C_0 \exp\left(-\frac{\alpha q V}{k_B T}\right) \qquad (1.24)$$

where C_0 is a constant that depends on the trap density, the temperature and the position of the transport level E_c. Therefore, for the density of trapped carriers, the capacitance gives a slope of $\alpha q/k_B T$ in a log-linear representation with respect to the applied voltage. As it will be discussed in subsequent chapters, surface modifications that result in shift of the band lead to parallel lines in the capacitance.

2.2. The multiple-trapping model.

It has been mentioned before that electron transport in disordered semiconductors occurs by thermal activation. The simplest model of transport that takes this feature into account is the *multiple-trapping* (MT) model (see **Figure 1.8**).[28,29,38] This can be mathematically expressed via the following expression

$$v_i = v_0 \exp\left(-\frac{(E_c - E_i)}{k_B T}\right) \qquad (1.25)$$

where v_i is the probability (expressed in units of frequency s^{-1}) that an electron is released from a trap and gets promoted to the transport level (E_c), v_0 is the so-called *attempt-to-jump* frequency, and E_i is the energy of the trap. The MT hence assumes that electron transport occurs via a succession of trapping and de-trapping events, the latter being controlled by thermal excitation from a trap to the transport level. As a consequence, electrons sitting in deep traps (with energies well below the transport level) have a low de-trapping probability and long residence times (inverse of v_i). The opposite occurs for shallow traps. Thus, deep distributions produce slow transport. An increase of the temperature or an occupation of the deepest traps accelerates transport.

It can be demonstrated by theoretical arguments and numerical simulation[39,40] that the diffusion coefficient of the MT model is

$$D_J^{MT} = \frac{n_0}{n} D_0 = \frac{N_0}{N_L} \exp\left[(E_F - E_0)\left(\frac{1}{k_B T} - \frac{1}{k_B T_0}\right)\right] D_0 \qquad (1.26)$$

which predicts an exponential dependence of the diffusion coefficient with respect to the voltage (straight line in the semilogarithmic plot with slope ($(1-\alpha)q/k_BT$). As it will be seen in **Chapter 3**, the diffusion coefficient is intimately related to the electron transport resistance.

3. References.

(1) Ashcroft, N. W.; Mermin, N. D. *Solid State Physics*; 1st ed.; Brooks Cole, 1976.
(2) Soga T. Nanostructured Material for Solar Energy Conversion. *Elsevier: 2006* **2006**.
(3) Memming, R. *Semiconductor Electrochemistry*; 1st ed.; Wiley-VCH, 2001.
(4) J. O'M Brockris. Modern Electrochemistry, Vol 2. **1970**.
(5) Crow, D. R.; Crow, D. R. *Principles and Applications of Electrochemistry*; 4th ed.; CRC Press, 1994.
(6) Marcus, R. A. On the Theory of Oxidation-Reduction Reactions Involving Electron Transfer. I. *J. Chem. Phys.* **1956**, *24*, 966–978.
(7) Marcus, R. A. Reorganization Free Energy for Electron Transfers at Liquid-Liquid and Dielectric Semiconductor-Liquid Interfaces. *J. Phys. Chem.* **1990**, *94*, 1050–1055.
(8) Dzhavakhidze, P. G.; Kornyshev, A. A.; Krishtalik, L. I. Activation Energy of Electrode Reactions: The Non-Local Effects. *J. Electroanal. Chem. Interfacial Electrochem.* **1987**, *228*, 329–346.
(9) Gerischer, H. Charge Transfer Processes at Semiconductor-Electrolyte Interfaces in Connection with Problems of Catalysis. *Surf. Sci.* **1969**, *18*, 97–122.
(10) Pleskov, Y. *Semiconductor Photoelectrochemistry*; 1986.
(11) Tributsch, H. Electrochemistry at Semiconductor and Oxidized Metal Electrodes. Von S. R. Morrison. Plenum Press, New York 1980. XIV, 401 S., Geb. $ 45.00. *Angew. Chem.* **1982**, *94*, 85–86.
(12) http://www.crcpress.com/product/isbn/9780748743780.
(13) Krishnan Rajeshwar. Fundamentals of Semiconductor Electrochemistry and Photoelectrochemistry. In *Encyclopedia of Electrochemistry*; Wiley-VCH Verlag GmbH & Co. KGaA, 2007.
(14) Gonzalez-Vazquez, J. P.; Oskam, G.; Anta, J. A. Origin of Nonlinear Recombination in Dye-Sensitized Solar Cells: Interplay between Charge Transport and Charge Transfer. *J. Phys. Chem. C* **2012**.
(15) Kelly, J. J.; Vanmaekelbergh, D. Charge Carrier Dynamics in Nanoporous Photoelectrodes. *Electrochimica Acta* **1998**, *43*, 2773–2780.
(16) Gerischer, H. The Impact of Semiconductors on the Concepts of Electrochemistry. *Electrochimica Acta* **1990**, *35*, 1677–1699.
(17) Peter, L. M. Characterization and Modeling of Dye-Sensitized Solar Cells. *J. Phys. Chem. C* **2007**, *111*, 6601–6612.
(18) Barnes, P.; Anderson, A.; Juozapavicius, M.; Liu, L.; Li, X.; Palomares, E.; Forneli, A.; O'Regan, B. Factors Controlling Charge Recombination under Dark and Light Conditions in Dye Sensitised Solar Cells. *Phys. Chem. Chem. Phys.* **2011**, *13*, 3547–3558.
(19) Yoshihara, T.; Katoh, R.; Furube, A.; Tamaki, Y.; Murai, M.; Hara, K.; Murata, S.; Arakawa, H.; Tachiya, M. Identification of Reactive Species in Photoexcited Nanocrystalline TiO2 Films by Wide-Wavelength-Range (400−2500 Nm) Transient Absorption Spectroscopy. *J. Phys. Chem. B* **2004**, *108*, 3817–3823.
(20) Hoffmann, M. R.; Martin, S. T.; Choi, W. Y.; Bahnemann, D. W. Environmental Applications of Semiconductor Photocatalysis. *Chem. Rev.* **1995**, *95*, 69–96.
(21) Boschloo, G. K.; Goossens, A.; Schoonman, J. Photoelectrochemical Study of Thin Anatase TiO2 Films Prepared by Metallorganic Chemical Vapor Deposition. *J. Electrochem. Soc.* **1997**, *144*, 1311–1317.
(22) Hagfeldt, A.; Graetzel, M. Light-Induced Redox Reactions in Nanocrystalline Systems. *Chem Rev* **1995**, *95*, 49–68.
(23) Kopidakis, N.; Schiff, E. A.; Park, N.-G.; van de Lagemaat, J.; Frank, A. J. Ambipolar Diffusion of Photocarriers in Electrolyte-Filled, Nanoporous TiO2†. *J. Phys. Chem. B* **2000**, *104*, 3930–3936.
(24) Bisquert, J. Physical Electrochemistry of Nanostructured Devices. *Phys. Chem. Chem. Phys.* **2008**, *10*, 49–72.

(25) Street, R. A.; Krakaris, A.; Cowan, S. R. Recombination Through Different Types of Localized States in Organic Solar Cells. *Adv. Funct. Mater.* **2012**, n/a – n/a.
(26) Mott, N. F. Conduction in Non-Crystalline Systems. I. Localized Electronic States in Disordered Systems. *Philos Mag* **1968**, *17*, 1259–1268.
(27) Barnes, P. R. F.; Anderson, A. Y.; Durrant, J. R.; O'Regan, B. C. Simulation and Measurement of Complete Dye Sensitised Solar Cells: Including the Influence of Trapping, Electrolyte, Oxidised Dyes and Light Intensity on Steady State and Transient Device Behaviour. *Phys. Chem. Chem. Phys.* **2011**, *13*.
(28) Tiedje, T.; Rose, A. A Physical Interpretation of Dispersive Transport in Disordered Semiconductors. *Solid State Commun.* **1981**, *37*, 49–52.
(29) Vanmaekelbergh, D.; de Jongh, P. E. Electron Transport in Disordered Semiconductors Studied by a Small Harmonic Modulation of the Steady State. *Phys. Rev. B* **2000**, *61*.
(30) Anta, J. A.; Mora-Sero, I.; Dittrich, T.; Bisquert, J. Interpretation of Diffusion Coefficients in Nanostructured Materials from Random Walk Numerical Simulation. *Phys. Chem. Chem. Phys.* **2008**, *10*, 4478–4485.
(31) Anta, J. A.; Mora-Sero, I.; Dittrich, T.; Bisquert, J. Dynamics of Charge Separation and Trap-Limited Electron Transport in TiO2 Nanostructures. *J. Phys. Chem. C* **2007**, *111*, 13997–14000.
(32) Lagemaat, J. van de; Frank, A. J. Effect of the Surface-State Distribution on Electron Transport in Dye-Sensitized TiO2 Solar Cells: Nonlinear Electron-Transport Kinetics. *J. Phys. Chem. B* **2000**, *104*, 4292–4294.
(33) Bisquert, J.; Fabregat-Santiago, F.; Mora-Sero, I.; Garcia-Belmonte, G.; Barea, E. M.; Palomares, E. A Review of Recent Results on Electrochemical Determination of the Density of Electronic States of Nanostructured Metal-Oxide Semiconductors and Organic Hole Conductors. *Inorganica Chim. Acta* **2008**, *361*, 684–698.
(34) Boschloo, G.; Hagfeldt, A. Activation Energy of Electron Transport in Dye-Sensitized TiO2 Solar Cells. *J. Phys. Chem. B* **2005**, *109*, 12093–12098.
(35) Forro, L.; Chauvet, O.; Emin, D.; Zuppiroli, L.; Berger, H.; Levy, F. High Mobility N-type Charge Carriers in Large Single Crystals of Anatase (TiO2). *J. Appl. Phys.* **1994**, *75*, 633–635.
(36) Peter, L. M.; Wijayantha, K. G. U. Intensity Dependence of the Electron Diffusion Length in Dye-Sensitised Nanocrystalline TiO2 Photovoltaic Cells. *Electrochem. Commun.* **1999**, *1*, 576–580.
(37) Frank, A. J.; Kopidakis, N.; Lagemaat, J. van de. Electrons in Nanostructured TiO2 Solar Cells: Transport, Recombination and Photovoltaic Properties. *Coord. Chem. Rev.* **2004**, *248*, 1165–1179.
(38) Schmidlin, F. W. Theory of Trap Controlled Transient Photoconduction. *Bull. Am. Phys. Soc.* **1977**, *22*, 346–346.
(39) Gonzalez-Vazquez, J.; Anta, J. A.; Bisquert, J. Determination of the Electron Diffusion Length in Dye-Sensitized Solar Cells by Random Walk Simulation: Compensation Effects and Voltage Dependence. *J. Phys. Chem. C* **2010**, *114*, 8552–8558.
(40) Bisquert, J.; Mora-Seró, I. Simulation of Steady-State Characteristics of Dye-Sensitized Solar Cells and the Interpretation of the Diffusion Length. *J. Phys. Chem. Lett.* **2010**, *1*, 450–456.

Chapter 2:

The semiconductor-electrolyte junction: Photocatalytic applications

1. Introduction.

The history of *photoelectrochemistry* of semiconductors[1] starts in the 19th century. It is difficult to quote the first work of photoelectrochemistry, although it seems that it was the work realized 170 years ago by Becquerel.[2] This author found that an electric current is generated when a semiconductor electrode immersed in an acidic aqueous solution is illuminated. Some concepts that have served as a basis for the development of the photoelectrochemistry of semiconductors are related to the photoelectrochemical behaviour of adsorbed layers and oxidized metals.[3] The photoelectrochemistry of semiconductors, as independent scientific branch, started in the 1950s, when Brattain and Garrett[4] managed to establish the relationship between the photoelectrochemical properties of monocrystalline semiconductors and their typical electronic structure. At the same time, this discipline started to use the principles of the classical theory of electrochemistry.

A fundamental advance in the development of this discipline was constituted by the work of Gerischer.[5] Photoelectrochemistry received a considerable impulse in 1970s when Fujishima and Honda[6] demonstrated water decomposition into oxygen and hydrogen under UV light illumination. Using a cell consisting of a semiconductor (TiO_2) and a metallic electrode (counter-electrode) immersed in an aqueous electrolyte, light energy was used to obtain chemical energy.

At present, fundamental studies try to clarify the essentials of electron transfer across the semiconductor/electrolyte interface. Starting from the initial Gerischer model, different systems have been studied, such as nanocrystalline electrodes, quantum dots arrays, dispersions of nanoparticles, hybrid materials, etc.[7] Besides, studies aim at a systematic optimization of the physicochemical material properties governing the photocatalytic process.

It is important to mention that photoelectrochemistry is intimately related to *heterogeneous photocatalysis* in solution,[8] which is, and has been, extensively studied due to its more direct applications. For photocatalysis to take place oxidation reactions (based on the transfer of photogenerated holes) and reduction reactions (involving photogenerated electrons) have to occur simultaneously. The overall reaction relies on a precise balance of these two processes. In the case of catalyst particles or particle agglomerates, this balance is limited to discrete units where oxidation and reduction processes occur in parallel with electron–hole recombination. Such photocatalyst particles or agglomerates may therefore be considered photoelectrochemical cells under short-circuit conditions.[9] A main advantage of electrochemistry for the analysis and manipulation of photocatalytic reactions is based on the possibility of separating anodic and cathodic processes at different electrodes and of performing experiments under potentiostatic control. This provides a very systematic and controlled way of gaining fundamental knowledge on processes of relevance for the overall photocatalytic event.

2. Photocatalysis.

2.1. Basic concepts and principles.

Photocatalysis relies on photochemical reactions at the surface of a solid semiconductor (*photocatalyst*), which are induced by the absorption of photons. The term photocatalysis is still under debate,[10] since it implies that during the reaction, photons are acting as catalyst, when in fact they are consumed like a reagent in a chemical process. Therefore, photocatalysis might be defined as the acceleration of a photoreaction by the presence of a photocatalyst. In the case of heterogeneous photocatalysis, the photocatalysts are normally particles of semiconductor oxides that, under illumination, photocatalyze different redox processes. One of the main practical aspects of heterogeneous photocatalysis is the decontamination of pollutants in solution as well as in the gas phase. The most commonly employed semiconductor in this regard is TiO_2 due to its favourable properties with respect to other semiconductors: (1) high photoactivity together with (2) high chemical stability and photostability.

All processes of decontamination or degradation of pollutants are based on a similar action mechanism (**Figure 2.1**). When the semiconductor oxide is exposed to photons with an energy exceeding the semiconductor's band gap, electron-hole pairs are formed. Valance band holes (h^+) are strong oxidizing agents in the case of a typical photocatalyst like TiO_2 and react with electron donor species (D) or generate active intermediates. On the other hand, the photogenerated electrons (e^-) are moderate reduction agents and react with electron acceptor species (A). Both oxidation and reduction reactions take place simultaneously and compete with the recombination (R) of photogenerated electrons and holes. By this way, the system is self-organized two-dimensionally in regions with reducing capability (with trapped electrons) and regions with oxidizing capability, where the holes are transferred to e.g. organic molecules.

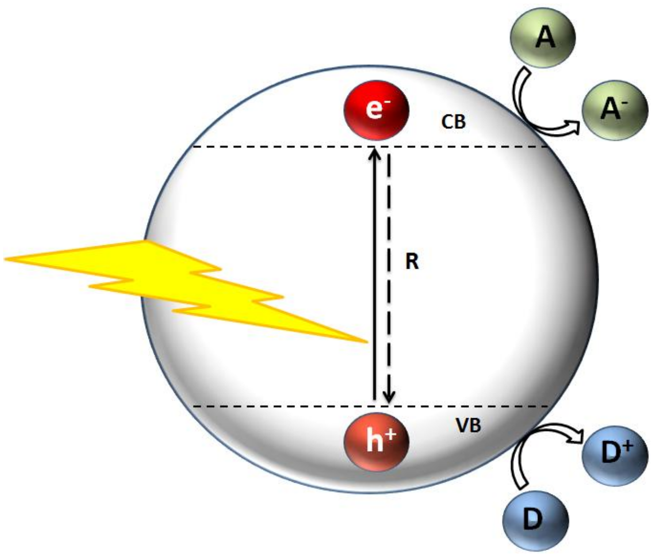

Figure 2.1: Scheme of photoinduced charge separation processes and redox reactions induced by photogenerated charge carriers (electrons and holes).

2.2. Mechanisms of photocatalysis.

Different models have been proposed to explain the mechanism governing photocatalysis on TiO_2. The model of Gerischer-Heller,[11–14] which is based on the balance between anodic processes (oxygen evolution, oxidation of organic compounds) and cathodic processes (reduction of oxygen to superoxide, peroxide or water; reductive doping of the semiconductor by means of hydrogen insertion). This model is based on electron trapping in certain areas of the oxide surface generating Ti(III) sites. A local increase of the electrical conductivity favours electron transfer to adsorbed species or species in solution. The detailed mechanism of photocatalytic processes, however, is not yet well understood[15] especially for the initial stages of the interfacial charge transfer. It is well-known that the electron transfer from the conduction band to oxygen, which is one of the most relevant electron acceptors in photocatalysis, is usually the rate-determining step in the global photocatalytic process.[16,17]

Different models describing the transfer of photogenerated holes across the semiconductor/electrolyte interface have been proposed to explain experimental findings. Some authors claimed that the generation of OH radicals would be able to diffuse away from the semiconductor surface to induce oxidation reactions of dissolved species. [18,19] The direct/indirect model on the other hand considers hole transfer via two possible paths:[20,21]

- Indirect transfer (IT), where a hole trapped at the semiconductor surface is isoenergetically (without energy loss, elastic process) transferred to dissolved pollutant molecules.
- Direct transfer (DT), where a VB free hole is adiabatically transferred (with energy loss, inelastic process) to (specifically) adsorbed pollutant molecules.

The ability of the model to explain experimental findings was highlighted by studying the photooxidation of model molecules such as methanol and formic acid, which differ significantly in their adsorption behaviour. This determines the branching ratio between the direct and the indirect transfer paths.

3. Photoelectrocatalysis.

Photoelectrocatalysis relies on the improvement of the photocatalytic performance of an immobilized catalyst film by the action of an externally applied electrical field. The external field enhances the separation of photogenerated electrons and holes and drives oxidation and reduction reactions on two spatially separated electrodes. Hence, oxidation and reduction half-reactions, which in conventional photocatalysis (i.e. in the absence of an externally applied potential) take place on a single semiconductor particle or aggregate, can be in this case decoupled leading to decreased charge carrier recombination. A prerequisite for photoelectrocatalysis is the immobilization of the electro- and photoactive material on a conducting substrate, which allows for externally modifying the Fermi level of the photocatalyst. Similar to conventional photocatalysis, the flow of electrons towards the surface or to the conductive substrate must equal the corresponding flow of holes.

Photocatalysis	Photoelectrocatalysis
No control of potential applied	Control of potential applied
Suspension or thin film	Thin film
Non-/conductive substrate	Conductive substrate

Table 2.1: Differences and similitaries between photocatalysis and photoelectrocatalysis

The quantum efficiency of a photocatalyst is defined as the ratio between the rate of the photocatalytic reaction in units of elementary charge and the flow of incident photons. In photoelectrocatalysis the quantum efficiency is increased by an external electrical field, which allows for spatially separating the photogenerated charge carriers (**Figure 2.2**). In the typical case, where the photoactive material forms part of a photoanode (n-type semiconductor), photogenerated electrons will flow via the external circuit to the counter-electrode where they induce a reduction reaction. The oxidation reaction, on the other hand, takes place at the semiconductor.

From a fundamental point of view, the application of a photoactive material in the form of a thin film electrode opens the possibility of using standard electrochemical methods[22] for studying independently the anodic and cathodic parts of the overall reaction.

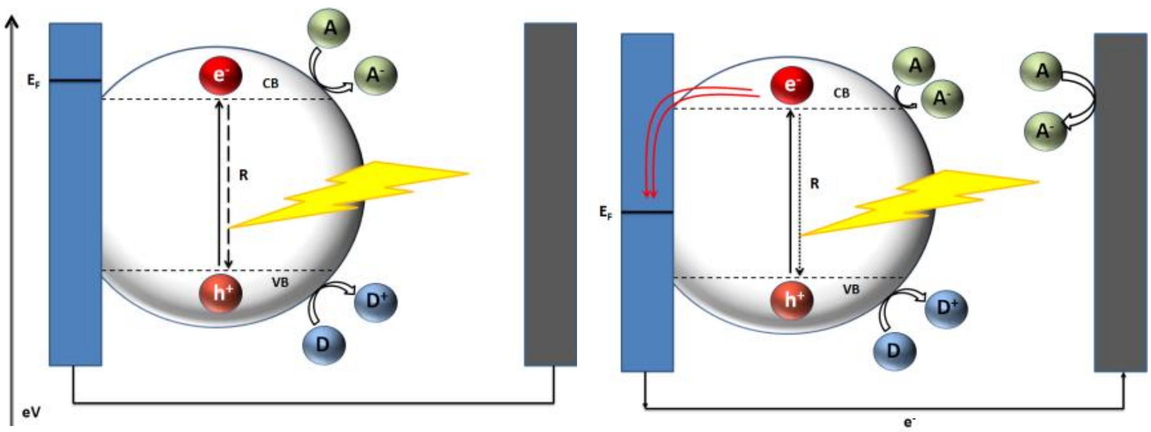

Figure 2.2: Scheme of a photoelectrochemical cell at two positions of the Fermi level. This can be induced by application of an external bias or under exposure to photons with energy exceeding the band gap.

The high relevance of semiconductor electrochemistry in the field of photocatalysis is highlighted by

- studies of decontamination or degradation of organic and inorganic compounds in solution or in the gas phase.[23–26]
- preparation and characterization of new catalysts.[27,28]
- Hydrogen generation and water splitting.[29–31]
- Fundamental studies.[32–34]

In this context, the impact of electrochemistry on photocatalysis can be ascribed to two main aspects: the possibility to gain fundamental knowledge by using electrochemical methods as an analytical tool and the improvement of the performance of an immobilized catalyst film by the action of an externally applied electrical field.

4. Approaches to modify the photocatalytic activity.

Heterogeneous photocatalysis in suspension or on thin semiconductor layers present a series of intrinsic limitations, which can reduce the efficiency of photoinduced redox processes. They are the following

- Low light absorption in the visible range of the solar spectrum.
- Competition between recombination of photogenerated holes and electrons with interfacial charge transfer.
- Different rates of interfacial charge transfer of electrons and holes that can limit the global process by introducing rate-determining steps.[35]

The use of wide band gap semiconductor oxides such as anatase TiO_2 (3.2eV) represents an advantage with respect to photocorrosion processes. Nevertheless, this characteristic limits the light absorption to the UV region of the solar spectrum. However, the spectral response of semiconductors can be improved by means of different strategies:

- The doping of the semiconductor, by the introduction of dopants; or in case of metal oxides, by the introduction of oxygen deficiency.[36,37] The inclusion of metals and non-metals (V, Cr, Mn, Fe, N, C, S) in the crystalline network of the semiconductor oxide is a method that allows for the displacement of the absorption threshold, from the UV region to the visible. The optical response of materials is determined by the electronic structure, which is related to chemical composition, structural properties and physical dimensions.
- The sensitization of the semiconductor with dye molecules that absorb light in the visible range and that are capable of injecting electrons into the electronic structure of the semiconductor from its excited state.[38] This strategy has successfully been applied in photovoltaic systems (Dye-Sensitized Solar Cells or Grätzel cells).[39,40] (See **Chapter 3**).

As discussed in the previous chapter, it is generally accepted that due to the penetration of the mesoporous network by an electrolyte of high ionic strength and due to the small size and the low doping level of the particle no significant electric fields are present in the semiconductor thin film.[41,42] Electron transport is, therefore, based on electron diffusion and consequently recombination of charge carriers depends critically on the nature of the semiconductor, as well as on the interfacial redox reactions. The decrease of charge carrier recombination is a prerequisite to improve the photocatalytic performance of semiconductor electrodes.

To accelerate the interfacial charge transfer processes and to reduce recombination, systems based on metal/semiconductor or semiconductor/semiconductor *nanocomposites* have been used.[43,44] In the latter case semiconductors with different band gaps are used.

The connection of two semiconductors allows to increase the charge separation and to extend the range of photoexcitation energies.

Another strategy is the use of systems with quantum confinement (*quantum dots*),[45] the superficial modification by adsorption[46,47] or the modification of the semiconductor bulk.[48,49] A purely electrochemical method has been studied in this thesis to improve the photocatalytic activity. This method consist of an electron accumulation in the semiconductor accompanied by charge compensation via proton/cation adsorption or intercalation.[50] The influence of electrochemical doping on the photoelectrocatalytic and photovoltaic properties of mesoporous TiO_2 films will be discussed in **Chapters 5** and **6**.

5. References.

(1) Pleskov, Y. *Semiconductor Photoelectrochemistry*; 1986.
(2) E. Becquerel. *Comptes Rendus Acad. Sci.* **1839**, *9*, 145–149.
(3) V. I. Veselovsky. *Zh Fiz Khim* **1946**, *20*.
(4) Brattain, W. H.; Garrett, C. G. B. Experiments on the Interface between Germanium and an Electrolyte. *Bell Syst. Tech. J.* **1955**, *34*, 129–176.
(5) Gerischer, H.; Lübke, M. On the Etching of Silicon by Oxidants in Ammonium Fluoride Solutions: A Mechanistic Study. *J. Electrochem. Soc.* **1988**, *135*, 2782–2786.
(6) FUJISHIMA, A.; HONDA, K. Electrochemical Photolysis of Water at a Semiconductor Electrode. *Nature* **1972**, *238*, 37–38.
(7) Koval, C. A.; Howard, J. N. Electron Transfer at Semiconductor Electrode-Liquid Electrolyte Interfaces. *Chem. Rev.* **1992**, *92*, 411–433.
(8) M. A. Blesa. Eliminación de Contaminantes Por Fotocatálisis Heterogénea. Usos de Óxidos Semiconductores Y Materiales Relacionados Para Aplicaciones Ambientales Y Ópticas. *Elimin. Contam. Por Fotocatálisis Heterogénea Texto Colect. Elabor. Por Red CYTED VIII-G* **2001**.
(9) Bard, A. J. Photoelectrochemistry and Heterogeneous Photo-Catalysis at Semiconductors. *J. Photochem.* **1979**, *10*, 59–75.
(10) Mills, A.; Le Hunte, S. An Overview of Semiconductor Photocatalysis. *J. Photochem. Photobiol. Chem.* **1997**, *108*, 1–35.
(11) Wang, C. M.; Heller, A.; Gerischer, H. Palladium Catalysis of O2 Reduction by Electrons Accumulated on TiO2 Particles during Photoassisted Oxidation of Organic Compounds. *J. Am. Chem. Soc.* **1992**, *114*, 5230–5234.
(12) Gerischer, H.; Heller, A. Photocatalytic Oxidation of Organic Molecules at TiO2 Particles by Sunlight in Aerated Water. *J. Electrochem. Soc.* **1992**, *139*, 113–118.
(13) Schwitzgebel, J.; Ekerdt, J. G.; Gerischer, H.; Heller, A. Role of the Oxygen Molecule and of the Photogenerated Electron in TiO2-Photocatalyzed Air Oxidation Reactions. *J. Phys. Chem.* **1995**, *99*, 5633–5638.
(14) Gerischer, H.; Heller, A. The Role of Oxygen in Photooxidation of Organic Molecules on Semiconductor Particles. *J. Phys. Chem.* **1991**, *95*, 5261–5267.
(15) Minero, C.; Mariella, G.; Maurino, V.; Pelizzetti, E. Photocatalytic Transformation of Organic Compounds in the Presence of Inorganic Anions. 1. Hydroxyl-Mediated and Direct Electron-Transfer Reactions of Phenol on a Titanium Dioxide−Fluoride System. *Langmuir* **2000**, *16*, 2632–2641.
(16) Gerischer, H. Photocatalysis in Aqueous Solution with Small TiO2 Particles and the Dependence of the Quantum Yield on Particle Size and Light Intensity. *6th Int. Fisch. Symp. Nanotechniques Electeochemistry* **1995**, *40*, 1277–1281.
(17) Kesselman, J. M.; Shreve, G. A.; Hoffmann, M. R.; Lewis, N. S. Flux-Matching Conditions at TiO2 Photoelectrodes: Is Interfacial Electron Transfer to O2 Rate-Limiting in the TiO2-Catalyzed Photochemical Degradation of Organics? *J. Phys. Chem.* **1994**, *98*, 13385–13395.
(18) Turchi, C. S.; Ollis, D. F. Photocatalytic Degradation of Organic Water Contaminants: Mechanisms Involving Hydroxyl Radical Attack. *J. Catal.* **1990**, *122*, 178–192.
(19) Helz, G. R.; Zepp, R. G.; Crosby, D. G. *Aquatic and Surface Photochemistry*; Lewis Publishers: Boca Raton, 1994.
(20) Villarreal, T. L.; Gómez, R.; González, M.; Salvador, P. A Kinetic Model for Distinguishing between Direct and Indirect Interfacial Hole Transfer in the Heterogeneous Photooxidation of Dissolved Organics on TiO2 Nanoparticle Suspensions. *J. Phys. Chem. B* **2004**, *108*, 20278–20290.
(21) Mora-Sero, I.; Villarreal, T. L.; Bisquert, J.; Pitarch, A.; Gomez, R.; Salvador, P. Photoelectrochemical Behavior of Nanostructured TiO2 Thin-Film Electrodes in Contact with Aqueous Electrolytes Containing Dissolved Pollutants: A Model for

Distinguishing between Direct and Indirect Interfacial Hole Transfer from Photocurrent Measurements. *J. Phys. Chem. B* **2005**, *109*, 3371–3380.
(22) Fabregat-Santiago, F.; Mora-Sero, I.; Garcia-Belmonte, G.; Bisquert, J. Cyclic Voltammetry Studies of Nanoporous Semiconductors. Capacitive and Reactive Properties of Nanocrystalline TiO2 Electrodes in Aqueous Electrolyte. *J. Phys. Chem. B* **2003**, *107*, 758–768.
(23) Vinodgopal, K.; Kamat, P. V. Enhanced Rates of Photocatalytic Degradation of an Azo Dye Using SnO2/TiO2 Coupled Semiconductor Thin Films. *Environ. Sci. Technol.* **1995**, *29*, 841–845.
(24) Martínez-Huitle, C. A.; Brillas, E. Decontamination of Wastewaters Containing Synthetic Organic Dyes by Electrochemical Methods: A General Review. *Appl. Catal. B Environ.* **2009**, *87*, 105–145.
(25) Fraga, L. E.; Anderson, M. A.; Beatriz, M. L. P. M. A.; Paschoal, F. M. M.; Romão, L. P.; Zanoni, M. V. B. Evaluation of the Photoelectrocatalytic Method for Oxidizing Chloride and Simultaneous Removal of Microcystin Toxins in Surface Waters. *Electrochem. Healthy PLANETENVIRONMENTAL Anal. Eng. Asp. Sel. Pap. 6th ISE Spring Meet. 16-19 March 2008 Foz Iguaçu Braz.* **2009**, *54*, 2069–2076.
(26) Nissen, S.; Alexander, B. D.; Dawood, I.; Tillotson, M.; Wells, R. P. K.; Macphee, D. E.; Killham, K. Remediation of a Chlorinated Aromatic Hydrocarbon in Water by Photoelectrocatalysis. *Environ. Pollut.* **2009**, *157*, 72–76.
(27) Osugi, M. E.; Zanoni, M. V. B.; Chenthamarakshan, C. R.; de Tacconi, N. R.; Woldemariam, G. A.; Mandal, S. S.; Rajeshwar, K. Toxicity Assessment and Degradation of Disperse Azo Dyes by Photoelectrocatalytic Oxidation on Ti/TiO2 Nanotubular Array Electrodes. *J. Adv. Oxid. Technol.* **2008**, *11*, 425–434.
(28) Liu, W.; Quan, X.; Cui, Q.; Ma, M.; Chen, S.; Wang, Z.-J. Ecotoxicological Characterization of Photoelectrocatalytic Process for Degradation of Pentachlorophenol on Titania Nanotubes Electrode. *Ecotoxicol. Environ. Saf.* **2008**, *71*, 267–273.
(29) Sun, Y.; Murphy, C. J.; Reyes-Gil, K. R.; Reyes-Garcia, E. A.; Lilly, J. P.; Raftery, D. Carbon-Doped In2O3 Films for Photoelectrochemical Hydrogen Production. *Int. J. Hydrog. Energy* **2008**, *33*, 5967–5974.
(30) Ichikawa, S. Photoelectrocatalytic Production of Hydrogen from Natural Seawater under Sunlight. *Int. J. Hydrog. Energy* **1997**, *22*, 675–678.
(31) Szklarczyk, M.; Bockris, J. O. Hydrogen Production through Photoelectrocatalysis on P-Type Molybdenum Sulphide. *Int. J. Hydrog. Energy* **1984**, *9*, 831–834.
(32) Szklarczyk, M.; Bockris, J. O. Photoelectrocatalysis and Electrocatalysis on P-Silicon. *J. Phys. Chem.* **1984**, *88*, 1808–1815.
(33) Szklarczyk, M.; Bockris, J. O. Photoelectrocatalysis on Silicon in Solar Light. *Appl. Phys. Lett.* **1983**, *42*, 1035–1036.
(34) Alonso-Vante, N.; Colell, H.; Tributsch, H. Influence of Low Temp. and Electrical Field Strength on Oxygen Evolution (photo)catalysis with N-Ruthenium Disulfide Electrodes. *J. Phys. Chem.* **1993**, *97*, 8261–8268.
(35) Minero, C. Kinetic Analysis of Photoinduced Reactions at the Water Semiconductor Interface. *Catal. Today* **1999**, *54*, 205–216.
(36) Fujishima, A.; Zhang, X.; Tryk, D. A. TiO2 Photocatalysis and Related Surface Phenomena. *Surf. Sci. Rep.* **2008**, *63*, 515–582.
(37) Chen, X.; Mao, S. S. Titanium Dioxide Nanomaterials: Synthesis, Properties, Modifications, and Applications. *Chem. Rev.* **2007**, *107*, 2891–2959.
(38) Lana-Villarreal, T.; Rodes, A.; Pérez, J. M.; Gómez, R. A Spectroscopic and Electrochemical Approach to the Study of the Interactions and Photoinduced Electron Transfer between Catechol and Anatase Nanoparticles in Aqueous Solution. *J. Am. Chem. Soc.* **2005**, *127*, 12601–12611.
(39) O'Regan, B.; Gratzel, M. A Low-Cost, High-Efficiency Solar-Cell Based on Dye-Sensitized Colloidal Tio2 Films. *Nature* **1991**, *353*, 737–740.

(40) Grätzel, M. Recent Advances in Sensitized Mesoscopic Solar Cells. *Acc. Chem. Res.* **2009**, *42*, 1788–1798.

(41) Sodergren, S.; Hagfeldt, A.; Olsson, J.; Lindquist, S. E. Theoretical-Models for the Action Spectrum and the Current-Voltage Characteristics of Microporous Semiconductor-Films in Photoelectrochemical Cells. *J. Phys. Chem.* **1994**, *98*, 5552–5556.

(42) Watson, D. F.; Meyer, G. J. ELECTRON INJECTION AT DYE-SENSITIZED SEMICONDUCTOR ELECTRODES. *Annu. Rev. Phys. Chem.* **2004**, *56*, 119–156.

(43) Rajeshwar, K.; de Tacconi, N. R.; Chenthamarakshan, C. R. Semiconductor-Based Composite Materials: Preparation, Properties, and Performance. *Chem. Mater.* **2001**, *13*, 2765–2782.

(44) Harraz, F. A.; Ismail, A. A.; Al-Sayari, S. A.; Al-Hajry, A. Novel A-Fe2O3/polypyrrole Nanocomposite with Enhanced Photocatalytic Performance. *J. Photochem. Photobiol. Chem.* **2015**, *299*, 18–24.

(45) Henglein, A. Small-Particle Research: Physicochemical Properties of Extremely Small Colloidal Metal and Semiconductor Particles. *Chem. Rev.* **1989**, *89*, 1861–1873.

(46) Abdullah, M.; Low, G. K. C.; Matthews, R. W. Effects of Common Inorganic Anions on Rates of Photocatalytic Oxidation of Organic Carbon over Illuminated Titanium Dioxide. *J. Phys. Chem.* **1990**, *94*, 6820–6825.

(47) Erjavec, B.; Kaplan, R.; Pintar, A. Effects of Heat and Peroxide Treatment on Photocatalytic Activity of Titanate Nanotubes. *Symp. Catal. Pollut. Treat. 11th Ed. Eur. Congr. Catal. Eur. XI Lyon Fr.* **2015**, *241, Part A*, 15–24.

(48) Wang, C. M.; Mallouk, T. E. Photoelectrochemistry and Interfacial Energetics of Titanium Dioxide Photoelectrodes in Fluoride-Containing Solutions. *J. Phys. Chem.* **1990**, *94*, 423–428.

(49) Gatto, S.; Sansotera, M.; Persico, F.; Gola, M.; Pirola, C.; Panzeri, W.; Navarrini, W.; Bianchi, C. L. Surface Fluorination on TiO2 Catalyst Induced by Photodegradation of Perfluorooctanoic Acid. *Symp. Catal. Pollut. Treat. 11th Ed. Eur. Congr. Catal. Eur. XI Lyon Fr.* **2015**, *241, Part A*, 8–14.

(50) Lyon, L. A.; Hupp, J. T. Energetics of the Nanocrystalline Titanium Dioxide/Aqueous Solution Interface: Approximate Conduction Band Edge Variations between H0 = −10 and H- = +26. *J Phys Chem B* **1999**, *103*, 4623–4628.

Chapter 3:

The semiconductor-electrolyte junction: Photovoltaic applications

1. Introduction.

Most of the solar cells used up to now are bulk-type, single- or multi-crystalline silicon solar cells. The typical structure of silicon cells (bulk-type) is based on the combination of a thin n-type emitter layer (1μm) and a thick p-type substrate (300μm). This combination is known as p-n junction[1] and is fabricated by doping different regions of the same semiconductor with different impurities. In this way, an interface between n-type and p-type material is obtained, which creates a built-in electric field as a consequence of the different chemical potentials. This intrinsic electric field favours charge separation of electron-hole pairs when a photon of higher energy than the band gap is absorbed. In particular, the photogenerated electrons and holes diffuse toward the space charge layer in the interface where they become separated by the internal electrical field. This effective charge separation is due to the relative long diffusion length of electrons and holes in crystalline silicon.

There have been several theoretical calculations on the maximum power conversion obtainable for solar radiation using a single-junction (p-n) solar cell. The theoretical considerations of Shockley and Queisser establish an upper limit of the efficiency of 31% for a semiconductor with a bad gap energy of 1.3 eV under AM 1.5 illumination.[2] It has been known for some time that a drastic reduction of cell cost and increase of the conversion efficiency cannot be expected by using conventional materials and solar cell structures. Based on the theoretical maximum conversion efficiency and on the nature of the materials, photovoltaic cells can be grouped in different categories (**Figure 3.1**).

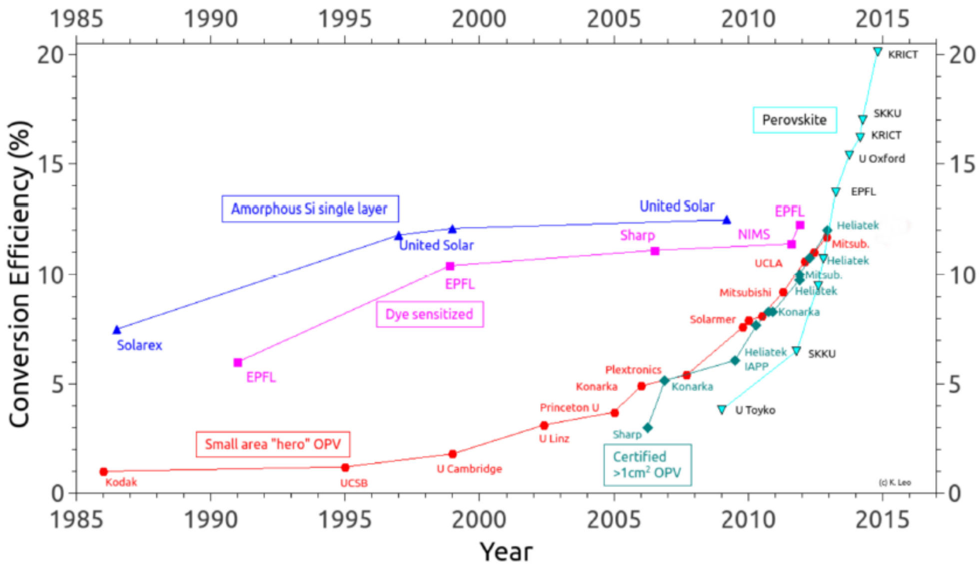

Figure 3.1: Certificated maximum record efficiency (%) for different thin film technologies (taken from www.orgworld.de)

Crystalline silicon solar cells (*first generation*) showed a confirmed record efficiency of 25% in 2011;[3] however these cells use materials of high purity with low concentrations of structural defects, which is associated to considerable manufacturing costs. The *second generation* of solar cells are based in a thin film technology (≈2μm). This is the case of amorphous silicon cells, which attracted attention for the possibility to reduce the manufacturing cost with respect to bulk-type crystalline silicon cells. However, other materials for thin film technologies have been explored, like for example CdTe.[4–6] These materials are direct band gap semiconductors. For this reason, only a thin film is required for complete light absorption. The highest performance obtained among all thin-film technologies was 19.4%[3] for a CIGS cell of 1 cm^2. Nevertheless, the main issue associated with this kind of devices is that they contain toxic materials.

In the 1990s, a new concept of solar cells (*third generation*) based on nanostructured and organic materials were conceived as a new approach to low-cost and biocompatible photovoltaic devices. In particular the most active research fields comprise organic heterojuntion solar cells,[7] extremely thin absorber (ETA) cells,[8,9] hybrid solar cells[10,11] and dye-sensitized solar cells (DSSC).[12] This technology is one of the main topics of study in this thesis.

DSSCs combine the processes of absorption of light and charge separation thanks to the association of dye molecules and a semiconductor with a wide band gap. This architecture was first developed by O'Regan and Grätzel in 1991[12] although, energy conversion in a dye-sensitized TiO_2 electrode immersed in an electrolyte had already been reported by Vlachopoulos in 1988.[13] Although the charge separation was found to occur with a relatively large quantum yield, the energy conversion efficiency was not high due to the low light absorption capabilities of the cells. This problem was overcome by O'Regan and Grätzel by using a mesoporous electrode that increases the surface area. By employing an optimal electrode thickness and designing proper sensitization dyes, they measured as energy conversion efficiency over 11%.[14] This figure has slowly been improved over the years and a new record efficiency of 13% has been reported recently using cobalt complexes as redox mediators and a modified porphyrin as dye molecule.[15]

Leaving aside records in energy conversion efficiency, DSSCs have been considered an attractive new class of solar cells and a promising alternative to silicon solar cells due to a collection of appealing properties:

- Low cost: The manufacturing cost of these cells is expected to be relatively low because they are assembled from cheap materials and their preparation does not require high temperatures or vacuum.
- Flexibility: It is possible to deposit these materials onto flexible polymer materials that can be used as substrates.
- Colour availability: The colour of these cells can be controlled by changing the molecular structure of the dye or by playing with the refraction index.
- Potential for indoor applications: Under relative low intensity irradiation conditions, these cells maintain a relatively good performance.

During the development of this thesis, a new concept of solar cells based on a new perovskite material has appeared. This kind of solar cells, that in its initial stages employ perovskite as light absorbers instead of dye molecules, has emerged from the field of DSSCs.[12,16,17] The perovskite appeared as an alternative approach, such as quantum dots or extremely thin semiconductor absorber layers, that should enable complete light absorption in much thinner films and may in addition open possibilities for pushing the photoactivity further into the near-infrared (NIR).[18–20] The first peer-reviewed journal publication of a perovskite-sensitized solar cell came up in 2009, where the $CH_3NH_3PbI_3$ absorber resulted in a 3.5% efficient sensitized solar cell employing the iodide/tri-iodide redox couple.[21] N. G. Park and co-workers improved on this further via optimization of the titania surface and perovskite processing, reporting a 6.5% $CH_3NH_3PbI_3$ liquid electrolyte solar cell.[22] However, the main handicap of these electrolyte-based perovskite-sensitized cells is that the perovskite absorber dissolves or decomposes in the electrolyte, and the cells rapidly degrade within a few minutes.[21,22] The solution was to optimize the perovskite absorber with a solid-state hole conductor, as Miyasaka and co-workers had initially attempted in 2008.[23] Fortuitously, the collaboration between some researchers (Snaith, T. N. Murakami, T. Miyasaka, N. G. Park, M. Grätzel and co-workers) developed solid-state perovskite solar cells employing (2,2(7,7)-tetrakis-(N,Ndipmethoxyphenylamine) 9,9(-spirobifluorene)) (*spiro-OMe-TAD*) as the hole transporter[24] and presented maximum full sun power conversion efficiencies of between 8 - 10% employing $CH_3NH_3PbI_{3-x}Cl_x$ mixed halide perovskite and $CH_3NH_3PbI_3$, respectively.[25,26] At the time of writing, the record efficiency with this kind of solar cells is 20.1% (Figure 3.1) The primary advantage that the perovskite absorbers have over molecular dyes is that they are much stronger light absorbers and over a broader range, enabling complete light absorption in films as thin as 500 nm. Due to the impressive performance, the latest investigation lines do not try to push forward the efficiencies of such devices, but to improve its long-term stability instead.

2. Structure of Dye-Sensitized Solar Cells.

A DSSC is a photovoltaic device where the working electrode consists of a mesoporous semiconductor oxide film with dye molecules adsorbed on its surface by chemical bonds to absorb the sunlight. In addition, an electrolyte solution containing a redox mediator and a counter-electrode are needed to complete these light harvesting systems and energy conversion devices (**Figure 3.2**). The photophysical, photochemical, optical and electrochemical properties depend critically on each component and on an adequate combination of them.

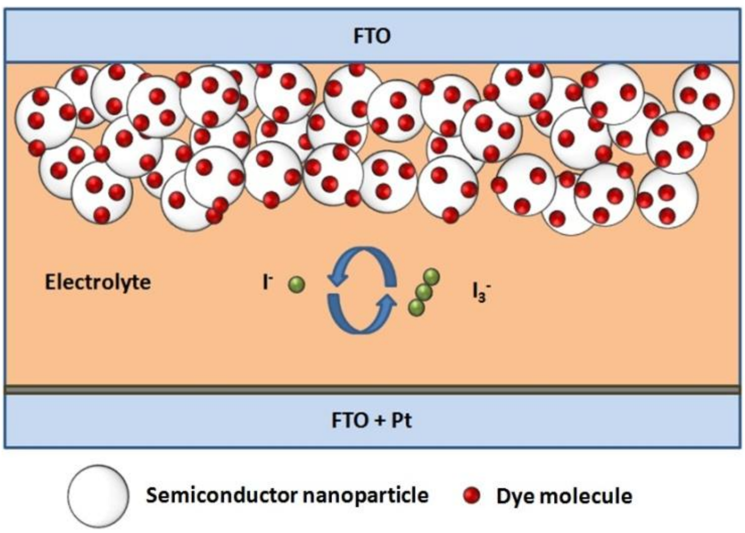

Figure 3.2: Schematic view of the structure of DSSC.

2.1. Semiconductor: Working electrode.

The semiconductor oxide film acts as the electron conductor (n-type) and physical support of the sensitizer dye molecules in DSSC. An important factor for a high adsorption of light by dye molecules is its mesoporous condition. A mesoporous structure could have a surface area available for dye absorption more than a thousand times larger than a flat electrode of the same geometric area. On the other hand, it is known that the structure of the semiconductor film does not only determine the dye loading, but also another properties like electron transport or recombination processes.[27–30] For this reason, nanostructures such as nanoparticles, nanotubes, nanowires, core-shells among others have been studied in the literature.

The oxide semiconductor TiO_2 has been by far the most widely used electrode film in DSSC. The TiO_2 is a cheap and stable material, a non-toxic oxide with a high refractive index and several crystalline forms: rutile, anatase and brookite. In spite of rutile being the thermodynamically most stable phase, anatase is, however, the most common form used in DSSC due to its larger band gap (3.2 eV) and higher conduction band edge energy.

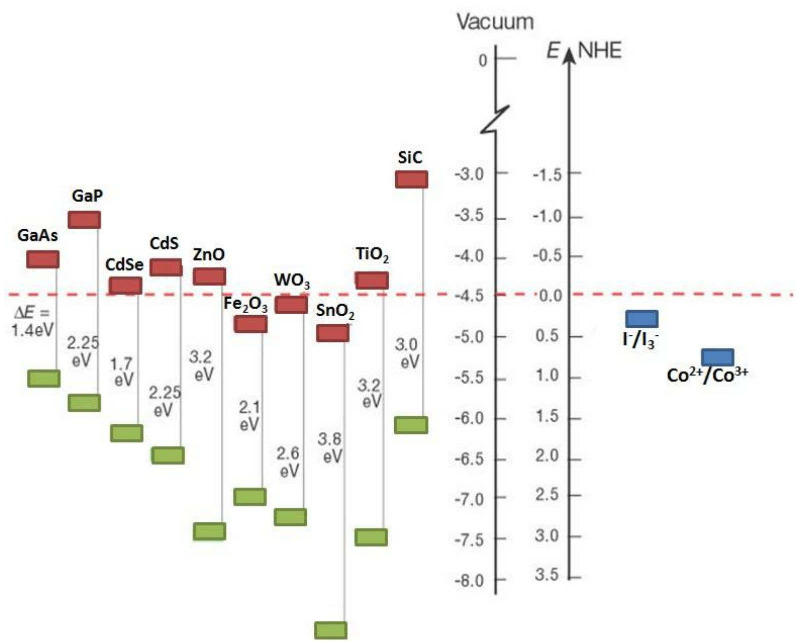

Figure 3.3: (left) Energetic scheme of conduction band, valence band and band gap for different semiconductors in contact with aqueous electrolyte at pH 1.[31] (right) Redox potential of redox couples employed in this thesis.

It is important to mention that many alternative wide band gap semiconductor oxides[32] (ZnO, SnO_2 and Nb_2O_5) have also been explored as electron conductors in DSSC. The most accepted alternative to TiO_2 is ZnO, whose most thermodynamically stable phase is the wurtzite structure. This oxide shows a band gap and a conduction band edge very similar to anatase TiO_2 (**Figure 3.3**) among other potentially favourable characteristics.[32,33] For instance, single-crystalline ZnO presents much higher electron mobility than anatase TiO_2 and a rich variety of nanostructures and synthetic routes.[34] However, ZnO has certain drawbacks as photoanode material that will be discussed in this thesis. In fact, up to now, no other material has reached efficiencies comparable to TiO_2.[14,35]

2.2. Dye: Light-harvesting unit and charge separation.

As a consequence of the wide band gap of the semiconductor (≈ 3.2 eV for anatase TiO_2) no visible light can be absorbed by the semiconductor on its own. For this reason, the function of harvesting solar light is carried out by dye molecules, which must absorb light across the entire visible range and even part of the near-infrared. The addition of the dye molecules to the semiconductor surface thus *sensitizes* the electrode with respect to visible light, being this process, together with the mesoporous morphology of the semiconductor, the fundamental aspect that makes a dye solar cell an efficient photoconversor. The attachment to the surface of semiconductor depends on the nature of dye. However, most of the dyes used are linked by acidic groups, basically carboxylic groups, allowing a good electronic contact between different parts.[36] In **Chapter 10** of this thesis other chemical groups as anchoring moieties for dyes will be analyzed.

Upon illumination, the dye molecules are promoted to their excited state[i], from where the dye molecules can relax towards its ground state or can inject an electron into the conduction band of the semiconductor. For efficient charge separation, the electron injection rate must be 100 times faster than the relaxation of the excited dye.[37] This kinetics depends on the interaction of semiconductor with the dye[38] as well as on the energy difference between the conduction band of the semiconductor and the excited state of the dye.[39] Furthermore, the electronic coupling between their orbitals also plays a fundamental role.[40] The excited state of the dye must remain higher enough with respect to the TiO_2 conduction band edge for efficient charge separation. However, the spatial orientation of the ground state and excited state influences not only the electron injection but also the electron recombination between the photoinjected electrons in the semiconductor and the oxidized dye[41]. For optimal performance, the molecular orbitals of the excited electronic state should be in close contact with the semiconductor surface, in contrast to those of the ground state, which should be far apart from the surface.

Ruthenium-complex dyes (N719, Z907, N3, C101…)[42,43] are the most used as well as one of the most successful sensitizers for application in DSSC. This kind of sensitizers consists of a central metal ion with ancillary ligands having at least one anchoring group. These dyes exhibit a strong absorption in the visible range due to a metal-to-ligand charge transfer process (MLCT) with moderate absorption coefficient (ε < 18000 $cm^{-1}M^{-1}$). Generally, it is accepted that electron injection by these dyes is very fast and this process is not considered a limiting factor in the DSSC performance, at least when the semiconductor is TiO_2.[38] However, based on their chemical, thermal and optical properties and on their electrochemical stability, many other molecules have been examined as an alternative to Ru-complex dyes. Metal-free organic dyes (D358, D149, Eosin-Y, RK1…),[44,45] porphyrins (LD14, YD2-0-C8…),[15,46] phtalocyanines (ZnPc5, TT40…)[47,48] or donor-π-acceptor dyes (C219, D205…)[49,50] among other dyes families have been studied along the literature.

In **Chapter 9**, we will analyze in detail the kinetics of the electron injection process for the N719 dye in contact with both TiO_2 and ZnO photoanodes and in **Chapter 10** a new generation of dyes will be tested as sensitizers for ZnO.

---

[i] Some authors call LUMO (Lowest Unoccupied Molecular Orbital) the excited state of the dye molecule. However, the LUMO strictly refers to unoccupied molecular orbitals of the molecule in its ground state, without any optical excitation.

2.3. Electrolyte: Hole conductor.

The electrolyte is a crucial component in a DSSC, playing several roles in the functioning of these devices.[51–59] It is, as a matter of fact, one of the main objects of study in this thesis. The electrolyte acts as a redox mediator with respect to the electron injection process of the dye and as hole conductor. It is in fact the analogue of the p-type semiconductor layer in a traditional silicon p-n solar cell.

The basic components of the electrolyte used in DSSC are a solvent and a redox couple. A great number of redox mediators and solvents have been explored. However, up to now, the most frequently used and at the same time the most successful electrolytes are composed of the redox pair I^-/I_3^- or, alternatively, complexes of Co^{2+}/Co^{3+} in an organic solvent (commonly acetonitrile).[14, 15]

The aim of the redox couple in the electrolyte is the regeneration of the dye after photoinduced electron injection into the electronic states of the semiconductor. After electron injection the dye must be reduced by an electron donor (I^- or Co^{2+}) to be regenerated. For an efficiently charge separation, the dye regeneration rate must be faster (typical rate constant are in the order of 10^{-6} - 10^{-9} s^{-1}) than the electron recombination from semiconductor oxide to oxidized dye.[60] For example, in a high-performance DSSC system such as N3 adsorbed onto TiO_2, a regeneration time of 10^{-7} s^{-1} has been measured, which is much faster than the recombination time ($10^{-3}s^{-1}$).[61] For this fast regeneration, high concentrations of iodide ions (10^{20} cm^{-3} – 0.5M) in the electrolyte are required.

The most important parameter controlling the dye regeneration is the free energy difference between the ground state of the dye and the redox potential of electrolyte (ΔG_{reg}). This is the *driving force* that makes it possible the electron transfer. For ruthenium-complex sensitizers and also for some organic dyes this is in the order of 0.5V.[62] However, in addition to the redox potential of electrolyte, the dye regeneration rate has been found to depend on the nature and concentration of the cations present in the electrolyte as well as on the presence of additives that can modify ΔG_{reg}.[60]

Apart from solvent and redox mediator, electrolytes contain, as mentioned, *additives*. They are not necessary for the functioning of the cells but increase the performance of the devices modifying the photocurrent and/or photovoltage. The most common additives are Lewis acids and bases such as Li ions (Li^+), 4-tert-butilpyridine (Tbp) and related compounds. The basic action of these additives is that electronic band system (more positive electrochemical potentials, see **Figure 3.3**) of the semiconductor becomes shifted. For instance, it shifts toward lower energies upon addition of Li^+ to the electrolyte due to surface adsorption and intercalation of Li^+ ions in the lattice of the semiconductor. In contrast, electronic band shifts toward higher energies (more positive electrochemical potentials) take place upon addition of Tbp, possibly due to Tbp adsorption on the surface of semiconductor. These additives play not only an important role in the regeneration dye rate, but also affect the electron injection and the recombination rate of electrons in the semiconductor with electron acceptors in the electrolyte. All these effects will be discussed thoroughly in **Chapter 9**. [40,63,64]

The transport of the redox mediator between the electrodes is carried out by ion diffusion. The oxidized species of the electrolyte must migrate to the counter-electrode, where it will be reduced. After the regeneration of the reduced species, they must diffuse to the vicinity of the oxidized dye attached to the surface of the semiconductor to regenerate it. These processes of diffusion depend on the viscosity of the electrolyte solvent, which can originate mass-transport limitations of both species, affecting the regeneration of the dye.[65] Mass-transport limitations not only slow down the regeneration of the dye, but also enhance the recombination of injected electrons with the oxidized species in the electrolyte in the vicinity of the semiconductor surface. This latter process represents one of the most important loss mechanisms in the cells. Electron recombination depends strongly on the chemical nature of the electrolyte (solvent and redox pair). For example, the iodide/tri-iodide couple shows a much slower kinetics of electron recombination than the Co^{2+}/Co^{3+} redox couple.

In relation to (liquid) electrolyte solvents, two kinds have been employed in DSSC: organic solvents (acetonitrile, methoxypropionitrile, propylene carbonate…) and room temperature ionic liquids (salts of imidazolium, pyrrolidinium…). The main advantage of organic solvents is its low viscosity, which allows for rapid diffusion of ionic species in the electrolyte, hence facilitating dye regeneration and rapid reaction in the counter-electrode. In contrast, room temperature ionic liquids are characterized by a high viscosity, which usually leads to mass-transport limitations. However, this disadvantage is compensated by an insignificant vapour pressure. For this reason, ionic liquids have been employed as non-volatile alternatives to organic solvents.

2.4. Counter-electrode.

The counter-electrode in a DSSC is usually formed by a thin catalytic layer of platinum deposited onto a conducting substrate. However, another materials have been tested like graphite or conducting polymers such as PEDOT[49] or cobalt sulphide.[66] In any case, the function of the counter-electrode is the reduction of the oxidized species of the redox couple of the electrolyte. This electron transfer reaction becomes rapid thanks to the catalytic effect of substances like platinum.

3. Operational principles of Dye-Sensitized Solar Cells. Requirements for efficient devices.

We now describe shortly the functioning of a DSSC device (**Figure 3.4**). Upon illumination and after photoexcitation of the dye [1], electron injection from its excited state into the semiconductor takes place [2]. Photogenerated electrons travel through the mesoporous film[67,68] by a diffusion gradient toward the collector substrate [3]. The extracted electrons can then perform work in an external circuit and return to the counter-electrode [4], where the oxidized species of the redox couple is reduced [5]. After the electron injection by the dye molecule, the oxidized dye molecules (radical cation) have to be regenerated by the reduced species of redox couple present in the electrolyte [6]. Thus, this electron transfer closes up the electron cycle and enables the current to flow through the solar cell circuit. Nevertheless, several unwanted processes can compete with efficient charge separation and electron collection. After excitation of the dye molecule, the electronic relaxation of the dye may occur before electron injection [R_1]. After electron injection into the semiconductor, the photoinjected electrons can recombine before reaching the collector substrate with the oxidized dye [R_2] or with the oxidized species of the redox pair [R_3].

[1] Photoexcitation	$S + h\nu \rightarrow S^*$
[2] Electron injection	$S^* \rightarrow e^-_{(SC)} + S^+$
[R_1] Relaxation	$S^* \rightarrow S + h\nu$
[3] Electron transport	$e^-_{(SC)} \rightarrow e^-_{(FTO)}$
[R_2] Recombination-dye	$S^+ + e^-_{(SC)} \rightarrow S$
[R_3] Recombination	$2e^-_{(SC)} + I_3^- \rightarrow 3I^-$
[4] External circuit	$e^-_{(W-E)} \rightarrow e^-_{(C-E)}$
[5] Reaction in C-E	$I_3^- + 2e^-(Pt) \rightarrow 3I^-$
[6] Dye regeneration	$2S^+ + 3I^- \rightarrow 2S + I_3^-$

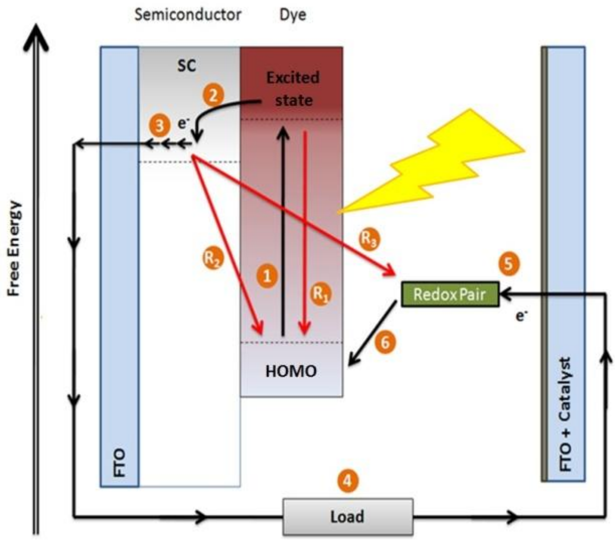

Figure 3.4: (Left) Reactions that describe the functioning of DSSC based on the iodide/tri-iodide redox couple and (right) energetic diagram including the different electron transfer processes that take place in a DSSC.

As have been described above, DSSC are photoelectrochemical devices where several electron transfer processes run in parallel and in competition. Charge separation and electron transport processes favour the current flow through the device; however processes such as relaxation of the dye or electron recombination constitute the main loss channels. The most characteristic feature of this type of solar cell (in contrast to others like p-n solar cells) is that the current flow is not only favoured energetically, but also kinetically due to the difference in rate constants associated to all the processes involved (**Figure 3.5**).

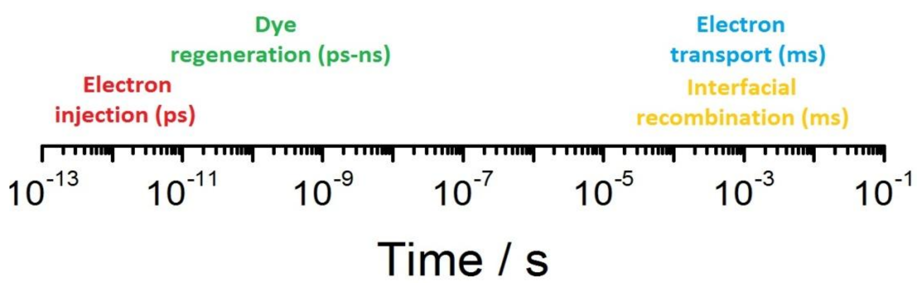

Figure 3.5: Time-scale of the different electron transfer processes in a DSSC.

4. Theoretical description of Dye-Sensitized Solar Cells.

4.1. Current voltage characteristics.

A solar cell is a particular case of a diode, which favours current flow in one direction, but not in the opposite. A diode has a certain characteristic relationship between produced current and applied voltage. This relationship, known as the current-voltage characteristics or IV curve, can be written in general as

$$J = J(V) \qquad (3.1)$$

where J is the dc electrical current density running through the device and V is an externally applied electric bias. The universal shape of an IV curve in a solar cell (**Figure 3.6**) is a consequence of the balance of two opposing mechanisms: (1) light-induced charge separation and subsequent current generation and (2) loss processes (recombination). The application of an external forward bias to the solar cell brings about the accumulation of electrons within the anode, which leads to an increase of the dark current that opposes the current generated by the device. The net current tends to cancel at sufficiently high bias (open-circuit condition). In this situation, the charge generation (G_n) is equal to the rate of electron recombination (U_n), that is, all photogenerated electrons are recombined. On the other hand, the maximum current is produced at zero bias (short-circuit condition), when the recombination processes are minimized.

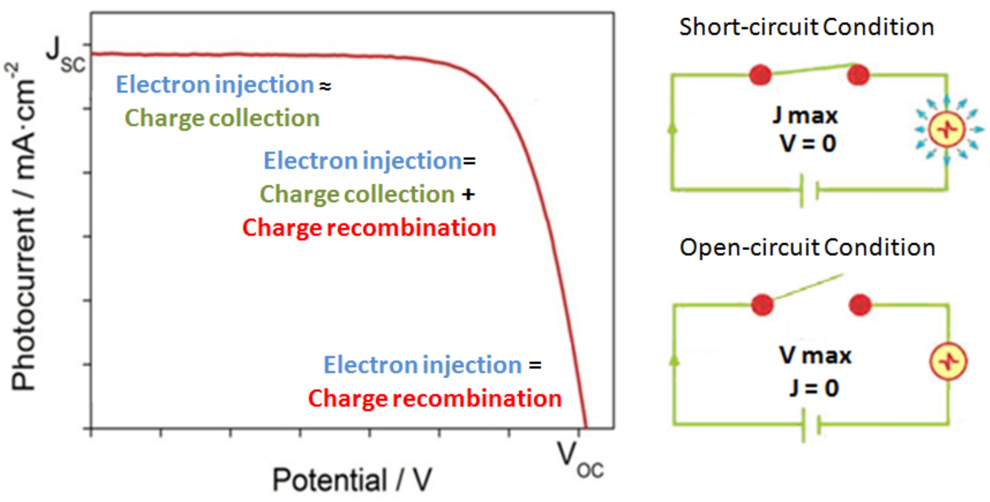

Figure 3.6: Universal shape of an IV curve where different key parameters are shown: J_{sc} (short-circuit photocurrent) and V_{oc} (open-circuit photovoltage).

The behaviour of a solar cell can be described by the diode equation. Assuming no series resistance, this can be written as[1]

$$J = J_{sc} - J_0\left(\exp\left(\frac{qV}{mk_BT} - 1\right)\right) \qquad (3.2)$$

where J_{sc} is the short-circuit photocurrent, J_0 is the exchange-current, q is the elementary charge, k_B is the Boltzmann constant, T is the absolute temperature and m is the ideality factor.

4.2. Photovoltage and Electron recombination.

In a DSSC, the open-circuit photovoltage (V_{OC}) corresponds to the free energy difference between the Fermi level of the semiconductor under illumination (E_F) and the free electron energy of the redox system (E_{redox}). Under working conditions, E_F gets raised in energy because trap sites located in the band-gap are occupied by photogenerated electrons. Thus, V_{OC} is heavily influenced by the choice of semiconductor (α parameter, see **Chapter 1**) and the redox mediator[69] used for the device. At present, the most widely used materials are TiO_2 for the semiconductor electrode and (I^-/I_3^-) for the redox system. However, the V_{OC} can be affected by energetic shifts of the electronic band system of the semiconductor induced by additives like Li^+ and Tbp as mentioned above.

Nevertheless, the presence of additives in the electrolyte is not the only factor that determines the V_{OC}. Among the different electron transfer processes of efficiency loss, the most important channel is the electron recombination from electronic states in the semiconductor to oxidized species of the redox couple present in the electrolyte. Therefore, DSSCs with the same energetic difference between the conduction band edge of semiconductor and E_{redox} of electrolyte can show different V_{OC} depending on the recombination rate. According to classical chemical kinetics, the rate of the so-called *back reaction* (U_n) depends on the reactant concentrations and the rate constants for electron transfer:

$$U_n = k_0 n^{\upsilon_n} [I_3^-]^{\upsilon_{I_3^-}} \qquad (3.3)$$

where k_0 is the constant rate for the back reaction of electron, n is the electron concentration and the power exponents represent the partial reaction orders with respect to electrons and tri-iodide ions, respectively. To simplify the model that describes the electron recombination, several assumptions can be considered:

- The reaction is first order with respect to electron and tri-iodide concentration.
- Electrons can be transferred **from "conduction band" only**.
- Tri-iodide concentration is many orders of magnitude larger than the electron concentration, thus, it can be considered constant.

Assuming these statements,

$$U_n = k_r n_c \qquad (3.4)$$

where k_r corresponds to $k_r = k_0[I_3^-]$ and n_c is the free electron concentration of electrons (that can be interpreted as electrons in the conduction band). This **linear recombination** term was introduced in the theoretical model proposed by Södergren et al. in an early stage of DSSC research.[70] However, evidence for non-linearity in the recombination is often found in DSSC.[71] Nonlinear features are detected in the non-ideal dependence of the open-circuit photovoltage on illumination intensity and in the non-ideal behaviour of the recombination resistance with respect to applied electric bias.

At open-circuit conditions and under illumination, all injected electrons will be recombined. Therefore,

$$G_n = U_n \qquad (3.5)$$

where G_n in the generation rate, describing the rate of electron injection into the electronic states of the semiconductor. This parameter is proportional to the intensity of the incident light (I_0). Thus, if we assume linear recombination kinetics, from **Equation 3.4, 3.5** and **1.18**, the following relationship between photovoltage and light intensity is found

$$V_{OC} \ \alpha \ \frac{k_B T}{q} \ln I_0 \qquad (3.6)$$

This approximation predicts, therefore, that DSSC should be behave as an ideal diode,[72] and a semilogarithmic plot of V_{OC} versus light intensity should give a linear response with a slope of 26 mV at room temperature. However, usually DSSC photovoltage shows higher slopes than 26 mV. To account for this non-linear behaviour an empirical non-ideality factor m (**Equation 3.2**) is considered[ii]

$$V_{OC} \ \alpha \ \frac{m k_B T}{q} \ln I_0 \qquad (3.7)$$

Nonlinear features in DSSC do also show up in the nonideal behaviour of the recombination resistance with respect to applied bias. To get insight into this point, we relate the recombination current (j_{rec}) to the recombination rate via

$$j_{rec} = q d U_n \qquad (3.8)$$

where d is the film thickness. From the reciprocal derivative of this recombination current with respect to voltage[73] the recombination resistance (R_{rec}) is obtained

$$R_{rec} = \frac{1}{A}\left(\frac{\partial j_{rec}}{\partial V}\right)^{-1} \qquad (3.9)$$

where A is the surface area. Combining **Equations 3.8** and **3.9**, the recombination resistance can be related to the derivative of the recombination rate

$$R_{rec} = \frac{1}{qdA}\left(\frac{\partial U_n}{\partial V}\right)^{-1} \qquad (3.10)$$

As we will see in subsequent chapters, the recombination resistance can be extracted from spectroscopy impedance measurements. In these experiments, it is typically found that the resistance fits to the following empirical equation when measured as a function of applied bias:

[ii] This equation can easily be obtained if one imposes the open-circuit condition (J = 0) in the non-ideal diode equation (Equation 3.2) and it is assumed that the J_{sc} is directly proportional to the illumination intensity I_0.

$$R_{rec} = R_{ct,0}\exp\left(-\beta\frac{qV}{k_B T}\right) \qquad (3.11)$$

where $R_{ct,0}$ is a constant and β the so-called transfer parameter o recombination parameter. In a linear (ideal) model β would be equal to one. However, in actual cases, β takes usually values smaller than 1. This is interpreted as an indication of the non-linear character of recombination in DSSC.[71] Thus, a non-linear recombination model can be written as

$$U_n = k_r n_c^{\beta} \qquad (3.12)$$

where β, the transfer parameter, defines the recombination order in the sub-linear recombination kinetics with respect to free electrons. Identifying **Equations 3.11** and **3.12** with the diode equation (**Equation 3.2**), it can be found that β can be related to the non-ideality factor m by its inverse (m=1/ β).

The origin of **non-linearity** or **non-ideality** is an open problem. A recombination order lower than 1 is an empirical way of describing that electron transfer from the TiO_2 layer to the electron acceptor of the redox couple in the electrolyte may take place from other different routes to the conduction band. Therefore, two different routes for the electron recombination have been considered: (1) from "**conduction band" or "nearly-free" electrons** and (2) from **surface states localized** in the band gap of the oxide.[73–75]

In this connection, a number of studies have already been devoted in the literature to study electron recombination in DSSC from a fundamental point of view.[76–81] However, the most accepted view of this topic was devised by Bisquert and co-workers.[76,82] This model can explain the electron recombination in DSSC, whose recombination rate is determined by the energetics of electron in the semiconductor, mediated by the distribution of localized states, and by the energetics of electron acceptors, which depend on the composition of electrolyte. The recombination rate can be estimated by the following equation

$$U_n = d\int_{E_{redox}}^{E_c} g(E)f(E-E_F)\,P_R(E)dE \qquad (3.13)$$

where $f(E\text{-}E_F)$ is the occupation probability in the semiconductor at a certain position of the electron quasi-Fermi level E_F (Fermi-Dirac distribution) and $P_R(E)$ is the probability of recombination at a given value of the energy (density of acceptor states). If we assume a one-electron charge transfer from semiconductor to electron acceptors in the electrolyte, as mentioned in Chapter 1, this latter parameter can be qualitatively described by the Marcus-Gerischer[83–85] formula (**Equation 1.11**)

$$P_R(E) = k_r\exp\left[-\frac{(E - E_{redox} - \lambda)^2}{4\lambda k_B T}\right] \qquad (3.14)$$

where λ is the reorganization energy, E_{redox} is the redox potential of the redox pair and k_r is a prefactor that depends on the concentration of oxidized species in the electrolyte, the temperature and the reorganization energy.

4.3. Photocurrent and Incident Photon-to-Current Efficiency.

As explained before, the short-circuit current (J_{SC}) is the photocurrent obtained under short-circuit conditions, without any resistance, and then it is the maximum photocurrent that can be extracted from the DSSC. This parameter can be calculated by the overlap between the spectral incident photon-to-current efficiency (*IPCE*) and the spectral photon flux (I_0) of the incident illumination[86]

$$J_{SC} = q \int_{\lambda_{min}}^{\lambda_{max}} I_0(\lambda) \cdot IPCE(\lambda) \cdot d\lambda \qquad (3.15)$$

In turn, the *IPCE* depends on the efficiency of three different processes that determine the electrical conversion in a DSSC. This is given by (**Figure 3.6**)

$$IPCE(\lambda) = \eta_{lh}(\lambda) \cdot \eta_g(\lambda) \cdot \eta_{col}(\lambda) \qquad (3.16)$$

where η_{lh} is the sunlight-harvesting efficiency, η_g is the generation efficiency of conducting electrons under sunlight irradiation, and η_{col} is the charge collection efficiency from the device to the external circuit.

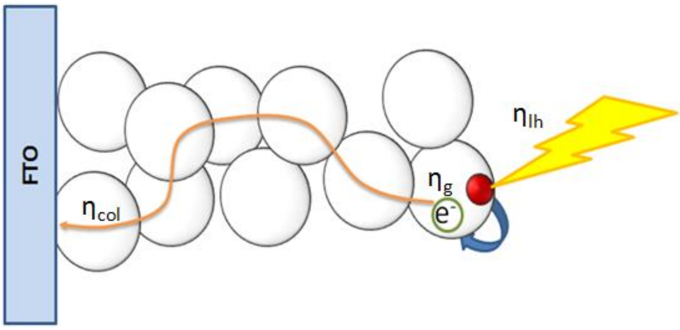

Figure 3.6: Scheme of the processes that determine the IPCE.

For DSSCs, η_{lh} indicates how efficiently the adsorbed dye molecules *harvest* incident photons. This efficiency becomes large when dye molecules absorb light in a wide wavelength range. However, up to now, there are no known sensitizer dyes that absorb light beyond wavelengths as long as 1100 nm, indicating that there is still room for improvement. In addition to optimize the properties of sensitizer dyes, the structure of nanocrystalline semiconductor films play an important role in this process and should also be optimized to obtain higher η_{lh} values by increasing the amount of dye molecules adsorbed. This important parameter is known as *dye loading*.

The η_g corresponds to the probability that an electron is generated in electronic states of the semiconductor as a consequence of the electron injection from the dye. As mentioned above, just after electron injection, electrons are located in a particle and travel to the collector substrate. However, one of the routes of recombination is the reaction (reduction) with an oxidized dye. When the reduction of an oxidized dye by a redox mediator occurs before the electron recombination, this generated electron is left behind in the particle and can migrate in the nanocrystalline film through hopping between nanoparticles. Accordingly, the generation efficient can be written as

$$\eta_g = \eta_{ei} \cdot \eta_{reg} \qquad (3.17)$$

where η_{ei} is the electron injection efficiency and η_{reg} is the efficiency of regeneration of the oxidized dye by the redox system. For this reason, for a high η_g and efficient charge separation, both a high electron injection rate and a high dye regeneration rate is needed. Both processes (electron injection and dye regeneration) involve sensitizer dye electron transfer reactions, and therefore the free energy change ($-\Delta G$) of the reaction is a key factor to control the efficiency. $-\Delta G_{inj}$ for electron injection can be, as a first approximation, evaluated from the energy difference between the LUMO (Lowest Unoccupied molecular orbital) of the dye and the conduction band edge of the semiconductor. In relation to dye regeneration, as mentioned above, $-\Delta G_{reg}$ can be described as the free energy difference between HOMO (Highest Occupied molecular orbital) of the dye and the oxidation potential of the redox couple.

Finally, η_{col} is the collection efficiency of the conducting electrons from the semiconductor electrode to the external circuit. In other words, it is an indicator of the probability that a photogenerated electron reaches the collector substrate before it is lost by recombination. This parameter depends on the average distance that electrons can travel before recombination. This distance is known as the *electron diffusion length* (L_n).[87]

4.4. Continuity equation for electron transport in Dye-Sensitized Solar Cells.

There are many publications that describe the physics of DSSC and simulate the current–voltage curve. Södergren et al.[70] introduced a simple continuity equation based on the assumption that electron transport occurs by diffusion and that the kinetics of electron recombination is first-order with respect to the free electron concentration. However, using this work as first approximation, other models that simulates the IV curve and the time-dependence respond of DSSCs have been developed.[58,82,88–91] In a general form, the continuity equation for the electron density can be expressed as

$$\frac{\partial n_c(x,t)}{\partial t} = G_n(x,t) + \frac{1}{q}\nabla J_n + -U_n(x,t) \qquad (3.18)$$

In this continuity equation of the electron transport, n_c is the free electron concentration according to the distance (x) to the collector substrate and the time (t), G_n is the electron generation rate, J_n is the electron current density and U_n is the term related to the processes of electron recombination.

Features related to illumination, light-harvesting efficiency and charge separation (electron injection and regeneration of the dye) are included in the generation term. As described above, this term is expressed by the charge generation efficiency (η_g) and the Lambert-Beer law for light absorption as a function of the distance.

$$G_n(x,\lambda) = \eta_g \cdot I_0(\lambda) \cdot \alpha_{abs} \cdot exp(-\alpha_{abs}\ x) \qquad (3.19)$$

where α_{abs} is the wavelength-dependent absorption coefficient of the layer.

In relation to the electron current density (J_n), two major mechanisms govern the transport in a semiconductor: *drift* and *diffusion*. However, in a mesoporous nanocrystalline electrode the only mechanism of transport is diffusion. As described in **Chapter 1**, due to the small size of the nanoparticles, the low charge carrier concentration in TiO_2 colloids and the screening of nanoparticles by an electrolyte with a high ionic strength, a depletion layer cannot be formed. Thus, no significant local electric field can assist the charge separation and electron transport and, therefore, the electron transport occurs mainly by a gradient in the electron concentration of the nanocrystalline electrode (diffusion). The diffusion current density can be expressed in terms of free electrons using Fick's first law

$$J_n = qD_0 \frac{\partial n_c}{\partial x} \qquad (3.20)$$

where D_0 is the diffusion coefficient of free electrons. Combining **Equation 3.20** and **1.19** an expression for the electron transport resistance (R_t) in the semiconductor can be found

$$R_t = R_{t,0} \exp\left(-\frac{qV}{k_B T}\right) \qquad (3.21)$$

where $R_{t,0}$ is a constant that depends on the morphology of the photoanode.

Finally, the last term of the continuity equation can be described according **Equation 3.12**, where k_0 are the recombination rate constant of free electrons, which can be related to the inverse of an electron lifetime of these free electrons

$$\tau_0 = \frac{1}{k_0} \qquad (3.22)$$

Therefore, taking into account all these previous descriptions the continuity equation can be described as

$$\frac{\partial n_c(x,t)}{\partial t} = \eta_g \cdot I_0(\lambda) \cdot \alpha_{abs} \cdot \exp(-\alpha_{abs}\, x) + D_0 \frac{\partial^2 n_c(x,t)}{\partial x^2} - k_0 n_c^{\beta} \qquad (3.23)$$

At steady-state conditions and with no generation, the continuity equation (**Equation 3.23**) can be written as

$$D_0 \frac{\partial^2 n_c(x,t)}{\partial x^2} - k_0 n_c^{\beta} = 0 \qquad (3.23)$$

For the linear case (β = 1), the general solution of this differential equation is an exponential function for n_c where the diffusion length is the decay parameter. This is called the linear electron diffusion length, which is equal to[87,92,93]

$$L_0 = (D_0/k_0)^{1/2} = (D_0 \tau_0)^{1/2} \qquad (3.24)$$

Hence, the diffusion length should be constant under the assumptions of simple diffusion of free electrons and linear recombination (β = 1). However, due to the surface states located in the band gap, as discussed before, the electron recombination does not depend linearly on electron density (β < 1) and then the diffusion length cannot be defined from the product of the diffusion coefficient and the lifetime.

As described in **Chapter 1**, the diffusion coefficient and electron lifetime show an opposite behaviour with respect to the applied bias or illumination. This dependence is easily explained according to the Multiple-Trapping model. As the Fermi level rises, on the one hand, the rate of detrapping to the transport level is enhanced and the diffusion coefficient increases, whereas on the other hand, the lifetime becomes shorter. This latter behaviour has been explained by two different views. If the electron transport becomes faster, then the probability for an electron to find an acceptor is larger and the electron lifetime is shortened. This interpretation is known as *dynamic view*.[94–97] However if it is assumed that the rate trapping-detrapping are higher than the recombination rate, the free and trapped electron concentrations can be considered constants even if the system is perturbed by the recombination. This *quasi-static* approximation proposed by Bisquert[98] reduces the general multiple trapping to a simple diffusion formalism. The Fermi level dependence of the time constants is associated to trapping and detrapping of free carriers, and this process can be expressed by a single trapping factor: $\partial n_c/\partial n_t$, which affects in opposite directions diffusion coefficient and lifetime.

Therefore, due to the existence of trapping-detrapping events and, therefore, non-linear effects, the safest way to define an electron lifetime is by means of a "*small-perturbation lifetime*"

$$\tau_n = \left(\frac{dU_n}{dn}\right)^{-1} \qquad (3.25)$$

which is defined as the variation of the recombination rate for a small variation of the total density. As it will be described in **Chapter 4**, this magnitude can be obtained experimentally by different techniques.

In this connection, Bisquert and Mora-Seró[71] defined a "*small-perturbation diffusion length*" from separate measurements of the effective diffusion coefficient and the *small-perturbation lifetime*. In this case,

$$L_n = \sqrt{(D_n \tau_n)} \qquad (3.26)$$

For linear recombination $L_0 = L_n$. In any other case, this magnitude represents a first approximation of the mean average distance that electrons can travel between recombination events, provided that both diffusion coefficient and electron lifetime are measured at the same quasi-Fermi level position.

5. References.

(1) Nelson, J. *The Physics of Solar Cells*; 1st ed.; Imperial College Press, 2003.
(2) Shockley, W.; Queisser, H. J. Detailed Balance Limit of Efficiency of P-n Junction Solar Cells. *J. Appl. Phys.* **1961**, *32*, 510–519.
(3) Green, M. A.; Emery, K.; Hishikawa, Y.; Warta, W.; Dunlop, E. D. Solar Cell Efficiency Tables (Version 38). *Prog. Photovolt. Res. Appl.* **2011**, *19*, 565–572.
(4) Hashimoto, Y.; Kohara, N.; Negami, T.; Nishitani, N.; Wada, T. Chemical Bath Deposition of Cds Buffer Layer for GIGS Solar Cells. *Sol. Energy Mater. Sol. Cells* **1998**, *50*, 71–77.
(5) Singh, V. P.; Linam, D. L.; Dils, D. W.; McClure, J. C.; Lush, G. B. Electro-Optical Characterization and Modeling of Thin Film CdS–CdTe Heterojunction Solar Cells. *Sol. Energy Mater. Sol. Cells* **2000**, *63*, 445–466.
(6) Singh, V. P.; McClure, J. C. Design Issues in the Fabrication of CdS–CdTe Solar Cells on Molybdenum Foil Substrates. *CANCUN 2001 Nanoscale Mater. Amp Devices* **2003**, *76*, 369–385.
(7) Benanti, T.; Venkataraman, D. Organic Solar Cells: An Overview Focusing on Active Layer Morphology. *Photosynth. Res.* **2006**, *87*, 73–81.
(8) Belaidi, A.; Dittrich, T.; Kieven, D.; Tornow, J.; Schwarzburg, K.; Lux-Steiner, M. Influence of the Local Absorber Layer Thickness on the Performance of ZnO Nanorod Solar Cells. *Phys. Status Solidi RRL - Rapid Res. Lett.* **2008**, *2*, 172–174.
(9) Ernst, K.; Belaidi, A.; Konenkamp, R. Solar Cell with Extremely Thin Absorber on Highly Structured Substrate. *Semicond. Sci. Technol.* **2003**, *18*, 475–479.
(10) Greene, L. E.; Law, M.; Yuhas, B. D.; Yang, P. ZnO−TiO2 Core−Shell Nanorod/P3HT Solar Cells. *J. Phys. Chem. C* **2007**, *111*, 18451–18456.
(11) Lira-Cantu, M.; Krebs, F. C. Hybrid Solar Cells Based on MEH-PPV and Thin Film Semiconductor Oxides (TiO2, Nb2O5, ZnO, CeO2 and CeO2–TiO2): Performance Improvement during Long-Time Irradiation. *Sol. Energy Mater. Sol. Cells* **2006**, *90*, 2076–2086.
(12) O'Regan, B.; Gratzel, M. A Low-Cost, High-Efficiency Solar-Cell Based on Dye-Sensitized Colloidal Tio2 Films. *Nature* **1991**, *353*, 737–740.
(13) Vlachopoulos, N.; Liska, P.; Augustynski, J.; Graetzel, M. Very Efficient Visible Light Energy Harvesting and Conversion by Spectral Sensitization of High Surface Area Polycrystalline Titanium Dioxide Films. *J. Am. Chem. Soc.* **1988**, *110*, 1216–1220.
(14) Yu, Q.; Wang, Y.; Yi, Z.; Zu, N.; Zhang, J.; Zhang, M.; Wang, P. High-Efficiency Dye-Sensitized Solar Cells: The Influence of Lithium Ions on Exciton Dissociation, Charge Recombination, and Surface States. *ACS Nano* **2010**, *4*, 6032–6038.
(15) Yella, A.; Lee, H.-W.; Tsao, H. N.; Yi, C.; Chandiran, A. K.; Nazeeruddin, M. K.; Diau, E. W.-G.; Yeh, C.-Y.; Zakeeruddin, S. M.; Grätzel, M. Porphyrin-Sensitized Solar Cells with Cobalt (II/III)–Based Redox Electrolyte Exceed 12 Percent Efficiency. *Science* **2011**, *334*, 629–634.
(16) Hardin, B. E.; Snaith, H. J.; McGehee, M. D. The Renaissance of Dye-Sensitized Solar Cells. *Nat. Photonics* **2012**, *6*, 162–169.
(17) Snaith, H. J. Perovskites: The Emergence of a New Era for Low-Cost, High-Efficiency Solar Cells. *J. Phys. Chem. Lett.* **2013**, *4*, 3623–3630.
(18) Snaith, H. J.; Stavrinadis, A.; Docampo, P.; Watt, A. A. R. Lead-Sulphide Quantum-Dot Sensitization of Tin Oxide Based Hybrid Solar Cells. *Org. Photovolt. Dye Sensitized Sol. Cells* **2011**, *85*, 1283–1290.
(19) Kamat, P. V. Quantum Dot Solar Cells. Semiconductor Nanocrystals as Light Harvesters. *J. Phys. Chem. C* **2008**, *112*, 18737–18753.
(20) Lee, H.; Leventis, H. C.; Moon, S.-J.; Chen, P.; Ito, S.; Haque, S. A.; Torres, T.; Nüesch, F.; Geiger, T.; Zakeeruddin, S. M.; et al. PbS and CdS Quantum Dot-Sensitized Solid-State Solar Cells: "Old Concepts, New Results." *Adv. Funct. Mater.* **2009**, *19*, 2735–2742.

(21) Kojima, A.; Teshima, K.; Shirai, Y.; Miyasaka, T. Organometal Halide Perovskites as Visible-Light Sensitizers for Photovoltaic Cells. *J. Am. Chem. Soc.* **2009**, *131*, 6050–6051.
(22) Im, J.-H.; Lee, C.-R.; Lee, J.-W.; Park, S.-W.; Park, N.-G. 6.5% Efficient Perovskite Quantum-Dot-Sensitized Solar Cell. *Nanoscale* **2011**, *3*, 4088–4093.
(23) Kojima, A.; Teshima, K.; Shirai, Y.; Miyasaka, T. Novel Photoelectrochemical Cell with Mesoscopic Electrodes Sensitized by Lead-Halide Compounds (5). *Meet. Abstr.* **2007**, *MA2007-02*, 352–352.
(24) Bach, U.; Lupo, D.; Comte, P.; Moser, J. E.; Weissortel, F.; Salbeck, J.; Spreitzer, H.; Gratzel, M. Solid-State Dye-Sensitized Mesoporous TiO2 Solar Cells with High Photon-to-Electron Conversion Efficiencies. *Nature* **1998**, *395*, 583–585.
(25) Kim, H.-S.; Lee, C.-R.; Im, J.-H.; Lee, K.-B.; Moehl, T.; Marchioro, A.; Moon, S.-J.; Humphry-Baker, R.; Yum, J.-H.; Moser, J. E.; et al. Lead Iodide Perovskite Sensitized All-Solid-State Submicron Thin Film Mesoscopic Solar Cell with Efficiency Exceeding 9%. *Sci. Rep.* **2012**, *2*.
(26) Lee, M. M.; Teuscher, J.; Miyasaka, T.; Murakami, T. N.; Snaith, H. J. Efficient Hybrid Solar Cells Based on Meso-Superstructured Organometal Halide Perovskites. *Science* **2012**, *338*, 643–647.
(27) Tacchini, I.; Ansón-Casaos, A.; Yu, Y.; Martínez, M. T.; Lira-Cantu, M. Hydrothermal Synthesis of 1D TiO2 Nanostructures for Dye Sensitized Solar Cells. *Mater. Sci. Eng. B* **2012**, *177*, 19–26.
(28) Ghadiri, E.; Taghavinia, N.; Zakeeruddin, S. M.; Grätzel, M.; Moser, J.-E. Enhanced Electron Collection Efficiency in Dye-Sensitized Solar Cells Based on Nanostructured TiO2 Hollow Fibers. *Nano Lett.* **2010**, *10*, 1632–1638.
(29) Guillén, E.; Azaceta, E.; Vega-Poot, A.; Idígoras, J.; Echeberría, J.; Anta, J. A.; Tena-Zaera, R. ZnO/ZnO Core–Shell Nanowire Array Electrodes: Blocking of Recombination and Impressive Enhancement of Photovoltage in Dye-Sensitized Solar Cells. *J. Phys. Chem. C* **2013**, *117*, 13365–13373.
(30) Lupan, O.; Guerin, V. M.; Tiginyanu, I. M.; Ursaki, V. V.; Chow, L.; Heinrich, H.; Pauporte, T. Well-Aligned Arrays of Vertically Oriented ZnO Nanowires Electrodeposited on ITO-Coated Glass and Their Integration in Dye Sensitized Solar Cells. *J. Photochem. Photobiol. -Chem.* **2010**, *211*, 65–73.
(31) Gratzel, M. Photoelectrochemical Cells. *NATURE* **2001**, *414*, 338–344.
(32) Katoh, R.; Furube, A.; Yoshihara, T.; Hara, K.; Fujihashi, G.; Takano, S.; Murata, S.; Arakawa, H.; Tachiya, M. Efficiencies of Electron Injection from Excited N3 Dye into Nanocrystalline Semiconductor (ZrO2, TiO2, ZnO, Nb2O5, SnO2, In2O3) Films. *J. Phys. Chem. B* **2004**, *108*, 4818–4822.
(33) Bauer, C.; Boschloo, G.; Mukhtar, E.; Hagfeldt, A. Electron Injection and Recombination in Ru(dcbpy)2(NCS)2 Sensitized Nanostructured ZnO. *J. Phys. Chem. B* **2001**, *105*, 5585–5588.
(34) Forro, L.; Chauvet, O.; Emin, D.; Zuppiroli, L.; Berger, H.; Lévy, F. High Mobility N-type Charge Carriers in Large Single Crystals of Anatase (TiO2). *J. Appl. Phys.* **1994**, *75*, 633–635.
(35) Saito, M.; Fujihara, S. Large Photocurrent Generation in Dye-Sensitized ZnO Solar Cells. *Energy Environ. Sci.* **2008**, *1*, 280–283.
(36) Hagfeldt, A.; Graetzel, M. Light-Induced Redox Reactions in Nanocrystalline Systems. *Chem Rev* **1995**, *95*, 49–68.
(37) Koops, S. E.; O'Regan, B. C.; Barnes, P. R. F.; Durrant, J. R. Parameters Influencing the Efficiency of Electron Injection in Dye-Sensitized Solar Cells. *J Am Chem Soc* **2009**, *131*, 4808–4818.
(38) Sobuś, J.; Burdziński, G.; Karolczak, J.; Idígoras, J.; Anta, J. A.; Ziółek, M. Comparison of TiO2 and ZnO Solar Cells Sensitized with an Indoline Dye: Time-Resolved Laser Spectroscopy Studies of Partial Charge Separation Processes. *Langmuir* **2014**, *30*, 2505–2512.

(39) Katoh, R.; Furube, A.; Hara, K.; Murata, S.; Sugihara, H.; Arakawa, H.; Tachiya, M. Efficiencies of Electron Injection from Excited Sensitizer Dyes to Nanocrystalline ZnO Films as Studied by Near-IR Optical Absorption of Injected Electrons. *J. Phys. Chem. B* **2002**, *106*, 12957–12964.
(40) Yang, X.; Zhang, S.; Zhang, K.; Liu, J.; Qin, C.; Chen, H.; Islam, A.; Han, L. Coordinated Shifts of Interfacial Energy Levels: Insight into Electron Injection in Highly Efficient Dye-Sensitized Solar Cells. *Energy Env. Sci* **2013**, *6*, 3637–3645.
(41) Clifford, J. N.; Palomares, E.; Nazeeruddin, M. K.; Gratzel, M.; Nelson, J.; Li, X.; Long, N. J.; Durrant, J. R. Molecular Control of Recombination Dynamics in Dye-Sensitized Nanocrystalline TiO2 Films: Free Energy vs Distance Dependence. *J. Am. Chem. Soc.* **2004**, *126*, 5225–5233.
(42) Nazeeruddin, M. K.; Zakeeruddin, S. M.; Humphry-Baker, R.; Jirousek, M.; Liska, P.; Vlachopoulos, N.; Shklover, V.; Fischer, C.-H.; Grätzel, M. Acid−Base Equilibria of (2,2‘-Bipyridyl-4,4‘-Dicarboxylic acid)ruthenium(II) Complexes and the Effect of Protonation on Charge-Transfer Sensitization of Nanocrystalline Titania. *Inorg. Chem.* **1999**, *38*, 6298–6305.
(43) Gao, F.; Wang, Y.; Shi, D.; Zhang, J.; Wang, M. K.; Jing, X. Y.; Humphry-Baker, R.; Wang, P.; Zakeeruddin, S. M.; Gratzel, M. Enhance the Optical Absorptivity of Nanocrystalline TiO2 Film with High Molar Extinction Coefficient Ruthenium Sensitizers for High Performance Dye-Sensitized Solar Cells. *J. Am. Chem. Soc.* **2008**, *130*, 10720–10728.
(44) Joly, D.; Pellejà, L.; Narbey, S.; Oswald, F.; Chiron, J.; Clifford, J. N.; Palomares, E.; Demadrille, R. A Robust Organic Dye for Dye Sensitized Solar Cells Based on Iodine/Iodide Electrolytes Combining High Efficiency and Outstanding Stability. *Sci Rep* **2014**, *4*.
(45) Guillen, E.; Idigoras, J.; Berger, T.; Anta, J.; Fernandez-Lorenzo, C.; Alcantara, R.; Navas, J.; Martin-Calleja, J. ZnO-Based Dye Solar Cell with Pure Ionic-Liquid Electrolyte and Organic Sensitizer: The Relevance of the Dye-Oxide Interaction in an Ionic-Liquid Medium. *Phys. Chem. Chem. Phys.* **2011**, *13*, 207–213.
(46) Chang, Y.-C.; Wang, C.-L.; Pan, T.-Y.; Hong, S.-H.; Lan, C.-M.; Kuo, H.-H.; Lo, C.-F.; Hsu, H.-Y.; Lin, C.-Y.; Diau, E. W.-G. A Strategy to Design Highly Efficient Porphyrin Sensitizers for Dye-Sensitized Solar Cells. *Chem Commun* **2011**, *47*, 8910–8912.
(47) Mori, S.; Nagata, M.; Nakahata, Y.; Yasuta, K.; Goto, R.; Kimura, M.; Taya, M. Enhancement of Incident Photon-to-Current Conversion Efficiency for Phthalocyanine-Sensitized Solar Cells by 3D Molecular Structuralization. *J. Am. Chem. Soc.* **2010**, *132*, 4054–4055.
(48) Ragoussi, M.-E.; Cid, J.-J.; Yum, J.-H.; de la Torre, G.; Di Censo, D.; Grätzel, M.; Nazeeruddin, M. K.; Torres, T. Carboxyethynyl Anchoring Ligands: A Means to Improving the Efficiency of Phthalocyanine-Sensitized Solar Cells. *Angew. Chem. Int. Ed.* **2012**, *51*, 4375–4378.
(49) Idígoras, J.; Guillén, E.; Ramos, F. J.; Anta, J. A.; Nazeeruddin, M. K.; Ahmad, S. Highly Efficient Flexible Cathodes for Dye Sensitized Solar Cells to Complement Pt@TCO Coatings. *J. Mater. Chem. A* **2014**, *2*, 3175–3181.
(50) Ito, S.; Miura, H.; Uchida, S.; Takata, M.; Sumioka, K.; Liska, P.; Comte, P.; Pechy, P.; Graetzel, M. High-Conversion-Efficiency Organic Dye-Sensitized Solar Cells with a Novel Indoline Dye. *Chem. Commun.* **2008**, 5194–5196.
(51) Wang, H.; Peter, L. M. Influence of Electrolyte Cations on Electron Transport and Electron Transfer in Dye-Sensitized Solar Cells. *J. Phys. Chem. C* **2012**, *116*, 10468–10475.
(52) Seo, S. H.; Kim, S. Y.; Koo, B.-K.; Cha, S.-I.; Lee, D. Y. Influence of Electrolyte Composition on the Photovoltaic Performance and Stability of Dye-Sensitized Solar Cells with Multiwalled Carbon Nanotube Catalysts. *Langmuir 0*.
(53) Fabregat-Santiago, F.; Bisquert, J.; Garcia-Belmonte, G.; Boschloo, G.; Hagfeldt, A. Influence of Electrolyte in Transport and Recombination in Dye-Sensitized Solar Cells Studied by Impedance Spectroscopy. *Sol. Energy Mater. Sol. Cells* **2005**, *87*, 117–131.

(54) Jennings, J. R.; Wang, Q. Influence of Lithium Ion Concentration on Electron Injection, Transport, and Recombination in Dye-Sensitized Solar Cells. *J. Phys. Chem. C* **2010**, *114*, 1715–1724.
(55) Kambe, S.; Nakade, S.; Kitamura, T.; Wada, Y.; Yanagida, S. Influence of the Electrolytes on Electron Transport in Mesoporous TiO2−Electrolyte Systems. *J. Phys. Chem. B* **2002**, *106*, 2967–2972.
(56) Wang, P.; Wenger, B.; Humphry-Baker, R.; Moser, J. E.; Teuscher, J.; Kantlehner, W.; Mezger, J.; Stoyanov, E. V.; Zakeeruddin, S. M.; Gratzel, M. Charge Separation and Efficient Light Energy Conversion in Sensitized Mesoscopic Solar Cells Based on Binary Ionic Liquids. *J. Am. Chem. Soc.* **2005**, *127*, 6850–6856.
(57) Zistler, M.; Wachter, P.; Wasserscheid, P.; Gerhard, D.; Hinsch, A.; Sastrawan, R.; Gores, H. J. Comparison of Electrochemical Methods for Triiodide Diffusion Coefficient Measurements and Observation of Non-Stokesian Diffusion Behaviour in Binary Mixtures of Two Ionic Liquids. *Electrochimica Acta* **2006**, *52*, 161–169.
(58) Fabregat-Santiago, F.; Bisquert, J.; Palomares, E.; Otero, L.; Kuang, D. B.; Zakeeruddin, S. M.; Gratzel, M. Correlation between Photovoltaic Performance and Impedance Spectroscopy of Dye-Sensitized Solar Cells Based on Ionic Liquids. *J. Phys. Chem. C* **2007**, *111*, 6550–6560.
(59) Kawano, R.; Matsui, H.; Matsuyama, C.; Sato, A.; Susan, M.; Tanabe, N.; Watanabe, M. High Performance Dye-Sensitized Solar Cells Using Ionic Liquids as Their Electrolytes. *J. Photochem. Photobiol. -Chem.* **2004**, *164*, 87–92.
(60) Pelet, S.; Moser, J.-E.; Grätzel, M. Cooperative Effect of Adsorbed Cations and Iodide on the Interception of Back Electron Transfer in the Dye Sensitization of Nanocrystalline TiO2. *J. Phys. Chem. B* **2000**, *104*, 1791–1795.
(61) Haque, S. A.; Tachibana, Y.; Klug, D. R.; Durrant, J. R. Charge Recombination Kinetics in Dye-Sensitized Nanocrystalline Titanium Dioxide Films under Externally Applied Bias. *J. Phys. Chem. B* **1998**, *102*, 1745–1749.
(62) Montanari, I.; Nelson, J.; Durrant, J. R. Iodide Electron Transfer Kinetics in Dye-Sensitized Nanocrystalline TiO2 Films. *J. Phys. Chem. B* **2002**, *106*, 12203–12210.
(63) Hagfeldt, A.; Boschloo, G.; Sun, L.; Kloo, L.; Pettersson, H. Dye-Sensitized Solar Cells. *Chem. Rev.* **2010**, *110*, 6595–6663.
(64) Haque, S. A.; Palomares, E.; Cho, B. M.; Green, A. N. M.; Hirata, N.; Klug, D. R.; Durrant, J. R. Charge Separation versus Recombination in Dye-Sensitized Nanocrystalline Solar Cells: The Minimization of Kinetic Redundancy. *J Am Chem Soc* **2005**, *127*, 3456–3462.
(65) Vicent-Luna, J. M.; Idígoras, J.; Hamad, S.; Calero, S.; Anta, J. A. Ion Transport in Electrolytes for Dye-Sensitized Solar Cells: A Combined Experimental and Theoretical Study. *J. Phys. Chem. C* **2014**.
(66) Srinivasa Rao, S.; Gopi, C. V. V. M.; Kim, S.-K.; Son, M.-K.; Jeong, M.-S.; Savariraj, A. D.; Prabakar, K.; Kim, H.-J. Cobalt Sulfide Thin Film as an Efficient Counter Electrode for Dye-Sensitized Solar Cells. *Electrochimica Acta* **2014**, *133*, 174–179.
(67) Nelson, J.; Chandler, R. E. Random Walk Models of Charge Transfer and Transport in Dye Sensitized Systems. *Coord. Chem. Rev.* **2004**, *248*, 1181–1194.
(68) Anta, J. A. Random Walk Numerical Simulation for Solar Cell Applications. *Energy Environ. Sci.* **2009**, *2*, 387–392.
(69) Liu, Y.; Jennings, J. R.; Huang, Y.; Wang, Q.; Zakeeruddin, S. M.; Grätzel, M. Cobalt Redox Mediators for Ruthenium-Based Dye-Sensitized Solar Cells: A Combined Impedance Spectroscopy and Near-IR Transmittance Study. *J Phys Chem C* **2011**, *115*, 18847–18855.
(70) Sodergren, S.; Hagfeldt, A.; Olsson, J.; Lindquist, S. E. Theoretical-Models for the Action Spectrum and the Current-Voltage Characteristics of Microporous Semiconductor-Films in Photoelectrochemical Cells. *J. Phys. Chem.* **1994**, *98*, 5552–5556.

(71) Bisquert, J.; Mora-Seró, I. Simulation of Steady-State Characteristics of Dye-Sensitized Solar Cells and the Interpretation of the Diffusion Length. *J. Phys. Chem. Lett.* **2010**, *1*, 450–456.
(72) Peter, L. M. Characterization and Modeling of Dye-Sensitized Solar Cells. *J. Phys. Chem. C* **2007**, *111*, 6601–6612.
(73) K. Kalyanasundaram. Dye-Sensitized Solar Cells. *(EPFL Press: 2010)*.
(74) Bisquert, J.; Zaban, A.; Salvador, P. Analysis of the Mechanisms of Electron Recombination in Nanoporous TiO2 Dye-Sensitized Solar Cells. Nonequilibrium Steady-State Statistics and Interfacial Electron Transfer via Surface States. *J. Phys. Chem. B* **2002**, *106*, 8774–8782.
(75) Salvador, P.; Hidalgo, M. G.; Zaban, A.; Bisquert, J. Illumination Intensity Dependence of the Photovoltage in Nanostructured TiO2 Dye-Sensitized Solar Cells. *J. Phys. Chem. B* **2005**, *109*, 15915–15926.
(76) Bisquert, J.; Fabregat-Santiago, F.; Mora-Seró, I.; Garcia-Belmonte, G.; Giménez, S. Electron Lifetime in Dye-Sensitized Solar Cells: Theory and Interpretation of Measurements. *J. Phys. Chem. C* **2009**, *113*, 17278–17290.
(77) Zaban, A.; Greenshtein, M.; Bisquert, J. Determination of the Electron Lifetime in Nanocrystalline Dye Solar Cells by Open-Circuit Voltage Decay Measurements. *Chemphyschem* **2003**, *4*, 859–864.
(78) Ondersma, J. W.; Hamann, T. W. Measurements and Modeling of Recombination from Nanoparticle TiO2 Electrodes. *J. Am. Chem. Soc.* **2011**, *133*, 8264–8271.
(79) Ansari-Rad, M.; Abdi, Y.; Arzi, E. Simulation of Non-Linear Recombination of Charge Carriers in Sensitized Nanocrystalline Solar Cells. *J. Appl. Phys.* **2012**, *112*, 074319–074319 – 7.
(80) Gonzalez-Vazquez, J. P.; Oskam, G.; Anta, J. A. Origin of Nonlinear Recombination in Dye-Sensitized Solar Cells: Interplay between Charge Transport and Charge Transfer. *J. Phys. Chem. C* **2012**.
(81) Nakade, S.; Kanzaki, T.; Kubo, W.; Kitamura, T.; Wada, Y.; Yanagida, S. Role of Electrolytes on Charge Recombination in Dye-Sensitized TiO2 Solar Cell (1): The Case of Solar Cells Using the I-/I3⊖ Redox Couple. *J. Phys. Chem. B* **2005**, *109*, 3480–3487.
(82) Wang, Q.; Ito, S.; Gratzel, M.; Fabregat-Santiago, F.; Mora-Sero, I.; Bisquert, J.; Bessho, T.; Imai, H. Characteristics of High Efficiency Dye-Sensitized Solar Cells. *J. Phys. Chem. B* **2006**, *110*, 25210–25221.
(83) Marcus, R. A. On the Theory of Oxidation-Reduction Reactions Involving Electron Transfer. I. *J. Chem. Phys.* **1956**, *24*, 966–978.
(84) Gerischer, H. Über Den Ablauf von Redoxreaktionen an Metallen Und an Halbleitern. *Z. Für Phys. Chem.* **1960**, *26*, 223–247.
(85) Bisquert, J.; Marcus, R. A. Device Modeling of Dye-Sensitized Solar Cells. In; Topics in Current Chemistry; Springer Berlin Heidelberg, 2013; pp. 1–71.
(86) Halme, J.; Vahermaa, P.; Miettunen, K.; Lund, P. Device Physics of Dye Solar Cells. *Adv. Mater.* **2010**, *22*, E210–E234.
(87) Gonzalez-Vazquez, J.; Anta, J. A.; Bisquert, J. Determination of the Electron Diffusion Length in Dye-Sensitized Solar Cells by Random Walk Simulation: Compensation Effects and Voltage Dependence. *J. Phys. Chem. C* **2010**, *114*, 8552–8558.
(88) Cao, F.; Oskam, G.; Meyer, G. J.; Searson, P. C. Electron Transport in Porous Nanocrystalline TiO2 Photoelectrochemical Cells. *J. Phys. Chem.* **1996**, *100*, 17021–17027.
(89) Peter, L. M.; Wijayantha, K. G. U. Intensity Dependence of the Electron Diffusion Length in Dye-Sensitised Nanocrystalline TiO2 Photovoltaic Cells. *Electrochem. Commun.* **1999**, *1*, 576–580.
(90) Ferber, J.; Stangl, R.; Luther, J. An Electrical Model of the Dye-Sensitized Solar Cell. *Sol. Energy Mater. Sol. Cells* **1998**, *53*, 29–54.
(91) Anta, J. A.; Idígoras, J.; Guillén, E.; Villanueva-Cab, J.; Mandujano-Ramírez, H. J.; Oskam, G.; Pellejà, L.; Palomares, E. A Continuity Equation for the Simulation of the

Current–voltage Curve and the Time-Dependent Properties of Dye-Sensitized Solar Cells. *Phys. Chem. Chem. Phys.* **2012**, *14*, 10285–10299.
(92) Harrick, N. J. Lifetime Measurements of Excess Carriers in Semiconductors. *J. Appl. Phys.* **1956**, *27*, 1439–1442.
(93) Bisquert, J. Theory of the Impedance of Electron Diffusion and Recombination in a Thin Layer. *J. Phys. Chem. B* **2002**, *106*, 325–333.
(94) Nelson, J.; Haque, S. A.; Klug, D. R.; Durrant, J. R. Trap-Limited Recombination in Dye-Sensitized Nanocrystalline Metal Oxide Electrodes. *Phys. Rev. B* **2001**, *6320*.
(95) Kopidakis, N.; Benkstein, K. D.; Lagemaat, J. van de; Frank, A. J. Transport-Limited Recombination of Photocarriers in Dye-Sensitized Nanocrystalline TiO2 Solar Cells. *J. Phys. Chem. B* **2003**, *107*, 11307–11315.
(96) Anta, J. A.; Casanueva, F.; Oskam, G. A Numerical Model for Charge Transport and Recombination in Dye-Sensitized Solar Cells. *J. Phys. Chem. B* **2006**, *110*, 5372–5378.
(97) Villanueva-Cab, J.; Oskam, G.; Anta, J. A. A Simple Numerical Model for the Charge Transport and Recombination Properties of Dye-Sensitized Solar Cells: A Comparison of Transport-Limited and Transfer-Limited Recombination. *Sol. Energy Mater. Sol. Cells* **2010**, *94*, 45–50.
(98) Bisquert, J.; Vikhrenko, V. S. Interpretation of the Time Constants Measured by Kinetic Techniques in Nanostructured Semiconductor Electrodes and Dye-Sensitized Solar Cells. *J. Phys. Chem. B* **2004**, *108*, 2313–2322.

Chapter 4:

Experimental: Characterization techniques and preparation of devices

1. Standard solar spectrum and solar irradiation.

Since the solar spectrum depends on many variables, such as atmospheric conditions, time of the day, Earth-Sun distance and solar rotation and activity it is necessary to define a standard spectrum and power density to compare the response and behaviour of different devices. The Sun emits light resembling the spectrum of a blackbody at 5670 K with a power density at the surface of 62 MW/m^2. However, the solar power that arrives at the atmosphere of the Earth is reduced to 1353 W/m^2, which is defined as the *Solar Constant*.[1] Before reaching the Earth´s surface, the radiation must pass through the atmosphere, which modifies the solar spectrum in intensity and spectral distribution (**Figure 4.1**).

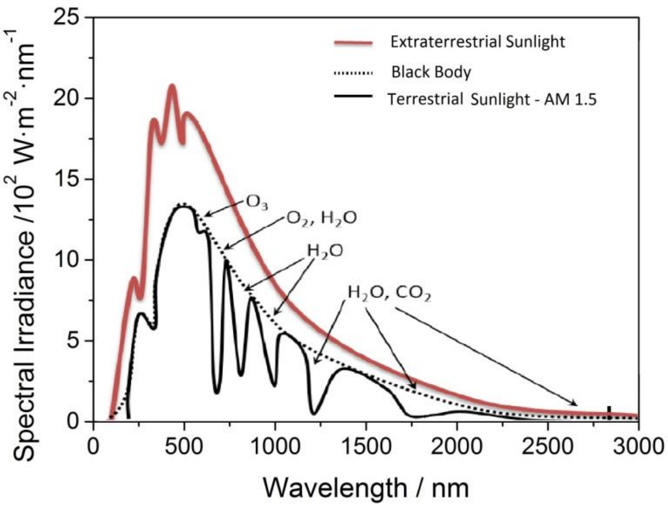

Figure 4.1: Spectra of a blackbody at 5670K, extraterrestrial and terrestrial (AM 1.5) solar spectrum.

The irradiation that finally reaches the suface will depend on the path length of the sunlight. The attenuation that the radiation suffers due to atmospheric absorption and which depends on the position of the Sun is taken into account by the *Air Mass* parameter (AM = 1 / cos Θ, where Θ is the angle of elevation of the Sun, **Figure 4.2**).

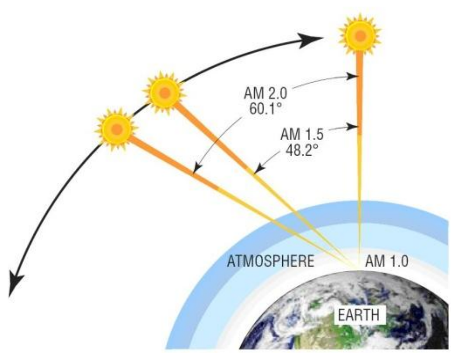

Figure 4.2: Schematic view of Air Mass as a function of angle of elevation of the Sun (taken from teknologisurya.wordpress.com)

The standard spectral distribution of the light used to study the response of solar cells is AM 1.5G, corresponding to ϴ = 48.2°. This atmosphere thickness should attenuate the solar spectrum to a mean irradiance of around 900 W/cm^2.[1] However, for consensus the standard spectrum is normalized so that the integrated irradiance of this spectrum per unit area and unit time is 1000 W/cm^2. This is known as 1 *sun* illumination.

In this thesis, two different sources of illumination and ways of calibration were used:

- The source used to measure the current-voltage characteristics was a solar simulator (*ABET Technologies Sun 2000,* **Figure 4.3 left**) with a xenon lamp of 150W and appropriate set of filters for the correct simulation of the AM 1.5G solar spectrum. The light intensity was calibrated to the standard value of 1 sun (100 mW/cm^2) using a reference solar cell (Oriel, 91150) (**Appendix**, Figure A-4.1).
- The source used for photoelectrochemical characterization was a Thermo Oriel Xenon 450W arc lamp coupled to a water filter to remove the IR radiation (**Figure 4.3 right**). The applied light irradiance was measured with an optical power meter (*Gentec TUNER*) equipped with a bolometer (*Gentec XLP12-1S-H2*).

Figure 4.3: Illumination sources employed in this thesis.

2. Techniques used for the characterization of mesoporous semiconductor films for photocatalytic and photovoltaic applications.

2.1. Photoelectrochemical techniques.

These techniques are based on the perturbation of one electric variable of the system (potential or current intensity). The response of the system to this perturbation is then measured. These techniques can be performed in the steady-state or be time-resolved.

2.1.1. Cyclic voltammetry.

In cyclic voltammetry the potential applied to the working electrode is varied linearly, and the current flowing between the working electrode and the counter-electrode is recorded. The perturbation function has a triangular form and changes from the start potential E_1 to the vertex potential E_2 and back (**Figure 4.4**). Both steps are carried out at a constant scan rate.

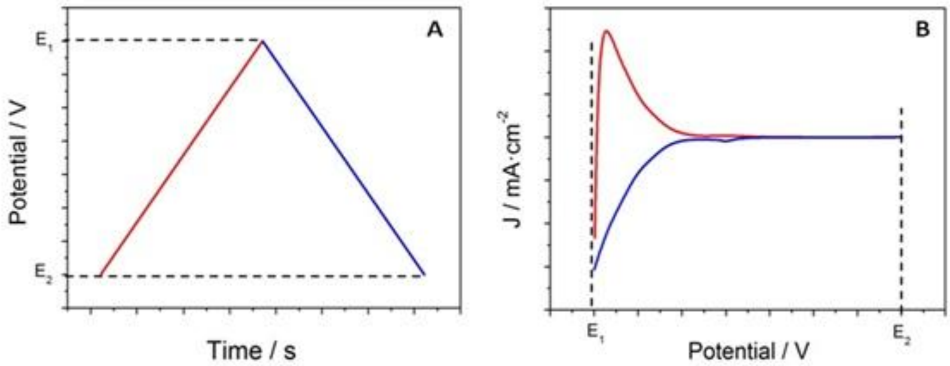

Figure 4.4: (A) Scheme of temporal variation of applied potential and (B) the response of the current density for a typical mesoporous TiO_2 electrode used in this thesis.

In the (photo)electrochemical characterization of mesoporous electrodes, cyclic voltammetry allows to study different capacitive and faradic processes taking place in the dark or under illumination. For instance, the process related to reversible charge accumulation in the mesoporous structure of semiconductor electrodes will be studied. Furthermore, the photooxidation of water or organic molecules (methanol or formic acid) can be addressed.

2.1.2. Intensity current-voltage characteristics or IV curve.

The characterization of solar devices by IV curves (**Figure 4.5**) relies also on a voltammetric measurement. The photocurrent generated by a photovoltaic device under illumination is recorded during a linear increase of the potential, which is applied externally to the solar cell. The main photovoltaic parameters of a solar cell can be extracted from the IV curve.

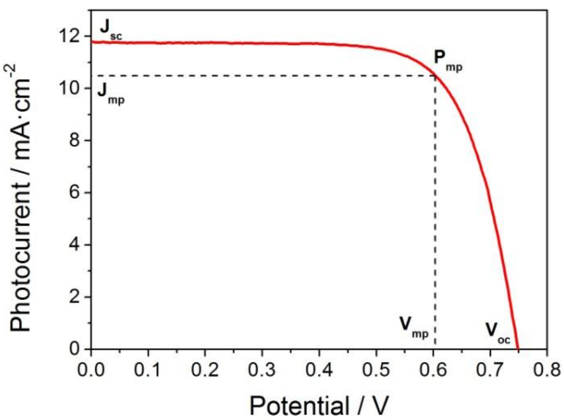

Figure 4.5: An example of an IV curve where the main photovoltaic parameters that characterize a solar cell are shown.

From a practical point of view, the most important piece of information is the maximum output power of the device per unit area (P_{mp}). The maximum power point is defined by the square under the IV curve with the largest area associated to a voltage and a photocurrent, or, in other words, to the maximum value of the product $V \cdot J$ ($P_{mp} = V_{mp} \cdot J_{mp}$). The maximum current flow is obtained when the cell operates under short-circuit condition, which means that the external circuit is closed (**Figure 3.6**) and the external potential (and resistance) is zero. The short-circuit photocurrent density (J_{sc} / mA·cm^{-2}) is expressed as the short-circuit photocurrent per unit of active area of the solar cell. The opposite case is the open-circuit condition (infinite resistance), where J_{sc} is zero and the photovoltage reaches its maximum value (V_{oc}).

The overall conversion efficiency (η) of the device is determined by the following relationship:

$$\eta = \frac{J_{sc} \cdot V_{oc} \cdot FF}{P_{sun}} \qquad (4.1)$$

where P_{sun} is the power of the incident light and FF is the fill factor of the cell. This latter parameter is defined by:

$$FF = \frac{J_{mp} \cdot V_{mp}}{J_{sc} \cdot V_{oc}} \qquad (4.2)$$

The fill factor strongly depends on the series resistance of the cell and on the non-ideality factor m (See Chapter 3).

2.1.3. Chronopotentiometry at open-circuit condition.

For mesoporous semiconductor electrodes, the photovoltage is related to the accumulation of photogenerated electrons in electronic states in the semiconductor.[2] Photovoltage measurements probe the potential of the working electrode at open-circuit conditions both in the dark and under steady illumination as a function of time (**Figure 4.6**). Upon excitation of the semiconductor with photons of energy exceeding the band gap (*light on*), electrons get accumulated in the semiconductor inducing a displacement of the Fermi level towards more negative potentials. This shift is measured as a change of the open circuit potential. When illumination is interrupted (*light off*), the photogenerated electrons react until the initial value of the potential is re-established. Photopotential measurements allow for studying the kinetics of the interfacial electron transfer.

In semiconductors such as TiO_2, the holes are typically transferred to the electrolyte faster than photogenerated electrons. Thus, a negative charge accumulation takes place under illumination. The required time to raise the stationary value under illumination or in dark depends on the kinetics of the different processes that occur at the semiconductor/electrolyte interface.

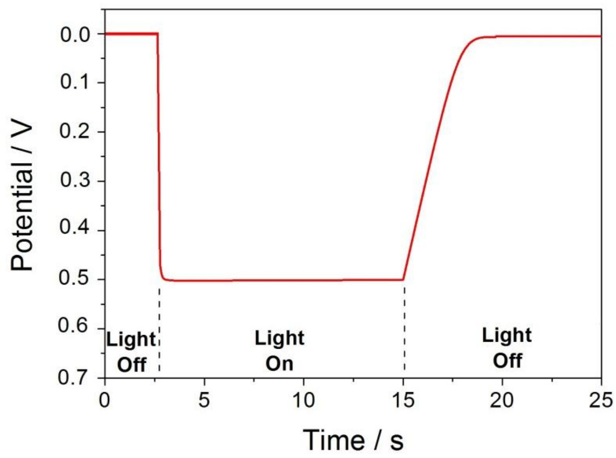

Figure 4.6: Profile of photovoltage versus time for a semiconductor upon light exposure.

2.1.4. Open-Circuit Voltage Decay (OCVD).

In photovoltaic applications, OCVD measurement is used to study the kinetics of electron recombination with the reduced species in the electrolyte. During OCVD measurements, the cell is first illuminated under open-circuit conditions to establish a steady-state photovoltage. Then, the illumination is turned off and the subsequent voltage decay upon electron recombination is monitored. As can be seen in **Figure 4.7**, the decay is very fast at the beginning, and then it slows down considerably. This slow-down is due to a slower detrapping of electrons as the quasi-Fermi level falls.

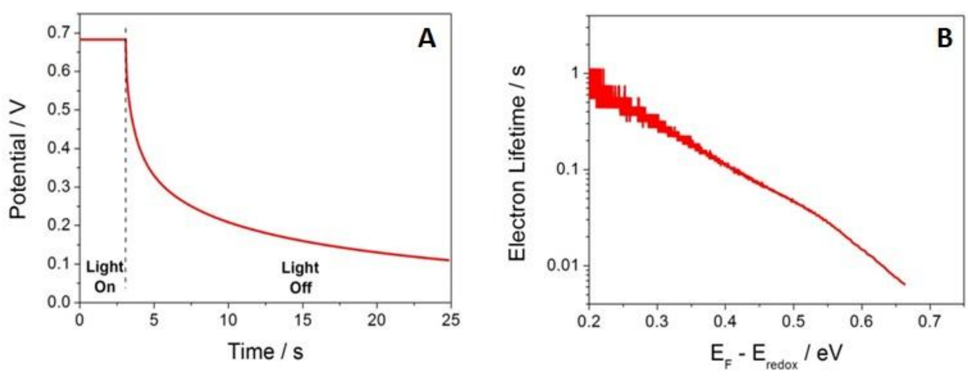

Figure 4.7: (A) Open-circuit voltage decay and (B) extracted electron lifetime.

Zaban et al.[3] demonstrated the validity of this method to measure the effective electron lifetime as a function of the open-circuit voltage. The electron lifetime can be obtained from the inverse of the derivate of the voltage decay transient normalized by the thermal voltage[4]

$$\beta\tau_n^{OCVD} = \frac{k_B T}{q}\left(\frac{d\,V_{oc}}{dt}\right)^{-1} \qquad (4.3)$$

where β is the recombination parameter (**Chapter 3**)The advantage of this technique with respect to alternative methods based on small perturbations in the time or frequency domain is that the lifetime can be determined in a wide potential range with one single and fast measurement, with as much resolution along the Fermi level axis as desired.

2.1.5. Short-circuit voltage (V_{sc}) measurements.

This method, first introduced by Boschloo et al.[5], is used to estimate the electron quasi-Fermi level of electrons in dye-sensitized semiconductors. At an initial stage, the cell is illuminated under short-circuit conditions. Then, the illumination is turned off and simultaneously the cell is switched to open-circuit (**Figure 4.8**).

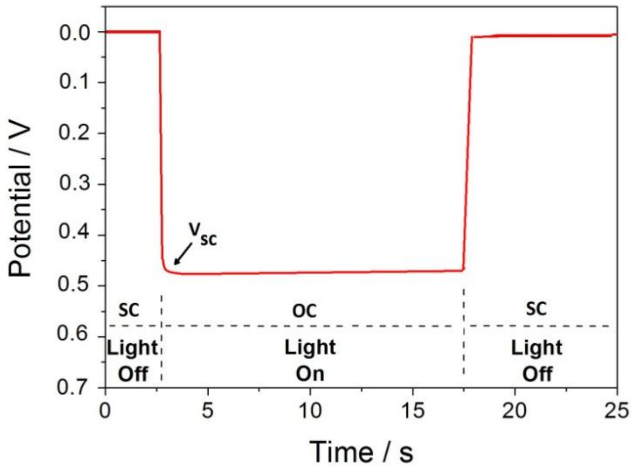

Figure 4.8: Scheme of a typical profile of a short-circuit voltage measurement.

The maximum voltage, which is measured after switching to open-circuit, is known as V_{sc} and gives a good estimate of the average electron quasi-Fermi level under short-circuit conditions. The difference between V_{sc} and V_{oc} determined by different light intensities is, as a matter of fact, almost constant for typical DSSC.[5–7]

2.1.6. Chronoamperometry.

In this technique a transient photocurrent is measured at a fixed applied potential (**Figure 4.9**). Thus, information on the kinetics of recombination and interfacial charge transfer at the semiconductor/electrolyte interface can be gained.

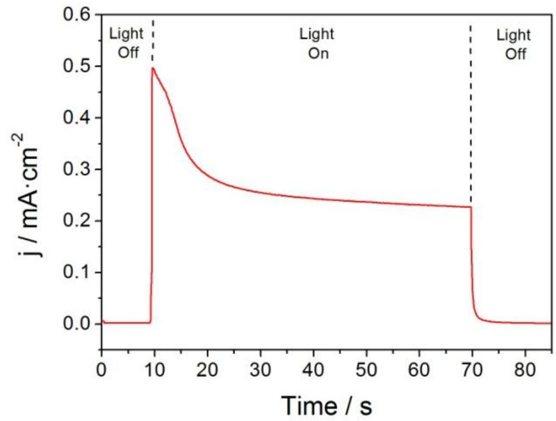

Figure 4.9: Typical transient photocurrent at fixed potential.

2.2. Incident Photon-to-Current Conversion Efficiency (IPCE).

This parameter indicates the amount of current that the cell can produce when it is irradiated by photons of a particular wavelength. If the IPCE is integrated over the whole solar spectrum, the short-circuit photocurrent J_{sc}, upon exposure to 1 *sun*, can be deduced (**Equation 3.15**) (**Appendix**, Figure A-4.1). IPCE is defined as the number of electrons generated in the solar devices with respect to the number of incident photons for a given wavelength, hence,

$$IPCE\ (\lambda) = \frac{n^o\, electrons}{n^o\ photons} = \frac{1240 \cdot J_{sc}(\lambda)}{\lambda \cdot P_{light}(\lambda)} \qquad (4.4)$$

where J_{sc} is the short-circuit photocurrent at a given wavelength (mA·cm^{-2}), λ is the wavelength (nm) of the incident light, P_{light} is the power of incident light (W·m^{-2}) and 1240 is a conversion factor.

In a DSSC the IPCE spectrum is related to the absorbance spectrum of the dye. An example of IPCE for DSSCs with different dyes is shown in **Figure 4.10**

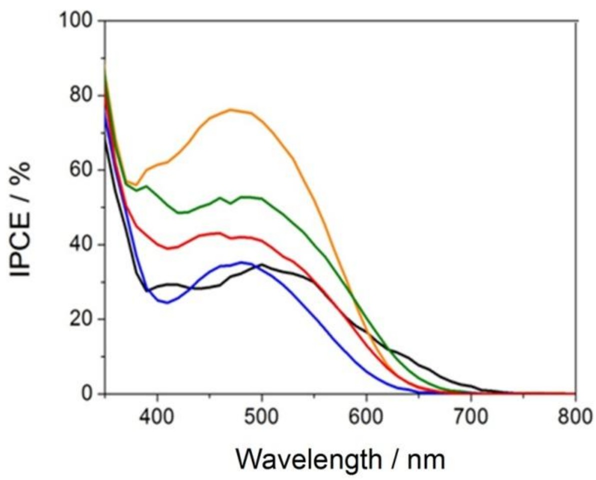

Figure 4.10: IPCE for DSSCs with different dyes.

2.3. Optical spectroscopy.

2.3.1. Attenuated total reflection infrared spectroscopy (ATR-IR).

ATR-IR spectroscopy[8] is a useful tool for the study of molecular species at the semiconductor/electrolyte interface or of shallow trapped electrons in the semiconductor. Using ATR-IR spectroscopy it is possible to minimize the background signal resulting from the electrolyte and to enhance the signals attributed to molecular species or trapped electrons at the semiconductor/electrolyte interface. In this technique, a single beam passes through an optically dense medium (high refractive index, n_2). At the interface with another medium of lower refractive index (n_1) the incident light will be totally reflected if the incident angle exceeds a critical value (α_c):

$$\alpha_c = \arcsin\left(\frac{n_1}{n_2}\right) \qquad (4.5)$$

However, an evanescence wave penetrates into the medium of lower refractive index and can get absorbed by samples in intimate contact with the ATR prism. In the used set-up, medium 1 is the mesoporous semiconductor electrode penetrated by the aqueous electrolyte and medium 2 is a hemispheric prism of ZnSe (**Figure 4.11**). The penetration depth (z_p) is given by[8]

$$z_p = \frac{\lambda_0}{2\pi n_2\sqrt{\sin^2\alpha - \left(\frac{n_1}{n_2}\right)^2}} \qquad (4.6)$$

where λ_0 is the wavelength of the IR beam and α is the incident angle, with $\alpha > \alpha_c$. Thus, if medium 1 is absorbent, the evanescence wave is absorbed and the intensity of reflected light will decrease with respect to a reference or background value (ATR).

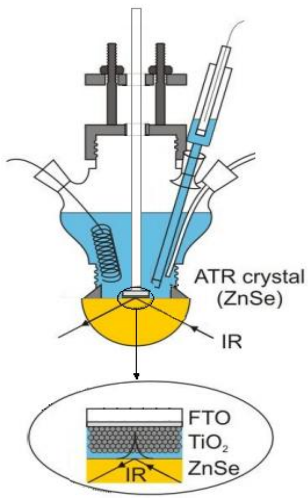

Figure 4.11: Scheme of the photoelectrochemical cell used in ATR-IR measurements.

It is important to mention that the reflective index of many semiconductor oxides is close to or higher than the index of a ZnSe prism (n_2 = 2.4)[9] as used in this thesis. Refractive indices of 2.4 and 2.2 have been found for TiO_2 and WO_3 respectively. In these cases, the condition for ATR is not fulfilled. However, due to the nanoparticulate morphology of the mesoporous electrodes, the refractive index of the thin film electrode is smaller than for the bulk semiconductor, allowing for the detection of an IR signal by ATR.

2.3.2. UV-Visible spectroscopy.

When powders or dispersive thin films are used as samples in UV-Vis spectroscopy measurements, absorption, dispersion, transmission and reflection of the incident light (**Figure 4.12**) have to be taken into account

$$A + T + R = 1 \qquad (4.7)$$

where *A, T* and *R* are the relative intensities of absorbed, transmitted and reflected and/or dispersed radiation, respectively.

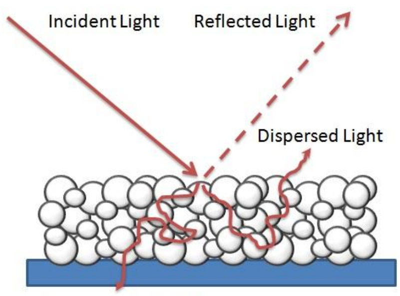

Figure 4.12: Interaction of light with a dispersive sample.

To measure effectively the UV-Vis spectrum of nanoporous electrodes, an integrating sphere (Ulbricht sphere, **Figure 4.13**) has been used. This sphere is coated with a highly scattering powder with a low absorption capacity. Thus, all radiation reflected by the sample is recorded by the detector.

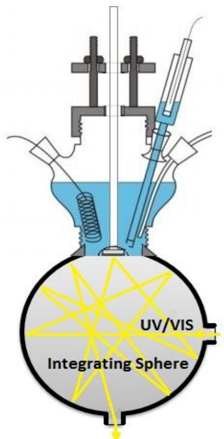

Figure 4.13: Scheme of the photoelectrochemical cell and the integrating sphere used in UV/VIS measurements.

2.3.3. Raman spectroscopy.

Raman spectroscopy was used to analyze the crystal structure of nanocrystalline samples (**Figure 4.14**). This technique relies on the inelastic scattering of laser light by the sample due to the excitation of vibrational, rotational and other low-frequency modes of the system. This makes it possible to determine the nature of the sample.

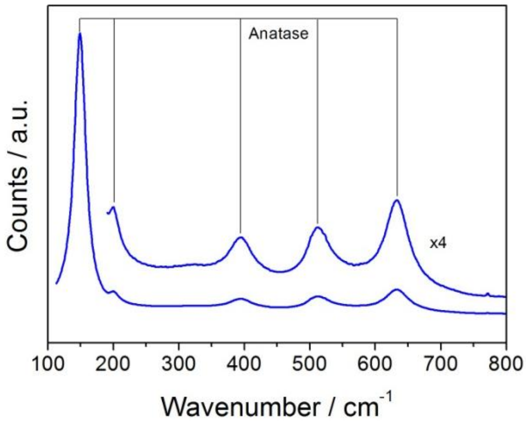

Figure 4.14: Characteristic Raman spectra of the nanocrystalline structure of TiO_2 anatase.

2.4. Frequency-domain small-perturbation analysis techniques.

Frequency-domain techniques are very useful tools for the characterization of solar cells. In these techniques, a sinusoidal modulation in light intensity or voltage is superimposed on a dc component and the phase and magnitude of the response relative to the input is measured. The modulation amplitude is small enough to ensure a linear response of the system. The measurement comprises a wide range of frequencies (mHz to MHz), corresponding to timescales relevant for processes occurring in the photoconversion process of the solar cell.

The illumination source for the frequency response techniques described below was provided by a 530 nm light emitting diode (LED, *LUXEON*) over a wide range of dc light intensities.

2.4.1. Electrochemical impedance spectroscopy.

Electrochemical impedance spectroscopy (*EIS*) is a powerful technique for the characterization of electrochemical systems. In the DSSC field it is one of the most useful experimental techniques as it permits a simultaneous characterization of the different processes taking place in the cell.[10,11] In an EIS measurement the voltage of the solar cell is perturbed by a small amplitude sinusoidal modulation and the resulting sinusoidal current response is measured as a function of the modulation frequency.[12]

The meaning of electrical impedance can be understood starting from the concept of resistance. The electrical resistance is the ability of a circuit element to *resist* the flow of electrical current. The well-known Ohm's Law defines resistance (R) in terms of the ratio between voltage (V) and current (I)

$$R = \frac{V}{I} \qquad (4.8)$$

This relationship is limited to only one circuit element, an ideal resistor. But usually the systems under study contain circuit elements that exhibit a much more complex behaviour. The simple concept of resistance needs to be replaced by a more general parameter: the impedance, which includes not only the relative amplitudes of the voltage and the current, but also the relative phases. Like resistance, impedance is a measure to the ability of a circuit to resist the flow of electrical current.

Electrochemical impedance is normally measured using a small excitation signal in order to obtain a linear response of the cell.[13,14] The electrical current response will be sinusoidal at the same frequency, but shifted in phase (**Figure 4.15**):

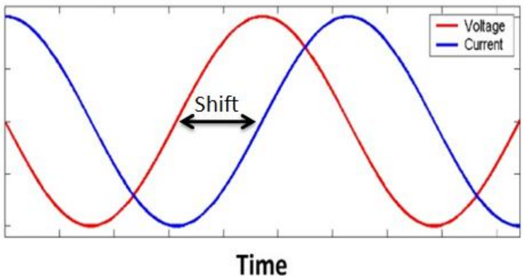

Figure 4.15: Sinusoidal current response in a linear system.

The excitation signal can be written as:

$$V(\omega) = V_0 \cos \omega t \qquad (4.9)$$

where $V(\omega)$ is the ac potential applied to the system, V_0 is the amplitude signal and ω is the angular frequency ($\omega = 2\pi f \; rad \; s^{-1}$). The current response will be shifted with respect to the applied potential:

$$I(\omega) = I_0 \cos(\omega t + \phi) \qquad (4.10)$$

where $I(\omega)$ is the ac electrical current response signal, I_0 the amplitude and ϕ the phase shift. The phase contains the current lag with respect to the voltage. An expression analogous to Ohm's Law allows for calculating the impedance of the systems as:

$$Z(\omega) = \frac{V(\omega)}{I(\omega)} = \frac{V_0 \cos \omega t}{I_0 \cos(\omega t + \phi)} \qquad (4.11)$$

Usually, it is convenient to use complex exponentials to express the impedance. Complex numbers allow for a simpler representation of the relative magnitude and phase of the input and output signal. Besides, it is a more powerful representation for circuit analysis purposes. Taking into account Euler's relationship,

$$e^{jx} = \cos(x) + j\ \sin(x) \qquad (4.12)$$

It is possible to express the potential as:

$$V(\omega) = V_0\, e^{j\omega t} \qquad (4.13)$$

And the current response can be described as:

$$I(\omega) = I_0\, e^{j(\omega t + \phi)} \qquad (4.14)$$

Since $Z(\omega) = V(\omega)/I(\omega)$ the exponential $\exp(j\omega t)$ cancels out, so that:

$$Z = \frac{V_0}{I_0}\, e^{-j\phi} = Z_0 e^{-j\phi} \qquad (4.15)$$

The impedance is, therefore, expressed in terms of a magnitude Z_0 and a phase shift φ. Using **Equation 4.12**, it is possible to separate the real part and imaginary part of the impedance,

$$Z_0 e^{-j\phi} = Z_0 \cos\phi - Z_0\, j \sin\phi \qquad (4.16)$$

By varying the frequency of the applied signal, one can get the impedance of the system as a function of frequency. The recorded data can either be represented as magnitude and phase versus frequency (Bode Plot) or on a complex plane (Nyquist Plot). In a Nyquist Plot the real part of the impedance (Z') is plotted on the X-axis and the imaginary part (Z'') is plotted on the Y-axis (**Figure 4.16 A** and **4.16 B**).

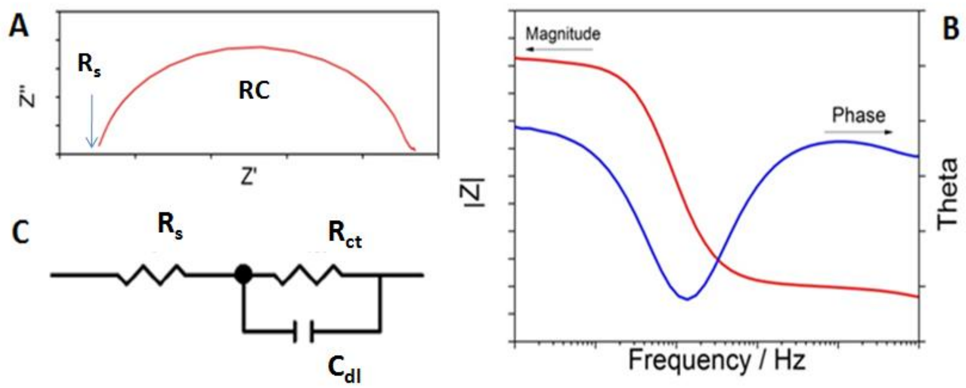

Figure 4.16: (A) Nyquist Plot, (B) Bode Plot and (C) equivalent circuit associated to a R_s-(RC) element.

EIS data are commonly analyzed in terms of an equivalent circuit model. Most of the circuit elements in the model are common electrical elements such as resistors, capacitors and inductors which can be combined in series or in parallel. For example, one of the simplest equivalent circuits is shown in **Figure 4.16 C**. This is the result of the combination of a resistance in series with a RC element (a resistor and capacitor in parallel). However, for electrochemical systems other more complex equivalent circuits have been used. A very important equivalent circuit is the *Randles circuit* (**Figure 4.17 A**).

This circuit models a cell where the polarization is due to a combination of kinetic and diffusion processes.

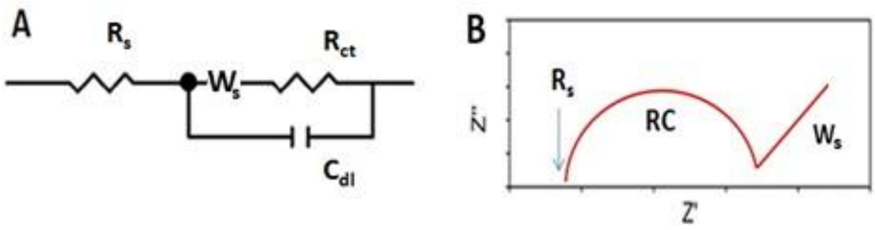

Figure 4.17: Equivalent circuit and Nyquist Plot for Randles Circuit

This model includes a series resistance (R_s), a double layer capacitor (C_{dl}), a charge transfer resistance (R_{ct}) and a Warburg diffusion impedance (W). **Figure 4.17 B** shows the Nyquist Plot for this circuit. The Nyquist Plot for a RC element is always a semicircle as is shown in Figure 4.16 A and Figure 4.17 B. The double layer capacitance and charge transfer resistance in parallel define the time constant (τ = RC) o relaxation time of the system. The series resistance is expressed by the real intercept at high frequencies of this semicircle. Finally, the Warburg diffusion impedance appears as a straight line with a slope of 45^o.

Using the Randles circuit as starting point, other more complex models can be devised. One of these cases is represented by DSSC. The impedance response of DSSC will be related to the response of different components of the devices. Generally, a model based on a transmission line of RC elements (**Figure 4.18**) is used to describe the system

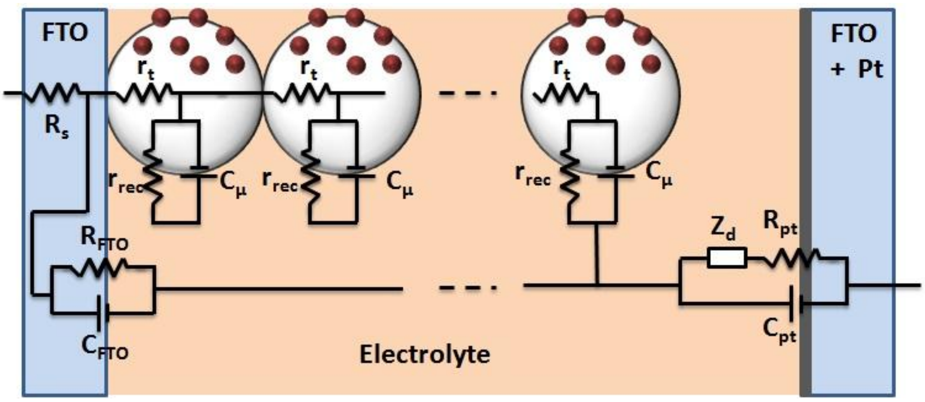

Figure 4.18: Transmission line model for DSSC.

Different circuit elements are attributed to the different processes taking place in the cell. The processes occurring in the mesoporous oxide film are usually modelled by a diffusion-recombination transmission line, whose application to DSCs was first proposed by Bisquert.[15] This transmission line is composed of a network of resistive and capacitive elements, which describe the transport and interfacial transfer of electrons that take place in the oxide. The mesoporous oxide film has two main contributions in the impedance spectrum. One feature is an intermediate frequency arc, which accounts for the parallel connection of the charge transfer resistance R_{rec} ($R_{rec} = r_{rec}/d$, being d the thickness of the film) and the capacitance of the film C_{μ} ($C_{\mu} = c_{\mu}{\cdot}d$). Secondly, a Warburg-line diffusion element, a 45º phase shift at high frequencies related to the electron transport resistance R_t ($R_t = r_t{\cdot}d$) in the mesoporous layer. The diffusion impedance of redox species in the electrolyte (Z_d) is usually modelled using a finite-length Warburg element of the type used for thin layer electrochemical cells. Generally, Z_d in DSCs is small and difficult to identify it in the overall impedance solar response. However, when an electrolyte based on ionic liquids (high viscosity) is used, a semicircle at low frequencies can be distinguished in the spectrum. A cathodic impedance due to the platinised electrode is also present in the spectrum and it is expressed as a parallel combination of the charge transfer resistance (R_{pt}) and the double layer capacitance (C_{pt}). In the spectrum, this feature appears as a semicircle at high frequencies. R_{FTO} and C_{FTO} stand for the charge-transfer resistance and the capacitance at the FTO/electrolyte interface. Finally, R_s accounts for the series resistance of the conducting glass plus any other elements that might be considered to be in series with the rest of the circuit.

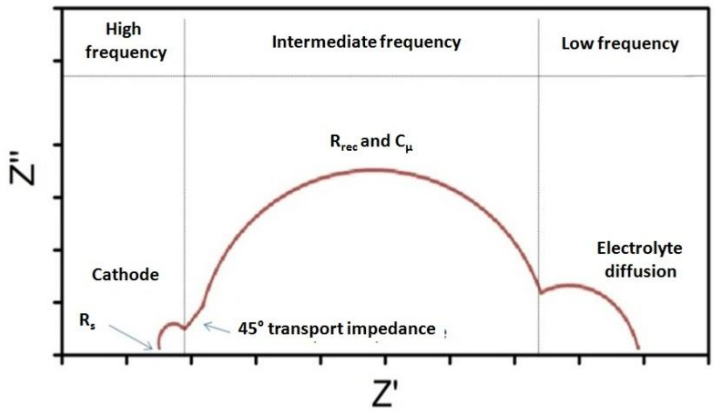

Figure 4.19: Nyquist impedance spectrum of a typical DSSC.

It must be pointed put that in many cases the contribution of the different components is not seen as clearly as in **Figure 4.19**. This depends on the nature and structure of semiconductor, the viscosity of electrolyte and the voltage at which the measurement is done.

For a solar cell with a good collection efficiency, the EIS spectrum can be well fitted to the diffusion-recombination model of Bisquert and coworkers.[15,16] As mentioned in the previous chapters, the chemical capacitance (C_{μ}) and the recombination resistance (R_{rec}) in the oxide/electrolyte interface have in typical DSSC, and in conditions in which trapping is dominant, a voltage dependence given by[17]

$$C_{\mu}^{-1} = \frac{\partial E_F}{\partial n} = C_{\mu,0}^{-1}\, exp\left(\frac{-\alpha(E_F - E_F^0)}{k_B T}\right) \qquad (1.24)$$

$$R_{rec}^{-1} = \frac{\partial J_R}{\partial E_F} = R_{rec,0}^{-1}\, exp\left(\frac{\beta(E_F - E_F^0)}{k_B T}\right) \qquad (3.11)$$

where α is a dimensionless parameter related to the mean energy of the exponential distribution of localized states in the oxide $g(E)$[18] as shown in Chapter 1 and β is a dimensionless parameter which can be related to the reaction order of the recombination reaction with respect to free electrons,[14] as shown in Chapter 3. In **Equations 1.24 and 3.11**, the voltage applying in the device (assuming no voltage drop in the substrate/oxide and electrolyte/counter-electrode interfaces) corresponds to the difference in Fermi levels in the oxide and in the electrolyte, i.e. $V = E_F - E_F^0$.

Apart from the parameters directly extracted from the impedance fitting mentioned above, we can obtain some basic electron transport and recombination parameters via the following relations:

- The time constant of the intermediate frequency semicircle can be used to determine the effective electron lifetime:[19]

$$\tau_n^{EIS} = R_{rec} \cdot C_\mu = \omega_{max}^{-1} \qquad (4.17)$$

In addition, combining **Equation 4.17**, **1.24** and **3.11**, the electron lifetime can be obtained by

$$\tau_n = \tau_{dark}\, exp\left[\left(\frac{(\alpha-\beta)V}{k_B T}\right)\right] \qquad (4.18)$$

- The small amplitude diffusion length can be extracted from the transport and transfer resistances, taking into account the thickness of the film (d):

$$\frac{L_n}{d} = \sqrt{\frac{R_{rec}}{R_t}} \qquad (4.19)$$

hence, the larger the recombination resistance and the smaller the transport resistance, the longer is the average distance travelled by the electrons in the semiconductor film. For cells with good collection properties, $L_n >> d$. Otherwise, the EIS spectrum does not fit to the scheme of Figure 4.18 and the extraction of the transport and recombination parameter is not trivial.[20]

In this thesis, EIS measurements have been carried out in three different ways:

- In the dark varying the applied dc voltage.
- At open-circuit condition under varying illumination intensities.
- Under illumination (fixed at *1sun*) and varying the applied dc voltage.

All electrochemical impedance spectra have been fitted using the Zview software (Scribner) and the equivalent circuit shown in **Figure 4.20**, where DX1 stands for the diffusion-recombination transmission line model:

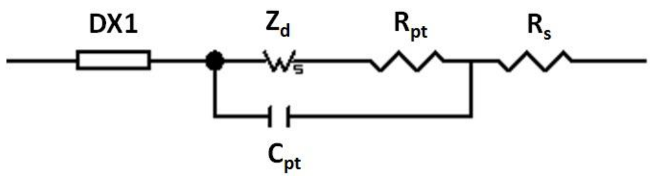

Figure 4.20: Equivalent circuit model used to fit impedance spectra. DX1 is the distributed element accounting for the diffusion-recombination transmission line (Figure 4.18).

2.4.2. Intensity-modulated spectroscopy.

Frequency-domain techniques with optical perturbation comprise *intensity modulated photocurrent spectroscopy* (IMPS) and *intensity modulated photovoltage spectroscopy* (IMVS). These techniques involve a small amplitude modulation of the photon flux incident on the cell.[21] In the IMVS measurement, the sample is illuminated at open-circuit and in the IMPS, at short-circuits conditions. Superimposed on a steady-state illumination level, a small sinusoidal modulation of the illumination intensity is applied. The magnitude of the photovoltage or photocurrent response to the modulation as well as the phase-shift of this response with respect to the modulated illumination is recorded. As already mentioned, the ac modulation must be sufficiently small so that a linear response of the system is obtained.

For both techniques, the simplest analysis of the results involves the determination of a time constant for the photocurrent or photovoltage response. IMVS is typically used to characterize the recombination process in solar cells, and the time constant that is extracted from an IMVS experiment is the effective electron lifetime.[13] The IMVS response in the frequency domain is a semicircle in the lower complex plane (**Figure 4.21 left**). The effective electron lifetime can be obtained from the experimental spectra, taking into account that the minimum of the semicircle is located at an angular frequency that is equal to:

$$\omega_{min} = \frac{1}{\tau_n^{IMVS}} \qquad (4.20)$$

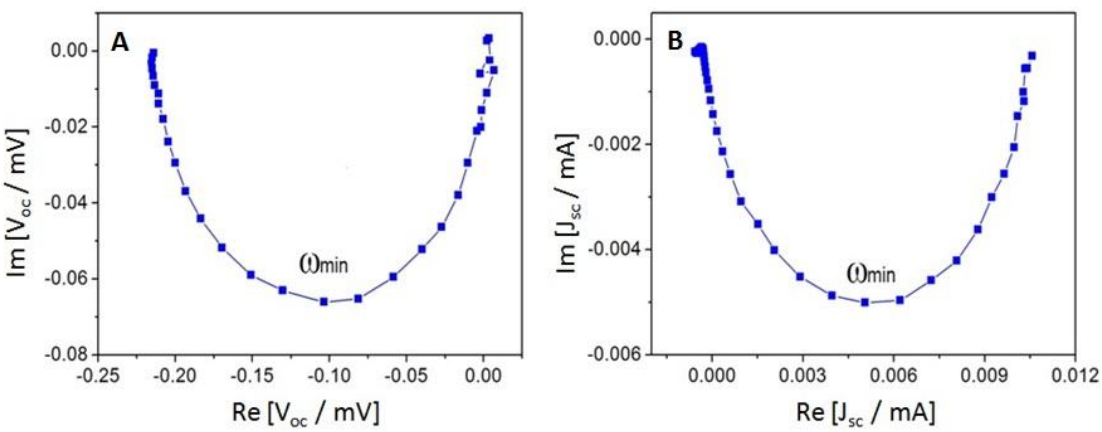

Figure 4.21: (A) IMVS and (B) IMPS response in the complex plane for a typical DSSC.

The time constant for the photocurrent response depends on both electron transport and electron recombination.[22] Under short-circuit conditions, the electron lifetime is assumed to be much larger than the electron transport time, so the measured photocurrent response is nearly equal to the transport time.[12]

The time constant τ_{IMPS} obtained from the inverse of the minimum angular frequency (ω_{min}) in an IMPS plot (**Figure 4.21 right**) can be related to the effective diffusion coefficient (D_n) by[23,24]

$$\tau_{IMPS} = \frac{d^2}{\gamma \, D_n} \qquad (4.21)$$

where γ is a numerical factor, which depends on layer thickness (d), absorption coefficient and illumination direction. In this thesis, a value of 2.5 has been used for γ parameter.

At low frequencies, the IMPS plots converge to a point on the real axis that corresponds to the steady-state photocurrent. At high frequencies, the modulating frequency is faster than the relaxation of the charge carrier density by transport to the contacts and the modulated photocurrent tends to zero. An additional phase shift is observed at high frequencies, due to the attenuation of the IMPS response by the series resistance and capacitance of the anode.

As in EIS, a small perturbation electron diffusion length (L_n), can be estimated by IMVS and IMPS data via the equation (**Chapter 3**):

$$L_n = \sqrt{(D_n \cdot \tau_n)} \qquad (3.26)$$

The pair of D_n and τ_n used to obtain L_n must be determined at the same value of the quasi-Fermi level with respect to the conduction band. However, at the same light intensity the position of the quasi-Fermi level is different in IMVS and IMPS measurements, which are performed at open-circuit and short-circuit, respectively. To estimate the shift, *short-circuit voltage* measurements (V_{sc}) have to be performed.[5,25]

2.5. Ultrafast time-resolved laser spectroscopy.

The standard techniques used for temporal characterization of solar cells (like electrochemical impedance spectroscopy, photovoltage decay studies, or intensity modulated spectroscopy) only provide information about the slowest processes (charge collection and/or recombination, in the range of milliseconds: see **Figure 3.5**). However, fast and ultrafast laser spectroscopy tools are needed to probe the fastest processes related to electron injection (10 fs−1 ns) from the excited state of the dye to the conduction band of the nanoparticle and dye regeneration (1 ns−100 µs) by redox pair of electrolyte.

2.5.1. Flash photolysis.

This technique is employed to analyze dye regeneration rate based on decay of absorption signal of radical cation (**Figure 4.22**). In principle, a decay of the radical cation absorption band observed in flash photolysis experiments can be due to electron recombination (back electron transfer from the semiconductor to the dye) and/or dye regeneration, which is determined by the dynamics of the redox couple.

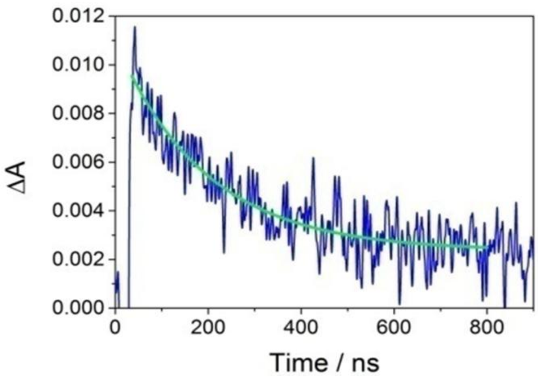

Figure 4.22: Typical kinetics obtained in a flash photolysis experiment. Green solid line represents a one-exponential fit.

As described before the electron recombination dynamics depends on the concentration of electrons in nanoparticles according to the multi-trapping model, which is determined by the excitation energy or, in other words, by the position of the Fermi level. Thus, an enough low energy is commonly used to avoid competition between electron recombination and dye regeneration.

2.5.2. Fluorescence decay.

In a fluorescence experiment, when a molecule absorbs a photon, it is excited to a higher energy state. After a short delay, it comes down to a lower state by losing some of the energy as heat and emitting the rest of the energy as another photon with different wavelength. Based on this effect, this technique allow us to study the electron injection rate in solar cells taking into account that the phosphorescence decay are due to two different processes: (1) the internal radiative and non-radiative decay of the excited state of the dye and (2) the electron injection from this excited state to electronic stated in the semiconductor. For this reason, materials such as ZrO_2 or Al_2O_3, where the electron injection is not possible due to the high energy of the conduction band edge, are customarily used as control samples.[26,27]

The time-resolved emission of this measurement was performed using a time-correlated single photon counting technique (TCSPC).[28] This technique evaluates the electron injection through the luminescence decays of radiative materials detecting single photons as a function of time. As the kinetics of these decays spread over many time scales (**Figure 4.23**), as it is commonly observed in DSSCs,[29,30] to fit the decays a stretched exponential function is used

$$A(t) = A_0 e^{-\left(\frac{t}{\tau}\right)^{\beta}} \qquad (4.22)$$

where τ the emission lifetime and β the stretching parameter. The electron constant rate (k_{AVG}) can be calculated by the following equation[31]

$$k_{AVG} = \left(\frac{\tau}{\beta}\Gamma\left(\frac{1}{\beta}\right)\right)^{-1} \qquad (4.23)$$

where Γ is the gamma function.

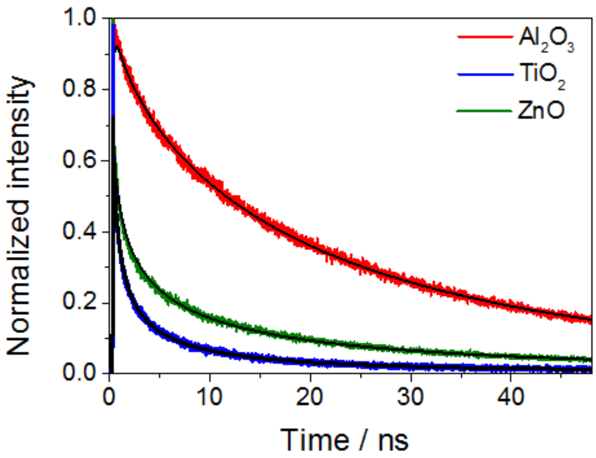

Figure 4.23: Fluorescence decay obtained in a TCSPC experiment for different samples.

Using this technique, the determination of the electron injection quantum yield (η_{ei}) can be obtained by the following equation:

$$\eta_{ei} = \frac{k_{AVG\ (sample)} - k_{AVG\ (control)}}{k_{AVG\ (sample)}} \qquad (4.24)$$

It is important to mention that the quality of the electrodes is very important in this kind of measurements. Optical properties, such as scattering of light at the surface and the dye concentration on the surface, should be the same between the control and DSSC electrodes. In spite of these experimental difficulties, luminescence intensity and decay measurements are used to obtain crucial information about the electron injection process.

2.5.3. Transient absorption.

This technique is used to directly look at the charge transfer dynamics through spectroscopic identification of various species present at various time delays with respect to an initial excitation light pulse. In contrast to fluorescence emission decays, not only excited states of dyes are probed, but also dye radical cations and electrons in electronic states of metal oxides.[32] Specifically, the changes of the transient spectra with time that it is observed in **Figure 4.24** are a consequence of the decrease of the population of the excited state (reactant) and to the increase of the population of electrons and radical cation (product) in the process of electron injection.[33,34]

Transient absorption measurements for a DSSC are not difficult to obtain; however, two experimental difficulties are common. First, the electron density in the semiconductor film determined by the light intensity must be taken into account. Higher concentration of electrons carries out faster recombination processes, which can modify the kinetics of dye cations with respect to smaller concentration of electrons. Secondly, the absorption spectra of sensitizer dyes used in DSSC commonly extend to a longer-wavelength region to capture efficiently sunlight. Thus, electron injection can be induced not only by the excitation light but also by the probe light used for transient absorption measurements.

The results presented in this thesis have been carried out in two different wavelength ranges: visible/near-IR (infrared) and mid-IR. In the first case, transient absorption probing in the visible/near-IR commonly detects electronic absorptions of the adsorbate (ground, excited, and oxidized state), as well as signals originating from the electron injected to the semiconductor. However, the transient absorption spectroscopy probing in the mid-IR has been used commonly to detect vibrational transitions. By this way, it easily detects absorption from electrons injected to the semiconductor (which is negligible in the visible region). As a consequence of the different absorption coefficients of the excited state and resultant absorption coefficient of radical cation and electrons in the semiconductor, different kinetics are observed. In particular, the band between 450-500 nm, 550-700nm and at longer wavelengths (>900 nm) monitor the decay of the triplet state. Both transitions are due to absorption from MLCT state of the dye (**Figure 4.24**). However, the formation of the product, the oxidized molecule, is shown by the rise of absorption around 810 nm after electron injection.

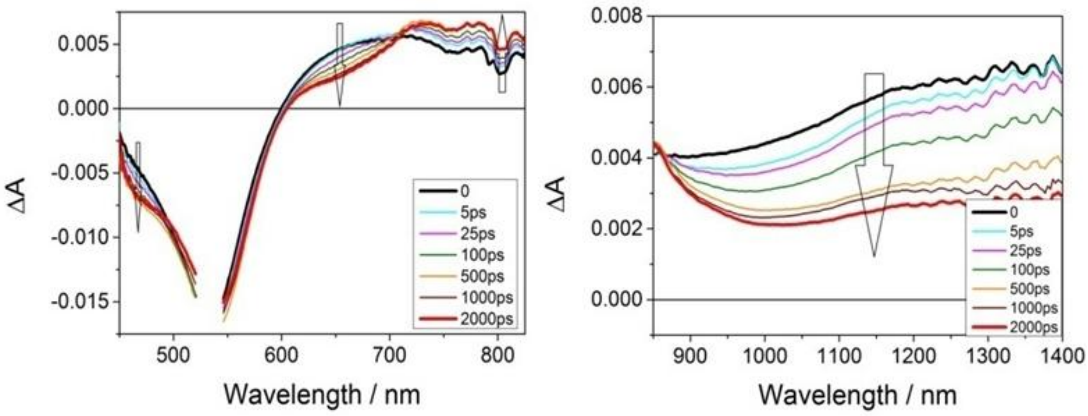

Figure 4.24: Dynamic transient absorption spectra measured for a complete DSSC. Vertical down arrows evidence the decay of the excited state whereas the up arrow reflects the formation of the oxidized dye.

To extract the electron injection rate from kinetics of all wavelength range, a global multi-exponential fit was employed. The procedure to analyze the transient absorption measurements will be explained in subsequent chapters.

3. Preparation of mesoporous semiconductor electrodes.

The materials and the deposition methods employed for the preparation of electrodes for (photo)electrochemical and photovoltaic applications are described below.

3.1. Substrates.

Mesoporous semiconductor electrodes comprise a three-dimensional network of nanoparticles deposited on conducting substrates. In particular, two different substrates have been used: (1) Fluorine-doped Tin Oxide (SnO_2:F) (FTO) conducting glass and (2) Ti Foil (Goodfellow, 99.6+%, 25 µm). For photovoltaic applications two kinds of FTO were employed as substrate due to its properties. The choice of FTO glass substrates is a compromise between optical transmittance and sheet resistance: higher conductivity is normally related to lower transmittance. For this reason, TEC15 (Pilkington, resistance 15Ω/square, 82-84.5% visible transmittance) was employed for the deposition of the semiconductor film as working electrode, whereas TEC8 (Pilkington, resistance 8Ω/square, 80-81.5% visible transmittance) as counter-electrode in DSSCs. For the electrodes employed in (photo)electrochemistry, TEC15 and a Ti Foil were used.

FTO substrates have been subjected to a rigorous cleaning protocol: 15min of sonication in baths of detergents, deionized water, isopropanol and ethanol successively, and finally, heated to 500°C before film deposition. It has been demonstrated that a good substrate cleaning is important in the final performance of the devices. A significant effect on the photovoltage behaviour due to recombination via the substrate can be observed experimentally.[35]

3.2. Deposition of semiconductor thin film electrodes.

Mesoporous semiconductor electrodes employed in this thesis have been prepared from commercial powders (*PI-KEM*, *Sachtleben* and *Sigma*) or commercial colloidal suspensions (*Solaronix* and *Dyesol*) of the semiconductor nanoparticles. Specifically, in the first case colloidal suspensions were prepared by mixing commercial TiO_2 nanopowders with appropriate solvents and tensoactives. Concretely, 1 g of the different nanopowders was mixed with 30 µl of Acetylacetone and 1.6 ml of ultrapure water (Millipore, Milli-Q) in a mortar. When the suspension is homogenous, 20 µl of surfactant Triton X-100 is added to the colloidal dispersion, to achieve a homogeneous spreading of the suspension over the conducting substrate.

Once the colloidal suspension has been obtained, two different deposition methods have been used:

- *Doctor blade deposition*. For thin film preparation the suspension was spread onto the substrates with a glass rod using a Scotch tape as spacer and channel. The resulting films are finally heated at 450°C for 1 hour.

The suspensions from commercial powders (PI-KEM, Sachtleben and Sigma) and the commercial colloidal suspension (Solaronix, Ti-Nanoxide-T paste) were deposited by this method. All these electrodes were used in (photo)electrochemical applications. To control the Fermi level of the electrodes, the FTO was connected electrically with a Cu wire inserted in a glass capillary and sealed using a two-component epoxy adhesive (**Figure 4.25**).

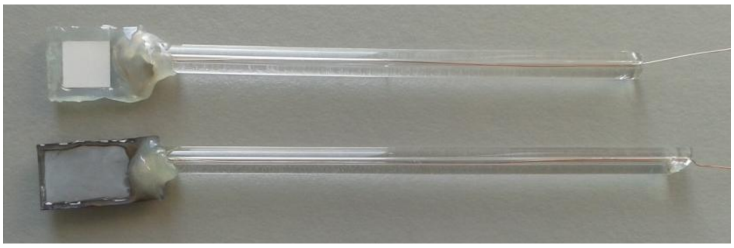

Figure 4.25: Electrodes employed in (photo)electrochemistry.

- *Screen-printing*. This method was used to deposit films with a controlled thickness and optimal reproducibility for electrodes used in photovoltaic applications. In practical terms, state-of-the-art DSSCs[36] were built by the combination of two different kinds of TiO_2 nanoparticles with the following architecture (**Figure 4.26**):

- A light absorption layer consisting of a ≈10 µm thick film of mesoporous TiO_2 (Dyesol 18NR-T, particle size: ≈20 nm). A high internal surface area of this layer assures a high dye loading.

- A light scattering layer on top of the mesoporous film, consisting of a ≈4 µm porous layer of TiO_2 (Dyesol 18NR-AO, particle size: ≈400 nm). The aim of this layer is to reflect the transmitted light back into the absorption layer where it can be absorbed by the dye.

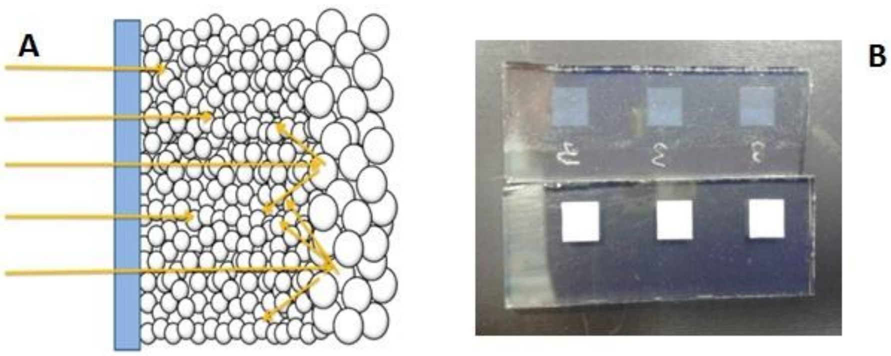

Figure 4.26: (Left) Scheme of the mesoporous TiO_2 architecture and (right) films deposited by screen-printing with and without scattering layer.

Prior to the deposition of the TiO_2 nanoparticles layer, the cleaned and treated substrates were immersed into a 40 mM $TiCl_4$ solution for 30 min at 70ºC and then washed with water and ethanol. After film deposition, the electrodes were gradually heated under airflow at 325°C for 5 min, 375°C for 5 min, 450°C for 15 min and 500°C for 15 min. After this process, the electrodes were immersed again into the same solution of $TiCl_4$.[12] Finally, films were heated at 500°C for 30 min and cooled down to room temperature before dye adsorption.

In some devices, a thin compact continuous TiO_2 layer was deposited by chemical bath deposition on the FTO substrates before spreading the colloidal TiO_2 nanoparticle suspension. This compact film acts as a blocking layer and prevents the contact between the redox mediator in the electrolyte and the FTO. By this method, back-recombination via the substrate is avoided.[35]

DSSCs based on ZnO electrodes were also prepared by screen-printing depositing a layer of 40-100 nm of ZnO nanoparticles. This colloidal suspension was prepared by Gerko Oskam's Group (CINVESTAV, Mexico).[37] Some differences with respect to TiO_2 film preparation are implemented. In this case, no treatment of $TiCl_4$ was carried out and the temperature used for heating the films was 420°C.

3.3. Fabrication of Dye-Sensitized Solar Cells.

3.3.1. Dye sensitization.

Dyes based on ruthenium-complexes and purely organic dyes (**Figure 4.27**) have been employed in this thesis for sensitization of semiconductor photoanodes. Before immersion in dye solution, the electrodes were heated again at 500°C or 420°C for TiO_2 and ZnO electrodes respectively to eliminate any traces of water inside the pores. For TiO_2 films, the electrodes were immersed overnight under dark at room temperature. Only when C101 dye was employed the immersion was carried out at -4°C. However, for ZnO films the immersion was reduced to 1 hour to prevent the surface dissolution of the oxide by acidic groups.[38]

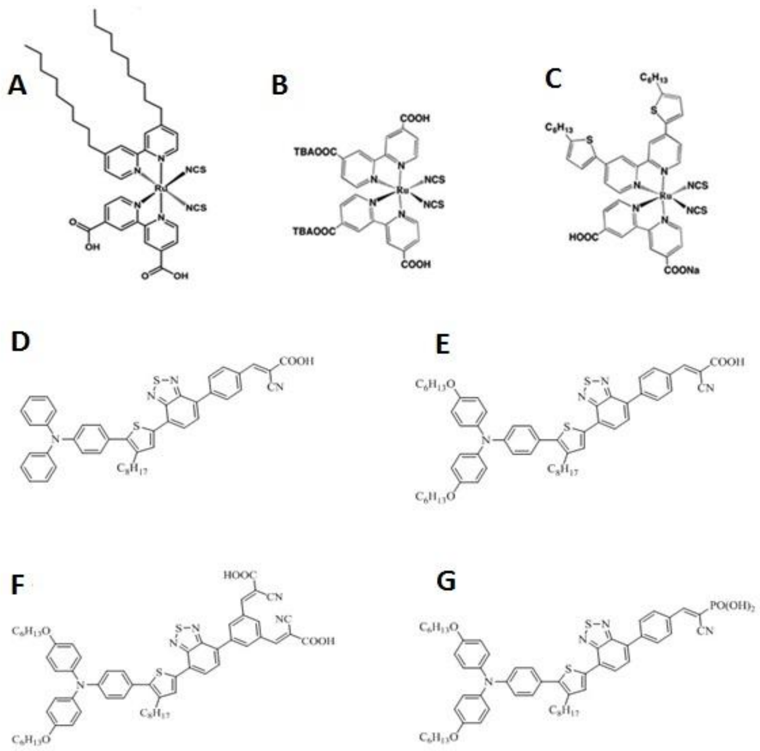

Figure 4.27: Dye molecules used as sensitizer in DSSCs: (A) Z907, (B) N719, (C) C101 (D) RK1, (E) 6ORK1, (E) MG-41 and (G) MG-100.

To avoid the aggregation of dye molecules chenodeoxycholic acid was used as co-adsorbent. The bulky size of this molecule keeps dye molecules attached onto the surface of semiconductor well separated. After sensitization, the films were washed in the same solvent as employed in the dye solution and dried under air.

3.3.2. Electrolyte solution.

One of the main objectives of this thesis has been to study the effect on the recombination of the chemical composition of the electrolyte. In all cases investigated, a redox pair (iodide/iodine, Co(II)/Co(III)-complexes was dissolved in a wide range of solvents (acetonitrile, valeronitrile, ethylene carbonate, pure ionic liquids). Furthermore, the presence of some additives (lithium ions, Tbp) has also been analyzed. The specific electrolyte composition will be described in each chapter.

3.3.3. Platinized counter-electrode.

Prior to deposition of platinum on substrates TEC8 (Pilkington, resistance 8Ω/square, 80-81.5% visible transmittance), a small hole was made to allow the introduction the electrolyte solution by vacuum. The deposition of platinum was carried out by spreading a drop of hexachloroplatinic acid (0.01M in isopropanol) or *Platisol* (*Solaronix*) over the FTO substrate and subsequent annealing at 390°C for 15 min.

3.3.4. Assembly of solar cells.

Once the electrodes were prepared, the working and counter-electrodes were sandwiched together using a thin thermoplastic (*Surlyn*) frame that melts at 100°C using pressure. The cells were filled then with the electrolyte through a hole previously made in the back of a platinized counter electrode by vacuum (**Figure 4.28**). Finally, the hole was sealed with a thermoplastic polymer and a cover-slide glass.

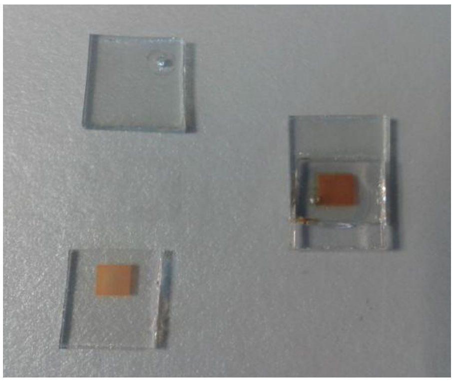

Figure 4.28: Working electrode and counter-electrode before and after assembly of DSSC.

4. References.

(1) Nelson, J. *The Physics of Solar Cells*; 1st ed.; Imperial College Press, 2003.

(2) Barnes, P.; Anderson, A.; Juozapavicius, M.; Liu, L.; Li, X.; Palomares, E.; Forneli, A.; O'Regan, B. Factors Controlling Charge Recombination under Dark and Light Conditions in Dye Sensitised Solar Cells. *Phys. Chem. Chem. Phys.* **2011**, *13*, 3547–3558.

(3) Zaban, A.; Greenshtein, M.; Bisquert, J. Determination of the Electron Lifetime in Nanocrystalline Dye Solar Cells by Open-Circuit Voltage Decay Measurements. *Chemphyschem* **2003**, *4*, 859–864.

(4) Ansari-Rad, M.; Abdi, Y.; Arzi, E. Reaction Order and Ideality Factor in Dye-Sensitized Nanocrystalline Solar Cells: A Theoretical Investigation. *J Phys Chem C* **2012**, *116*, 10867–10872.

(5) Boschloo, G.; Hagfeldt, A. Activation Energy of Electron Transport in Dye-Sensitized TiO2 Solar Cells. *J. Phys. Chem. B* **2005**, *109*, 12093–12098.

(6) Idígoras, J.; Berger, T.; Anta, J. A. Modification of Mesoporous TiO2 Films by Electrochemical Doping: Impact on Photoelectrocatalytic and Photovoltaic Performance. *J. Phys. Chem. C* **2013**, *117*, 1561–1570.

(7) Guillén, E.; Peter, L. M.; Anta, J. A. Electron Transport and Recombination in ZnO-Based Dye-Sensitized Solar Cells. *J Phys Chem C* **2011**, *115*, 22622–22632.

(8) Hind, A. R.; Bhargava, S. K.; McKinnon, A. At the Solid/liquid Interface: FTIR/ATR — the Tool of Choice. *Adv. Colloid Interface Sci.* **2001**, *93*, 91–114.

(9) McQuillan, A. J. Probing Solid–Solution Interfacial Chemistry with ATR-IR Spectroscopy of Particle Films. *Adv. Mater.* **2001**, *13*, 1034–1038.

(10) Lagemaat, J. van de; Frank, A. J. Effect of the Surface-State Distribution on Electron Transport in Dye-Sensitized TiO2 Solar Cells: Nonlinear Electron-Transport Kinetics. *J. Phys. Chem. B* **2000**, *104*, 4292–4294.

(11) Fabregat-Santiago, F.; Bisquert, J.; Garcia-Belmonte, G.; Boschloo, G.; Hagfeldt, A. Influence of Electrolyte in Transport and Recombination in Dye-Sensitized Solar Cells Studied by Impedance Spectroscopy. *Sol. Energy Mater. Sol. Cells* **2005**, *87*, 117–131.

(12) Hagfeldt, A.; Boschloo, G.; Sun, L.; Kloo, L.; Pettersson, H. Dye-Sensitized Solar Cells. *Chem. Rev.* **2010**, *110*, 6595–6663.

(13) Bisquert, J.; Vikhrenko, V. S. Interpretation of the Time Constants Measured by Kinetic Techniques in Nanostructured Semiconductor Electrodes and Dye-Sensitized Solar Cells. *J. Phys. Chem. B* **2004**, *108*, 2313–2322.

(14) Bisquert, J.; Mora-Seró, I. Simulation of Steady-State Characteristics of Dye-Sensitized Solar Cells and the Interpretation of the Diffusion Length. *J. Phys. Chem. Lett.* **2010**, *1*, 450–456.

(15) Bisquert, J. Theory of the Impedance of Electron Diffusion and Recombination in a Thin Layer. *J. Phys. Chem. B* **2002**, *106*, 325–333.

(16) Liu, Y.; Jennings, J. R.; Zakeeruddin, S. M.; Grätzel, M.; Wang, Q. Heterogeneous Electron Transfer from Dye-Sensitized Nanocrystalline TiO2 to [Co(bpy)3]3+: Insights Gained from Impedance Spectroscopy. *J. Am. Chem. Soc.* **2013**, *135*, 3939–3952.

(17) Anta, J. A.; Idígoras, J.; Guillén, E.; Villanueva-Cab, J.; Mandujano-Ramírez, H. J.; Oskam, G.; Pellejà, L.; Palomares, E. A Continuity Equation for the Simulation of the Current–voltage Curve and the Time-Dependent Properties of Dye-Sensitized Solar Cells. *Phys. Chem. Chem. Phys.* **2012**, *14*, 10285–10299.

(18) Bisquert, J. Chemical Capacitance of Nanostructured Semiconductors: Its Origin and Significance for Nanocomposite Solar Cells. *Phys. Chem. Chem. Phys.* **2003**, *5*, 5360–5364.

(19) Bisquert, J.; Fabregat-Santiago, F.; Mora-Seró, I.; Garcia-Belmonte, G.; Giménez, S. Electron Lifetime in Dye-Sensitized Solar Cells: Theory and Interpretation of Measurements. *J. Phys. Chem. C* **2009**, *113*, 17278–17290.
(20) Liu, Y.; Jennings, J. R.; Huang, Y.; Wang, Q.; Zakeeruddin, S. M.; Grätzel, M. Cobalt Redox Mediators for Ruthenium-Based Dye-Sensitized Solar Cells: A Combined Impedance Spectroscopy and Near-IR Transmittance Study. *J Phys Chem C* **2011**, *115*, 18847–18855.
(21) Peter, L. M. Dynamic Aspects of Semiconductor Photoelectrochemistry. *Chem. Rev.* **1990**, *90*, 753–769.
(22) Schlichthorl, G.; Park, N. G.; Frank, A. J. Evaluation of the Charge-Collection Efficiency of Dye-Sensitized Nanocrystalline TiO2 Solar Cells. *J. Phys. Chem. B* **1999**, *103*, 782–791.
(23) Dloczik, L.; Ileperuma, O.; Lauermann, I.; Peter, L. M.; Ponomarev, E. A.; Redmond, G.; Shaw, N. J.; Uhlendorf, I. Dynamic Response of Dye-Sensitized Nanocrystalline Solar Cells: Characterization by Intensity-Modulated Photocurrent Spectroscopy. *J. Phys. Chem. B* **1997**, *101*, 10281–10289.
(24) Frank, A. J.; Kopidakis, N.; Lagemaat, J. van de. Electrons in Nanostructured TiO2 Solar Cells: Transport, Recombination and Photovoltaic Properties. *Coord. Chem. Rev.* **2004**, *248*, 1165–1179.
(25) Peter, L. M. Characterization and Modeling of Dye-Sensitized Solar Cells. *J. Phys. Chem. C* **2007**, *111*, 6601–6612.
(26) Palomares, E.; Clifford, J. N.; Haque, S. A.; Lutz, T.; Durrant, J. R. Control of Charge Recombination Dynamics in Dye Sensitized Solar Cells by the Use of Conformally Deposited Metal Oxide Blocking Layers. *J. Am. Chem. Soc.* **2002**, *125*, 475–482.
(27) Luo, L.; Lin, C.-J.; Tsai, C.-Y.; Wu, H.-P.; Li, L.-L.; Lo, C.-F.; Lin, C.-Y.; Diau, E. W.-G. Effects of Aggregation and Electron Injection on Photovoltaic Performance of Porphyrin-Based Solar Cells with Oligo(phenylethynyl) Links inside TiO2 and Al2O3 Nanotube Arrays. *Phys Chem Chem Phys* **2010**, *12*, 1064–1071.
(28) Wróżowa, T.; Ciesielska, B.; Komar, D.; Karolczak, J.; Maciejewski, A.; Kubicki, J. Measurements of Picosecond Lifetimes by Time Correlated Single Photon Counting Method: The Effect of the Refraction Index of the Solvent on the Instrument Response Function. *Rev. Sci. Instrum.* **2004**, *75*, 3107–3121.
(29) Nelson, J.; Haque, S. A.; Klug, D. R.; Durrant, J. R. Trap-Limited Recombination in Dye-Sensitized Nanocrystalline Metal Oxide Electrodes. *Phys. Rev. B* **2001**, *6320*.
(30) Haque, S. A.; Tachibana, Y.; Willis, R. L.; Moser, J. E.; Gratzel, M.; Klug, D. R.; Durrant, J. R. Parameters Influencing Charge Recombination Kinetics in Dye-Sensitized Nanocrystalline Titanium Dioxide Films. *J. Phys. Chem. B* **2000**, *104*, 538–547.
(31) Anderson, A. Y.; Barnes, P. R. F.; Durrant, J. R.; O'Regan, B. C. Quantifying Regeneration in Dye-Sensitized Solar Cells. *J. Phys. Chem. C* **2011**, *115*, 2439–2447.
(32) Rothenberger, G.; Fitzmaurice, D.; Graetzel, M. Spectroscopy of Conduction Band Electrons in Transparent Metal Oxide Semiconductor Films: Optical Determination of the Flatband Potential of Colloidal Titanium Dioxide Films. *J. Phys. Chem.* **1992**, *96*, 5983–5986.
(33) Moser, J. E.; Noukakis, D.; Bach, U.; Tachibana, Y.; Klug, D. R.; Durrant, J. R.; Humphry-Baker, R.; Grätzel, M. Comment on "Measurement of Ultrafast Photoinduced Electron Transfer from Chemically Anchored Ru−Dye Molecules into Empty Electronic States in a Colloidal Anatase TiO2 Film." *J. Phys. Chem. B* **1998**, *102*, 3649–3650.
(34) Damrauer, N. H.; McCusker, J. K. Ultrafast Dynamics in the Metal-to-Ligand Charge Transfer Excited-State Evolution of [Ru(4,4'-Diphenyl-2,2'-bipyridine)3]2+. *J. Phys. Chem. A* **1999**, *103*, 8440–8446.
(35) Cameron, P. J.; Peter, L. M.; Hore, S. How Important Is the Back Reaction of Electrons via the Substrate in Dye-Sensitized Nanocrystalline Solar Cells? *J. Phys. Chem. B* **2005**, *109*, 930–936.

(36) Ardo, S.; Meyer, G. J. Photodriven Heterogeneous Charge Transfer with Transition-Metal Compounds Anchored to TiO2 Semiconductor Surfaces. *Chem. Soc. Rev.* **2009**, *38*, 115–164.

(37) Vega-Poot, A. G.; Macías-Montero, M.; Idígoras, J.; Borrás, A.; Barranco, A.; Gonzalez-Elipe, A. R.; Lizama-Tzec, F. I.; Oskam, G.; Anta, J. A. Mechanisms of Electron Transport and Recombination in ZnO Nanostructures for Dye-Sensitized Solar Cells. *ChemPhysChem* **2014**, *15*, 1088–1097.

(38) Guillen, E.; Casanueva, F.; Anta, J. A.; Vega-Poot, A.; Oskam, G.; Alcantara, R.; Fernandez-Lorenzo, C.; Martin-Calleja, J. Photovoltaic Performance of Nanostructured Zinc Oxide Sensitised with Xanthene Dyes. *J. Photochem. Photobiol. - Chem.* **2008**, *200*, 364–370.

Chapter 5:

In situ self-doping of mesoporous titanium dioxide films

1. Introduction.

The importance of semiconductor oxides for many applications results,[1–6] on the one hand, from their suitable intrinsic properties and, on the other hand, from the possibility to systematically alter their performance by bulk or surface modification. Semiconductor oxides such as ZnO, SnO_2 and TiO_2 amongst others show typically n-type conductivity due to a stoichiometric imbalance resulting from oxygen deficiency.[7] Consequently, these materials are characterized by the presence of reduced cation sites, a situation which is commonly referred to as *self-doping*. An impressive performance of self-doped semiconductor nanocrystals has only recently been demonstrated in different fields including the synthesis of novel nanocomposites,[8] sensors,[9] supercapacitors,[10] batteries,[11] synthetic chemistry[12] or solar fuel generation.[13] Semiconductor self-doping, however, not necessarily implies a deviation from the stoichiometric metal/oxygen ratio, but may result furthermore from the presence of hydrogen impurities acting as shallow donors.[14] Importantly, hydrogen sources are ubiquitous during the whole process chain (from synthesis, to processing and application) of a semiconductor material.[15]

In general, doping comprises the inclusion or substitution of metal or non-metal impurities into the semiconductor lattice and has proved to be a useful strategy to manipulate the properties of the material by introducing new electronic states and new optical transitions.[2,3] By these means, doping may affect charge transport, charge separation and charge generation. These processes influence the material performance in several applications. In particular, the effect of electrochemical doping on the photocatalytic and photovoltaic performance of mesoporous TiO_2 films has been attributed to accelerated charge transport together with reduced recombination, resulting in improved electron collection efficiencies, as reported in previous works and discussed in **Chapter 6**.[16–20] The intentional doping of oxide semiconductors relies on well-defined synthesis or post-synthesis strategies, which allow for a systematic modification of the material. Ideally, it is desirable to establish a feedback loop between semiconductor synthesis, properties and performance in the process of interest. This would allow for a systematic optimization of the material. However, some material properties, such as the doping degree, do not only depend on material history (synthesis procedure, post-synthesis treatments). Furthermore, they may significantly change *in situ*, i.e. during application, and have therefore to be considered a *dynamic property*.[21]

In this context, accumulation of electrons in a semiconductor electrode compensated by counter-ion uptake from solution is referred to as *electrochemical reductive doping*.[16,22] In the case of TiO_2 the proton-assisted electrochemical reduction can be described by

$$Ti^{IV}O_2 + e^- + H^+ \rightarrow Ti^{III}(O)(OH) \qquad (5.1)$$

where protons may adsorb at the surface or may get inserted into the bulk. This incorporation of counter-ions into the structure of the oxide compensates the negative charge build-up upon formation of Ti(III) donor centers.[23] As the compensating positive charge is protons, this process may thus formally be considered as *hydrogen-doping* of the semiconductor. A beneficial effect of electrochemical doping on the photoelectrochemical performance, which was first evidenced for anatase single crystals[22] and later corroborated for nanostructured TiO_2 films of adequate morphology,[16] was attributed to a temporarily persisting increase of the carrier density in the semiconductor.

An important difference of hydrogen-doping as compared to metal-doping is the nature of electron charge compensation. In the latter case, electrons are *persistently* compensated by lattice-bound metal ions, whereas in the former case compensation is established by *reversible* adsorption of protons at the surface or by insertion in the lattice.[24] While the reversibility of hydrogen-doping opens up the possibility of driving reduction reactions at charged semiconductors[25,26] it implies on the other hand a limited persistence of those effects, connected to the accumulation of the charges in the material. For mesoporous TiO_2 films, the limited persistence of charge accumulation and, thus, of performance enhancement was found to depend on thin film morphology, with a higher persistence being observed for electrodes consisting of larger particles.[16,17] The reversibility of the beneficial effect puts into question the relevance of electrochemical doping for a permanent performance improvement of nanostructured films in technological applications.

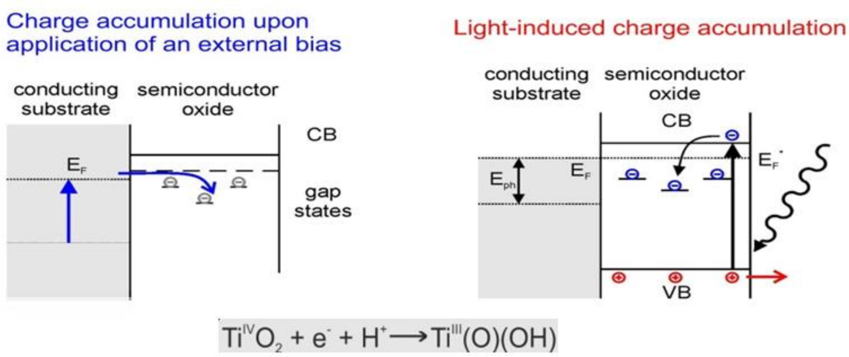

Figure 5.1: Perturbation methods to induce charge accumulation in nanocrystalline electrode.

In this chapter we show that the instability of electrochemical reductive doping is not an issue for all those applications where the accumulation of charges in the semiconductor takes place *in situ*, i.e. during operation. For instance, it is well known that dye-sensitized solar cells based on mesoporous TiO_2 show an improvement of their performance under light soaking.[18] In this chapter, the charge accumulation in TiO_2 electrodes was performed either by external cathodic polarization or, alternatively, during photocatalyst operation - by band gap excitation at open-circuit (**Figure 5.1**). In this study different semiconductor nanoparticles were used. Importantly, it is shown for the water and the formic acid photooxidation reactions that the enhancement of the photoelectrocatalytic performance of thin films depends on the Fermi level position during electrochemical doping, being however independent of the perturbation mode. This result is perfectly in line with recent observations indicating that the occupancy of electronic states does not depend on the type of external perturbation, if, alternatively, an external bias voltage or band gap excitation at open-circuit are used to set the Fermi level position in a mesoporous TiO_2 electrode.[27]

2. Experimental.

2.1. Mesoporous electrodes.

Slurries of the commercial TiO_2 nanoparticles were prepared by grinding 1 g TiO_2 powder with 1.6 ml H_2O (Milipore, Milli-Q), 30 µl Acetylacetone and 20 µl Triton X. The colloidal suspensions were spread with a glass rod onto fluorine-doped tin oxide (FTO) conducting glass (Pilkington, TEC 15, resistance 15 Ω/square) using Scotch tape as a spacer (*doctor blade*). The films then were annealed and sintered for 1 h at 450° C in air. A copper wire was attached to the conducting substrate with silver epoxy and inserted in a glass rod. The contact area and the uncovered parts of the substrate were finally sealed by epoxy resin.

2.2. Electrochemical and photoelectrochemical measurements.

Electrochemical measurements were performed in a standard three-electrode electrochemical cell, where a 0.1M solution of $HClO_4$ (Sigma-Aldrich, ACS reagent, 70%) in ultrapure water (Millipore, Milli-Q) was used as electrolyte. In addition, formic acid was added when a hole scavenger was required. The electrolyte was purged with N_2 to minimize the concentration of dissolved oxygen or with O_2 to maximize it. All potentials were measured against and are referred to a Ag/AgCl/KCl (3M) electrode (*CRISON*), whereas a Pt wire was used as a counter electrode. Measurements were performed with a computer-controlled Autolab PGSTAT302N potentiostat. A 450 W Xe arc lamp (*Oriel*) equipped with a water filter was used for UV/Vis irradiation of the electrode from the electrolyte side. The applied light irradiance was measured with an optical power meter (Gentec TUNER) equipped with a bolometer (*Gentec XLP12-1S-H2*) being 500 $mW\cdot cm^{-2}$.

2.3. MIR spectroelectrochemical measurements.

For MIR measurements TiO_2 films deposited on a Ti foil were used as the electrode. Electrochemical measurements were performed with a computer-controlled Autolab PGSTAT101 potentiostat. Details of the MIR-spectroelectrochemical cell can be found in **Chapter 4** (Section 2.3.1.) and Refs. 28 and 29. The spectra were obtained by averaging 500 scans at a resolution of 4 cm^{-1} and are represented as $-\log(R/R_0)$, where R and R_0 are the reflectance values corresponding to the single beam spectra of the sample and the reference, respectively.

3. Results and Discussion.

3.1. Kinetics of the electrochemical doping process.

The mesoporous TiO_2 thin films employed in this chapter are prepared from different commercial nanoparticles. These nanoparticles are not only characterized by different particle sizes, but also by different crystal structures (**Table 5.1** and **Appendix**, Figure A-5.1).

Nanoparticle	Solaronix	Sachtleben	PI-KEM	Sigma
Particle size (nm)	15-20	15-35	25-65	80-240
Crystal structure	Anatase	Rutile	Anatase/Rutile (1:1)	Anatase

Table 5.1: Particle sizes and crystal structures for the TiO_2 film employed.

The small crystallite size as well as its low doping level, good electronic connectivity and the presence of a surrounding equipotential surface allow to externally control the quasi–Fermi level in the semiconductor by electrochemical approaches.[30] In particular, the Fermi level can be shifted by the application of a bias voltage or, alternatively, by exposure of the electrode to photons with energy exceeding the band gap of each semiconductor (Figure 5.1).[6] In the latter case, after separation of photogenerated charge carriers, holes preferentially react at the semiconductor/electrolyte interface, whereas electrons are accumulated in the film under open-circuit conditions. The efficiency of this charge separation and, thus, the extent of the negative Fermi level shift can be enhanced by adding hole scavengers to the electrolyte, as discussed below. For both methods of Fermi level perturbation, charge compensation in the semiconductor film is established by adsorption or insertion of protons (Equation 5.1).

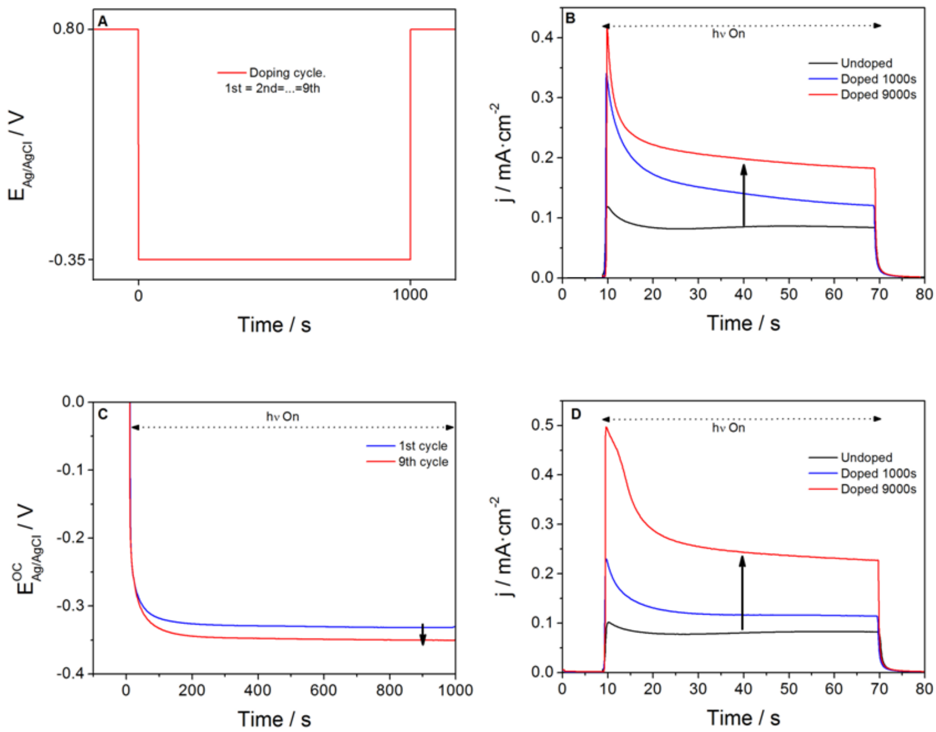

Figure 5.2: (A, B) Voltage-induced and (C, D) light-induced hydrogen-doping of PI-KEM electrodes. (A, C) Electrode potential profiles for the doping cycles: (A) externally applied bias and (C) open-circuit photopotential. (B, D) Photocurrent transients at $E_{Ag/AgCl}$ = 0.8 V of the undoped electrodes and after cumulative doping cycles. Electrolyte: 0.1 M $HClO_4$ in aqueous solution.

As reported previously,[16] TiO_2 electrodes can be electrochemically doped by cathodic polarization. One of the beneficial effects of this treatment can be demonstrated by photocurrent measurements of the photooxidation reaction of water. **Figure 5.2** shows the increase of photocurrent after electrochemical doping. To study the electrochemical doping process, the following sequence of experiments was performed. First, the photocurrent transient of the undoped electrode was recorded at $E_{Ag/AgCl}$ = 0.80V. Then the film was exposed to UV light at open-circuit and the photopotential was recorded for 1000 s (*light-induced doping*) or externally polarized for 1000 s in the dark at the same potential (*voltage-induced doping*). After this doping step the photocurrent was sampled again for 60 s at $E_{Ag/AgCl}$ = 0.80V. We define the photocurrent enhancement factor (*PCEF*) as the ratio of the stationary photocurrent in the saturation region ($E_{Ag/AgCl}$ = 0.80 V) after doping and the initial photocurrent of the undoped electrode. It is observed that the PCEF does not show significant changes for the two methods of Fermi level perturbation once the doping effect has reached saturation (**Table 5.2** and **Appendix,** Table A-5.1).

Hole scavenger	-----		Formic acid (HCOOH)	
Doping type	Light-induced	Voltage-induced	Light-induced	Voltage-induced
Doping potential (V)	-0.35		-0.61	
Doping time (s)	9000		2000	
PCEF	2.7	2.4	2.8	2.5

Table 5.2: Photocurrent enhancement factors (PCEF) determined for the PI-KEM electrodes upon voltage-induced and light-induced doping in the absence and in the presence of hole scavenger (1M HCOOH).

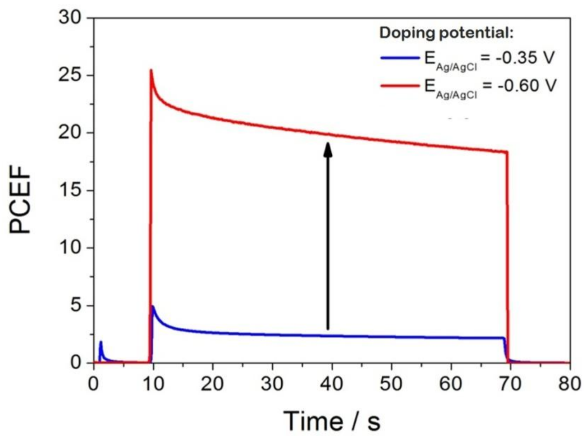

Figure 5.3: Photocurrent enhancement factor determined at $E_{Ag/AgCl}$ = 0.8 V for a PI-KEM electrode once the doping effect is saturated. Voltage-induced doping at $E_{Ag/AgCl}$ = -0.35 V and $E_{Ag/AgCl}$ = -0.60 V in N_2-purgued 0.1 M $HClO_4$ aqueous solution.

The PCEF depends on the doping time (**Appendix**, Figure A-5.2) as well as on the position of the Fermi level during doping. In this context it has to be mentioned that a change of the electrode potential directly translates into a shift of the Fermi level if the band positions are pinned upon semiconductor charging. For a PI-KEM electrode doped at

$E_{Ag/AgCl}$ = -0.35 V in a N_2-purged 0.1 M $HClO_4$ aqueous electrolyte a PCEF of 2.4 is determined (Table 5.2) once the doping effect has reached saturation (doping time 9000 s). However, if doping is performed at $E_{Ag/AgCl}$ = -0.60 V the PCEF increases to ≈18 (**Figure 5.3**) This is a consequence of higher charge accumulation in band gap states of anatase TiO_2 films. It has to be remember, as discussed in **Chapter 1**, that trap states and associated charge accumulation is known to increase exponentially with decreasing potential.[28,30–33]

However, the photocurrent enhancement due to electrochemical doping is a transient effect (**Figure 5.4**). The beneficial doping effect is completely reversible and the initial photoactivity is restored after hour to days in line with a previous report.[16]

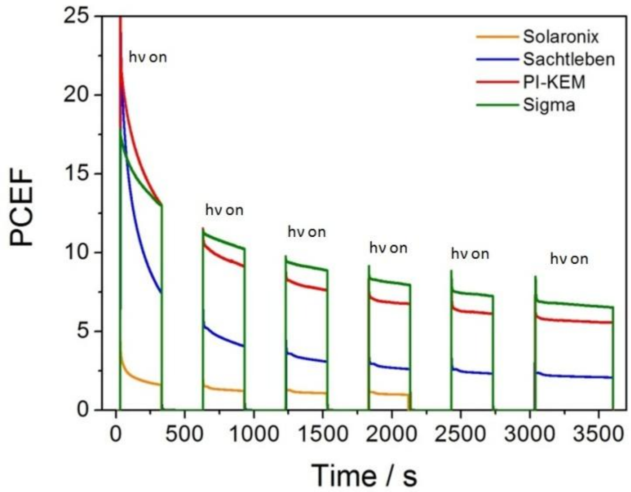

Figure 5.4: Temporal evolution of PCEF measured at $E_{Ag/AgCl}$ = 0.4V for different types of electrodes after electrochemical doping at $E_{Ag/AgCl}$ = -0.6V by means of voltage-induced doping and successive on/off steps of light excitation. Electrolyte: N_2-purged 0.1M $HClO_4$ aqueous solution.

It seems that the kinetics of doping and undoping process depends on structural properties of the semiconductor nanoparticles[16] (Figure 5.4 and Appendix, Figure A-5.2) as well as on the doping time and potential. In particular, the time necessary to reach a stationary doping effect strongly depends on the doping potential: shorter times are observed for more negative potentials (**Appendix**, Figure A-5.3). This is possibly connected to the increase of conductivity in the mesoporous film as the Fermi level is shifted upwards.[34,35] Fermi level equilibration over the whole film thickness is thus reached faster. Furthermore, proton insertion into the subsurface region of the semiconductor, which is expected to be an activated process, could limit the doping rate at less negative potentials.

Photocurrent and photopotential measurements are valuable tools for studying voltage- and light-induced changes of the macroscopic electrode behaviour as shown above. In addition, other electrochemical as well as spectroelectrochemical methods have been used for tracking modifications of the electronic thin film properties due to doping. Cyclic voltammograms of PI-KEM electrodes are shown in **Figure 5.5**. CVs of the electrodes in the dark are characterized by two pairs of capacitive peaks which are associated with electron accumulation at different regions in the semiconductor film.[16]

Whereas the capacitive currents at negative potentials ($E_{Ag/AgCl}$ < -0.4 V) have been attributed to the filling of the conduction band and/or an exponential distribution of surface states, an additional pair of peaks at more positive potentials ($E_{Ag/AgCl}$ = 0 V) has been assigned to the reversible filling of monoenergetic trap states at grain-boundaries.[6,16,36,37] Upon doping the well-defined pair of peaks located at $E_{Ag/AgCl}$ = 0 V shifts by ≈200 mV toward more positive potentials. Such a shift has tentatively been attributed to the build-up of a space charge layer throughout particle agglomerates.[16,36] In addition to the peak shift, voltage- as well as light-induced electrochemical doping induce significant changes of the intrinsic film capacitance. The capacitance per unit area $C = j_C/v$ has been calculated from the capacitive current density (j_C) and the scan rate (v).[6] **Figure 5.5A** and **5.5C** show moderately increased capacitance values at more negative potentials. From the semilogarithmic plots (**Figure 5.5B and 5.5D**) α-values between 0.2 and 0.4 can be estimated (see Equation 1.20), indicating that the capacitive currents result from electrons injected into exponentially distributed band gap states.[30] A similar behaviour is observed for all studied electrodes (**Appendix**, Table A-5.2). The capacitance increase may result from the formation of a depletion layer at the surface of particles or particle aggregates, as claimed by some authors.[38] In photocatalytic applications, the presence of a depletion layer would enhance the separation efficiency of photogenerated electrons and holes. However, a broadening of the density of states function could account for the observed capacitance modification.[18]

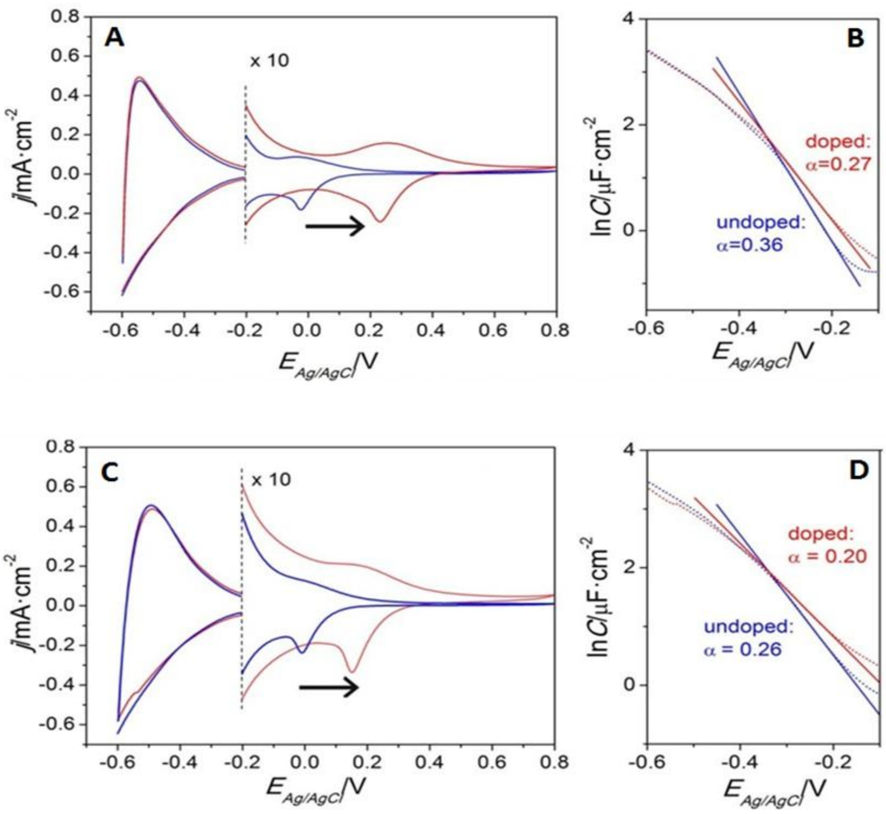

Figure 5.5: (A, C) Cyclic voltammograms and (B, D) semi-logarithmic capacitance plots of PI-KEM electrodes before and after (A, B) voltage-induced or (C, D) light-induced doping, respectively. Doping potential: (A, B) external bias: $E_{Ag/AgCl}$ = -0.60 V and (C,D) open-circuit photopotential: $E^{OC}_{Ag/AgCl}$ = -0.60 V; Electrolyte: (A, B) N_2-purged 0.1 M $HClO_4$ aqueous solution and (C, D) N_2-purged 1 M HCOOH/0.1 M $HClO_4$ aqueous solution.

The persistence of electrochemical doping can be evidenced by the detection of IR-active shallow trapped electrons[6] using a spectroelectrochemical approach.[16,27] Upon cathodic polarization at −0.6 V (potential of reductive electrochemical doping) a broad absorption appears in the ATR-IR difference spectrum of the PI-KEM TiO_2 electrode when referred to the corresponding background spectrum taken at 0.4 V (**Figure 5.6A**).[28] The appearance of the IR signal is associated with electron accumulation in the semiconductor film as may be seen from the chronocoulometric profiles (**Figure 5.6B**). The temporal evolution of the IR signal, whose shape does not change with polarization time, is shown in **Figure 5.6C** for the cathodic polarization at −0.6 V (absolute absorbance), meanwhile in **Figure 5.6D** the back polarization to 0.4 V (normalized absorbance) is shown. The IR absorption has recently been associated with shallow trapped electrons in an exponential distribution of band gap states.[27,28] For short polarization times at −0.6 V (t = 120 s) the IR signal is reversible with respect to back polarization to 0.4 V (Figures 5.6A and 5.6D) and a large amount of the charge injected to the electrode (Q_{in}) can be extracted at 0.4 V (Q_{ex}) (Figure 5.6B). However, the fact that not all of the injected charge is extracted upon anodic polarization ($Q_{in} \neq Q_{ex}$) indicates that the currents are not purely capacitive, which means that significant faradaic losses due to electron transfer to solution species (such as residual oxygen) may be taking place. A similar behaviour was observed in a recent study.[27] The discrepancy between Q_{in} and Q_{ex} could alternatively be explained by a persistent charge accumulation in the mesoporous film. However, the fact that the IR signal shows full reversibility (Figure 5.6A) suggests faradaic losses as the main reason for the observed discrepancy between Q_{in} and Q_{ex} for short polarization times.

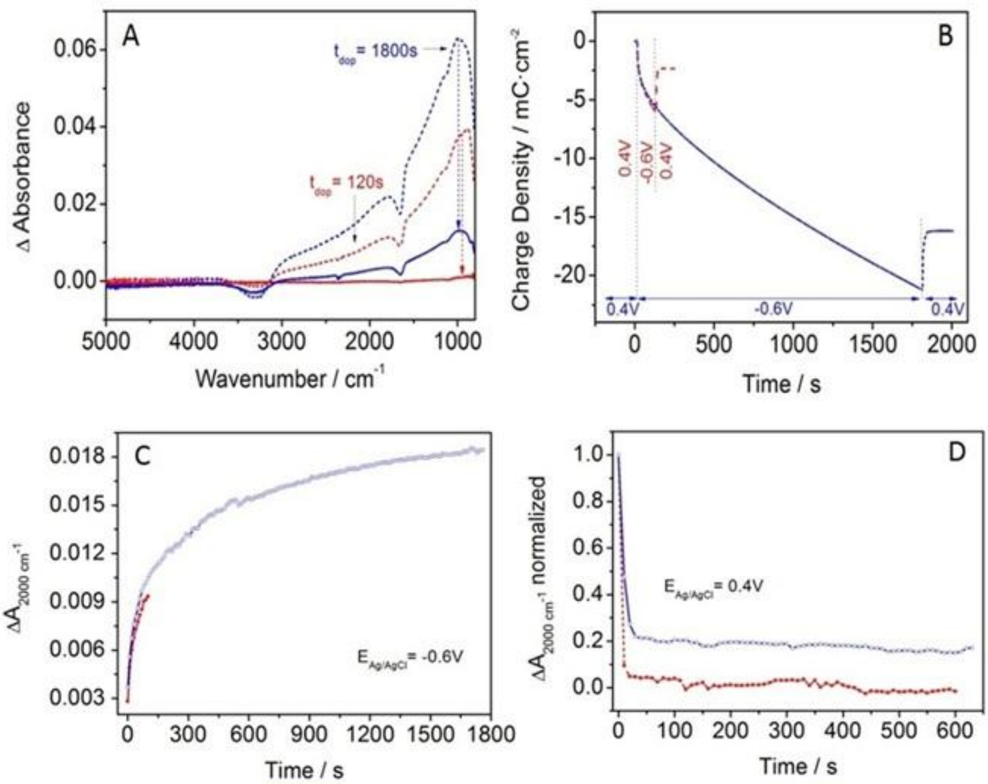

Figure 5.6: (A) ATR-IR spectra of a PI-KEM electrode after 120 s (dashed red line) and 1800 s (dashed blue line) of cathodic treatment at -0.6 V) and upon back-polarization (600 s) to 0.4 V (solid lines). Background spectra were taken at 0.4 V prior to the cathodic treatment. (B) Chronocoulometric profile and (C) absolute and (D) normalized absorbance at 2000 cm^{-1} as recorded simultaneously. Electrolyte: N_2-purged 0.1 M $HClO_4$ aqueous solution.

Prolonged polarization at –0.6 V (t = 1800 s), in contrast, results in a partial irreversibility of the IR absorption. In this case, a residual portion of ≈20% of the stabilized IR absorption (**Figures 5.6A and 5.6C**) persists even after prolonged polarization at 0.4 V (**Figures 5.6A and 5.6D**). The difference between Q_{in} and Q_{ex} (**Figure 5.6B**) includes therefore not only faradaic losses (which are still believed to be the main contribution), but also persistent electron accumulation.

As shown above, short polarization times involve a short persistence of charge accumulation. For instance, the symmetry of the cyclic voltammograms (**Figure 5.5**) indicates a high reversibility of charge accumulation/extraction for short residence times at negative potentials (scan velocity: 20 mV·s^{-1}). This highly reversible behaviour points to the involvement of electronic states located at the *semiconductor/electrolyte interface*. However, the long-lasting effect of electrochemical doping observed after extended cathodic polarization indicates a population of electronic states and a concomitant insertion of charge compensating protons in the *subsurface regions* of the semiconductor nanocrystals. In line with this interpretation a longer-lasting persistence of charge accumulation has been observed for electrodes consisting of larger particles (**Figure 5.7**). This is in line with the observation of a longer-lasting persistence of the beneficial doping effect on the photocurrent for electrodes consisting of larger particles (**Figure 5.4**).

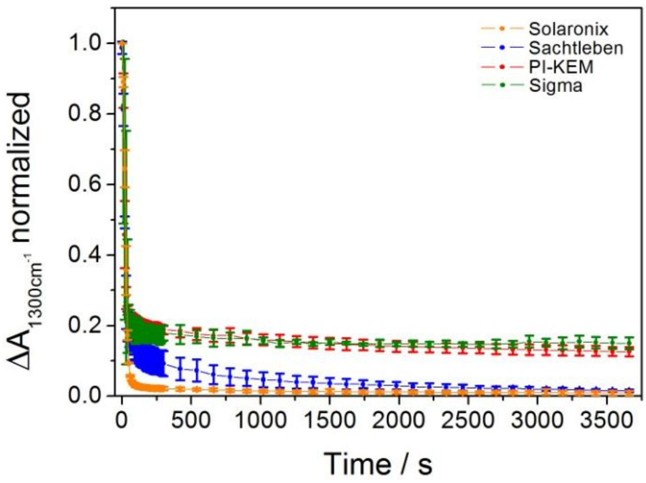

Figure 5.7: Temporal evolution of normalized absorbance at 1300cm^{-1} of ATR-IR spectra measured at $E_{Ag/AgCl}$ = 0.40 V for all the nanoparticles studied after electrochemical doping ($E_{Ag/AgCl}$ = -0.60 V, time: 1000 s). Electrolyte: N_2-purged 0.1 M $HClO_4$ aqueous solution.

As shown is Figures 5.4 and 5.7, the persistence of photocurrent enhancement is intimately related to the persistence of electron accumulation. With respect to particle size both kinetics show comparable relative trends: the larger the particle size, the slower the decay of both the photocurrent enhancement and the IR signal intensity resulting from shallow trapped electrons. Nevertheless, the changes are completely reversible on a time scale of hours to days upon thin film storage in the absence of UV light at potentials equal to or more positive than the open-circuit potential.

3.2. Effects of electron acceptors or hole scavengers on the electrochemical doping process.

The presence of hole and electron acceptors in the electrolyte critically influences the degree of charge accumulation during photocatalytic operation and thus the open-circuit potential. This effective doping potential (at open-circuit conditions) results from the kinetic balance between the photogeneration of electron-hole pairs and charge transfer to the electrolyte. However, even in the presence of dissolved oxygen, the most common electron acceptor in photocatalysis, electron accumulation is typically observed in photoexcited TiO_2 catalysts, though to a lesser extent.

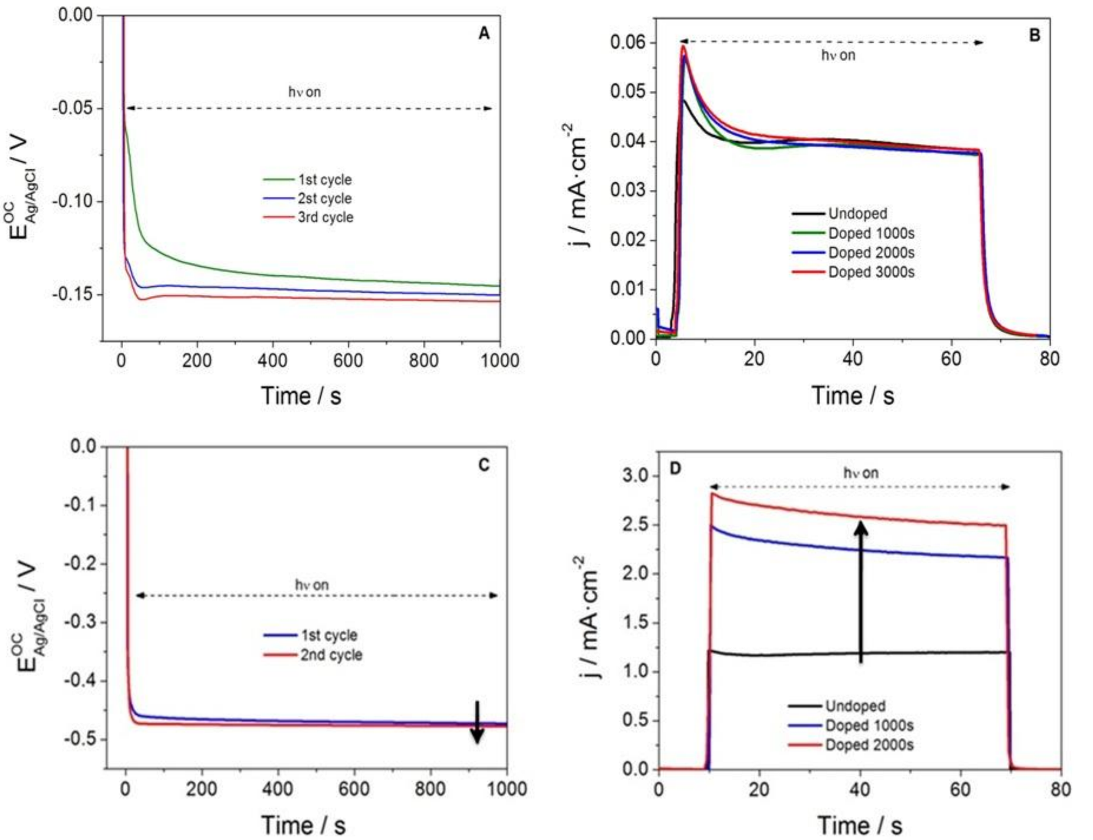

Figure 5.8: Voltage-induced hydrogen-doping of PI-KEM electrodes in the presence of electron acceptor (O_2-purged). (A, C) Electrode potential profiles during doping cycles. (B, D) Photocurrent transients at $E_{Ag/AgCl}$ = 0.8 V of the undoped electrodes and after cumulative doping cycles. Electrolyte: (A, B) 0.1 M $HClO_4$ or (C, D) 1 M HCOOH/0.1 M $HClO_4$.

Experiments in oxygen-saturated electrolyte solutions were performed in order to study under working conditions the influence of O_2 on the hydrogen doping of the photocatalyst. In the absence of a hole acceptor (formic acid in this case) the open-circuit potential measured on a PI-KEM electrode under UV exposure changes from -0.35 V in a N_2-purged electrolyte (Table 5.1) to -0.15 V in the O_2-purged electrolyte (**Figure 5.8A**). Concomitantly, only a small and short-lasting increase (initial 20 seconds) of the photocurrent is observed at anodic polarization (**Figure 5.8B**). Therefore, we can infer that under these conditions photogenerated electrons are efficiently transferred to the acceptor in solution. Consequently, electron accumulation in the semiconductor is too weak to give rise to a significant doping. Nevertheless, on the other hand, in the presence of formic acid an open-circuit potential of -0.48 V is observed even in the presence of dissolved oxygen (**Figure 5.8C**), which gives rise to a photocurrent enhancement by a factor of ≈2 as sampled upon anodic polarization (**Figure 5.8D**).

Whereas the presence of oxygen causes a decrease of the photocurrent enhancement as compared to the N_2-purged solution, the doping persistence is comparable in both cases (**Figure 5.9**). These observations indicate that oxygen significantly influences the doping process by decreasing the effective doping potential, whereas doping persistence is virtually independent of the O_2 concentration.

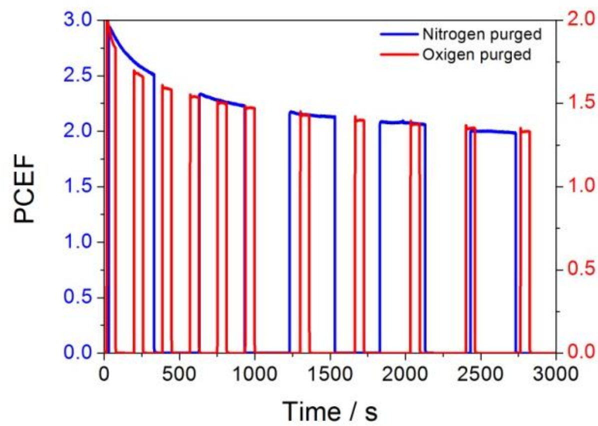

Figure 5.9: Temporal evolution of the photocurrent enhancement factor determined at $E_{Ag/AgCl}$ = 0.8 V following light-induced hydrogen doping at open-circuit. Doping and sampling was performed in 1 M $HCOOH$/0.1 M $HClO_4$ aqueous solution, which was purged with N_2 (doping potential: -0.60 V) or O_2 (doping potential: -0.48 V), respectively.

4. General discussion.

The main observation of the experiments here described is that the photoelectrocatalytic performance enhancement of the thin films depends on the Fermi level position during electrochemical doping but not on the perturbation mode. Importantly, voltage-induced and light-induced doping yield a similar PCEF as long as the electrode potential during doping (i.e. the externally applied bias or the generated photopotential, respectively) is the same.[29] This highlights the value of electrochemical methods for the characterization of photocatalytic systems, as processes taking place at open-circuit cannot be studied directly, but tracked by open-circuit potential measurements instead, and simulated to some extent by external Fermi level control.

It was found for the systems studied that the beneficial doping effect is completely reversible and the initial photoactivity is restored after hours to days. This reversibility would devaluate the importance of electrochemical doping for photocatalytic and photovoltaic applications. However, bearing in mind that electron accumulation, which constitutes the initial step of electrochemical hydrogen doping, takes place even at open-circuit on a working photocatalyst (i.e. *in situ*), one could envisage a continuous recharging of the doping level during semiconductor operation at open-circuit. The stationary doping degree would depend on the photovoltage that can be generated at the electrode and would result from the dynamic competition between charge (electrons and protons) accumulation in the semiconductor and the transfer to acceptors in solution. A constant doping level would be maintained as long as a photovoltage is generated in the semiconductor. This is even enhanced in the presence of a hole scavenger. Such a scenario could be of importance for conventional photocatalysis, where the active material is operated at open-circuit conditions and in contact with organic molecules that get oxidized.

The beneficial effect of in-situ doping on the performance of the TiO_2 thin film is observed both for the photopotential and for the photocurrent. On the one hand, an increase of the photocurrent with doping time reflects the increase of the *photoelectrocatalytic* activity of the TiO_2 electrode. More importantly, an increase of the photovoltage indicates a decrease of charge carrier recombination. A decreased recombination is expected to be connected to an enhancement of the *photocatalytic* activity of the TiO_2 thin film.

In contrast to voltage-induced doping, in the case of light-induced doping the Fermi level cannot be fixed to preset values just by setting the light irradiance. The Fermi level depends critically on system properties such as the catalyst activity, the thin film morphology or the electrolyte composition (presence of electron or hole acceptors). The doping potential can therefore not be varied arbitrarily in the case of light-induced doping.

The presence of a hole scavenger has an important impact on the recombination characteristics of the undoped semiconductor/electrolyte system, on the one hand, and on the light-induced doping process, on the other hand. As recombination is suppressed by hole scavenging, higher photopotentials can be generated. This effect is further enhanced in the case of formic acid as a consequence of photocurrent multiplication, i.e. the generation of more than one electron per absorbed photon due to charge injection from the highly reducing primary oxidation product (HCOO·) to the semiconductor.[39] Higher doping levels (more negative potentials) may therefore be obtained in the presence of formic acid. The relative impact of electrochemical doping on the photocatalytic activity thus clearly depends on the recombination characteristics of the undoped system. The influence of the reduction of recombination on the enhancement of the photovoltaic performance will be addressed in the next chapter.

5. Conclusions.

The results presented in this chapter show that the degree of hydrogen-doping of mesoporous TiO_2 electrodes in contact with an aqueous electrolyte has to be considered a dynamic thin film property, which may significantly change during operation. This has important implications for the design and optimization of materials used in photocatalytic and photovoltaic applications. Furthermore, it highlights the need for studying the dynamic properties of the photocatalytic material under working conditions. Knowledge on this is a prerequisite for the establishment of a feedback loop between semiconductor synthesis, properties and performance. Consequently, appropriate analytical tools for studying the properties of mesoporous semiconductor films *in situ* are urgently needed. In this context, electrochemical approaches prove to be highly valuable as they allow to some extent for simulating and studying processes taking place at open-circuit conditions. Concretely, we observe that the performance enhancement of a TiO_2 electrode depends on the Fermi level position during electrochemical doping, being however independent of the perturbation mode (external polarization versus photoinduced electron accumulation at open-circuit). This fact relaxes the demand of doping persistence for good performance, because continuous *in situ* doping might occur under certain conditions during operation at open-circuit. These observations could be of special relevance for photocatalysis, where the active material is operated at open-circuit and in the presence of hole scavengers (organic pollutants, for instance). Indeed, electrochemical hydrogen-doping constitutes a real *in situ* process, which may take place at the working photocatalyst under illumination.

6. References.

(1) Damrauer, N. H.; McCusker, J. K. Ultrafast Dynamics in the Metal-to-Ligand Charge Transfer Excited-State Evolution of [Ru(4,4‘-Diphenyl-2,2‘-bipyridine)3]2+. *J. Phys. Chem. A* **1999**, *103*, 8440–8446.

(2) Zhang, H.; Chen, G.; Bahnemann, D. W. Photoelectrocatalytic Materials for Environmental Applications. *J Mater Chem* **2009**, *19*, 5089–5121.

(3) Fujishima, A.; Zhang, X.; Tryk, D. A. TiO2 Photocatalysis and Related Surface Phenomena. *Surf. Sci. Rep.* **2008**, *63*, 515–582.

(4) Hagfeldt, A.; Boschloo, G.; Sun, L.; Kloo, L.; Pettersson, H. Dye-Sensitized Solar Cells. *Chem. Rev.* **2010**, *110*, 6595–6663.

(5) Gurlo, A.; Riedel, R. In Situ and Operando Spectroscopy for Assessing Mechanisms of Gas Sensing. *Angew. Chem. Int. Ed.* **2007**, *46*, 3826–3848.

(6) Berger, T.; Monllor-Satoca, D.; Jankulovska, M.; Lana-Villarreal, T.; Gómez, R. The Electrochemistry of Nanostructured Titanium Dioxide Electrodes. *ChemPhysChem* **2012**, *13*, 2824–2875.

(7) Wang, G.; Ling, Y.; Li, Y. Oxygen-Deficient Metal Oxide Nanostructures for Photoelectrochemical Water Oxidation and Other Applications. *Nanoscale* **2012**, *4*, 6682–6691.

(8) Macak, J. M.; Gong, B. G.; Hueppe, M.; Schmuki, P. Filling of TiO2 Nanotubes by Self-Doping and Electrodeposition. *Adv. Mater.* **2007**, *19*, 3027–3031.

(9) Su, J.; Zou, X.-X.; Zou, Y.-C.; Li, G.-D.; Wang, P.-P.; Chen, J.-S. Porous Titania with Heavily Self-Doped Ti3+ for Specific Sensing of CO at Room Temperature. *Inorg. Chem.* **2013**, *52*, 5924–5930.

(10) Lu, X.; Wang, G.; Zhai, T.; Yu, M.; Gan, J.; Tong, Y.; Li, Y. Hydrogenated TiO2 Nanotube Arrays for Supercapacitors. *Nano Lett.* **2012**, *12*, 1690–1696.

(11) Myung, S.-T.; Kikuchi, M.; Yoon, C. S.; Yashiro, H.; Kim, S.-J.; Sun, Y.-K.; Scrosati, B. Black Anatase Titania Enabling Ultra High Cycling Rates for Rechargeable Lithium Batteries. *Energy Env. Sci* **2013**, *6*, 2609–2614.

(12) Hamdy, M. S.; Amrollahi, R.; Mul, G. Surface Ti3+-Containing (blue) Titania: A Unique Photocatalyst with High Activity and Selectivity in Visible Light-Stimulated Selective Oxidation. *ACS Catal.* **2012**, *2*, 2641–2647.

(13) Wang, G.; Wang, H.; Ling, Y.; Tang, Y.; Yang, X.; Fitzmorris, R. C.; Wang, C.; Zhang, J. Z.; Li, Y. Hydrogen-Treated TiO2 Nanowire Arrays for Photoelectrochemical Water Splitting. *Nano Lett.* **2011**, *11*, 3026–3033.

(14) Di Valentin, C.; Pacchioni, G.; Selloni, A. Reduced and N-Type Doped TiO2: Nature of Ti3+ Species. *J. Phys. Chem. C* **2009**, *113*, 20543–20552.

(15) Zuo, F.; Wang, L.; Wu, T.; Zhang, Z.; Borchardt, D.; Feng, P. Self-Doped Ti3+ Enhanced Photocatalyst for Hydrogen Production under Visible Light. *J. Am. Chem. Soc.* **2010**, *132*, 11856–11857.

(16) Berger, T.; Lana-Villarreal, T.; Monllor-Satoca, D.; Gomez, R. Charge Transfer Reductive Doping of Nanostructured TiO2 Thin Film’s as a Way to Improve Their Photoelectrocatalytic Performance. *Electrochem. Commun.* **2006**, *8*, 1713–1718.

(17) Idígoras, J.; Berger, T.; Anta, J. A. Modification of Mesoporous TiO2 Films by Electrochemical Doping: Impact on Photoelectrocatalytic and Photovoltaic Performance. *J. Phys. Chem. C* **2013**, *117*, 1561–1570.

(18) Wang, Q.; Zhang, Z.; Zakeeruddin, S. M.; Gratzel, M. Enhancement of the Performance of Dye-Sensitized Solar Cell by Formation of Shallow Transport Levels under Visible Light Illumination. *J Phys Chem C* **2008**, *112*, 7084–7092.

(19) Meekins, B. H.; Kamat, P. V. Got TiO2 Nanotubes? Lithium Ion Intercalation Can Boost Their Photoelectrochemical Performance. *ACS Nano* **2009**, *3*, 3437–3446.

(20) Zhang, Z.; Hedhili, M. N.; Zhu, H.; Wang, P. Electrochemical Reduction Induced Self-Doping of Ti3+ for Efficient Water Splitting Performance on TiO2 Based Photoelectrodes. *Phys Chem Chem Phys* **2013**, *15*, 15637–15644.

(21) Wahl, A.; Augustynski, J. Charge Carrier Transport in Nanostructured Anatase TiO2 Films Assisted by the Self-Doping of Nanoparticles. *J. Phys. Chem. B* **1998**, *102*, 7820–7828.

(22) Pelouchova, H.; Janda, P.; Weber, J.; Kavan, L. Charge Transfer Reductive Doping of Single Crystal TiO2 Anatase. *J. Electroanal. Chem.* **2004**, *566*, 73–83.

(23) Lyon, L. A.; Hupp, J. T. Energetics of the Nanocrystalline Titanium Dioxide/Aqueous Solution Interface: Approximate Conduction Band Edge Variations between H0 = −10 and H- = +26. *J Phys Chem B* **1999**, *103*, 4623–4628.

(24) Schimpf, A. M.; Ochsenbein, S. T.; Buonsanti, R.; Milliron, D. J.; Gamelin, D. R. Comparison of Extra Electrons in Colloidal N-Type Al3+-Doped and Photochemically Reduced ZnO Nanocrystals. *Chem Commun* **2012**, *48*, 9352–9354.

(25) Schrauben, J. N.; Hayoun, R.; Valdez, C. N.; Braten, M.; Fridley, L.; Mayer, J. M. Titanium and Zinc Oxide Nanoparticles Are Proton-Coupled Electron Transfer Agents. *Science* **2012**, *336*, 1298–1301.

(26) Cohn, A. W.; Kittilstved, K. R.; Gamelin, D. R. Tuning the Potentials of “Extra” Electrons in Colloidal N-Type ZnO Nanocrystals via Mg2+ Substitution. *J. Am. Chem. Soc.* **2012**, *134*, 7937–7943.

(27) Berger, T.; Anta, J. A. IR–Spectrophotoelectrochemical Characterization of Mesoporous Semiconductor Films. *Anal Chem* **2012**, *84*, 3053–3057.

(28) Berger, T.; Anta, J. A.; Morales-Florez, V. Electrons in the Band Gap - Spectroscopic Characterization of Anatase TiO2 Nanocrystal Electrodes under Fermi Level Control. *J Phys Chem C* **2012**, *116*, 11444–11455.

(29) Berger, T.; Anta, J. A.; Morales-Flórez, V. Spectroscopic Properties of Electrochemically Populated Electronic States in Nanostructured TiO 2 Films: Anatase versus Rutile. *Phys. Chem. Chem. Phys.* **2013**, *15*, 13790–13795.

(30) Fabregat-Santiago, F.; Mora-Sero, I.; Garcia-Belmonte, G.; Bisquert, J. Cyclic Voltammetry Studies of Nanoporous Semiconductors. Capacitive and Reactive Properties of Nanocrystalline TiO2 Electrodes in Aqueous Electrolyte. *J. Phys. Chem. B* **2003**, *107*, 758–768.

(31) Bailes, M.; Cameron, P. J.; Lobato, K.; Peter, L. M. Determination of the Density and Energetic Distribution of Electron Traps in Dye-Sensitized Nanocrystalline Solar Cells. *J. Phys. Chem. B* **2005**, *109*, 15429–15435.

(32) Boschloo, G.; Hagfeldt, A. Activation Energy of Electron Transport in Dye-Sensitized TiO2 Solar Cells. *J. Phys. Chem. B* **2005**, *109*, 12093–12098.

(33) Lagemaat, J. van de; Frank, A. J. Effect of the Surface-State Distribution on Electron Transport in Dye-Sensitized TiO2 Solar Cells: Nonlinear Electron-Transport Kinetics. *J. Phys. Chem. B* **2000**, *104*, 4292–4294.

(34) Bisquert, J. Chemical Diffusion Coefficient of Electrons in Nanostructured Semiconductor Electrodes and Dye-Sensitized Solar Cells. *J. Phys. Chem. B* **2004**, *108*, 2323–2332.

(35) Anta, J. A. Electron Transport in Nanostructured Metal-Oxide Semiconductors. *Curr. Opin. Colloid Interface Sci.* **2012**, *17*, 124–131.

(36) Berger, T.; Lana-Villarreal, T.; Monllor-Satoca, D.; Gomez, R. An Electrochemical Study on the Nature of Trap States in Nanocrystalline Rutile Thin Films. *J. Phys. Chem. C* **2007**, *111*, 9936–9942.

(37) Jankulovska, M.; Berger, T.; Lana-Villarreal, T.; Gómez, R. A Comparison of Quantum-Sized Anatase and Rutile Nanowire Thin Films: Devising Differences in the Electronic Structure from Photoelectrochemical Measurements. *Electrochimica Acta* **2012**, *62*, 172–180.

(38) Fabregat-Santiago, F.; Barea, E. M.; Bisquert, J.; Mor, G. K.; Shankar, K.; Grimes, C. A. High Carrier Density and Capacitance in TiO2 Nanotube Arrays Induced by Electrochemical Doping. *J Am Chem Soc* **2008**, *130*, 11312–11316.

(39) Solarska, R.; Augustynski, J.; Sayama, K. Viewing Nanocrystalline TiO2 Photoelectrodes as Three-Dimensional Electrodes: Effect of the Electrolyte upon the Photocurrent Efficiency. *Electrochimica Acta* **2006**, *52*, 694–703.

Chapter 6:

Electrochemical hydrogen-doping: Impact on photoelectrocatalytic and photovoltaic applications

1. Introduction.

In the previous chapter it was shown that a simple electrochemical treatment, the cathodic polarization in aqueous electrolyte, known as reductive *electrochemical hydrogen-doping*, constitutes an appropriate tool to modify to some extent the properties of nanocrystalline TiO_2 electrodes.[1] Electrochemical doping was found to enhance in some cases the photocatalytic performance of the semiconductor.[2] This beneficial effect has been attributed to the generation of Ti^{3+} sites and the concomitant insertion of protons[1] or other cations like lithium cations[2] into the semiconductor bulk. Electrochemical doping of TiO_2 nanotube electrodes in alkaline aqueous solution was shown to induce significant changes of the capacitance of the thin film.[3] Whereas chemical capacitance and electronic conductivity of unmodified electrodes showed an exponential dependence on bias potential, capacity at low potentials increased dramatically upon electrochemical doping and a nearly constant transport resistance was observed. These changes were attributed to the doping of the semiconductor and to the concomitant transition from band pinning in unmodified electrodes to Fermi level pinning as a consequence of proton intercalation.

Wang et al.[4] observed an enhancement of the DSSC performance after visible light soaking and attributed it to the formation of shallow transport levels originating from photoinduced H^+ intercalation. These shallow trapping states are supposed to accelerate charge carrier transport within the nanocrystalline films without deteriorating the open circuit photovoltage. Importantly, a similar beneficial effect was observed upon cathodic polarization in the aprotic organic electrolyte. Sensitizer adsorption or residual water traces were proposed as possible proton sources. On the other hand, Gregg et al.[5] reported on the improvement of DSSC performance upon UV exposure and attributed it to the reversible generation of surface states. More recently Listorti et al.[6] detected band displacements and reduced recombination rates upon light soaking that explained the increased photocurrents. As discussed in **Chapter 5**, these results point to an analogy of bias- and photoinduced doping and that, consequently, both cathodic treatment and light exposure may render the modification of the thin film possible. In this context, a recent study highlighted the advantages of IR-spectroelectrochemical measurements to track both bias- and photoinduced charge accumulation in mesoporous semiconductor films.[7,8] This approach may thus contribute to a fundamental understanding of thin film modification under application relevant conditions.

In this chapter, the effect of electrochemical hydrogen-doping on the photoelectrocatalytic and photovoltaic properties of TiO_2 commercial powders is shown. Firstly, the persistence of thin film modification upon electrochemical doping in aqueous solution will be tracked in situ by the detection of IR active trapped electrons. Then the influence of the doping treatment on the macroscopic behaviour of the TiO_2 electrodes will be correlated with (1) the photoelectrocatalytic activity with respect to water oxidation and (2) the photoconversion efficiency of dye-sensitized solar cells (DSSC) based on the doped electrodes.

Most of the results presented in this chapter have been reported in the following publication: Idígoras et al. *Journal of Physical Chemistry C*, **2013**, 117(4), 1561-1570.

2. Experimental.

2.1. Preparation of nanocrystalline TiO_2 electrodes.

Mesoporous electrodes were prepared by spreading aqueous slurries of commercial TiO_2 nanoparticles (**PI-KEM**) or Ti-Nanoxide-T paste (**Solaronix**) onto fluorine-doped tin oxide (FTO) conducting glass (Pilkington, resistance 15 Ω/square, 82-84.5 % visible transmittance). For spectroelectrochemical experiments a Ti foil (Goodfellow, 99.6+%, 25 µm) was used as the conducting substrate. The suspension was spread over the substrate with a glass rod using Scotch tape as a spacer (*doctor blade*). The active area of the electrode was 0.64 cm^2. Afterwards, the films were annealed and sintered for 1 h at 450°C in air.

2.2. Photoelectrochemical measurements.

Photoelectrochemical measurements were performed at room temperature in a three-electrode cell equipped with a fused silica window. All potentials were measured against and referred to an Ag/AgCl/KCl (3M) reference electrode whereas a Pt wire was used as the counter electrode. Measurements were performed with a computer-controlled *Autolab PGSTAT302N* potentiostat. In all experiments an N_2 purged 0.1 M solution of $HClO_4$ (Merck p.a.) in ultrapure water (*Millipore, MilliQ*) was used as working electrolyte. Cyclic voltammograms (CVs) were recorded between -0.6 V and 0.8 V at a scan rate of 20 mV/s. The reductive doping of the nanocrystalline electrodes was carried out by applying a constant potential of -0.6V for different polarization times. A 450 W Xenon arc lamp (*Thermo Oriel*), coupled to a water filter to remove IR radiation, was used for UV/Vis irradiation. The applied light irradiance was measured with an optical power meter (*Gentec TUNER*) equipped with a bolometer (*Gentec XLP12-1S-H2*) being 500 mW·cm^{-2}.

2.3. IR spectroelectrochemical measurements.

For attenuated total reflection (ATR)-IR measurements a TiO_2 film deposited on a Ti foil was used as electrode. IR-spectroscopic measurements were performed at an incident angle of 55° using unpolarized light. The spectra were obtained by averaging 50 scans at a resolution of 4 cm^{-1}. The spectra are represented as $-\log(R/R_0)$, where R and R_0 are the reflectance values corresponding to the single beam spectra recorded for the sample and the reference, respectively. Electrode polarization was performed with the TiO_2 thin film being pressed against the ATR prism unless otherwise started. N_2-purged 0.1 M $HClO_4$ aqueous solution, which was prepared using ultrapure water (*Millipore, MilliQ*), was used as the working electrolyte. All potentials were measured against and are referred to a Ag/AgCl/KCl (3M) electrode. A Pt wire was used as the counter electrode. Measurements were performed with a computer-controlled *Autolab PGSTAT101* potentiostat. The ATR hemispheric ZnSe prism was placed in a reflection unit (*PIKE Technologies, Veemax II*) attached to a *Bruker IFS 66/S FTIR* spectrometer equipped with an MCT detector.

2.4. Fabrication and characterization of Dye-Sensitized Solar Cells.

Prior to cell assembly the DSSC, all electrodes were stored for 25 min in 0.1 M $HClO_4$ aqueous solution. In the following we refer to films which have been stored in the electrolyte without applying an external potential as **undoped electrodes** and those which have been subjected to a cathodic polarization as **doped electrodes**. Subsequently, the films were washed extensively with H_2O and dried at room temperature under vacuum conditions. Then, the electrodes were immersed in a 0.5 mM ethanolic solution of the N719 dye (Di-tetrabutylammonium cis-bis(isothiocyanato)bis(2,2'-bipyridyl-4,4'-dicarboxylato) ruthenium(II)) for 1h and rinsed with the same solvent. The counter-electrode was prepared by spreading 20 µl of Platisol (*Solaronix*) over FTO substrates (Pilkington, resistance 8 Ω/square, 80-81.5% visible transmittance) and subsequent annealing at 390°C for 20 min. Finally, the two electrodes were clamped together to form a sandwich, where a polymer film (*Surlyn*, Solaronix) was used as spacer around the titanium oxide area. The cells were sealed with two component epoxy adhesive, without thermal treatment.

Two types of electrolytes have been employed in this chapter: electrolytes based on organic solvents (**Electrolyte A**: 0.5M LiI, 0.05M I_2 and 0.5M 4-tert-butylpyridine in methoxypropionitrile; and **Electrolyte B**: 0.1M LiI, 0.05M I_2, 0.5M 4-tert-butylpyridine, 0.6M 1,2-dimethyl-3-propylimidazolium iodide and 0.1M guanidine thiocyanate in acetonitrile-Valeronitrile (1:1 v/v)) and a solvent-free electrolyte (**Electrolyte C**: 0.05 M I_2 in 1-ethyl-3-methylimidazolium tetracyanoborate and 1-propyl-3-methylimidazoliumiodide (35:65 v/v)).

The devices were characterized using a solar simulator with AM 1.5G filter (*ABET*). The light intensity was calibrated to the standard value of 1 sun (100 mW/cm^2) using a reference solar cell with temperature output (*Oriel,* 91150). The current-voltage characteristics were determined by applying an external potential bias to the cell and measuring the photocurrent using an *Autolab/PGSTAT302N* potentiostat. Open-circuit voltage decay measurements (OCVD)[9] were made by keeping the solar cell at open-circuit and registering the voltage transient after interrupting the illumination.

Electrochemical Impedance Spectroscopy (EIS), Intensity Modulated Photovoltage Spectroscopy (IMVS) and Intensity Modulated Photocurrent Spectroscopy (IMPS) were utilized to obtain electron transport and recombination parameters in the DSSC test devices.[10] The illumination for these small perturbation (frequency response) techniques was provided by a 530 nm light emitting diode (*LUXEON*) over a wide range of DC light intensities. This allows for probing the devices at different positions of the Fermi level in the semiconductor. A response analyzer module (*PGSTAT302N/FRA2, AutoLab*) was utilized to analyze the frequency response of the devices. To avoid voltage drop due to series resistance, EIS measurements were performed at open circuit, the Fermi level (related to the open-circuit voltage)[11] is fixed by the DC illumination intensity. A 10 mV perturbation in the 10^5-10^{-2} Hz range was utilized to obtain the spectra. Intensity Modulated Photovoltage Spectroscopy (IMVS) and Intensity Modulated Photocurrent Spectroscopy (IMPS) measurements were carried out by coupling the *PGSTAT302N/FRA2 module* to the light emitting diode, so that an AC signal can be generated. In all cases the samples were illuminated from the dye-coated TiO_2 electrode side. IMVS measurements were performed at open circuit in the 10^4-10^{-1} Hz range and IMPS measurements at short-circuit in the 10^4-10^{-3} Hz range with a light perturbation corresponding to 10% of the DC background illumination intensity. The NOVA 1.7 software was used to generate and treat the IMPS and IMVS data. Zview equivalent circuit modelling software (Scribner) was used to fit the EIS spectra, including the distributed element DX11 (transmission line model).[12,13] To obtain the Fermi level shift between open-circuit and short-circuit conditions "short circuit voltage" (V_{sc})[11] measurements were performed.[14,15] For this purpose, the solar cell was first illuminated under short-circuit conditions using the 530 nm light emitting diode at various light intensities. The diode was then turned off and the cell was switched to open circuit simultaneously. The voltage evolution was finally monitored by the potentiostat.

3. Results and Discussion.

3.1. Spectroelectrochemical *in situ* study of the doping process.

As mentioned in **Chapter 5**, mesoporous PI-KEM TiO_2 thin films consist of a mixture of the anatase and the rutile crystal structure (with an estimated ratio of 1:1). These films with a thickness of ≈ 8.5 μm are formed by crystallites with well-defined surface planes and a mean particle diameter of 45 nm. However, Solaronix electrodes based on a commercial particle suspension (*Ti-Nanoxide-T*) with a film thickness of ≈ 4 μm exhibit pure anatase structure and are built up of much smaller particles with a mean diameter of 20 nm[8] (**Appendix**, Figure A-5.1).

As shown in the previous chapter, upon cathodic polarization at $E_{Ag/AgCl}$ = -0.6 V TiO_2 electrodes show the characteristic absorption of shallow trapped electrons in the mid-IR (**Figure 6.1A**).[8] Importantly, these signals are temporarily persisting even upon polarization to potentials more positive that the open-circuit potential. In particular, anodic polarization at $E_{Ag/AgCl}$ = 0.4 V for 1 h leads only to a partial decrease of the signal intensity demonstrating the temporary persistence of electron accumulation. However, different behaviour can be found for different nanoparticles (**Figure 6.1B**).

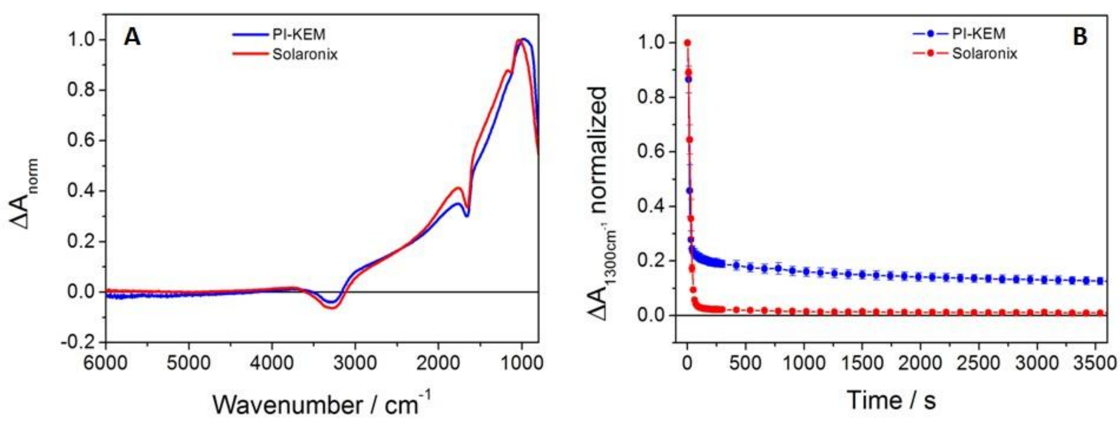

Figure 6.1: (A) ATR-IR spectra of PI-KEM and Solaronix electrodes after 1000s of cathodic polarization at $E_{Ag/AgCl}$ = -0.6V. Reference spectra were taken at 0.4 V. (B) Temporal evolution of normalized absorbance at 1300 cm^{-1} and at positive polarization potential (+0.4V) Electrolyte: N_2-purged 0.1M $HClO_4$ aqueous solution.

For PI-KEM electrodes a residual portion of ≈ 20% of the stabilized IR absorption persists even after prolonged polarization at 0.4 V. The same observation is made when charge injection/extraction is performed with the TiO_2 electrode being located in the electrolyte bulk of the electrochemical cell, instead of being pressed against the ATR prism. However, the persistence of electron accumulation is in contrast to the behaviour of anatase Solaronix TiO_2 electrodes paste. In this case, a full reversibility of the IR absorption was observed independent of polarization time at –0.6 V (**Figure 6.1B**).

Obviously, structural properties (such as crystal structure, particle size and shape...) play an important role in the processes of doping and undoping as it was shown in **Chapter 5**. In any case, electron accumulation within the mesoporous TiO_2 film is coupled to H^+ uptake (adsorption/intercalation) from the electrolyte.[16] However, the thin film properties governing the extent of proton uptake/release are far from being identified, but apart from semiconductor bulk properties (crystal structure, particle size) the nature of the semiconductor/electrode interface (surface charge, atomic arrangement) is expected to have a significant effect. Clearly, more efforts are needed to elucidate the interplay between electrode properties and the reversibility of charge accumulation.

3.2. Photoelectrochemical measurements.

The electrodes were mounted in a photoelectrochemical cell to study the influence of electrochemical doping on the photoelectrocatalytic performance. For this purpose the photooxidation of water was studied in 0.1 M $HClO_4$ aqueous electrolyte. **Figure 6.2** shows CVs under polychromatic illumination before and after electrochemical doping ($E_{Ag/AgCl}$ = -0.6 V, t = 750 s). CVs of the electrodes in 0.1 M $HClO_4$ aqueous solution in the dark, as described in **Chapter 5**, are characterized by two pairs of capacitive peaks which are associated with electron accumulation at different regions in the semiconductor film (**Appendix**, Figure A-6.1).[1] It has to be mentioned that after electrochemical doping a minor changes may be observed in the CVs in dark. In particular, a shift towards more positive potentials of the capacitive peak at $E_{Ag/AgCl}$ = 0 V is observed for PI-KEM electrodes, whereas for Solaronix electrodes these peaks are virtually absent on undoped electrodes and appear, though at very low intensity, after doping.

The cathodic treatment results in the enhancement of the saturated photocurrent by a factor of ≈3 for PI-KEM electrode (**Figure 6.2A**). Increase of the polarization time at –0.6 V does not induce further changes. These observations are in perfect agreement with a previous study.[1] In the photoelectrochemical experiment the polarization time necessary to obtain a constant photocurrent for water oxidation is somewhat shorter than the polarization time needed in spectroelectrochemical experiments to reach a constant IR absorption. This results from significant differences in the geometry of the two electrochemical cells. In the ATR cell diffusion from the electrolyte bulk to the semiconductor surface is significantly slowed down by the thin electrolyte layer, which forms between the electrode and the surface of the ZnSe hemisphere, when the electrode is pressed against the ATR crystal.[7,8] Importantly, no modification of the photoelectrochemical properties was observed after electrochemical doping for Solaronix electrodes (**Figure 6.2B**) in line with the spectroelectrochemical measurements evidencing the absence of persistent doping for this type of thin film, as mentioned above.[7,8]

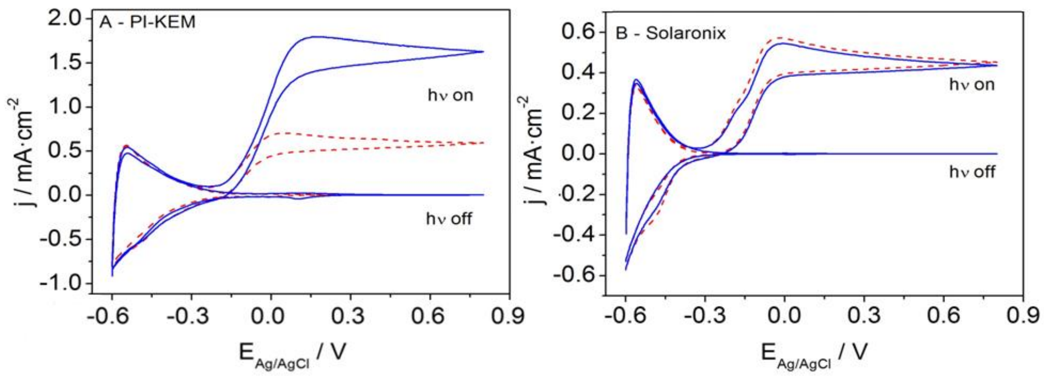

Figure 6.2: CVs in the dark and under illumination for undoped (dashed red lines) and doped (solid blue lines) (A) PI-KEM and (B) Solaronix electrodes. Electrolyte: N_2-purged 0.1 M $HClO_4$ aqueous solution. Irradiance: 500 $mW \cdot cm^{-2}$. Electrochemical doping: $E_{Ag/AgCl}$ = -0.6 V; t_{dop} = 750 s.

The photocurrent increase in PI-KEM electrodes has previously been attributed to the build-up of a space charge layer within particle agglomerates which may form due to the well-defined morphology of the nanocrystals.[1] The depletion layer would enhance the separation efficiency of photogenerated electron-hole pairs and thus reduce recombination. Alternatively, Meekins et al.[2] attributed an increase in the photoconversion efficiency observed upon Li^+ or H^+ intercalation into nanotube arrays to the blocking of charge recombination sites within the TiO_2 lattice.

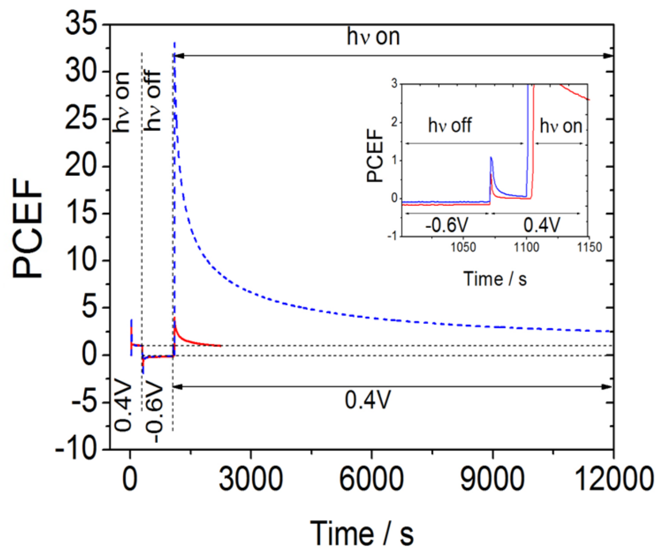

Figure 6.3: Current transients for PI-KEM (dashed blue line) and Solaronix (solid red line) electrodes. The current is normalized to the photocurrent of the undoped electrodes. Electrolyte: N_2-purged 0.1 M $HClO_4$ aqueous solution. Irradiance: 500 $mW \cdot cm^{-2}$. Inset shows a blow-up of the current transient upon back-polarization at 0.4 V in the dark.

The photocurrent enhancement factor (PCEF) has been used to quantify the persistence of electrochemical doping. **Figure 6.3** shows the photocurrent after electrochemical doping, normalized to the photocurrent of the undoped electrode, as a function of time.

The following experimental sequence was applied: First, the photocurrent of the unmodified electrode was determined at 0.4 V. Then the electrode was polarized for 750 s at −0.6 V in the dark. After back-polarization to 0.4 V in the dark, the electrode was finally again exposed to polychromatic light and the time profile of the photocurrent was recorded. As observed, the PCEF decreases rapidly at 0.4 V. However, even after 3 h at 0.4 V still a PCEF of ≈2.5 is observed for PI-KEM electrode. In contrast, the effect of electrochemical doping is small in the case of a Solaronix sample. After only 20 min at 0.4 V the initial photocurrent is completely recovered. This experiment shows that electrochemical doping persists on a time scale of hours to days in the case of PI-KEM electrodes. Similar results were obtained in **Chapter 5**.

This persistence provides thus sufficient time for the assembly and characterization of DSSC test devices before the beneficial effect is lost and opens up the possibility of studying the influence of electrochemical doping on the photovoltaic performance. Thus, to obtain doped electrodes for photovoltaic characterization, cathodic polarization was performed in the photoelectrochemical cell at **$E_{Ag/AgCl}$ = -0.6 V for t_{dop} = 750 s.**

3.3. Impact of the electrochemical doping on dye-sensitized solar cells.

To study the impact of electrochemical doping on the photovoltaic performance of the TiO_2 electrodes, DSSC test devices based on doped and undoped electrodes were characterized. In **Figure 6.4** and **Table 6.1** results for the current-voltage characteristics under 1-sun AM 1.5 illumination are presented. For DSSC base on PI-KEM electrodes a beneficial effect of the electrochemical doping is observed both for the short-circuit photocurrent and for the open-circuit photovoltage, whereas the fill factor remains virtually unchanged. On the contrary, no significant effect of electrochemical doping is detected for the Solaronix DSSC. In a blind experiment electrodes were stored in the acidic electrolyte without the application of an external voltage and no significant modification of the DSSC performance with respect to the untreated electrodes was observed.

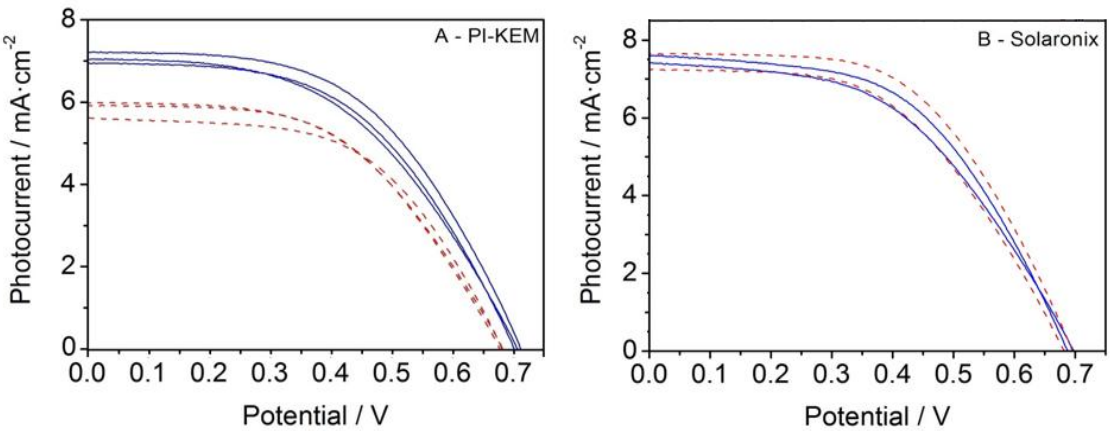

Figure 6.4: Current-voltage characteristics under 1-sun AM 1.5 illumination of DSSC test devices (electrolyte A) based on doped (solid blue lines) and undoped (dashed red lines) PI-KEM (A) and Solaronix (B) electrodes. Electrochemical doping in 0.1 M $HClO_4$ aqueous solution: $E_{Ag/AgCl}$ = -0.6 V; t_{dop} = 750 s.

Configuration		J_{sc} (mA·cm^{-2})	V_{oc} (mV)	Fill Factor / %	Efficiency (%)
Electrolyte A	PI-KEM Undoped	5.8 ± 0.2	682 ± 1	53 ± 1	2.1 ± 0.1
	PI-KEM Doped	7.1 ± 0.2	707 ± 1	51 ± 1	2.6 ± 0.1
	Solaronix Undoped	7.4 ± 0.2	690 ± 1	52 ± 2	2.7 ± 0.2
	Solaronix Doped	7.5 ± 0.1	692 ± 1	51 ± 1	2.6 ± 0.1
Electrolyte B	PI-KEM Undoped	5.7	692	64	2.5
	PI-KEM Doped	7	722	59	3
Electrolyte C	PI-KEM Undoped	4.4	495	45	1
	PI-KEM Doped	5.7	522	48	1.4

Table 6.1: Photovoltaic parameters for solar test devices studied in this chapter. Main values and error intervals are estimated from the preparation of several devices with the same configuration.

The results indicate that the persistent accumulation of negative charge in the PI-KEM electrodes, with concurrent insertion of protons, improves not only the photoelectrocatalytic activity of the films, but also the photovoltaic performance in DSSCs. It has to be mentioned at this point that Wang and coworkers[4] observed a similar effect, i.e. a simultaneous improvement of J_{sc} and V_{oc}, as a result of visible light soaking or, alternatively, upon cathodic polarization in an aprotic organic electrolyte. The importance of the persistence of electron accumulation for beneficial thin film modification is highlighted by the behaviour of Solaronix electrodes, which are characterized by fast electron extraction.[7,8] In this case neither an enhancement of the photoelectrocatalytic activity nor an improvement of the photovoltaic performance is observed after the cathodic treatment.

To cast light on the origin of the positive effect of electrochemical doping on DSSC performance, parameters describing electron transport (diffusion coefficient) and electron recombination (lifetime) have been determined for the test devices at specific positions of the Fermi level in the TiO_2 electrode.[11] In addition, the electron diffusion length, corresponding to the average distance travelled by electrons in the electrode,[17,18] has also been estimated.

3.3.1. Electron recombination properties in solar devices.

In this chapter, the electron lifetime τ_n has been determined by different techniques: IMVS,[10] EIS[12,13] and OCVD.[9,19,20] **Figure 6.5** shows the lifetimes obtained by the different techniques employed as a function of the potential in the semiconductor electrode ($E_F - E_{F,redox}$). EIS and IMVS yield essentially the same results whereas the OCVD measurements are found to lead to a systematic shift to lower values. As mentioned, this can be attributed to direct charge transfer via the TCO/electrolyte interface[21] or non-linear effects which would only multiply the lifetime by a potential-independent constant.[19] Furthermore, it must be born in mind that OCVD is a dark technique, whereas EIS and IMVS are obtained under illumination.

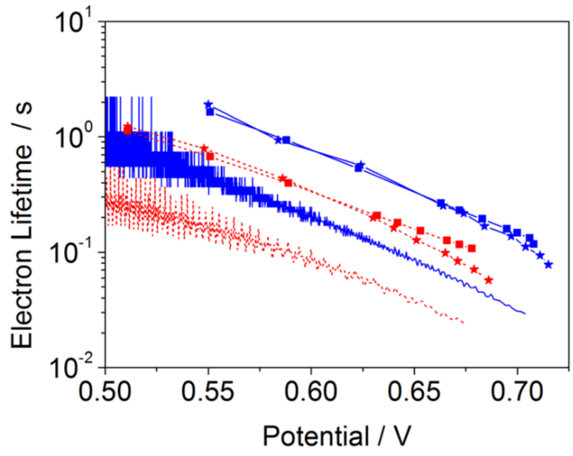

Figure 6.5: Electron lifetime for DSSC test devices (electrolyte A) based on doped (solid blue line) and undoped (dashed red line) PI-KEM electrodes obtained from OCVD (lines), EIS (lines and squares) and IMVS (lines and stars). Electrochemical doping in 0.1 M $HClO_4$ aqueous solution: $E_{Ag/AgCl}$ = -0.6 V; t_{dop} = 750 s. Lines are a guide to the eye.

The results of Figure 6.5 show unambiguously that electrochemical doping leads to a reduced recombination rate, which explains the increased open-circuit photovoltage, and, possibly, the higher short-circuit photocurrent. The origin of this beneficial effect can be analyzed by EIS, which relates the lifetime to the recombination resistance and chemical capacitance of the semiconductor/electrolyte interface.

In **Figure 6.6** the recombination resistance and the chemical capacitance extracted from the EIS spectra at different illumination intensities are reported.

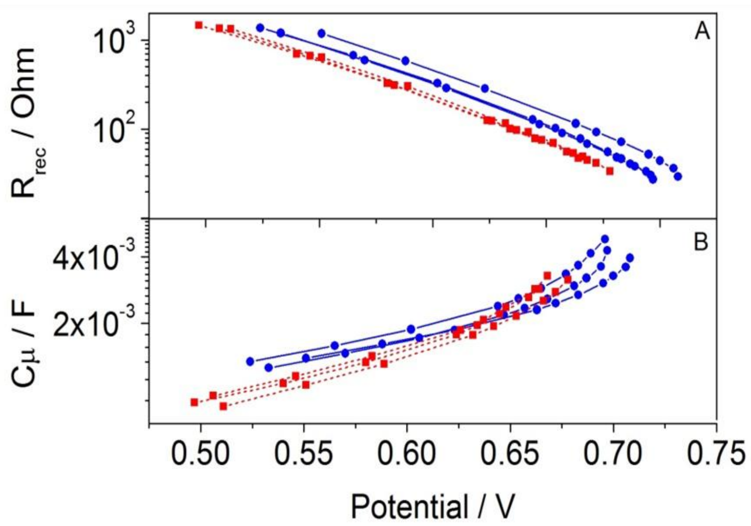

Figure 6.6: Impedance parameters extracted from EIS data by fitting: (A) recombination resistance and (B) chemical capacitance for DSSC test devices (electrolyte A) based on doped (solid blue line and circles) and undoped (dashed red line and squares) PI-KEM electrodes. Electrochemical doping in 0.1 M $HClO_4$ aqueous solution: $E_{Ag/AgCl}$ = -0.6 V; t_{dop} = 750 s. Lines are a guide to the eye.

The EIS analysis shows that electrochemical doping induces only minor changes of the capacitance (**Figure 6.6B**). Concretely, somewhat increased capacitance values are observed at low potentials. This capacitance increase is most likely due to the formation of a depletion layer[3] at the surface of PI-KEM particles or particle aggregates. Such a band bending was previously proposed to improve the photoelectrocatalytic activity of doped PI-KEM electrodes as observed for water photooxidation. In photocatalytic applications, the presence of a depletion layer would enhance the separation efficiency of photogenerated electrons and holes.[1] Band bending can also explain the deviation from the straight line in the capacitance semilogarithmic plot, as recently pointed out by Jennings et al.[22] Alternatively, Wang et al.[4] attributed the increase of the capacitance at low potentials upon cathodic polarization in the DSSC electrolyte to the broadening of the density of states function. In DSSCs, on the other hand, the surface electrical fields resulting from band bending are expected to reduce the recombination of electrons with electron acceptors in solution. Indeed, an increase of the recombination resistance can clearly be observed upon electrochemical doping (**Figure 6.6A**). Importantly, it has to be mentioned that accumulation of negative charge (accompanied by proton insertion) does not produce a significant shift of the TiO_2 conduction band. This is perfectly in line with the observation in aqueous electrolyte that electrochemical doping does not modify the onset potential for capacitive currents at $E_{Ag/AgCl}$ < -0.4 V (**Appendix**, Figure A-6.1A). The absence of a significant conduction band shift can be attributed to the compensation of the accumulated negative charge by the insertion of protons. From an experimental point of view the absence of significant band shifts guarantees that the comparison of the transport and recombination parameters between modified and unmodified electrodes is performed at the same position of the Fermi level with respect to the conduction band edge (electron density). Further details on this are provided in the following sections. Therefore, the observed increase of the lifetime is mainly related to an increment of the recombination resistance (R_{rec}) rather than to a modification of the chemical capacitance of the electrodes. The increase of R_{rec} may be rationalized by the build-up of a space-charge layer within large particles or particle agglomerates as a consequence of a persistent doping of the semiconductor. The extent of such a beneficial effect is expected to strongly depend on thin film morphology such as particle size and shape as well as on particle agglomeration.

However, the results obtained in the present chapter are in contrast to the observations made by Fabregat-Santiago et al.[3] upon proton intercalation in TiO_2 nanotube arrays. These authors observed detrimental effects of electrochemical doping on DSSC characteristics, concretely, an increased capacitance, a decreased recombination resistance, a nearly constant transport resistance with unexpected high values at low potentials and a low open circuit voltage. These modifications were attributed to the pinning of the Fermi level and to an increased recombination upon doping. It has to be mentioned that cathodic polarization was performed in that case at more negative potentials, i.e. $E_{Ag/AgCl}$ = -1 V (t_{dop} = 1200 s; pH 2), whereas our electrodes were polarized at $E_{Ag/AgCl}$ = -0.6 V (t_{dop} = 750 s; pH 1). This discrepancy indicates that the degree of electrochemical doping is a critical issue in the optimization of the DSSC device performance as extensive doping may induce detrimental effects. Importantly, optimal doping parameters might strongly depend on the respective thin film morphology. In this regard, it has to be mentioned that 1-dimensional geometries like those studied in Ref. 3, are more prone to show band bending[23] than nanoparticulate electrodes.

3.3.2. Electron transport properties in solar devices.

The electron lifetime was determined by IMVS measurements (**Equation 4.20** and **Figure 6.7A**), whereas the electron diffusion coefficient was determined by IMPS measurements at various illumination intensities which modifies the positions of Fermi level. The diffusion coefficients can be determined according to **Equation 4.21**.[23–25]

$$D_n = \frac{d^2}{\gamma \tau_{min}^{\text{IMPS}}} \qquad (4.21)$$

In this work values of γ = 2.5 and d = 8.5 μm have been used. Results for the diffusion coefficient can be found in **Figure 6.7B**.

The diffusion coefficient is found to increase exponentially with Fermi level as usually observed in DSSCs[26,27] and predicted by the multiple-trapping model.[28,29] Measured values range between 10^{-5} and 10^{-4} cm^2/s, characteristic of nanocrystalline TiO_2. However, D_n increases by a factor of 2-3, upon electrochemical doping,.

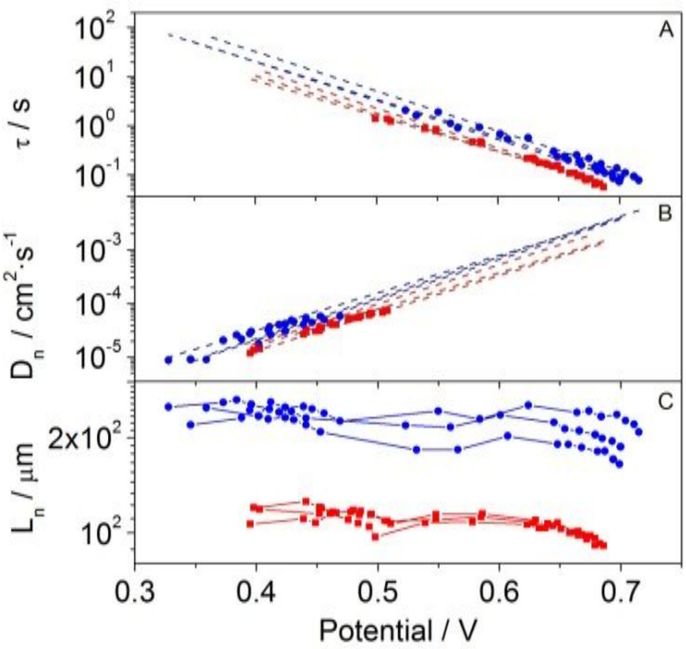

Figure 6.7: Results from IMVS and IMPS data under illumination: (A) electron lifetime, (B) electron diffusion coefficient and (C) electron diffusion length for DSSC PI-KEM based on doped (blue circles) and undoped (red squares) PI-KEM electrodes. Note that symbols represent experimental data for lifetimes and diffusion coefficients as extracted from the IMVS and the IMPS spectra, whereas dashed lines stand for linear extrapolations of the experimental data, required to compute the diffusion length at coincident positions of the Fermi level. Electrochemical doping in 0.1 M $HClO_4$ aqueous solution: $E_{Ag/AgCl}$ =-0.6 V; t_{dop} =750s.

As described in **Chapter 3** and **4**, the electron diffusion length, that provides information about charge collection in photoanodes[11,17,30] has been determined here by combining IMVS and IMPS data via the Equation 3.26

$$L_n = D_n \tau_n{}^{1/2} \qquad (3.26)$$

It is known that pairs of τ_n and D_n used to obtain L_n must be determined at the same value of the quasi-Fermi level with respect to the conduction band. However, at the same light intensity the position of the quasi-Fermi level is different in IMVS measurements, which are executed at open-circuit, and in IMPS experiments, performed at short-circuit conditions. To estimate the shift, V_{sc} measurements were performed as described in the Chapter 4.[14] The profiles of V_{SC} and V_{OC} determined at different light intensities are represented in **Appendix** (Figure A-6.2). The shift of the quasi-Fermi level between open and short circuit conditions is obtained from the difference between both voltages. This procedure yields values of 0.18 and 0.26 V for undoped and doped electrodes, respectively. Taking into account this shift, L_n data are shown in **Figure 6.7C.**

The L_n estimates obtained from the IMPS/IMVS analysis reveal that electrochemical doping leads to a clear increase of the small-perturbation electron diffusion length. Values of L_n ≈100 μm are found for the undoped electrodes, which are increased by a factor of ≈2 for the doped electrodes. These values are similar to those of state-of-the art DSSC and suggest (see discussion below) that the collection efficiency approaches 100% at short-circuit, even for untreated electrodes.[11] The improvement in L_n is a consequence of the simultaneous blocking of recombination (R_{rec}) and the acceleration of transport (D_n). In this context, Meekins and Kamat[2] and Wang et al.[4] also explained the improvement in photocatalytic activity[2] and photovoltaic performance[4] by favoured electron transport in electrodes. The better transport properties were attributed to the creation of localized Ti^{3+} states and concomitant insertion of either protons or lithium ions. The present results show that a similar effect might be taking place for the doped PI-KEM electrodes. However, in addition, a reduced recombination rate is observed, possibly due to the formation of a depletion layer. Hence, the improvement detected in the electron diffusion length is based on a double beneficial effect.

The fact that $L_n >> d$ for both doped and undoped electrodes, leads to the conclusion that the photocurrent increase would not be due to improved electron collection, which is already quantitative for the undoped electrodes. However, it has to be born in mind that L_n is a magnitude which is measured from a small-perturbation of a flat Fermi level. This a different situation to that occurring at short-circuit, where a gradient of the electron density drives electrons towards the external circuit.[31] To clarify this point we have performed a simple experiment following the method of Halme et al.[32] The IV curves of devices based on undoped and doped electrodes, respectively, were measured under illumination through the counter-electrode (back) and the resulting J_{sc} value was compared to the one obtained from illumination through the working electrode (front) (**Appendix**, Figure A-6.3). The ratio J_{sc}(front)/J_{sc}(back) gives information on the electron collection efficiency at short circuit. These experiments yielded a very similar ratio for both the undoped and doped electrodes (1.37 and 1.41), suggesting that improved collection in not the main contribution to the photocurrent enhancement of the solar cell after electrochemical doping. In fact, the measured ratio is very similar to that found by Halme et al.[32] when comparing "front" and "back" IPCEs for solar cells with long diffusion lengths. This finding supports the conclusion derived from the small-perturbation analysis that electron collection efficiency approaches 100% in both the doped and undoped solar cells.

The observation that electron collection is not the reason for the enhancement performance at short-circuit points to either light harvesting or electron injection as two only possible explanations for the obtained results. To provide extra information in this respect, measurements of reflectance spectrum of the sensitized PI-KEM electrodes, with and without doping were performed (**Appendix**, Figure A-6.4). The results show that the doping process does not modify the optical properties. Hence, light harvesting is not either the origin of the enhancement in the short-circuit photocurrent. This fact, together with the observation that electron collection is very similar for both kinds of electrode, points to enhanced injection as the most likely reason why electrochemical doping increases the short-circuit photocurrent.

However, the beneficial effect of improved electron collection upon electrochemical doping is clearly observed if an electrolyte with a more pronounced recombination character is used. In **Figure 6.8** current-voltage characteristics for DSSC test devices with the alternative electrolytes B and C are presented. DSSCs constructed with ionic-liquid electrolytes, although leading to more stable devices, are characterized by smaller lifetimes and lower photovoltages.[15,33,34] For both kinds of electrolytes an improvement of the entire current-voltage curve and a reduction of the recombination rate, in line with the results reported above, is observed. The effect of the electrochemical doping can even change the shape of the EIS spectrum from a Gerischer-type impedance (characteristic of cells with small collection efficiencies: $L_n << d$)[13] to the typical shape of high-efficiency DSSCs ($L_n >> d$)[21] A similar effect has been observed recently by Liu et al.[35] when a DSSC with cobalt-based electrolyte was compared to the standard I^-/I_3^- electrolyte. Importantly, the present results show that electrochemical doping (and concomitant proton insertion) can improve substantially the collection efficiency of DSSCs based on novel electrolytes with strong recombination character.

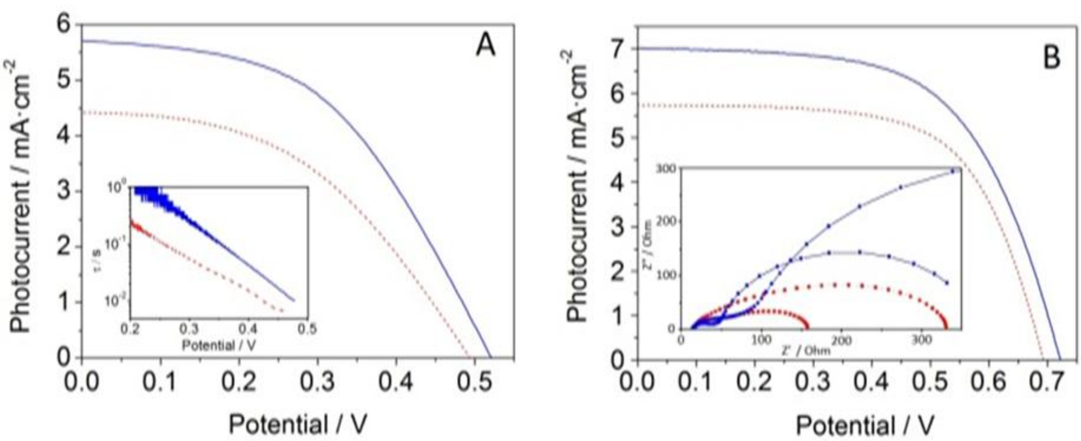

Figure 6.8: (A) Current-voltage characteristics under 1-sun AM 1.5 solar illumination of DSSC test devices (electrolyte B) based on doped (solid blue line) and undoped (dashed red line) PI-KEM electrodes. The inset shows the electron lifetime obtained from OCVD. (B) As above, but using electrolyte C. The inset shows impedance spectra obtained at 675 mV (line and squares) and 615 mV (line and circles) in the dark. Electrochemical doping in 0.1 M $HClO_4$ aqueous solution: $E_{Ag/AgCl}$ = -0.6 V; t_{dop} = 750 s.

3.4. Persistence of the doping effects.

As mentioned above electrochemical doping comprises electron accumulation (accompanied by proton insertion) in PI-KEM TiO_2 electrodes, which persist on a time scale of hours to days. As a consequence, the modified electrodes exhibit improved photoelectrocatalytic activity and better photovoltaic properties in DSSC test devices. The reversibility of the beneficial doping effect, which has been tracked in the photocatalytic experiments by the decrease of the photocurrent, can also be observed in the photovoltaic application of the doped PI-KEM electrodes. The current-voltage characteristics of DSSC devices based on doped and undoped electrodes are presented in **Figure 6.9** and **Appendix** (Table A-6.1). The Figure 6.9 contains, furthermore, the IV-characteristics of a DSSC based on a doped electrode, which was stored prior to cell assembly for 24 h at open circuit in the aqueous electrolyte. It is observed that the beneficial effect of doping is partially lost after the prolonged storage. The main degradation is detected in the photocurrent, whereas the photovoltage tends to remain at the characteristic value of the doped electrodes. It is reasonable to think that the stored charge and the inserted protons tend to diffuse out of the nanostructured electrodes at prolonged storage times. The reversibility of the beneficial effect may put into question the relevance of electrochemical doping for the improvement of DSSC devices. However, it has to be kept in mind that Wang et al.[4] recently demonstrated the analogy of (visible) light-induced and (cathodic) potential-induced improvement of the DSSC performance. As in the present case, authors attributed the beneficial effect to the intercalation of surface-adsorbed protons into the TiO_2 lattice. This point has also been further demonstrated in the previous chapter in the context of photocatalytic performance. Hence, "in situ" doping of the TiO_2 electrode might occur during the operation of the DSSC, thus, eliminating the need for applying an external potential to reach the desired performance increase.

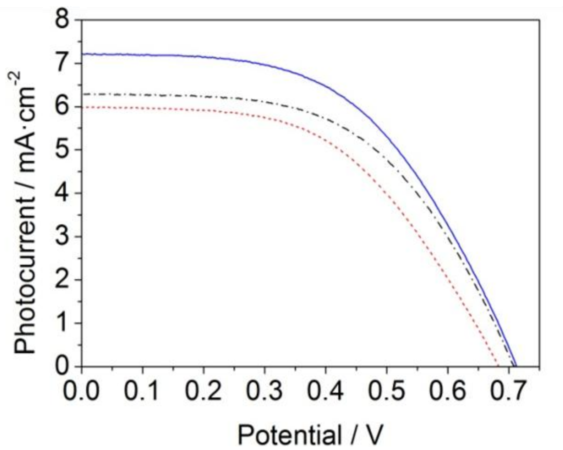

Figure 6.9: Current-voltage characteristics under 1-sun AM 1.5 solar illumination of DSSC test devices (electrolyte A) based on doped (solid blue line) and undoped (dotted red line) PI-KEM electrodes. The dashed-dotted black line represents the IV-characteristics of a DSSC based on a doped electrode, which was stored prior to cell assembly for 24 h at open circuit in the aqueous electrolyte. Electrochemical doping in 0.1 M $HClO_4$ aqueous solution: $E_{Ag/AgCl}$ = -0.6 V; t_{dop} = 750 s.

4. Conclusions.

We have studied the effect of a cathodic treatment in an acidic aqueous electrolyte on the performance of nanocrystalline TiO_2 electrodes in a photoelectrocatalytic process (water photooxidation) and in a photovoltaic application (dye-sensitized solar cell). The results demonstrate that the electrochemical doping, i.e. the persistent electron accumulation (accompanied by proton intercalation) in nanocrystalline TiO_2 electrodes, which depends critically of the crystalline properties of the semiconductor nanoparticles, improves the photoelectrocatalytic and photovoltaic properties. The improvement can be attributed to accelerated transport together with reduced recombination, as well as improved electron injection in DSSC. All these contributions lead thus to higher photocatalytic yields and a more efficient solar cell performance, respectively, in particular for those configurations characterized by larger recombination losses.

5. References.

(1) Berger, T.; Lana-Villarreal, T.; Monllor-Satoca, D.; Gomez, R. Charge Transfer Reductive Doping of Nanostructured TiO2 Thin Film's as a Way to Improve Their Photoelectrocatalytic Performance. *Electrochem. Commun.* **2006**, *8*, 1713–1718.

(2) Meekins, B. H.; Kamat, P. V. Got TiO2 Nanotubes? Lithium Ion Intercalation Can Boost Their Photoelectrochemical Performance. *ACS Nano* **2009**, *3*, 3437–3446.

(3) Fabregat-Santiago, F.; Barea, E. M.; Bisquert, J.; Mor, G. K.; Shankar, K.; Grimes, C. A. High Carrier Density and Capacitance in TiO2 Nanotube Arrays Induced by Electrochemical Doping. *J Am Chem Soc* **2008**, *130*, 11312–11316.

(4) Wang, Q.; Zhang, Z.; Zakeeruddin, S. M.; Gratzel, M. Enhancement of the Performance of Dye-Sensitized Solar Cell by Formation of Shallow Transport Levels under Visible Light Illumination. *J Phys Chem C* **2008**, *112*, 7084–7092.

(5) Gregg, B. A.; Chen, S.-G.; Ferrere, S. Enhanced Dye-Sensitized Photoconversion Efficiency via Reversible Production of UV-Induced Surface States in Nanoporous TiO2. *J Phys Chem B* **2003**, *107*, 3019–3029.

(6) Listorti, A.; Creager, C.; Sommeling, P.; Kroon, J.; Palomares, E.; Fornelli, A.; Breen, B.; Barnes, P. R. F.; Durrant, J. R.; Law, C.; et al. The Mechanism behind the Beneficial Effect of Light Soaking on Injection Efficiency and Photocurrent in Dye Sensitized Solar Cells. *Energy Env. Sci* **2011**, *4*, 3494–3501.

(7) Berger, T.; Anta, J. A. IR–Spectrophotoelectrochemical Characterization of Mesoporous Semiconductor Films. *Anal Chem* **2012**, *84*, 3053–3057.

(8) Berger, T.; Anta, J. A.; Morales-Flórez, V. Electrons in the Band Gap: Spectroscopic Characterization of Anatase TiO2 Nanocrystal Electrodes under Fermi Level Control. *J. Phys. Chem. C* **2012**, *116*, 11444–11455.

(9) Zaban, A.; Greenshtein, M.; Bisquert, J. Determination of the Electron Lifetime in Nanocrystalline Dye Solar Cells by Open-Circuit Voltage Decay Measurements. *Chemphyschem* **2003**, *4*, 859–864.

(10) Halme, J. Linking Optical and Electrical Small Amplitude Perturbation Techniques for Dynamic Performance Characterization of Dye Solar Cells. *Phys. Chem. Chem. Phys.* **2011**, *13*.

(11) Peter, L. M. Characterization and Modeling of Dye-Sensitized Solar Cells. *J. Phys. Chem. C* **2007**, *111*, 6601–6612.

(12) Bisquert, J. Theory of the Impedance of Electron Diffusion and Recombination in a Thin Layer. *J. Phys. Chem. B* **2002**, *106*, 325–333.

(13) Fabregat-Santiago, F.; Bisquert, J.; Garcia-Belmonte, G.; Boschloo, G.; Hagfeldt, A. Influence of Electrolyte in Transport and Recombination in Dye-Sensitized Solar Cells Studied by Impedance Spectroscopy. *Sol. Energy Mater. Sol. Cells* **2005**, *87*, 117–131.

(14) Boschloo, G.; Hagfeldt, A. Activation Energy of Electron Transport in Dye-Sensitized TiO2 Solar Cells. *J. Phys. Chem. B* **2005**, *109*, 12093–12098.

(15) Guillén, E.; Peter, L. M.; Anta, J. A. Electron Transport and Recombination in ZnO-Based Dye-Sensitized Solar Cells. *J Phys Chem C* **2011**, *115*, 22622–22632.

(16) Lyon, L. A.; Hupp, J. T. Energetics of the Nanocrystalline Titanium Dioxide/Aqueous Solution Interface: Approximate Conduction Band Edge Variations between H0 = −10 and H- = +26. *J Phys Chem B* **1999**, *103*, 4623–4628.

(17) Gonzalez-Vazquez, J.; Anta, J. A.; Bisquert, J. Determination of the Electron Diffusion Length in Dye-Sensitized Solar Cells by Random Walk Simulation: Compensation Effects and Voltage Dependence. *J. Phys. Chem. C* **2010**, *114*, 8552–8558.

(18) Navas, J.; Guillén, E.; Alcántara, R.; Fernández-Lorenzo, C.; Martín-Calleja, J.; Oskam, G.; Idígoras, J.; Berger, T.; Anta, J. A. Direct Estimation of the Electron Diffusion Length in Dye-Sensitized Solar Cells. *J. Phys. Chem. Lett.* **2011**, *0*, 1045–1050.

(19) Ansari-Rad, M.; Abdi, Y.; Arzi, E. Reaction Order and Ideality Factor in Dye-Sensitized Nanocrystalline Solar Cells: A Theoretical Investigation. *J Phys Chem C* **2012**, *116*, 10867–10872.

(20) Bisquert, J.; Zaban, A.; Greenshtein, M.; Mora-Sero, I. Determination of Rate Constants for Charge Transfer and the Distribution of Semiconductor and Electrolyte Electronic Energy Levels in Dye-Sensitized Solar Cells by Open-Circuit Photovoltage Decay Method. *J. Am. Chem. Soc.* **2004**, *126*, 13550–13559.

(21) Cameron, P. J.; Peter, L. M.; Hore, S. How Important Is the Back Reaction of Electrons via the Substrate in Dye-Sensitized Nanocrystalline Solar Cells? *J. Phys. Chem. B* **2005**, *109*, 930–936.

(22) Jennings, J. R.; Liu, Y.; Wang, Q. Efficiency Limitations in Dye-Sensitized Solar Cells Caused by Inefficient Sensitizer Regeneration. *J Phys Chem C* **2011**, *115*, 15109–15120.

(23) Dloczik, L.; Ileperuma, O.; Lauermann, I.; Peter, L. M.; Ponomarev, E. A.; Redmond, G.; Shaw, N. J.; Uhlendorf, I. Dynamic Response of Dye-Sensitized Nanocrystalline Solar Cells: Characterization by Intensity-Modulated Photocurrent Spectroscopy. *J. Phys. Chem. B* **1997**, *101*, 10281–10289.

(24) Lagemaat, J. van de; Frank, A. J. Effect of the Surface-State Distribution on Electron Transport in Dye-Sensitized TiO2 Solar Cells: Nonlinear Electron-Transport Kinetics. *J. Phys. Chem. B* **2000**, *104*, 4292–4294.

(25) Nakade, S.; Kanzaki, T.; Wada, Y.; Yanagida, S. Stepped Light-Induced Transient Measurements of Photocurrent and Voltage in Dye-Sensitized Solar Cells: Application for Highly Viscous Electrolyte Systems. *Langmuir* **2005**, *21*, 10803–10807.

(26) Peter, L. M.; Wijayantha, K. G. U. Electron Transport and Back Reaction in Dye Sensitised Nanocrystalline Photovoltaic Cells. *Electrochimica Acta* **2000**, *45*, 4543–4551.

(27) Wang, Q.; Ito, S.; Gratzel, M.; Fabregat-Santiago, F.; Mora-Sero, I.; Bisquert, J.; Bessho, T.; Imai, H. Characteristics of High Efficiency Dye-Sensitized Solar Cells. *J. Phys. Chem. B* **2006**, *110*, 25210–25221.

(28) Bisquert, J. Chemical Diffusion Coefficient of Electrons in Nanostructured Semiconductor Electrodes and Dye-Sensitized Solar Cells. *J. Phys. Chem. B* **2004**, *108*, 2323–2332.

(29) Anta, J. A.; Mora-Sero, I.; Dittrich, T.; Bisquert, J. Interpretation of Diffusion Coefficients in Nanostructured Materials from Random Walk Numerical Simulation. *Phys. Chem. Chem. Phys.* **2008**, *10*, 4478–4485.

(30) Bisquert, J.; Mora-Seró, I. Simulation of Steady-State Characteristics of Dye-Sensitized Solar Cells and the Interpretation of the Diffusion Length. *J. Phys. Chem. Lett.* **2010**, *1*, 450–456.

(31) Anta, J. A.; Idígoras, J.; Guillén, E.; Villanueva-Cab, J.; Mandujano-Ramírez, H. J.; Oskam, G.; Pellejà, L.; Palomares, E. A Continuity Equation for the Simulation of the Current–voltage Curve and the Time-Dependent Properties of Dye-Sensitized Solar Cells. *Phys. Chem. Chem. Phys.* **2012**, *14*, 10285–10299.

(32) Halme, J.; Boschloo, G.; Hagfeldt, A.; Lund, P. Spectral Characteristics of Light Harvesting, Electron Injection, and Steady-State Charge Collection in Pressed TiO2 Dye Solar Cells. *J. Phys. Chem. C* **2008**, *112*, 5623–5637.

(33) Fabregat-Santiago, F.; Bisquert, J.; Palomares, E.; Otero, L.; Kuang, D. B.; Zakeeruddin, S. M.; Gratzel, M. Correlation between Photovoltaic Performance and Impedance Spectroscopy of Dye-Sensitized Solar Cells Based on Ionic Liquids. *J. Phys. Chem. C* **2007**, *111*, 6550–6560.

(34) Guillén, E.; Fernández-Lorenzo, C.; Alcántara, R.; Martín-Calleja, J.; Anta, J. A. Solvent-Free ZnO Dye-Sensitised Solar Cells. *Sol. Energy Mater. Sol. Cells* **2009**, *93*, 1846–1852.

(35) Liu, Y.; Jennings, J. R.; Huang, Y.; Wang, Q.; Zakeeruddin, S. M.; Grätzel, M. Cobalt Redox Mediators for Ruthenium-Based Dye-Sensitized Solar Cells: A Combined Impedance Spectroscopy and Near-IR Transmittance Study. *J Phys Chem C* **2011**, *115*, 18847–18855.

Chapter 7:

The influence of the chemical environment of the redox pair on the recombination loss in Dye-Sensitized Solar Cells

1. Introduction.

Dye-sensitized solar cells (DSSC)[1,2] have lately received a renewed boost of attention[3] due to new efficiency records based on novel dye-electrolyte combinations[4] and on the use of inorganic sensitizers.[5–7] Recent advances in performance, durability and cost based on a better management of light trapping[8,9] and light absorption[10], and on the use of more stable electrolytes[6] have also contributed to the advancement of the field. In this context, a key factor to make substantial progress in DSSC research is the minimization of recombination losses.

Even if it is assumed that electron collection is quantitative at short-circuit conditions,[11–13] recombination losses affect DSSC performance in two ways. On the one hand, for a given position of the redox couple reduction potential, they control the maximum photovoltage attainable at 1 *sun* at open-circuit conditions. For instance, it has been established that a 10-fold decrease in the recombination rate will produce an increase of the open-circuit photovoltage of up to 60 mV.[12] On the other hand, recombination influences the fill factor of the solar cell via a non-ideality factor (**Chapter 3**).[14,15] Assuming that the series resistance of the device is minimized, the non-ideality factor will still limit the maximum efficiency that can be obtained. For instance, for typical values of the ideality factor of 1.5 and an open-circuit photovoltage of 700mV, a maximum value of the fill factor of 77% is estimated.[14]

Recombination losses are known to be important in novel electrolytes that offer advantages in terms of stability (room temperature ionic liquids,[16,17] solid-state hole conductors[18]) or with a more positive redox potential that can improve the open-circuit photovoltage.[19] The recombination drawback requires engineering the oxide/sensitizer/hole-conductor interface to minimize the loss.[3,4,20–22] This is commonly accomplished either by using different dyes or by passivating the semiconductor surface. However, no clear interpretation is available in the literature about the reasons why recombination is more rapid in these systems. In this scenario, two issues become relevant: (1) to quantify properly the recombination rate (separating thermodynamic and kinetic factors) and (2) to gain a deeper insight into the molecular mechanisms that control recombination.

The extent of recombination losses can be quantified via the electron lifetime[23]. As described in **Chapter 3**, the recombination in DSSC is a highly non-linear electrochemical reaction ($\beta < 1$). Thus, the safest way to define an electron lifetime is by means of a *small-perturbation lifetime.*[23] As indicated in **Chapter 4**, this magnitude can be obtained experimentally by means of Electrochemical Impedance Spectroscopy (EIS),[24] Intensity Modulated Photovoltage Spectroscopy (IMVS),[25] open-circuit voltage decay (OCVD)[26] and small perturbation voltage decays.[27]

As discussed in Chapter 3, the most accepted view of electron transfer across the oxide/electrolyte interface suggests that recombination rate is determined by **Equation 3.13**[23,28]

$$U_n = d \int_{E_{redox}}^{E_c} g(E) f(E - E_F) P_R(E) dE \qquad (3.13)$$

where the term $P_R(E)$ can formally be described by the Marcus-Gerischer model[29,30] for one-electron outer sphere redox couples. In this description, this term, is related to the reorganization energy (λ) among other factors (see **Equation 3.14**). Although, spectroscopic studies suggest that it is tri-iodide[31] the real electron acceptor, in any case the recombination reaction necessarily implies the existence of a first step of electron transfer to a species in the electrolyte with an associated reorganization energy. As the electrochemistry of the standard iodide/tri-iodide redox couple is quite complex,[32] Ondersma and Hamann[33] solved the problem posed by Equation 3.13 for single-electron outer-sphere redox couples. By explicit consideration of trap distributions and reorganization energies, they obtained the theoretical behaviour of the electron lifetime with respect to voltage in an OCVD experiment. They found that this behaviour is quite different depending on the value of the reorganization energy, including the appearance of a parabolic shape of the electron lifetime when the reorganization energy is relatively small. In addition, evidence of recombination via surface states was found.

In a recent work,[34] Random Walk Numerical Simulation (RWNS) with explicit consideration of electron recombination based on the Marcus-Gerischer model was applied to study recombination in DSSC on a molecular basis.[30,35] By considering simultaneously transport and charge transfer mediated by a broad distribution of donor and acceptor states, it is possible to obtain the electron lifetime and the electron diffusion length for specific positions of the electron Fermi level in the semiconductor (controllable by illumination or by an externally applied potential), the redox couple potential and the reorganization energy. It was concluded that the value of λ is especially critical to establish the voltage dependence of the electron lifetime and the electron diffusion length. Furthermore, it was observed that both recombination processes from trapped electrons and from *quasi-free* electrons ("recombination from conduction band")[11] is required to explain the complete phenomenology in DSSC based on standard iodide/tri-iodide redox couples. This phenomenology includes the non-linear features observed, for instance, by impedance spectroscopy[14,36] and the behaviour of the lifetime and diffusion length upon modification of the electrolyte composition.[37,38] In this respect, a value of $\lambda \approx 0.6$ eV was found to best describe the experiments for electrolytes containing the iodide/tri-iodide redox couple in organic solvents.

This chapter is motivated by the necessity of clarifying the role of the reorganization energy and to cast light on the reasons why certain electrolytes tend to originate larger recombination losses. The reorganization energy is a strong function of the chemical environment, as it depends on the interactions between charged species and the surroundings, composed of solvent and dye molecules. As most previous studies focused on a particular class of electrolyte, or just compared two types of electrolytes on non-optimized configurations, in this chapter we have considered that a more global perspective is required to draw *general* conclusions. Hence, the most widely used electrolyte combinations have been studied, all of them supported on the same semiconductor films and dyes, and using as a reference a state-of-the-art architecture. Although this chapter is focused on liquid electrolytes, most of the conclusions than can be drawn from the present study can be extended to solid-state electrolytes. Furthermore, the electron lifetime has been obtained by a variety of techniques, which helps to safely obtain its value and behaviour, as well as to conveniently separate out kinetic and thermodynamic effects (band shifts and position of the redox potential).

Most of the results presented in this chapter have been reported in the following publication: Idígoras et al. *J. Phys. Chem. C*, **2014**, 118 (8), pp 3878–3889.

2. Experimental section.

2.1. Fabrication of Dye-Sensitized Solar Cells.

For optimized cell efficiencies, devices were made using 13 μm thick films consisting of a layer of 9 μm of 20 nm TiO_2 nanoparticles (Dyesol© paste) and a layer of 4 μm of 400 nm TiO_2 particles (scattering layer).[39] Prior to the deposition of the TiO_2 paste the conducting glass substrates (Hartford Glass inc. with 15 Ω cm^{-2} resistance) were immersed in a solution of $TiCl_4$ (40 mM) for 30 minutes at 70°C and then dried. For some of the devices (all cobalt-based electrolytes and electrolytes E5 and E10), and to prevent recombination of electrons from the glass substrates with the oxidized species in the electrolyte a thin insulating layer (called a *blocking layer*) was placed between the mesoporous oxide and the substrate. This thin film was prepared by spin coating from the next dissolution: 20ml of H_2O MilliQ + 2.2ml of Titanium (IV) isopropoxide + 1.5ml of Acetylacetone. After deposition, the substrate was heated to 500° C. The TiO_2 nanoparticle paste was deposited onto a conducting glass substrate using the screen printing technique. The TiO_2 electrodes were gradually heated under an airflow at 325°C for 5 min, 375°C for 5 min, 450°C for 15 min and 500°C for 15 min. The heated TiO_2 electrodes were immersed again in a solution of $TiCl_4$ (40 mM) at 70°C for 30 min and then washed with water and ethanol. Finally, the electrodes were heated again at 500°C for 30 min and cooled before dye adsorption. The DSSC active area was 0.16 cm^2.

The counter-electrode was made by spreading a 10 mM solution of H_2PtCl_6 in ethanol onto a conducting glass substrate with a small hole to allow the introduction of the liquid electrolyte using vacuum, followed by heating at 390°C for 15 minutes.

The electrodes were immersed at 4 ºC overnight in a solution containing ruthenium dye coded **C101**[12] (NaRu (4,4′-bis(5-hexylthiophen-2-yl)-2,2′-bipyridine) (4-carboxylic acid-4′-carboxylate-2,2′-bipyridine) $(NCS)_2$). This solution was composed of 0.3mM C101 and 0.3mM chenodeoxycholic acid in ethanol. For DSSC with cobalt-based electrolytes amphiphilic polypyridyl ruthenium complex: cis-RuLL'(SCN) 2 (L =4,4'-dicarboxylic acid-2,2'-bipyridine,L' = 4,4'-dinonyl-2,2'-bipyridine) (**Z907**) was used as dye.[12] The sensitized electrodes were washed with ethanol and dried under air. Finally, the working and counter-electrodes were sandwiched together using a thin thermoplastic (Surlyn) frame that melts at 100°C. The cells were filled with the electrolyte through a hole previously made in the back of a platinized counter electrode. Then, the hole was sealed with a thermoplastic polymer and a cover-slide glass. A drop of silver conductive paint was spread at the electrode contacts to increase the conductivity.

The composition of the electrolytes studied in this chapter is shown in **Table 7.1**. To test the reproducibility of the results, two cells were fabricated for each composition. No significant deviations were found between these two cells in all cases.

Electrolyte	Solvent	Solute
E1	Acetonitrile	$0.03M\ I_2 + 0.5M$ LiI
E2	Valeronitrile	
E3	Ethylene Carbonate	
E4	Acetonitrile / Valeronitrile (85:15)	
E5	Acetonitrile / Valeronitrile (85:15)	$0.03M\ I_2 + 1M$ BMiI + 0.05M LiI + 0.5M Tbp + 0.1M GuSCN
E6		$0.03M\ I_2 + 1M$ BMiI
E7		$0.03M\ I_2 + 1M$ BMiI + 0.5M Tbp
E8		$0.03M\ I_2 + 1M$ BMiI + 0.05M LiI
E9	PMII	$0.03M\ I_2$
E10	PMII/EMIBCN (2:3)	
E11	Acetonitrile	$0.2M\ Co^{2+} + 0.02M\ Co^{3+}$
E12		$0.2M\ Co^{2+} + 0.02M\ Co^{3+}$ + 0.5M Tbp + 0.1M $LiClO_4$

Table 7.1: Composition of the liquid electrolytes studied in this work. (I_2: Iodine (99.5%, Fluka), LiI: Lithium iodide (99%, Aldrich), BMiI: 1-butyl-3-methylimidalozlium iodide (99%, Aldrich), PMiI: 1-methyl-3-propylimidazolium iodide (>98%, Iolitec), EMIBCN: 1-ethyl-3-methylimidazolium tetracianoborate (Merck), Tbp: 4-tert-butylpiridine (96%, Aldrich), GuSCN: Guanidine thiocyanate (Aldrich), $LiClO_4$: Lithium perchlorate (Aldrich), Co^{2+}/Co^{3+}: $[Co(bpy)_3](PF_6)_2$ / $[Co(bpy)_3](PF_6)_3$). Cobalt complexes where synthesized according to the procedure described in Ref[40].

2.2. Characterization of devices and determination of the electron lifetime.

The devices were characterized using a solar simulator with AM 1.5G filter (*ABET*). The light intensity was calibrated to the standard value of 1 sun (100 mW/cm^2) using a reference solar cell with temperature output (*Oriel, 91150*). The current-voltage characteristics were determined by applying an external potential bias to the cell and measuring the photocurrent using an Autolab/PGSTAT302N potentiostat. Open-circuit Voltage Decay measurements (OCVD)[26] were made by keeping the solar cell at open-circuit at 1-sun and registering the voltage transient after interrupting the illumination.

Electrochemical Impedance Spectroscopy (EIS), Intensity Modulated Photovoltage Spectroscopy (IMVS) and Open-circuit voltage decay was utilized to study recombination and extract electron lifetimes in the studied DSSC devices.[25] The illumination for the small perturbation (frequency response) techniques was provided by a 530 nm light emitting diode (*LUXEON*) over a wide range of DC light intensities. This allows for probing the devices at different positions of the Fermi level in the semiconductor. A response analyzer module (*PGSTAT302N/FRA2, AutoLab*) was utilized to analyze the frequency response of the devices. Most EIS measurements were performed at the open circuit potential, the Fermi level (related to the open-circuit voltage)[11] being fixed by the DC illumination intensity. By working at the open-circuit potential one avoids to correct for voltage drop due to series resistance. A 10 mV perturbation in the 10^5-10^{-2} Hz range was utilized to obtain the spectra. For some of the devices the EIS measurements were carried out at fixed illumination and the applied voltage was varied. In this case there is a voltage drop due to series resistance which was corrected for to obtain the lifetime versus the Fermi level within the semiconductor. Intensity Modulated Photovoltage Spectroscopy (IMVS) measurements were carried out by coupling the PGSTAT302N/FRA2 module to the light emitting diode, so that an AC signal can be generated. In all cases the samples were illuminated from the dye-coated TiO_2 electrode side. IMVS measurements were performed at open circuit in the 10^4-10^{-1} Hz range with a light perturbation corresponding to 10% of the dc background illumination intensity. The NOVA 1.7 software was used to generate and treat the IMVS data. Zview equivalent circuit modelling software (Scribner) was used to fit the EIS spectra, including the distributed element DX11 (transmission line model).[24,41]

3. Results.

3.1. Photovoltaic performance.

Photovoltaic parameters for the fabricated devices can be found in **Table 7.2**. Best performing electrolytes are based on organic solvents. The maximum efficiency was found for electrolyte E5, where an optimized electrolyte composition is employed.[39] This good efficiency is achieved by a proper combination of additives and solvents, which maximize open-circuit photovoltage and fill factor, without deteriorating significantly the photocurrent. For cells containing no additives (E1 to E4), the best performance was obtained for electrolyte E1 (pure acetonitrile). This is an expected result commonly attributed to the low viscosity of this solvent. Results for electrolytes E7 (with Tbp) and E8 (with LiI) illustrate the well-known band-shift effects[42,43] produced by these additives. The actual extension of the band-shift was determined and accounted for by EIS, as explained below.

Solar cells made of pure room temperature ionic liquid electrolytes and no additives (E9 and E10) yielded open-circuit photovoltages larger than those of their equivalents with organic solvents (electrolytes E1-E4). However, photocurrents for these cells fall well below those obtained for their organic solvent counterparts.

	J_{sc} /mA·cm^{-2}	V_{oc} /mV	FF / %	Efficiency / %	α	β
E1	20.5 ± 0.3	500 ± 4	51 ± 1	5.7 ± 0.2	0.29	0.53
E2	14.2 ± 1.5	478 ± 7	24 ± 1	1.5 ± 0.5	0.31	0.49
E3	14.7 ± 0.1	558 ± 1	45 ± 5	3.5 ± 0.6	0.25	0.65
E4	18.1	462 ± 6	53 ± 1	4.5	0.27	0.65
E5	18.9 ± 0.3	766 ± 1	66 ± 2	9.6 ± 0.1	0.18	0.79
E6	13.7 ± 0.4	731	68 ± 1	6.9 ± 0.3	0.27	0.70
E7	13.7 ± 0.2	787 ± 5	70 ± 1	7.5 ± 0.3	0.29	0.74
E8	17.2 ± 0.1	600 ± 8	65 ± 1	6.8 ± 0.1	0.24	0.63
E9	3.0 ± 0.2	657 ± 7	54 ± 1	1.1	0.27	0.63
E10	5.7 ± 0.4	657 ± 3	64 ± 3	2.4 ± 0.1	0.29	0.56
E11	1.8 ± 0.2	645 ± 1	58 ± 2	0.7	- - - -	- - - -
E12	11.1 ± 0.1	777	64 ± 1	5.6 ± 0.1	0.24	0.71

Table 7.2: Photovoltaic and impedance spectroscopy parameters for the devices studied in this chapter. Results shown are based on the average of two samples for the same electrolyte.

Finally, DSSC based on the Co(II)/Co(III) redox couple (electrolytes E11 and E12) showed in general large open-circuit photovoltages, due to the more positive redox potential of the Co(II)/Co(III) system. When the proper additives are utilized,[40] the photocurrent becomes greatly enhanced, although it remained below the values obtained for the optimized cells with the I_3^-/I^- redox couple.

3.2. Extraction and interpretation of the electron lifetime.

Typical open-circuit voltage decays and impedance spectra at the OC photovoltage can be found in **Figure 7.1** for electrolytes E5, E10 and E12. The OCVD data provide a simple and ready means of probing the recombination process, but care should be taken to avoid naïve interpretations based on how fast the voltage drops. A proper interpretation of OCVD data involves the extraction of the lifetime via **Equations 3.25** and **4.3**, which is actually related to the time derivative of the voltage decay. In this connection, the two different shapes observed in the decays, with a clear shoulder feature for cells with I_3^-/I^- in organic solvents, indicate a quite different behaviour of the lifetime. The origin of this feature is discussed below.

The EIS spectra show the characteristic three semicircles typically observed in DSSC,[24] one at high frequencies accounting for charge transfer at the platinum counter-electrode, and another one at mid frequencies arising from electronic processes at the oxide/electrolyte interface. Additionally, a third semicircle at low frequencies appears for the most viscous electrolytes. This is due to mass transport limitations in the electrolyte.[16,17]

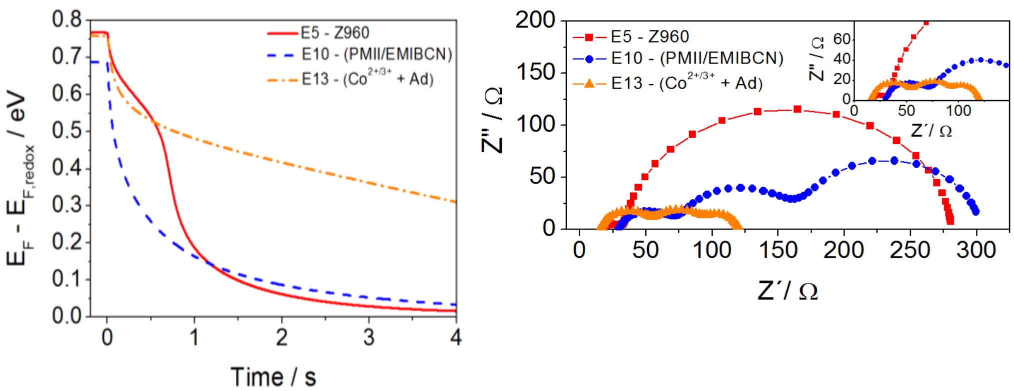

Figure 7.1: Methods to study recombination in DSSC used in this chapter: (left) Open-circuit photovoltage decay and (right) Impedance spectra (Nyquist plots) obtained under illumination at the same approximate value of the electron density (i.e. V = 691 mV, 620 mV and 763 mV, for electrolytes E5, E10 and E12 respectively).

The EIS results can be well fitted to the diffusion-recombination model of Bisquert and co-workers described in Chapter 4.[24,41] As a general observation, resistance and capacitance data for the studied cells fit quite well to **Equations 1.24** and **3.11**, although small departures from the exponential law are detected for C_μ at larger voltages, as discussed recently.[22] Representative results for R_{rec} and C_μ are presented in **Figure 7.2A**. The values for α and β obtained from the fittings are collected in **Table 7.2**.

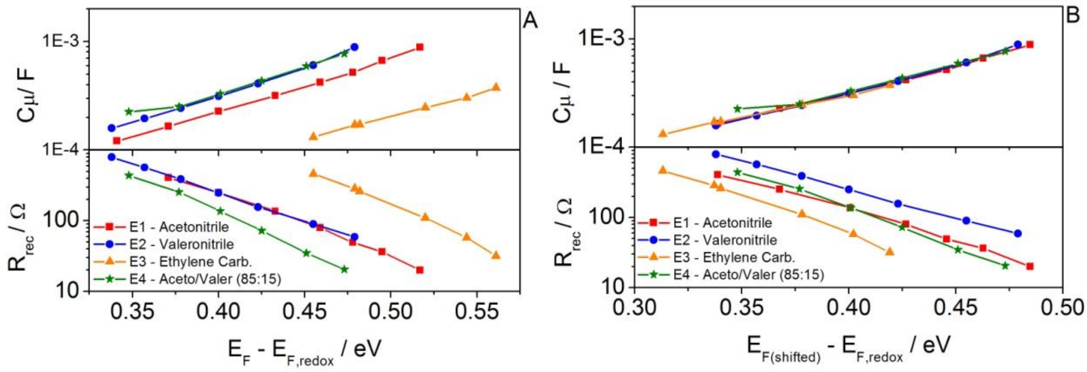

Figure 7.2: (A) Chemical capacitance and recombination resistance data as extracted from EIS measurements for electrolytes E1 to E4. (B) Same data but plotted after applying a shift on the Fermi level, so that all capacitance lines overlap.

In **Figure 7.3** a comparison of lifetimes extracted from OCVD and EIS is presented. In general, good agreement between both techniques, as well as with IMVS (see **Appendix**, Figure A-7.1) is accomplished for the studied electrolytes. This agreement is remarkable because one technique is a simple decay measurement whereas the others are based on the small-perturbation concept. Furthermore, it must be born in mind that OCVD is a dark technique, whereas the EIS/IMVS lifetimes are obtained under illumination, which may lead to small differences in some cases.[20] The lifetime is found to follow the exponential behaviour predicted by **Equation 4.18** except at low voltages. Since lifetimes at high voltages from EIS/IMVS and OCVD exhibit the same behaviour and very similar values for all electrolytes studied, only OCVD data are reported hereafter, unless otherwise stated.

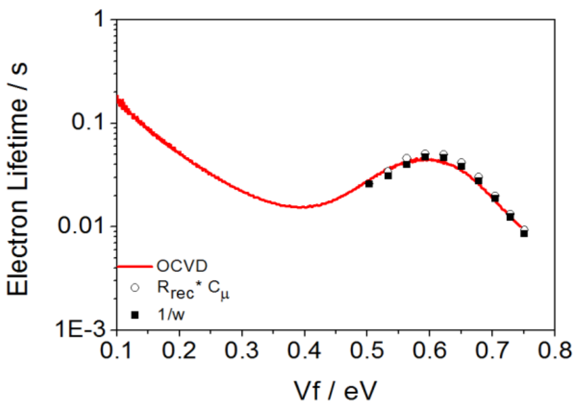

Figure 7.3: Electron lifetimes as extracted from OCVD (lines) and EIS (circles and squares) for electrolyte E5.

It is known that OCVD can be affected by charge transfer through the FTO/TiO_2 interface at low potentials.[44] This artefact is commonly prevented by depositing a blocking layer between the FTO and the TiO_2 film. To make sure that the departure from the exponential behaviour and the appearance of a minimum for some electrolytes is not due to this artefact cells with and without blocking layers have been compared. The results are presented in the **Appendix** (Figure A-7.2), where it is shown that cells with blocking layer do also exhibit the same behaviour as that observed in **7.3.**

The departure from the exponential behaviour and the appearance of a minimum in the lifetime-voltage curves is a consequence of a lowering of the number of available acceptor states ($P_R(E)$ in **Equation 3.13**) in a certain voltage range. If we assume a one-electron charge transfer from TiO_2 to electron acceptors in the electrolyte, the observed behaviour can be qualitatively described by the Marcus-Gerischer formula (see Chapter 3),

$$P_R(E) = k_r exp\left[-\frac{(E - E_{redox} - \lambda)^2}{4\lambda k_B T}\right] \tag{3.14}$$

where λ is the reorganization energy and E_{redox} is the redox potential of the redox couple. Besides, k_r is a prefactor that depends on the concentration of oxidized species in the electrolyte, the temperature and the reorganization energy.

Equation 3.14 predicts a parabolic shape for the density of acceptor states. Hence, as shown below and discussed in Refs. 33 and 45, the minimum in the lifetime-voltage curve provides a rough estimate of the reorganization energy λ. However, it is important to note that if the contribution of recombination from a distribution of surface states is important, the minimum is expected to depart widely from λ, or even might not appear. In this connection RWNS calculations of the transport-recombination process, taking into account the Marcus-Gerischer formula, and including explicit recombination from surface states and nearly-free electrons, show indeed a departure from the exponential behaviour when the reorganization energy has a relatively small value.[34] In contrast, if λ is very large with respect to the photovoltage (difference between Fermi levels in the oxide and in the electrolyte) a pure exponential behaviour for the lifetime, as described by **Equation 4.18**, can be predicted[23,28] and confirmed by simulation.[34] In the following, a wide variety of behaviours are found for the electrolytes studied in this chapter, which are attributed to different values of the reorganization energy.

It is important to clarify that iodide/tri-iodide is not a one-electron redox-couple. Furthermore, the nature of the electron acceptor has not been definitely assessed although there are indications that it is tri-iodide.[31] Therefore, the direct application of the standard Marcus formalism for this redox mediator is arguable. However, the observed behaviour of the lifetime in this case strongly suggests that there is a contribution from the reorganization energy of the acting electron acceptor that depends on the chemical environment surrounding the acceptors.

To ensure an adequate comparison of the lifetimes obtained for each electrolyte, it is necessary to take into account band shifts produced by the additives and by the solvent itself.[42,43,46,47] The driving force for electron transfer depends on the free energy difference between initial and final states but the lifetime does also depend, for a fixed driving force, on the population of donor states as considered in **Equation 3.13**. Hence, it is necessary to separate out this effect so that the lifetimes are compared at the same value of the total electron density stored in the semiconductor oxide. In this chapter this correction has been applied by looking at the shift of the capacitance lines detected in the EIS measurements. This shift is due to the different positions of the conduction band edge in **Equation 1.24** with respect to the redox potential. By shifting the potential by an amount such as all capacitance lines overlap (see **Figure 7.2B** and **Appendix** (Figure A-7.3)), one makes sure that the lifetime is plotted versus the same position of the Fermi level with respect to the conduction band edge, which corresponds to the same value of the total electron density. More details of this procedure can be found in Refs. 46 and 48. In this regard it is important to bear in mind that the α parameter is roughly independent of the electrolyte composition, as observed in **Table 7.2**. This fact makes it possible that the capacitance lines overlap when shifted, and confirms that the distribution of donor states is exponential and an inherent property of the semiconductor oxide. It has to be mentioned that if the α parameter were not constant, still this correction can be implemented. In that case it would be necessary to extract the accumulated negative charge in the semiconductor for each voltage. This would make it possible to compare the lifetime at the same value of the electron density.

With the capacitance correction one also can account for the different positions of the redox potential in the electrolyte (as it happens when comparing iodide/tri-iodide and Co(II)/Co(III) redox couples, see below). Hence, in the following, the lifetimes are plotted versus the *shifted* values of the Fermi level. In this regard, the capacitance and band position of electrolytes E2 and E4 (which are quite similar) has been used as a common reference for the rest of the electrolytes.

3.3. Dye-Sensitized Solar Cells based on organic solvent electrolytes.

In **Figure 7.4A** and **Figure 7.4B** IV curves and electron lifetimes for electrolytes E1, E2, E3 and E4 are reported. DSSCs with acetonitrile and ethylene carbonate make good performing devices even in the absence of additives. Ethylene carbonate is found to produce a negative band-shift (**Figure 7.2A**) which leads to a decrease of the photocurrent and an increase of the photovoltage. In contrast, all cells made with nitrile solvents show a very similar value of the capacitance. The use of valeronitrile as only solvent results in cells with very low fill factors. However, the popular blend acetonitrile/valeronitrile (85:15) increases substantially the performance, approaching the values obtained for pure acetonitrile.

The lifetime-voltage curves, when corrected for band-shifts, indicate that valeronitrile is the most efficient solvent to block recombination, as the longest lifetimes (corresponding to the largest recombination resistances) are obtained for this solvent. This explains why its right mixture with acetonitrile, a less viscous solvent, makes it possible to maximize efficiency. Ethylene carbonate, in spite of the negative band-shift and larger V_{oc} that induces in the cell, produces an acceleration of the recombination rate, i.e., a shortening of the lifetime.

Cells based on electrolytes E1 to E4 exhibit non-exponential behaviour and occurrence of a minimum in the lifetime-voltage curve. According to the analysis described above, this finding suggests that the I_3^-/I^- redox couple behaves as an electrochemical system characterized by a relatively small reorganization energy. A more detailed discussion of the effect of the reorganization energy is provided below.

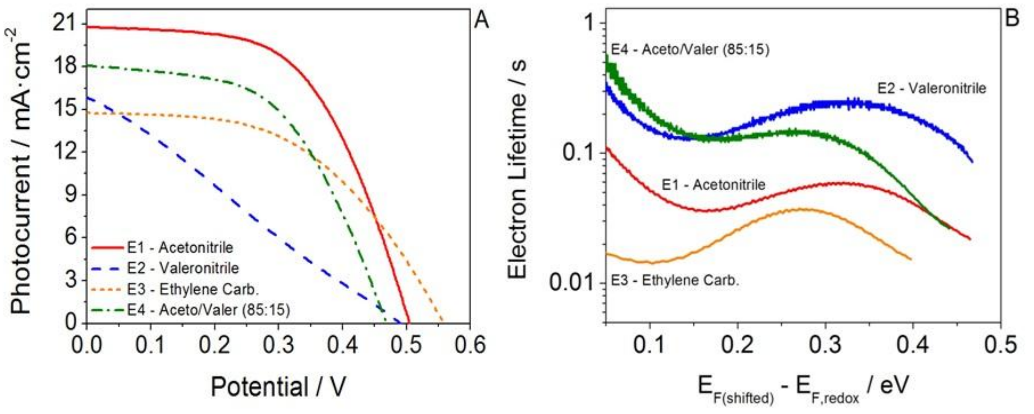

Figure 7.4: (A) Current-voltage curves under 1-sun AM1.5 illumination and (B) electron lifetimes extracted from OCVD for electrolytes E1, E2, E3 and E4. Fermi level values in the x-axis have been shifted as explained in Section 3.2.

In **Figure 7.5A** and **Figure 7.5B** IV curves and electron lifetimes for electrolytes E5, E6, E7 and E8 are reported. As mentioned above, E5 electrolyte corresponds to a state-of-the art composition which leads to an efficiency of 9.5% under AM1.5 illumination (1 *sun*). In the **Appendix** (Figure A-7.3) EIS parameters for the electrolytes E5, E6, E7 and E8 are shown. Lifetimes for the same electrolytes, as extracted from the three techniques (OCVD, EIS and IMVS) can also be found in the **Appendix** (Figure A-7.1).

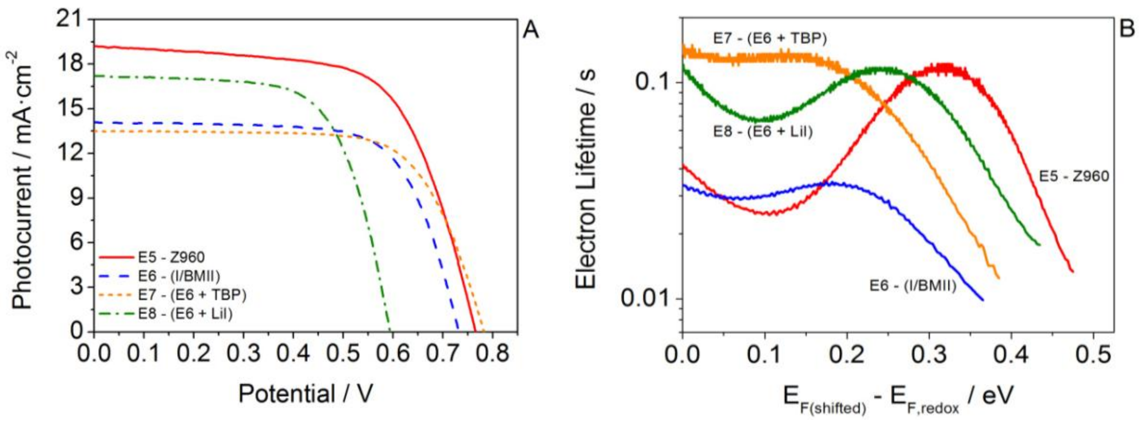

Figure 7.5: (A) Current-voltage curves under 1-sun AM1.5 illumination and (B) electron lifetimes extracted from OCVD for electrolytes E5, E6, E7 and E8. Fermi level values in the x-axis have been shifted as explained in Section 3.2.

Tbp and LiI are found to produce well-known effects in photovoltage and photocurrent. These are a consequence of negative and positive band-shifts in the semiconductor oxide band edge, produced by Tbp and LiI, respectively.[47] The ionic liquid BMII also produces a negative shift, which suggests that imidazolium cations can adsorb selectively into the TiO_2 surface,[49] in analogy to Tbp.

As the effect of most of the studied additives is to produce a band displacement, no changes in the reorganization energy are expected. This conclusion is confirmed in the corrected lifetime-voltage plots (**Figure 7.5B**), where the minima appear at approximately the same position. However, electrolyte E7, where the effects of Tbp and BMII are mixed together, exhibits a flat behaviour at low voltages, although a slight minimum can be detected at the same position as the rest of the electrolytes. The corrected lifetimes show that the E5 composition is especially effective in blocking recombination, with the longest lifetimes observed at V_{oc}. This result highlights the decisive role of additives such as GuSCN in the performance of DSSC.

3.4. Dye-Sensitized Solar Cells based on pure ionic-liquid electrolytes.

In **Figure 7.6A** and **Figure 7.6B** IV curves and electron lifetimes for DSSC based on room temperature ionic-liquid electrolytes (electrolytes E9 and E10) are presented. Recombination resistances and capacitances for the same electrolytes can be found in the **Appendix** (Figure A-7.3). In cell E9 a simple electrolyte made of a pure imidazolium iodide (PMII) plus iodine is studied. In cell E10 PMII is diluted by adding a less viscous ionic-liquid (EMIBCN).

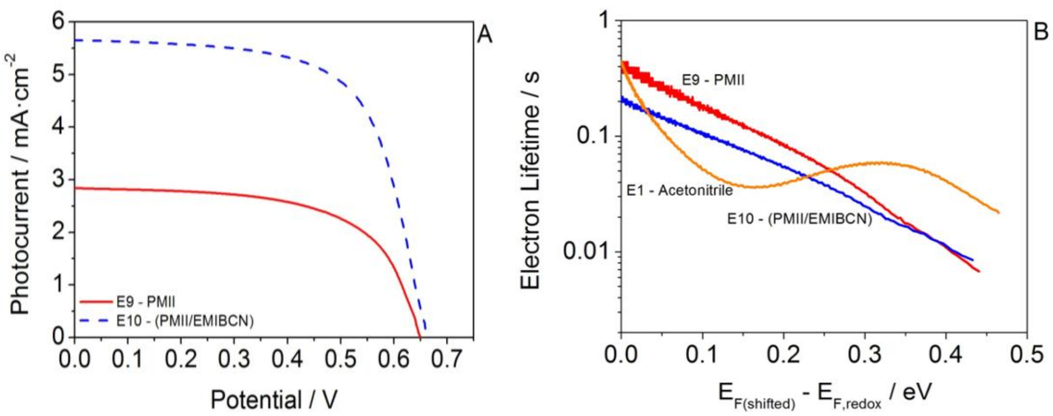

Figure 7.6: (A) Current-voltage curves under 1-sun AM1.5 illumination and (B) electron lifetimes extracted from OCVD for electrolytes E1, E9 and E10. Fermi level values in the x-axis have been shifted as explained in Section 3.2.

DSSC based on pure ionic-liquid electrolytes show photovoltages that lie close to those obtained for the best cells made of organic solvent electrolytes. This effect can be interpreted as a favourable band position due to the interaction of imidazolium cations and the oxide surface, as discussed above. However, the photocurrents are relatively small. This is due to a mass transport limitation that also affects the kinetics of the dye regeneration process, as indicated by several authors previously.[16,17,50] In line with this interpretation, the addition of a less viscous ionic liquid leads to a straight increment in the photocurrent, without a substantial modification of the photovoltage.

A remarkable feature of solvent-free DSSC is that the lifetime-voltage plots do not show any minimum. This observation strongly suggests that the I_3^-/I^- redox couple has a large reorganization energy in an ionic liquid medium. Previous studies for room temperature ionic liquids[51] have shown that the Marcus picture of charge-transfer reaction holds also for an ionic liquid and that the reorganization energy is similar to that of aqueous electrolytes. In this respect, preliminary results with the I_3^-/I^- redox couple and water as solvent do show the same behaviour of the lifetime (exponential, with no minimum), as it corresponds to a polar solvent.

3.5. Dye-Sensitized Solar Cells based on the Co(II)/Co(III) redox pair.

In **Figure 7.7A** and **Figure 7.7B** IV curves and electron lifetimes for electrolytes E1, E11 and E12 are presented. Recombination resistances and capacitances for the same electrolytes can be found in the **Appendix** (Figure A-7.3).

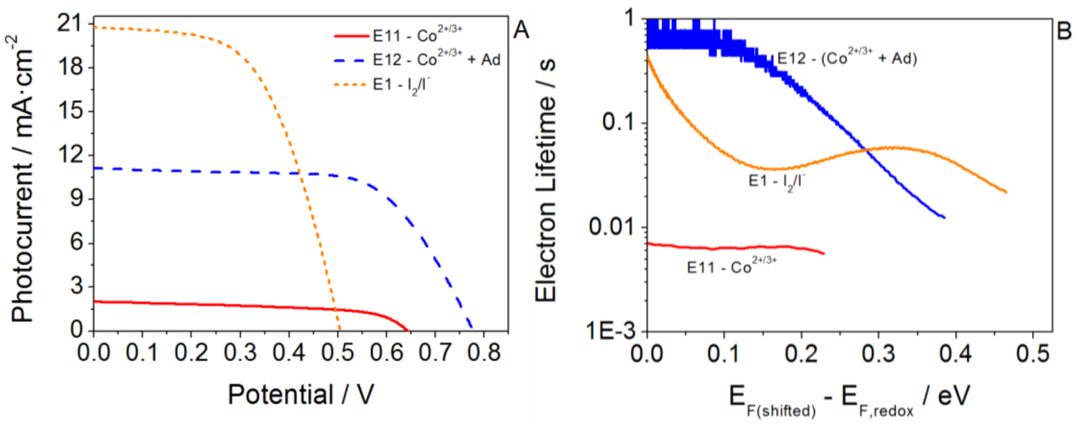

Figure 7.7: (A) Current-voltage curves under 1-sun AM1.5 illumination and (B) electron lifetimes extracted from OCVD for electrolytes E1, E11 and E12. Fermi level values in the x-axis have been shifted as explained in Section 3.2.

The Co(II)/Co(III) couple has a more positive redox potential than the I_3^-/I^- couple as can be observed in the capacitance data (**Appendix**, Figure A-7.3), where a positive shift of around 0.35 eV can be detected, in line with previous reports.[40] As a consequence, DSSC made with the Co(II)/Co(III) redox couple exhibit larger open-circuit photovoltages at 1 *sun* illumination. The more positive redox potential causes also a decrease in the photocurrent, which can be attributed to the lower driving force for dye regeneration.[52]

Once corrected for the different E_c-E_{redox} alignment in the Co(II)/Co(III) and I_3^-/I^- systems, the lifetime-voltage plots reveal, as explained, purely kinetics effects in the recombination reaction. Co(II)/Co(III) data do not show the minimum in the lifetime, which is an indication of the large reorganization energy acting in the redox system. As a matter of fact, a reorganization energy of 1.41 eV[33] has been estimated from electron transfer theory for redox mediators based on cobalt-complexes. Feldt et al.[53] also estimated a reorganization energy of 1.05 eV for cobalt-complexes by fitting to the Marcus equation dark current density data versus redox potential. These are larger values than the 1 *sun* photovoltage (≈0.7-0.8 eV), and hence a pure exponential behaviour is expected. In contrast, the I_3^-/I^- redox couple acts with a much lower reorganization energy.

The quite different values of the reorganization energy have an important side effect, as shown in the lifetimes in **Figure 7.7B**. Once corrected for the redox potential shifts, the cobalt-based electrolyte exhibits a more rapid recombination than that of the iodide/tri-iodide. For instance, this is clearly seen when electrolytes E1 and E11 are compared. Lifetimes for the E11 electrolyte lie more than one order of magnitude below those of the E1 electrolyte. When additives such as Tbp and $LiClO_4$ are present in the electrolyte, the recombination rate is clearly reduced (longer lifetime), but still is larger than for I_3^-/I^- (in the vicinity of open-circuit). This feature of the cobalt-based electrolytes is a well-known drawback which has to be dealt with by engineering the molecular structure of the dye.[4] In this chapter it is shown that this rapid recombination dynamics is related to the large value of the reorganization energy. A more detailed discussion is presented in the next section.

4. Discussion.

The results presented in the previous section show a rich phenomenology as regards electron recombination. As a general rule, once thermodynamic effects are separated out (i.e. band shifts in the oxide and different positions of the redox potential in the electrolyte), a correlation between larger reorganization energy and more rapid recombination is found.

In a previous work[34] a theoretical investigation of the recombination across the oxide/electrolyte interface was conducted. This work considered explicitly the distribution of intra-band electron traps, electron transport via a transport level (multiple-trapping model) and recombination with electron acceptors in the electrolyte governed by Marcus-Gerischer kinetics. A random walk numerical simulation technique (RWNS) was used to implement all these mechanisms simultaneously, so that both the electron lifetime and the electron diffusion length can be obtained. It was observed that two types of processes should be considered to explain the non-linear features of the recombination reaction (evidenced by a β-factor smaller than unity): (1) direct recombination from trap states and (2) recombination of quasi-free electrons from states close to the transport level. A schematic representation of these two processes and the role played by the donor states and the effect of the reorganization energies is presented in **Figure 7.8.**

As shown in our previous theoretical work, focused on DSSC with iodide/tri-iodide redox couple in organic solvent, a reorganization energy of the order of 0.6 eV was found to reproduce well the behaviour of the electron lifetime. More importantly, the model was able to predict the transition towards a linear regime when the band is displaced. The linear regime is characterized by a β close to unity and a constant diffusion length with respect to applied voltage. This was interpreted as an enhancement of process (2) in **Figure 7.8** with respect to process (1). As the transport level is moved towards the redox potential of the electrolyte, the density of acceptor states, governed by a reorganization energy of the order of the open-circuit photovoltage, facilitates recombination of quasi-free electrons. The experimental data obtained for electrolytes E1 to E8 seem to confirm this interpretation.

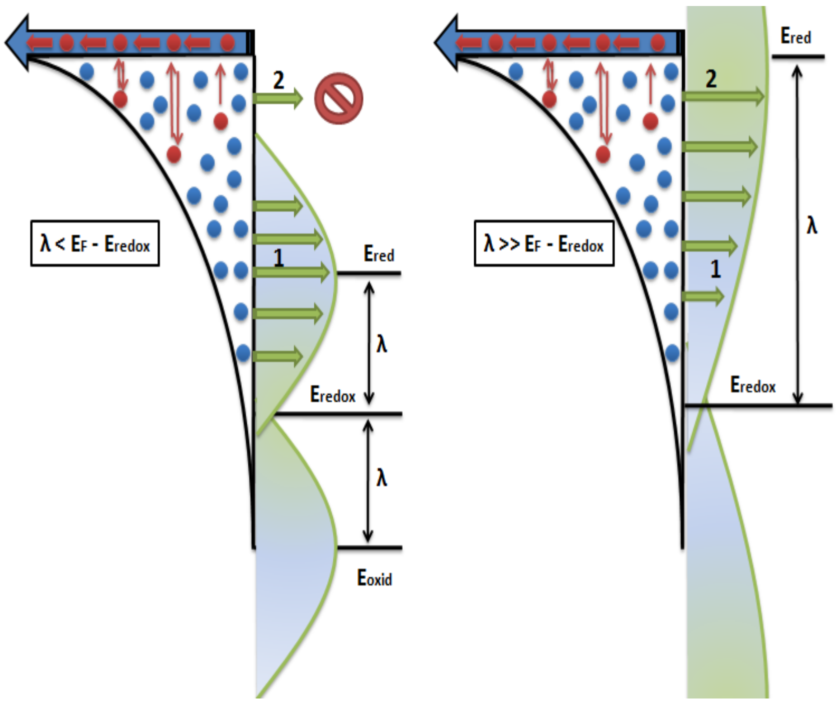

Figure 7.8: Illustration of the effect of reorganization energy and chemical environment on the recombination kinetics across the oxide/electrolyte interface. Left: redox mediator in weak-interacting chemical environment. Right: redox mediator in a strong-interacting chemical environment. In the figure (1) represents direct recombination from trap states and (2) recombination of quasi-free electrons from states close to the transport level.

On the contrary, electrolytes based on polar solvents, or those based on cobalt complexes, exhibit a much larger value of the reorganization energy. As mentioned above, the reorganization energy of cobalt complexes has been estimated to be of the order of 1.0-1.4 eV.[33,53] The reorganization energy for electron transfer from the oxide is expected to be large for room temperature ionic liquids.[51] As a consequence, a much wider distribution of acceptor states is expected for these systems. This has two important effects. First, no minimum in the lifetime-voltage plot is observed. As demonstrated by Bisquert and coworkers[23] and confirmed by random walk numerical simulation[34], **Equation 3.13** reduces to a simple exponential law when $\lambda >> E_F - E_{redox}$. Second, the larger availability of acceptor states multiplies the number of recombination routes for photogenerated electrons, hence reducing the lifetime and increasing the recombination losses at a given value of the electron density. It has to be noted that, in contrast to the interpretation given in Ref. 33, the recombination in the case of large reorganization energies takes place both from trap states and by quasi-free electrons, not only from the "conduction band". This is important to be stressed because a recombination reaction occurring strictly via the conduction band would not originate non-linear features (i.e $\beta < 1$). All electrolytes studied in this chapter show non-linear features (**Table 7.2**). Only if the electronic band system is artificially moved towards very positive potentials a linear regime is reproduced.[34,38] The same effect can be produced by changing the position of the redox potential of the electrolyte and keeping the band fixed, as recently observed by Feldt and coworkers.[53]

The decisive role played by the reorganization energy on the behaviour and magnitude of the electron lifetime evidences the importance of the chemical environment surrounding the electrochemical actives species in the electrolyte. The reorganization energy is commonly expressed as a sum of inner-sphere and outer-sphere contributions

$$\lambda = \lambda_{inner} + \lambda_{out}$$

The inner-sphere contribution arises from the interaction of ions with ligands covalently bonded to the central ions. The outer-sphere contribution corresponds to the interaction of the ion with solvent molecules. λ_{inner} can be very large for systems composed of coordinated complexes. This is the case of cobalt bipyridyl redox couples. On the other hand, λ_{out} depends on the dielectric constant of the semiconductor and the solvent, as well as on the effective distance to the electrode.[54,55] Polar solvents like water or room temperature ionic liquids are expected to have large values of the reorganization energy with respect to electron transfer from the semiconductor due to strong interaction between ions and solvent molecules.[29,56] In any other case, a strong interaction between redox mediators and their surrounding molecules appears to lead to a wider dispersion of acceptor states. As recombination also takes place from a wide dispersion of donor states, the consequence is an overall enhancement of the recombination rate, i.e., the decrease of the lifetime.

Some electrolytes studied recently offered promising advantages in terms of stability (ionic liquids, solid-state hole conductors) or in terms of more positive redox potential, which makes it possible to reach larger values of the open-circuit photovoltage (electrolytes based on cobalt complexes). However, these novel electrolytes are also characterized by a less favourable chemical environment, which increases the recombination rate, in spite of the positive thermodynamic effect associated to a fairly positive redox potential or a more negative band edge position. This appears to be the case for cobalt-based electrolytes.[19] The energy dispersion in acceptor states is also expected to be crucial for solid-state conductors,[57] where recombination losses are also known to be important.[18] In line with the interpretation presented here, this is a consequence of a large value of the reorganization energy, which increases the number of recombination routes. We believe that this feature has been overlooked so far in the literature.

According with this interpretation, further progress in electrolyte design should focus on the use of redox mediators with low reorganization energies, especially if the redox potential is very positive (which is desirable for large V_{oc}). This has in fact been theoretically predicted by Ondersma and Hamann.[58] In the present work, we show that this effect is decisively related with the trap distribution in the semiconductor (from which recombination is possible) and with the distribution of acceptor states in the electrolyte. Hence, the use of redox mediators that do not interact strongly with their environments, either because the solvent is non-polar or because they are not chemically bonded to ligands, seems to be more adequate to minimize recombination losses. It has to be mentioned, however, that recombination is not the only factor that determines the performance of the solar cells. The use of different electrolytes might result in lower injection or regeneration rates[53] or in transport limitations.[16] Nevertheless, electrolytes characterized by shorter lifetimes do generally lead to longer diffusion lengths and better collection efficiencies, as the electrolyte composition is found not to influence electron transport significantly.[46,59] In summary, the minimization of recombination via modification of the chemical composition of the electrolyte or hole-conductor proves to be an important ingredient in the optimization of DSSC. In the next chapter, it will be shown how a systematic variation of the electrolyte composition by playing with the ration between a polar and a non-polar solvent can be used to control the electron recombination rate.

5. Conclusions.

In this chapter a comprehensive study of the main factors determining the electron lifetime in DSSC has been performed. This study has been conducted by characterizing a wide variety of liquid electrolytes, including "standard" systems based on the iodide/tri-iodide redox couple and different organic solvents, solvent-free electrolytes made of room temperature ionic liquids and electrolytes with cobalt-based redox mediators. The lifetime for electron recombination has been determined as a function of Fermi level position by Impedance Spectroscopy, Intensity Modulated Photovoltage Spectroscopy and Open-Circuit Voltage Decay, finding good correspondence between data from all techniques. Two types of behaviours have been observed: one characterized by a small value of the reorganization energy, which leads to a minimum in the lifetime-voltage curve, and other characterized by a large value of the reorganization energy, which produces a pure exponential behaviour in the voltage range of interest. Once thermodynamic effects (i.e. band shifts due to additives and solvent molecules, and different positions of the redox potential) are separated out, the results show that systems with large reorganization energies tend to have large recombination losses. This finding shows that the chemical environment of the redox mediator can have a negative effect on the kinetics of recombination if there is a wider overlap in energies between donor and acceptor states, which favours extra routes for electron recombination.

6. References.

(1) O'Regan, B.; Gratzel, M. A Low-Cost, High-Efficiency Solar-Cell Based on Dye-Sensitized Colloidal Tio2 Films. *Nature* **1991**, *353*, 737–740.

(2) Grätzel, M. Recent Advances in Sensitized Mesoscopic Solar Cells. *Acc. Chem. Res.* **2009**, *42*, 1788–1798.

(3) Hardin, B. E.; Snaith, H. J.; McGehee, M. D. The Renaissance of Dye-Sensitized Solar Cells. *Nat. Photonics* **2012**, *6*, 162–169.

(4) Yella, A.; Lee, H.-W.; Tsao, H. N.; Yi, C.; Chandiran, A. K.; Nazeeruddin, M. K.; Diau, E. W.-G.; Yeh, C.-Y.; Zakeeruddin, S. M.; Grätzel, M. Porphyrin-Sensitized Solar Cells with Cobalt (II/III)–Based Redox Electrolyte Exceed 12 Percent Efficiency. *Science* **2011**, *334*, 629–634.

(5) Kim, H.-S.; Lee, C.-R.; Im, J.-H.; Lee, K.-B.; Moehl, T.; Marchioro, A.; Moon, S.-J.; Humphry-Baker, R.; Yum, J.-H.; Moser, J. E.; et al. Lead Iodide Perovskite Sensitized All-Solid-State Submicron Thin Film Mesoscopic Solar Cell with Efficiency Exceeding 9%. *Sci. Rep.* **2012**, *2*.

(6) Chung, I.; Lee, B.; He, J.; Chang, R. P. H.; Kanatzidis, M. G. All-Solid-State Dye-Sensitized Solar Cells with High Efficiency. *Nature* **2012**, *485*, 486–489.

(7) Ball, J. M.; Lee, M. M.; Hey, A.; Snaith, H. Low-Temperature Processed Mesosuperstructured to Thin-Film Perovskite Solar Cells. *Energy Environ. Sci.* **2013**.

(8) Colodrero, S.; Mihi, A.; Anta, J. A.; Ocaña, M.; Míguez, H. Experimental Demonstration of the Mechanism of Light Harvesting Enhancement in Photonic-Crystal-Based Dye-Sensitized Solar Cells. *J. Phys. Chem. C* **2009**, *113*, 1150–1154.

(9) Mihi, A.; Calvo, M. E.; Anta, J. A.; Miguez, H. Spectral Response of Opal-Based Dye-Sensitized Solar Cells. *J. Phys. Chem. C- Lett.* **2008**, *112*, 13–17.

(10) Justin Thomas, K. R.; Hsu, Y.-C.; Lin, J. T.; Lee, K.-M.; Ho, K.-C.; Lai, C.-H.; Cheng, Y.-M.; Chou, P.-T. 2,3-Disubstituted Thiophene-Based Organic Dyes for Solar Cells. *Chem. Mater.* **2008**, *20*, 1830–1840.

(11) Peter, L. M. Characterization and Modeling of Dye-Sensitized Solar Cells. *J. Phys. Chem. C* **2007**, *111*, 6601–6612.

(12) Hagfeldt, A.; Boschloo, G.; Sun, L.; Kloo, L.; Pettersson, H. Dye-Sensitized Solar Cells. *Chem. Rev.* **2010**, *110*, 6595–6663.

(13) Anta, J. A.; Guillén, E.; Tena-Zaera, R. ZnO-Based Dye-Sensitized Solar Cells. *J. Phys. Chem. C* **2012**, *116*, 11413–11425.

(14) Bisquert, J.; Mora-Seró, I. Simulation of Steady-State Characteristics of Dye-Sensitized Solar Cells and the Interpretation of the Diffusion Length. *J. Phys. Chem. Lett.* **2010**, *1*, 450–456.

(15) Anta, J. A.; Idígoras, J.; Guillén, E.; Villanueva-Cab, J.; Mandujano-Ramírez, H. J.; Oskam, G.; Pellejà, L.; Palomares, E. A Continuity Equation for the Simulation of the Current–voltage Curve and the Time-Dependent Properties of Dye-Sensitized Solar Cells. *Phys. Chem. Chem. Phys.* **2012**, *14*, 10285–10299.

(16) Fabregat-Santiago, F.; Bisquert, J.; Palomares, E.; Otero, L.; Kuang, D. B.; Zakeeruddin, S. M.; Gratzel, M. Correlation between Photovoltaic Performance and Impedance Spectroscopy of Dye-Sensitized Solar Cells Based on Ionic Liquids. *J. Phys. Chem. C* **2007**, *111*, 6550–6560.

(17) Guillén, E.; Fernández-Lorenzo, C.; Alcántara, R.; Martín-Calleja, J.; Anta, J. A. Solvent-Free ZnO Dye-Sensitised Solar Cells. *Sol. Energy Mater. Sol. Cells* **2009**, *93*, 1846–1852.

(18) Wang, M.; Chen, P.; Humphry-Baker, R.; Zakeeruddin, S. M.; Gratzel, M. The Influence of Charge Transport and Recombination on the Performance of Dye-Sensitized Solar Cells. *CHEMPHYSCHEM* **2009**, *10*, 290–299.

(19) Wang, H.; Nicholson, P. G.; Peter, L.; Zakeeruddin, S. M.; Grätzel, M. Transport and Interfacial Transfer of Electrons in Dye-Sensitized Solar Cells Utilizing a Co(dbbip)2 Redox Shuttle. *J. Phys. Chem. C* **2010**, *114*, 14300–14306.

(20) Jennings, J. R.; Liu, Y.; Wang, Q.; Zakeeruddin, S. M.; Grätzel, M. The Influence of Dye Structure on Charge Recombination in Dye-Sensitized Solar Cells. *Phys. Chem. Chem. Phys.* **2011**, *13*.

(21) Jang, S.-R.; Zhu, K.; Ko, M. J.; Kim, K.; Kim, C.; Park, N.-G.; Frank, A. J. Voltage-Enhancement Mechanisms of an Organic Dye in High Open-Circuit Voltage Solid-State Dye-Sensitized Solar Cells. *ACS Nano* **2011**, *5*, 8267–8274.

(22) Liu, Y.; Jennings, J. R.; Zakeeruddin, S. M.; Grätzel, M.; Wang, Q. Heterogeneous Electron Transfer from Dye-Sensitized Nanocrystalline TiO2 to [Co(bpy)3]3+: Insights Gained from Impedance Spectroscopy. *J. Am. Chem. Soc.* **2013**, *135*, 3939–3952.

(23) Bisquert, J.; Fabregat-Santiago, F.; Mora-Seró, I.; Garcia-Belmonte, G.; Giménez, S. Electron Lifetime in Dye-Sensitized Solar Cells: Theory and Interpretation of Measurements. *J. Phys. Chem. C* **2009**, *113*, 17278–17290.

(24) Fabregat-Santiago, F.; Bisquert, J.; Garcia-Belmonte, G.; Boschloo, G.; Hagfeldt, A. Influence of Electrolyte in Transport and Recombination in Dye-Sensitized Solar Cells Studied by Impedance Spectroscopy. *Sol. Energy Mater. Sol. Cells* **2005**, *87*, 117–131.

(25) Halme, J. Linking Optical and Electrical Small Amplitude Perturbation Techniques for Dynamic Performance Characterization of Dye Solar Cells. *Phys. Chem. Chem. Phys.* **2011**, *13*.

(26) Zaban, A.; Greenshtein, M.; Bisquert, J. Determination of the Electron Lifetime in Nanocrystalline Dye Solar Cells by Open-Circuit Voltage Decay Measurements. *Chemphyschem* **2003**, *4*, 859–864.

(27) Barnes, P. R. F.; Miettunen, K.; Li, X.; Anderson, A. Y.; Bessho, T.; Gratzel, M.; O'Regan, B. C. Interpretation of Optoelectronic Transient and Charge Extraction Measurements in Dye-Sensitized Solar Cells. *Adv. Mater.* **2013**, n/a – n/a.

(28) Wang, Q.; Ito, S.; Gratzel, M.; Fabregat-Santiago, F.; Mora-Sero, I.; Bisquert, J.; Bessho, T.; Imai, H. Characteristics of High Efficiency Dye-Sensitized Solar Cells. *J. Phys. Chem. B* **2006**, *110*, 25210–25221.

(29) Bisquert, J.; Marcus, R. A. Device Modeling of Dye-Sensitized Solar Cells. In; Topics in Current Chemistry; Springer Berlin Heidelberg, 2013; pp. 1–71.

(30) Marcus, R. A. On the Theory of Oxidation-Reduction Reactions Involving Electron Transfer. I. *J. Chem. Phys.* **1956**, *24*, 966–978.

(31) Rowley, J.; Meyer, G. J. Reduction of I2/I3− by Titanium Dioxide. *J. Phys. Chem. C* **2009**, *113*, 18444–18447.

(32) Boschloo, G.; Gibson, E. A.; Hagfeldt, A. Photomodulated Voltammetry of Iodide/Triiodide Redox Electrolytes and Its Relevance to Dye-Sensitized Solar Cells. *J Phys Chem Lett* **2011**, 3016–3020.

(33) Ondersma, J. W.; Hamann, T. W. Measurements and Modeling of Recombination from Nanoparticle TiO2 Electrodes. *J. Am. Chem. Soc.* **2011**, *133*, 8264–8271.

(34) Gonzalez-Vazquez, J. P.; Oskam, G.; Anta, J. A. Origin of Nonlinear Recombination in Dye-Sensitized Solar Cells: Interplay between Charge Transport and Charge Transfer. *J. Phys. Chem. C* **2012**, *116*, 22687–22697.

(35) Gerischer, H. Über Den Ablauf von Redoxreaktionen an Metallen Und an Halbleitern. *Z. Für Phys. Chem.* **1960**, *26*, 223–247.

(36) Villanueva-Cab, J.; Wang, H.; Oskam, G.; Peter, L. M. Electron Diffusion and Back Reaction in Dye-Sensitized Solar Cells: The Effect of Nonlinear Recombination Kinetics. *J. Phys. Chem. Lett.* **2010**, *1*, 748–751.

(37) Jennings, J. R.; Wang, Q. Influence of Lithium Ion Concentration on Electron Injection, Transport, and Recombination in Dye-Sensitized Solar Cells. *J. Phys. Chem. C* **2010**, *114*, 1715–1724.

(38) Jennings, J. R.; Li, F.; Wang, Q. Reliable Determination of Electron Diffusion Length and Charge Separation Efficiency in Dye-Sensitized Solar Cells. *J. Phys. Chem. C* **2010**, *114*, 14665–14674.

(39) Reynal, A.; Forneli, A.; Palomares, E. Dye Structure-Charge Transfer Process Relationship in Efficient Ruthenium-Dye Based Dye Sensitized Solar Cells. *Energy Env. Sci* **2010**, *3*, 805–812.
(40) Liu, Y.; Jennings, J. R.; Huang, Y.; Wang, Q.; Zakeeruddin, S. M.; Grätzel, M. Cobalt Redox Mediators for Ruthenium-Based Dye-Sensitized Solar Cells: A Combined Impedance Spectroscopy and Near-IR Transmittance Study. *J Phys Chem C* **2011**, *115*, 18847–18855.
(41) Bisquert, J. Theory of the Impedance of Electron Diffusion and Recombination in a Thin Layer. *J. Phys. Chem. B* **2002**, *106*, 325–333.
(42) Watson, D. F.; Meyer, G. J. Cation Effects in Nanocrystalline Solar Cells. *Coord. Chem. Rev.* **2004**, *248*, 1391–1406.
(43) Boschloo, G.; Haggman, L.; Hagfeldt, A. Quantification of the Effect of 4-Tert-Butylpyridine Addition to I-/I-3⊖ Redox Electrolytes in Dye-Sensitized Nanostructured TiO2 Solar Cells. *J. Phys. Chem. B* **2006**, *110*, 13144–13150.
(44) Cameron, P. J.; Peter, L. M. How Does Back-Reaction at the Conducting Glass Substrate Influence the Dynamic Photovoltage Response of Nanocrystalline Dye-Sensitized Solar Cells? *J. Phys. Chem. B* **2005**, *109*, 7392–7398.
(45) Bisquert, J.; Zaban, A.; Greenshtein, M.; Mora-Sero, I. Determination of Rate Constants for Charge Transfer and the Distribution of Semiconductor and Electrolyte Electronic Energy Levels in Dye-Sensitized Solar Cells by Open-Circuit Photovoltage Decay Method. *J. Am. Chem. Soc.* **2004**, *126*, 13550–13559.
(46) Guillén, E.; Peter, L. M.; Anta, J. A. Electron Transport and Recombination in ZnO-Based Dye-Sensitized Solar Cells. *J Phys Chem C* **2011**, *115*, 22622–22632.
(47) Raga, S. R.; Barea, E. M.; Fabregat-Santiago, F. Analysis of the Origin of Open Circuit Voltage in Dye Solar Cells. *J. Phys. Chem. Lett.* **2012**, *3*, 1629–1634.
(48) González-Pedro, V.; Xu, X.; Mora-Seró, I.; Bisquert, J. Modeling High-Efficiency Quantum Dot Sensitized Solar Cells. *ACS Nano* **2010**, *4*, 5783–5790.
(49) Kambe, S.; Nakade, S.; Kitamura, T.; Wada, Y.; Yanagida, S. Influence of the Electrolytes on Electron Transport in Mesoporous TiO2–Electrolyte Systems. *J. Phys. Chem. B* **2002**, *106*, 2967–2972.
(50) Kubo, W.; Kambe, S.; Nakade, S.; Kitamura, T.; Hanabusa, K.; Wada, Y.; Yanagida, S. Photocurrent-Determining Processes in Quasi-Solid-State Dye-Sensitized Solar Cells Using Ionic Gel Electrolytes. *J. Phys. Chem. B* **2003**, *107*, 4374–4381.
(51) Lynden-Bell, R. M. Does Marcus Theory Apply to Redox Processes in Ionic Liquids? A Simulation Study. *Electrochem. Commun.* **2007**, *9*, 1857–1861.
(52) Feldt, S. M.; Wang, G.; Boschloo, G.; Hagfeldt, A. Effects of Driving Forces for Recombination and Regeneration on the Photovoltaic Performance of Dye-Sensitized Solar Cells Using Cobalt Polypyridine Redox Couples. *J Phys Chem C* **2011**, *115*, 21500–21507.
(53) Feldt, S. M.; Lohse, P. W.; Kessler, F.; Nazeeruddin, M. K.; Grätzel, M.; Boschloo, G.; Hagfeldt, A. Regeneration and Recombination Kinetics in Cobalt Polypyridine Based Dye-Sensitized Solar Cells, Explained Using Marcus Theory. *Phys. Chem. Chem. Phys.* **2013**, *15*, 7087–7097.
(54) Marcus, R. A. Reorganization Free Energy for Electron Transfers at Liquid-Liquid and Dielectric Semiconductor-Liquid Interfaces. *J. Phys. Chem.* **1990**, *94*, 1050–1055.
(55) Dzhavakhidze, P. G.; Kornyshev, A. A.; Krishtalik, L. I. Activation Energy of Electrode Reactions: The Non-Local Effects. *J. Electroanal. Chem. Interfacial Electrochem.* **1987**, *228*, 329–346.
(56) Hartnig, C.; Koper, M. T. M. Molecular Dynamics Simulations of Solvent Reorganization in Electron-Transfer Reactions. *J. Chem. Phys.* **2001**, *115*, 8540–8546.
(57) Bisquert, J.; Palomares, E.; Quiñones, C. A. Effect of Energy Disorder in Interfacial Kinetics of Dye-Sensitized Solar Cells with Organic Hole Transport Material. *J. Phys. Chem. B* **2006**, *110*, 19406–19411.

(58) Ondersma, J. W.; Hamann, T. W. Recombination and Redox Couples in Dye-Sensitized Solar Cells. *Coord. Chem. Rev.* **2013**, *257*, 1533–1543.
(59) Wang, H.; Peter, L. M. Influence of Electrolyte Cations on Electron Transport and Electron Transfer in Dye-Sensitized Solar Cells. *J. Phys. Chem. C* **2012**, *116*, 10468–10475.

Chapter 8:

Control of recombination rate by changing the polarity of the electrolyte in Dye-Sensitized Solar Cells

1. Introduction.

As mentioned in previous chapters, an energy conversion efficiency of 13% has been reported for DSSC[1] thanks to the combination of a porphyrin dye and a cobalt complex using acetonitrile as solvent electrolyte. However, losses by leakage and evaporations, which endanger long-life devices, have been associated to the use of volatile solvents. Due to concerns about the long-term stability of DSSCs, there has been a great interest in finding a substitute for volatile electrolytes based on organic solvents.

During the last decade, Room Temperature Ionic Liquids (RTIL) have been investigated as alternative solvent in DSSCs due to their appealing properties for DSSC applications, that is, wide electrochemical windows, thermal stability, extremely low volatility or negligible vapour pressure, high ionic conductivity and ability to dissolve organic and inorganic compounds. However, the viscosity of typical RTILs is about 100 times higher than the viscosity of acetonitrile, a fact that has been used to explain the lower performance of RTIL-based DSSC. In addition, high recombination rates have systematically been reported for these electrolytes.[2] In spite of that, conversion efficiencies of around 9% have been reported for ionic liquid-based DSSC.[3] Indeed, the recent 300 m^2 solar façade of the Swiss Tech Convention Centre (Lausanne, Switzerland), which can be considered the first real architectural integration of this technology, is based on RTIL-based DSSC, demonstrating their potential in *Building Integrated Photovoltaics* (BIPV) applications.

The origin of the high recombination rate and a systematic study of the fundamental impact of the chemical nature of the electrolyte on the electron transfer reaction in DSSC are still lacking. In this respect, **Chapter 7**[4] pointed to the importance of ligand (inner) and solvent (outer) interactions and the polarity of the solvent in the recombination rate. As mentioned and discussed in the previous chapter, it is known that when $\lambda >> E_F - E_{redox}$, **Equation 3.13** leads to an exponential dependence of the lifetime with respect to voltage.[5,6] This is the case of polar solvents such as RTILs, whose reorganization energy is larger, due to strong polar interaction between ions and solvent molecules.[7] However, a relatively low value of the reorganization energy leads to a departure from the exponential law, and the appearance of a minimum due to the depletion of acceptor states as the Fermi level is raised.[8]

On the other hand, in the search for new RTILs, it has to be taken into account that their physical and chemical properties depend on the interactions between the cations (imidazolium, pyridinium, alkylammonium or pyrrolidinium) and the anions (dycianamide, thiocyanate or tetracianoborate, among others). Imidazolium have been the most used component of solvent-free electrolytes in DSSCs. However, several investigations revealed significant influence of the RTIL composition upon processes relevant to the overall dynamic of DSSC, such as electron injection yield,[9,10] electron lifetimes[11] and the rate of regeneration of the oxidized dye.[12] Additionally, the nature of the RTIL can also affect the electron diffusion coefficient in the photoanodes due to the electrical coupling with counter-ion charges in the electrolyte.[13,14]

The aim of this chapter is two-fold. On the one hand (1), we pursue to cast some light on the mechanism of electron recombination in DSSC taking into account the polar nature of the RTILs, which can be tuned by mixing with an organic solvent such as acetonitrile. In this respect, this work intents to gain a deeper insight into the findings of the previous chapter,[4] where exponential and non-exponential lifetimes were found to depend on the composition of the electrolyte. On the other hand (2), we have investigated the capability of hybrid electrolytes composed of mixtures of RTILs with a low-viscosity and low-polarity solvent as acetonitrile to achieve good performing cells with non-volatile solvents and small mass-transport limitations. It has already been shown by Yu and coworkers[15] that "incompletely solvated ionic liquid mixtures" are very stable under light soaking conditions.

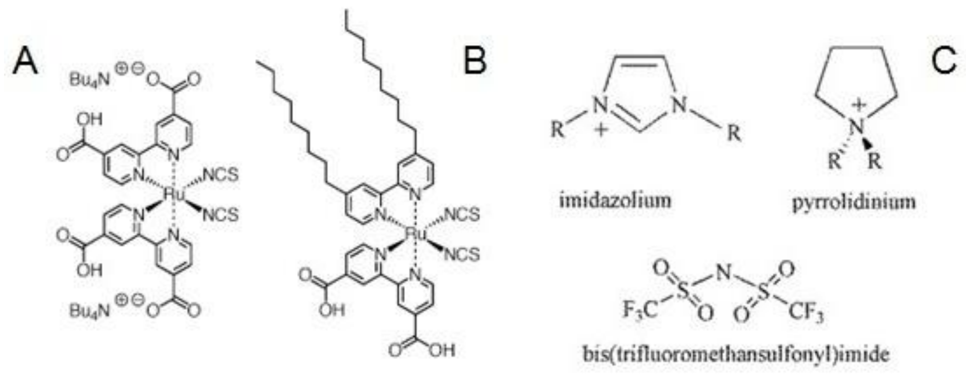

Figure 8.1: Structures of dye molecules used in this chapter: (A) N719 and (B) Z907; and Room Temperature Ionic Liquids employed as solvents (C): imidazolium (Imid) and pyrrolidinum (Pyr).

In this line, two different dyes (hydrophilic N719 and hydrophobic Z907) and two RTILs with two different cations (imidazolium and pyrrolidinium) have been used as components in the polar/apolar mixed DSSC electrolytes (**Figure 8.1**). The influence of the RTIL/acetonitrile mixing ratio on photovoltaic performance and the recombination kinetics has been investigated by voltammetry, Electrochemical Impedance Spectroscopy (EIS), Intensity-Modulated Photovoltage and Photocurrent Spectroscopies (IMVS/IMPS) and Open-Circuit Voltage Decays (OCVD).

Most of the results presented in this chapter have been reported in the following publication: Idígoras et al. *Physical Chemistry Chemical Physics,* **2014**, 16, 21513-21523.

2. Experimental section.

2.1. Fabrication of Dye-sensitized Solar Cells.

For optimized cell efficiencies, devices were made using 12 μm thick films consisting of a layer of 8 μm of 20 nm TiO_2 nanoparticles (*Dyesol© paste*) and a layer of 4 μm of 400 nm TiO_2 particles (scattering layer).[16] Prior to the deposition of the TiO_2 paste the conducting glass substrates (Pilkington-TEC 15) were immersed in a solution of $TiCl_4$ (40 mM) for 30 minutes at 70°C and then dried. For some of the devices (*control cells*), and to prevent recombination of electrons from the glass substrates with the oxidized species in the electrolyte a thin insulating layer (called a *blocking layer*) was placed between the mesoporous oxide and the substrate. This thin film was prepared by spin coating from the following solution: 20ml of H_2O MilliQ + 2.2ml of Titanium (IV) isopropoxide + 1.5ml of Acetylacetone. After deposition, the substrate was heated to 500°C. The TiO_2 nanoparticle paste was deposited onto a conducting glass substrate using the screen printing technique. The DSSC active area was 0.16 cm^2. The TiO_2 electrodes were gradually heated under airflow at 325°C for 5 min, 375°C for 5 min, 450°C for 15 min and 500°C for 15 min. The heated TiO_2 electrodes were immersed again in a solution of $TiCl_4$ (40 mM) at 70°C for 30 min and then washed with water and ethanol. Finally, the electrodes were heated again at 500°C for 30 min and cooled before dye adsorption.

The counter-electrode was made by spreading a *Platisol solution* (Solaronix) onto a conducting glass substrate (Pilkington-TEC 8) with a small hole to allow for the introduction of the liquid electrolyte using vacuum. This is followed by a thermal treatment at 390°C for 15 minutes.

The electrodes were immersed overnight in a solution containing ruthenium dyes coded **N719** (*cis-diisothiocyanato-bis(2,2'-bipyridyl-4,4'-dicarboxylato) ruthenium(II) bis (tetrabutylammonium*) and **Z907** (*cis-disothiocyanato-(2,2'-bipyridyl-4,4'-dicarboxylic acid)-(2,2'-bipyridyl-4,4'-dinonyl) ruthenium(II)*). These solutions were composed of 0.3mM dye and 0.3mM chenodeoxycholic acid in ethanol. The sensitized electrodes were washed with ethanol and dried in air. Finally, the working- and counter-electrodes were sandwiched together using a thin thermoplastic frame (*Surlyn*, Solaronix) that melts at 100°C. The cells were filled with the electrolyte through a hole previously made in the back of a platinized counter-electrode. Then, the hole was sealed with a thermoplastic polymer and a cover-slide glass.

The composition of the electrolytes studied in this chapter is shown in **Table 8.1**. Only the solvent composition is varied, and both redox pair and additives are kept the same for all studied devices.

Electrolyte	Solvent (v/v, %)	Solutes
Acn	100% Acetonitrile	$0.1M\ I_2$ + 1M BMII + 0.05M LiI + 0.5M TBP + 0.1M GuSCN
Imid25 or Pyr25	75% Acn + 25% RTIL	
Imid50 or Pyr50	50% Acn + 50% RTIL	
Imid75 or Pyr75	25% Acn + 75% RTIL	
Imid or Pyr	100% RTIL	

Table 8.1: Composition of the electrolytes studied in this work. (I_2: Iodine (99.5%, Fluka), LiI: Lithium iodide (99%, Aldrich), BMiI: 1-butyl-3-methylimidalozlium iodide (99%, Aldrich), TBP: 4-tert-butylpiridine (96%, Aldrich), GuSCN: Guanidine thiocyanate (99%, Aldrich), Acn: Acetonitrile (99.9%, Panreac), Imid: 1-Ethyl-3-Methylimidazolium bis(trifluoromethanesulfonyl)imide (99.9%, Solvionic), Pyr: 1-Buthyl-1-Methylpyrrolidinium bis(trifluoromethanesulfonyl)imide (99.9%, Solvionic).

2.2. Characterization of devices

The devices were characterized using a solar simulator with AM 1.5G filter (*ABET*). The light intensity was calibrated to the standard value of 1 sun (100 mW/cm^2) using a reference solar cell with temperature output (*Oriel*, 91150). The current-voltage characteristics were determined by applying an external potential bias to the cell and measuring the photocurrent using an *Autolab/PGSTAT302N* potentiostat. Open-circuit Voltage Decay (OCVD) measurements were made by keeping the solar cell at open-circuit at 1-sun and recording the voltage decay after interrupting the illumination.

Electrochemical Impedance Spectroscopy (EIS), Intensity Modulated Photovoltage Spectroscopy (IMVS), Intensity Modulated Photocurrent Spectroscopy (IMPS) and Open-Circuit Voltage Decay (OCVD) were utilized to study electron transport, recombination, chemical capacitance and to extract electron lifetimes.[17,18] The illumination for the small perturbation (frequency response) techniques was provided by a 530 nm light emitting diode (*LUXEON*). A response analyzer module (*PGSTAT302N/FRA2*, Autolab) was utilized to analyze the frequency response of the devices. EIS measurements were carried out under a varying bias potential and a fixed illumination (related to the open-circuit voltage) provided by the light emitting diode. The bias potential was corrected for voltage drop due to series resistance. A 10 mV perturbation in the 10^5-10^{-2} Hz range was utilized to obtain the spectra. IMVS and IMPS measurements were carried out by coupling the PGSTAT302N/FRA2 module to the light emitting diode. This makes it possible to probe the devices at different positions of the Fermi level in the semiconductor. In all cases the samples were illuminated from the dye-coated TiO_2 electrode side. IMVS measurements were performed at open-circuit in the 10^4-10^{-1} Hz range and IMPS measurements at short-circuit in the 10^4 to 10^{-3} Hz range with a light perturbation corresponding to 10% of the dc background illumination intensity. The NOVA 1.7 software was used to generate and treat the IMVS data. Zview equivalent circuit modelling software (*Scribner*) was used to fit the EIS spectra, including the distributed element DX11 (transmission line model).[19,20] To obtain the Fermi Level shift between open-circuit and short-circuit condition,[21] short-circuit voltage (V_{sc})[22,23] measurements were performed. For this purpose, the solar cell was first illuminated under short-circuit conditions at various light intensities. The diode was then turned off and the cell was switched to open circuit simultaneously. The voltage evolution was finally monitored by the potentiostat.

For “blank” cells containing just the different electrolytes sandwiched between two platinized FTOs, cyclic voltammograms (CV) were recorded at a scan rate of 20 mV·s^{-1}. These measurements were utilized to obtain diffusion limiting currents.

3. Results.

3.1. Photovoltaic performance.

Figure 8.2 shows current-voltage characteristics of cells employing the N719 as sensitizer for the studied electrolytes. To test the reproducibility of the results, four cells were fabricated for each composition, and no significant deviations were found between them. The photovoltaic parameters (short-circuit current density (J_{sc}), open-circuit voltage (V_{oc}), fill factor and power conversion efficiency (η)) for each configuration are given in **Table 8.2**.

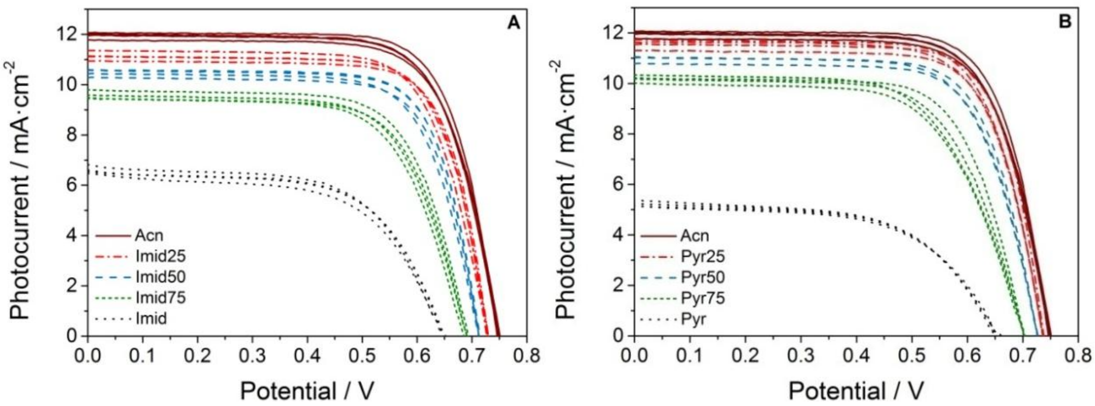

Figure 8.2: Current-voltage curves under 1-sun AM1.5 for different RTIL/Acn mixing ratios. Results for both ionic liquids studied are shown: (A) Imid and (B) Pyr.

Electrolyte	J_{sc} ($mA \cdot cm^{-2}$)	V_{oc} (mV)	Fill Factor	Efficiency (η)
Acn	12.1	745	74	6.6
Imid25	11.5	728	74	6.0
Imid50	10.6	712	73	5.6
Imid75	9.7	690	69	4.7
Imid	6.8	650	60	2.8
Pyr25	11.8	735	73	6.2
Pyr50	11.0	727	72	5.8
Pyr75	10.2	702	68	4.9
Pyr	5.3	655	57	2.0

Table 8.2: Photovoltaic parameters measured under simulated AM 1.5 sun illumination of the best DSSC for each electrolyte composition and employing the N719 dye.

The maximum efficiency (6.6%) was found for the pure acetonitrile-based electrolyte. This good efficiency is achieved by a proper combination of additives, which maximize open-circuit photovoltage (745 mV), fill factor (74%) and photocurrent (12.1 $mA \cdot cm^{-2}$). The electrolyte composition used is very similar to the best-performing electrolyte employed in **Chapter 7**. To compensate the high viscosity of the ionic liquids a higher concentration of iodine (0.1M) was used. However, the increment of the concentration of I_3^- can lead to a lower performance of the cell. It must be born in mind that iodine absorbs light, which produces a diminution of the photocurrent.[24] In addition, an increase in the iodine concentration can accelerate the recombination since more tri-iodide ions are available for accepting electrons. Nevertheless, efficiencies of 2.8% and 2.0% were obtained for pure Imid and Pyr, respectively. Importantly, efficiencies around 5% are obtained for the mixtures where the RTILs are the majority component (25% Acn + 75% RTIL). This efficiency is comparable to that reported by Yu et al.[15] for a similar composition. The relative high viscosity of Imid and Pyr (35.55cP and 85.33cP at 298K, respectively), which are about several orders of magnitude higher than the viscosity of acetonitrile (0.34cP at 298K),[25] appears to limit their efficiency due to severe mass-transport limitations[24,26] related to their ionic diffusion coefficients. This has been confirmed by measuring cyclic voltammograms in blank cells (**Figure 8.3**). Consequently, the efficiency of regeneration of the oxidized dye by the reduced form of the redox couple is limited. These limitations, which are primarily reflected in the J_{sc} and in the fill factor, are reduced as more acetonitrile is added to the RTIL. Therefore, the photovoltaic parameters are improved. However, it is noteworthy that adding just a 25% in volume of acetonitrile doubles the short-circuit photocurrent and the efficiency. This effect is more pronounced for Pyr-based electrolytes than for Imid-based electrolyte (**Appendix**, Figure A-8.1). Specifically, the addition of acetonitrile (25% in volume) into Imid and Pyr produces an increase in the J_{sc} of 42% and 92% respectively. In order to be sure that the observed effect does not depend on the used dye, another ruthenium sensitizer, Z907, was employed, which yielded similar results to those obtained with the N719 dye (**Appendix**, Figure A-8.2).

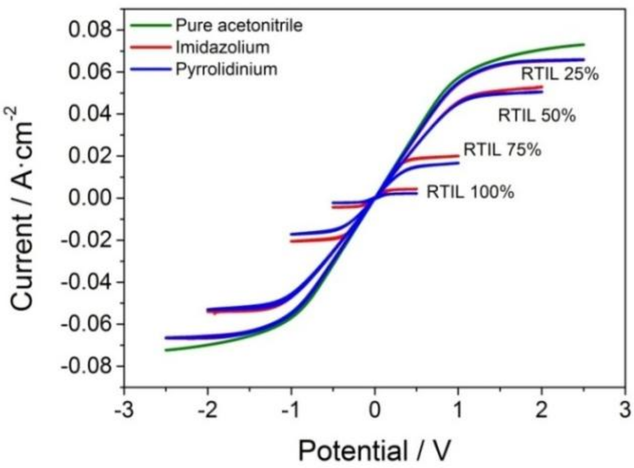

Figure 8.3: Cyclic voltammetry of Pt@FTO/ Pt@FTO (blank cells) for all RTIL/Acn mixing ratios.

It is very important to point out that the benefit of using Pyr versus Imid has nothing to do with a lower transport limitation, as the limiting currents of Pyr/Acn and Imid/Acn electrolytes with the same mixing ratio are very similar (**Figure 8.3**), in spite of Pyr being even slightly more viscous. Furthermore, the overall improvement in performance as more acetonitrile is added is not only observed in short-circuit photocurrents and fill factors, but also in the open-circuit voltage, when no current is running through the device. This observation indicates that the origin of the lower performance of RTIL electrolytes is not due to transport limitations only. This issue is further investigated in the following sections.

3.2. Electrochemical impedance spectroscopy.

EIS Nyquist plots at the open-circuit photovoltage are presented in **Figure 8.4** for all Pyr-based electrolytes in N719-DSSC. The spectra show the characteristic three semicircles typically observed in DSSC.[2,19] The high-frequency one is related to charge transfer at the platinum counter-electrode, the one at mid frequencies arises from electronic processes at the oxide/electrolyte interface and the semicircle appearing at low frequencies reflects the diffusion of redox species in the electrolyte. This semicircle only appears in the most viscous electrolytes (high RTIL/Acn mixing ratio) due to the mass-transport limitation in the electrolyte.

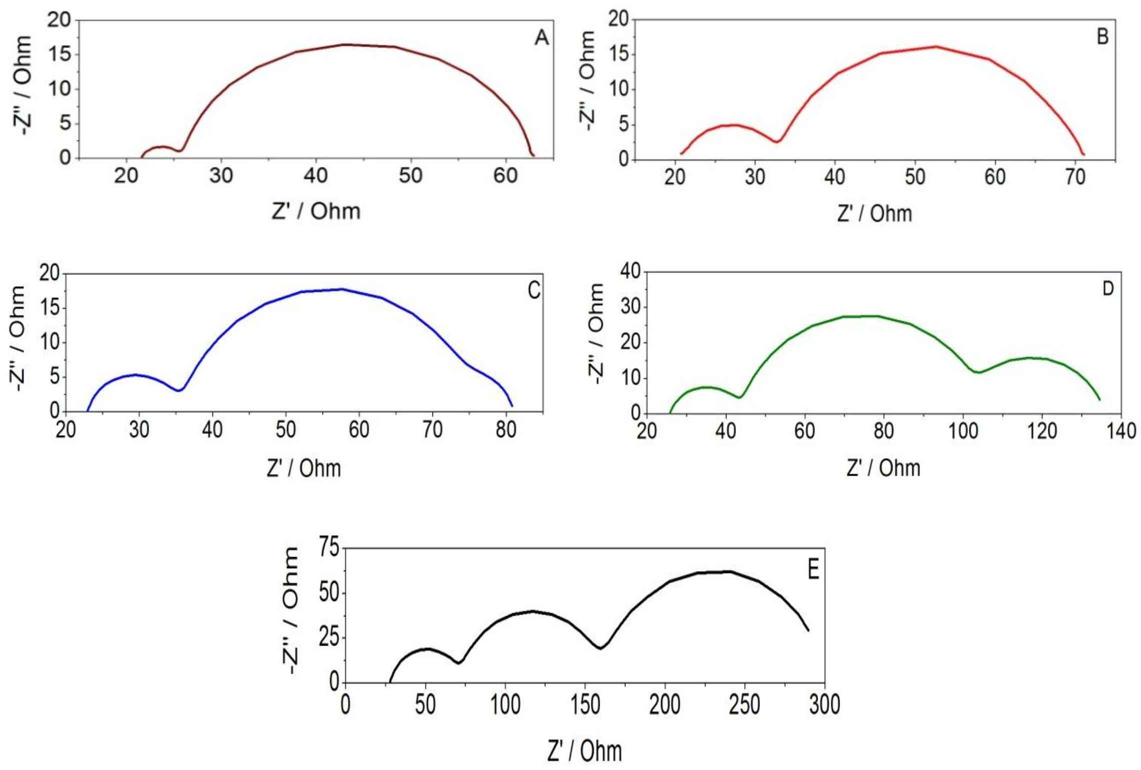

Figure 8.4: EIS Nyquist plots for all Pyr-based electrolytes and acetonitrile in N719-cells at the different ratio RTIL/Acn: (A) Acn, (B) Pyr25, (C) Pry50, (D) Pyr75 and (E) Pyr. All these spectra have been measured under illumination and at the open-circuit photovoltage of each cell at 1 sun.

The EIS results fitted well to the diffusion-recombination model of Bisquert and coworkers[19,20] (see Section 2.4.1 in **Chapter 4** for details of the equivalent circuit featuring these parameters). However, it has to be noted that it was not possible to fit to diffusion-recombination equivalent circuit for cells with pure RTIL, possibly due to the short electron diffusion length, as discussed below. Furthermore, this equivalent circuit was not found suitable at low potentials either (< 0.55 V). As it is in this regime where direct electron transfer between the FTO substrate and the electrolyte becomes significant,[20,21] this problem was attributed to the lack of additional circuit elements, as indicated in Ref. 30. However, as said, the diffusion-recombination model works well at moderate and high potentials, which is the region of interest for cell operation. The region of low potentials is better explored with the OCVD technique, although with limitations, as explained below.

In the **Appendix** (Figure A-8.3), the chemical capacitances extracted from EIS analysis at different potentials are shown. The EIS results show that the capacitance is not altered by the RTIL/Acn mixing ratio, which indicates that, probably as a consequence of using the same additives in all electrolytes, no significant shifts of the conduction band are occurring. Therefore, taking into account **Equation 4.17,** if the capacitance is not altered, the electron lifetime is determined by the electron recombination resistance at the TiO_2/electrolyte interface only. In **Figure 8.5**, electron recombination resistances and electron lifetimes using both RTILs are shown for all the RTIL/Acn mixing ratios considered in this chapter.

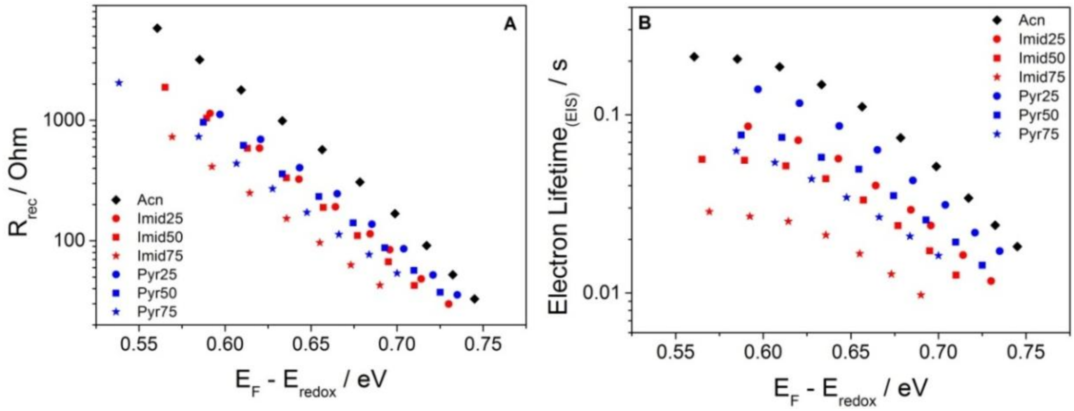

Figure 8.5: (A) Electron recombination resistance and (B) electron lifetime data are extracted from EIS measurement in N719-cells.

Figures 8.5 show a systematic increase of the recombination resistance and electron lifetime when the RTIL/Acn mixing ratio is reduced, which explains the improvement of the photovoltage with respect to pure RTIL. Consequently, cells with pure acetonitrile in the electrolyte show the highest V_{oc}. Furthermore, it is important to stress that the results obtained point to a more intense blocking of electron recombination with tri-iodide ions by pyrrolidinium cations than by imidazolium ones. Similar results were obtained in Z907-cells (**Appendix**, Figure A-8.4). In conclusion, the cells with Pyr-based electrolytes show better performance than with Imid-based electrolytes in spite of being a slightly more viscous ionic liquid. However, solar cells containing Pyr show, systematically, lower fill factors. This difference can be related to its viscosity and/or a higher charge transfer resistance at the counter-electrode for cells with Pyr-based electrolytes. As can be observed in **Figure 8.6**, the semicircle at high frequencies, related to charge transfer at the platinum counter-electrode, features a higher resistance for Pyr than for Imid-based electrolytes.

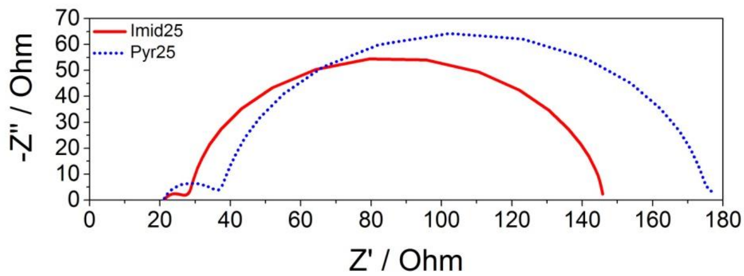

Figure 8.6: EIS Nyquist plots at 0.665mV for cells with Imid and Pry-based electrolytes in N719-cells of the same RTIL/Acn mixing ratio (25%).

3.3. Open-Circuit Voltage Decays.

The OCVD data provide a simple and ready means of probing the recombination process. A proper interpretation of OCVD data involves the extraction of the lifetime via **Equation 4.3**, which is actually related to the time derivative of the voltage decay.[18,27]

In **Figure 8.7** OCVD lifetimes for different mixing ratios and different dyes (N719 and Z907) are shown. Two main observations can be derived from the results in Figure 8.7. First, as discussed below, the addition of acetonitrile reduces the recombination rate, leading to longer lifetimes, similar to results obtained by EIS. Second, all solar cells with acetonitrile in a major or minor proportion exhibit non-exponential behaviour in the lifetime-voltage curve. However, solar cells with pure RTILs yield exponential lifetimes (straight lines in the semilogarithmic plot). A transition from exponential to non-exponential behaviour in OCVD data takes place as more acetonitrile is added. This observation suggests that a modification of recombination mechanism, probably produced by the change in polarity of electrolyte.

To make sure that the departure from the exponential behaviour and the appearance of a minimum for some electrolytes is not due to charge transfer through the FTO/TiO_2 interface,[21] like in **Chapter 7**, cells with and without blocking layers were compared. The results are presented in the **Appendix** (Figure A-8.5), where it is shown that cells with and without blocking layer, although with slightly smaller lifetimes for the latter, especially in the region of low potentials, exhibit the same features described above (similar to Figure A-7.2 in **Appendix**).

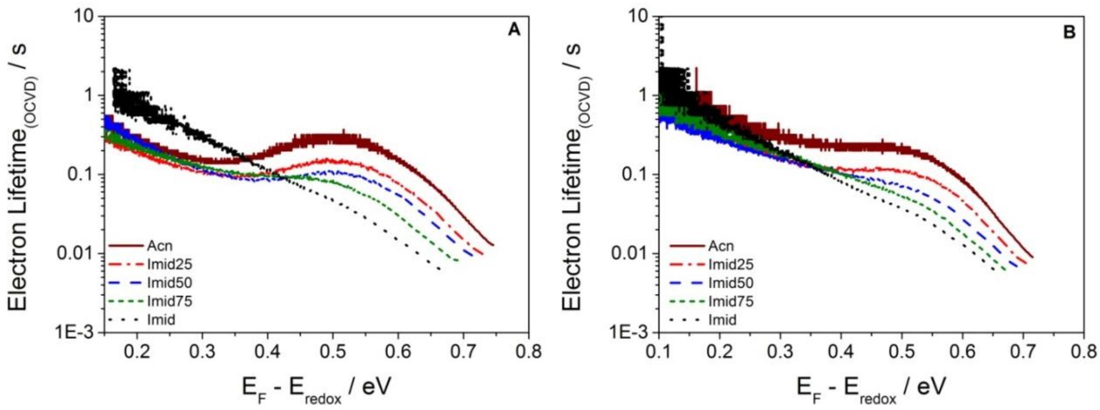

Figure 8.7: Electron lifetimes as extracted from OCVD for various Imid/Acn mixing ratios in (A) N719-cells and (B) Z907-cells.

3.4. Stability test.

It is known that the addition of a non-volatile component into acetonitrile is appealing in terms of stability. In **Figure 8.8**, the evolution of key photovoltaic parameters during 9 hours under the irradiance of AM 1.5G is shown. After light soaking, the photocurrent and power conversion efficiency of the solar cell increases; this behaviour is related to the improved penetration of the ionic liquid electrolyte through the mesoporous film electrode due to an increase of temperature. After this period, a stabilization of the performance is observed.

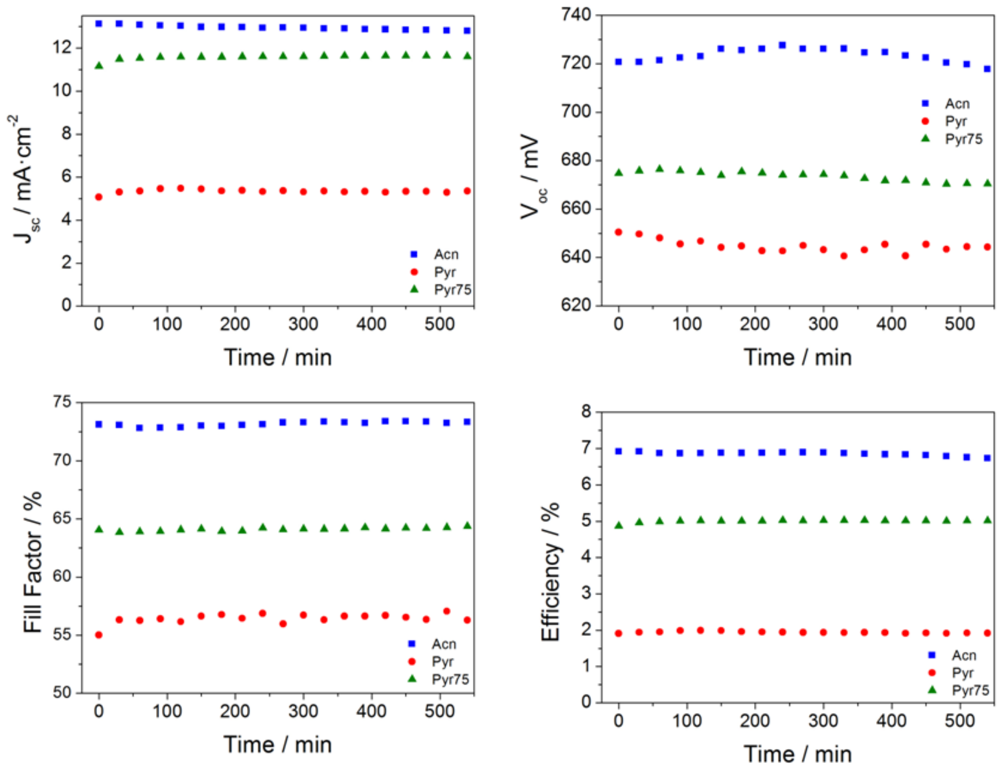

Figure 8.8: Temporal evolution of photovoltaic parameters under irradiance of AM 1.5 for N719-cells using Acn, Pyr and Pry75 as solvent electrolyte.

However, under light soaking for 1000h, a deterioration of 80% and 50% in efficiency have been reported in DSSC containing electrolytes based on pure acetonitrile and mixed solvents (Acn/RTIL, 2:1 v/v), respectively.[15] Therefore, the combination of both components (organic solvent and RTIL) as solvent electrolyte can be interesting for working devices in terms of long stability and low recombination.

3.5. Random Walk Numerical Simulation (RWNS).

The model employed in Ref. 6 has been used to obtain normalized lifetimes for different values of the reorganization energy. The Random Walk Numerical Simulations (RWNS) were performed at room temperature using a simulation box 20 x 20 x 20 nm^3 and an exponential distribution of trap energies (**Equation 1.20**) with α = 0.43 and a total density of traps of N_t = 10^{21} cm^3. A multiple-trapping mechanism of transport was assumed for electrons and a probability of electron recombination described by **Equation 3.14** was considered. Here, it was used E_{redox} − E_c = 0.95 eV, where E_c is the position of the TiO_2 conduction band. On the basis of Ref. 6, two mechanisms of electron recombination were considered: (1) direct recombination for electrons immobilized in traps and (2) recombination for electrons that get detrapped and mobile and can recombine from shallow traps. The relative weight of these two mechanisms is crucial to reproduce the change of behaviour observed in the lifetime. For instance, if process (1) is too slow with respect to (2), the increase in the reorganization energy is not accompanied by a reduction of the lifetime, as observed in the experiments. In accordance to this, a ratio of k_r (1)/ k_r (2) = 10^4 has been considered between the prefactor k_r in Equation 3.14 for both types of recombination. The calculations were arranged to simulate an open-circuit voltage experiment. Hence, 300 electrons were placed at random at T = 0, and then they are allowed to move between traps and recombine. The total population of electrons is then found to decrease with time. From **Equation 3.25** a lifetime can be extracted. Further numerical details can be found in Ref. 6.

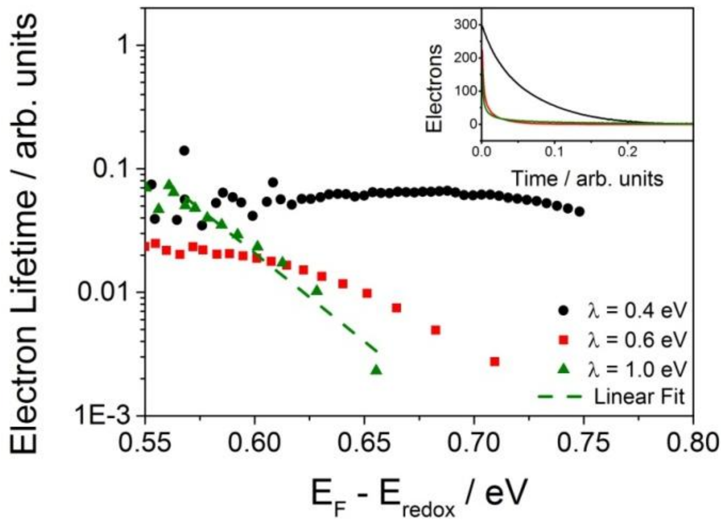

Figure 8.9: Electron lifetime versus voltage ($E_F - E_{redox}$) as derived from RWNS calculations at different values of the reorganization energy λ. The inset shows the time decay of electron population for the three studied cases.

Results for the lifetime-voltage plots for various values of the reorganization energy are presented in **Figure 8.9**. The simulation predicts a change of regime from an exponential trend at large values of reorganization energy to a weaker dependence with respect to voltage at low reorganization energies. Note that in contrast to the simple model of Ref. 18, the simulation does not predict a minimum at $E_F = \lambda$. The fact that recombination takes place simultaneously from an ensemble of surface states implies that there is not a clearly defined minimum when $E_F = \lambda$. What is clearly seen is that the increase of the reorganization energy is accompanied by a shortening of the lifetime. For instance, changing λ from 0.4 to 0.6 eV reduces the lifetime by more than one order of magnitude, which is quite similar to the changes observed in the experiment. Hence, the numerical model reproduces qualitatively the experimental behaviour of the lifetime when the polarity of the solvent is changed.

4. Discussion.

As showed in **Chapter 7**, an exponential behaviour is expected for large reorganization energies. In contrast, a relatively small value of λ implies, from **Equation 3.14**, that the probability of electron recombination is reduced if the starting energy E of electrons is larger than $E_{redox} + \lambda$ (inverted regime), so that a curvature in the lifetime-voltage plot appears. The observed behaviour of the lifetime strongly suggests that the reorganization energy is large for pure and high concentrations of RTILs, whereas for acetonitrile the reorganization energy is smaller. However, as mentioned in the previous chapter, the iodide/tri-iodide system is not a one-electron redox couple and the use of the Marcus model to describe electron transfer from TiO_2 is not straightforward. Nevertheless, it has been demonstrated that the dye regeneration process takes place by one-electron transfer.[28] The real electron acceptor has not been clearly identified, although spectroscopic studies suggest that it is tri-iodide.[29] In any case, the recombination reaction necessarily implies the existence of a first step of electron transfer to a species in the electrolyte. This should involve reorganization energy, associated to the interaction with solvent molecules of this species, whatever it is. A quite different polarity of the surrounding medium will critically determine the value of this reorganization term. Furthermore, it is well-known[7] that λ is larger for polar solvents than for non-polar ones. The observed behaviour of the electron lifetime is then consistent with this interpretation. Recent reports have shown that the dielectric constant of the RTILs studied in this chapter do not have, contrary to what is commonly believed, very high dielectric constants.[30] This would indicate that polarity by itself is not the cause of the effect observed in the present study. However, not only the dielectric constant affects the reorganization energy (outer sphere or solvent component)[15] but also the direct chemical interaction between ligands or solvent molecules with the electrochemically active species.[4] In this regard, the ionic nature of the RTILs makes them strongly solvating agents[31] which explains the huge impact on the lifetime-voltage behaviour.

Apart from the different shape in the lifetime-voltage plot, as already pointed out, the increase in the polarity of the solvent is accompanied by an enhancement of the recombination loss. Similar to **Chapter 7**, larger values of λ accelerates electron recombination. Assuming that the probability of recombination is determined by the Marcus model, i.e., Equation 3.14, a more rapid recombination is explained by the larger availability of acceptor states at higher energies, provided that electrons recombine from high energies as well. The fact that electron recombination takes places from the conduction band, has been considered to explain the behaviour of electron lifetimes and diffusion lengths with respect to illumination and addition of Li^+ ions to the electrolyte.[32,33] However, a recombination mechanism *exclusively* via the conduction band does not explain the non-linear features of the recombination rate, i.e., a β coefficient smaller than one[6,23,34] as observed in the present experiments. To explain the non-linear features, it is necessary to use the model proposed in previous works.[4,6] According to this model, the recombination can take place via: (1) direct electron transfer from localized states in the band gap, and (2) from quasi-free electrons, that get transferred to the electrolyte from high energy levels (**Figure 8.10**). Thus, a larger value of the reorganization energy leads to an enhancement of process (2) added to process (1), hence explaining the change of shape in the lifetime-voltage plot and the shortening of the lifetime.

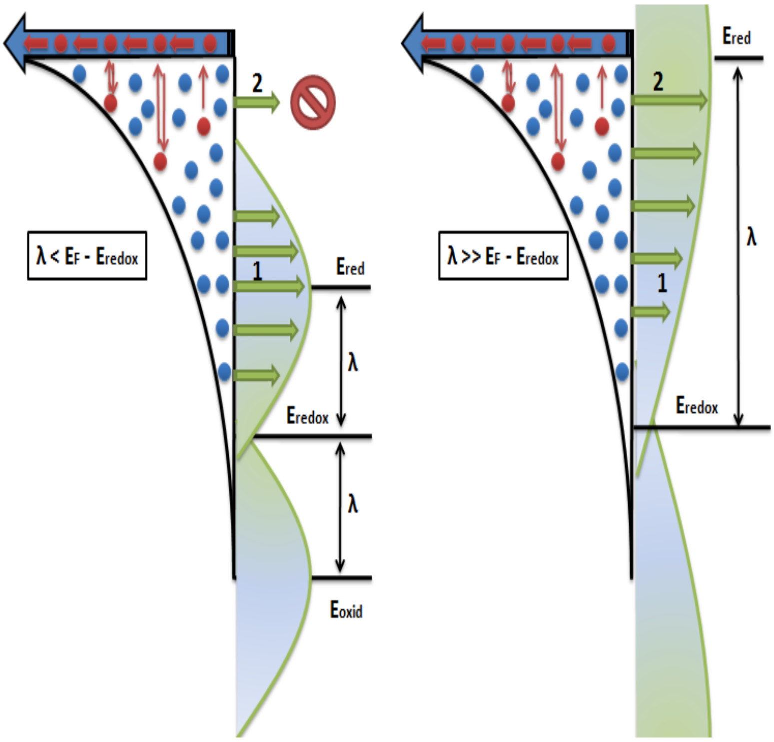

Figure 8.10: Illustration of the effect of reorganization energy and chemical environment on the recombination kinetics across the oxide/electrolyte interface. Left: redox mediator in weak-interacting chemical environment. Right: redox mediator in a strong-interacting chemical environment. In the figure (1) represents direct recombination from trap states and (2) recombination of quasi-free electrons from states close to the transport level.

It has to be mentioned that a different interpretation for the observed trends can be envisioned. As established above, electron recombination is likely to occur with tri-iodide electrons. However, this species is at equilibrium with iodine:

$$I_3^- \leftrightarrow I_2 + I^-$$

The presence of a non-polar solvent will displace this equilibrium to (I_2 + I^-), hence reducing the effective concentration of tri-iodide and then the recombination rate. However, a displacement of the equilibrium will modify the redox potential of the couple. In fact a positive redox potential shift has been reported for water with respect to methoxypropionitrile.[35] A displacement of the redox potential would produce a shift in the measured chemical capacitances. Nonetheless, as already discussed, no shift is observed in the capacitance as the RTIL/Acn mixing ratio is varied (**Appendix**, Figure A-8.3). Therefore, the change of both the shape and the absolute value of the lifetime-voltage plots are due to purely kinetic effects rather than to thermodynamic contributions.

To ascertain the origin of the better short-circuit photocurrent for Pyr-based electrolytes, electron diffusion lengths were estimated, providing information about charge collection.[23,36,37] For small perturbation of the Fermi level, a small-perturbation diffusion length (L_n) was defined and determined by combining IMVS and IMPS data. Values of $L_n \approx$ 30-35 μm and 40-50 μm for Imid75 and Pyr75 respectively (**Appendix**, A-Figure 8.6) were determined. The difference between these values is a consequence of the more effective blocking of recombination for Pyr, evidenced by the higher electron recombination resistance and electron lifetime. In contrast, the electron transport is similar in both cases. The diffusion coefficients increase exponentially with Femi level,[38,39] as usually observed in DSSCs in accordance to the multiple-trapping or hopping models[40,41] in the range between 10^{-5} and 10^{-3} cm^2/s, characteristic of nanocrystalline TiO_2. However, the values of $L_n \approx 3d$ and $4d$ for Imid75 and Pry75 respectively (where d is the thickness of film) suggest that the collection efficiency cannot be considered as exactly 100% at short-circuit conditions.[36,42] Hence, the larger value of L_n for Pry-based electrolytes points to a higher collection efficiency and therefore to a higher photocurrent at short-circuit.

As with the two RTILs, a different behaviour for the two ruthenium dyes N719 and Z907 used to fabricate the solar cells were found. When the I^-/I_3^- redox couple is present in the electrolyte lower performances are reported in Z907-cells respect to N719 as a consequence of higher recombination losses (**Appendix**, Figure A-8.7). The electron lifetimes in N719-cell show a more pronounced departure from the exponential behaviour with the appearance of a minimum, whereas in Z907-cells the curves are flatter. According to the interpretation discussed above, higher reorganization energies are expected for Z907-cells, which could explain the higher recombination losses. (It has to be mentioned that in Z907-cells with cobalt complex as redox couple, these faster recombination kinetics is compensated by the standard redox potential, which is 210mV more positive[43] in the case of $[Co(byp)_3]^{3+/2+}$ than of I^-/I_3^-). A possible explanation for the different reorganization energies for both dyes is the presence of two hydrocarbon chains in the Z907 sensitizer. These bulky and apolar groups can modify the local chemical environment of the electron acceptors in the vicinity of the TiO_2 surface by pushing away acetonitrile molecules, hence increasing the reorganization energy.

5. Conclusions

In this chapter a comprehensive study of the photovoltaic performance of acetonitrile/room-temperature-ionic-liquid (RTIL) mixtures in Dye-sensitized solar cells has been carried out. In particular, a comparison of the two ionic liquids that differ by the nature of the cations that enter their composition (*Imidazolium*- and *Pyrrolidinium*-based) and two ruthenium dyes (N719 and Z907) have been performed. The electron recombination resistance, chemical capacitance and electron lifetime have been determined as a function of Fermi level position by Impedance Spectroscopy and Open-Circuit Voltage Decay.

The electron lifetime shows two types of behaviour: one exhibiting a minimum in the lifetime-voltage plot (acetonitrile), and the other characterized by a pure exponential behaviour (RTIL). A progressive transition between both kinds of shape in the lifetime-voltage plot is observed as the acetonitrile/RTIL mixing ratio is modified. According to previous experimental and theoretical reports, as well as exploratory Random Walk Numerical Simulations, this behaviour of the electron lifetime can be explained by an increase in the value of the reorganization energy for electron recombination as we move from a less polar environment (acetonitrile) to a more polar one. Assuming this interpretation, systems with large reorganization energies have higher recombination losses, as it is the case in electrolytes based on ionic liquids. These observations can be related to the existence of two electron recombination routes, one produced from deep traps and the other mediated by shallow traps, in such a way that a large reorganization energy allows for a larger contribution of this second route, hence reducing the lifetime.

Interestingly, the change of behaviour in the lifetime-voltage plot for pure ionic liquids is produced by solvation with only a minor fraction of acetonitrile. Hence, ionic liquids solvated with relatively small amounts of organic solvents are not only an interesting electrolyte formulation in DSSC due to a diminution of the mass-transport limitation, but also due to the decrease of the electron recombination rate (as a result of the reduction of reorganization energy). Furthermore, according to the results here presented, it is found that the reorganization energy is not only determined by polarity of the solvents, but also by the dye used.

Finally, it is important to point out that the nature of the cation of the RTIL is also critical when it comes to reduce the electron recombination. In this respect pyrrolidinium cations show a much better performance than the more commonly used imidazolium. As a consequence of the blocking of recombination, not only an increase in V_{oc} is observed, but also an enhancement of J_{sc} (consequence of a not too long diffusion length). This finding may open opportunities for the application of pyrrolidinium-based RTIL, largely used in batteries, in the DSSC field.

6. References.

(1) Yella, A.; Lee, H.-W.; Tsao, H. N.; Yi, C.; Chandiran, A. K.; Nazeeruddin, M. K.; Diau, E. W.-G.; Yeh, C.-Y.; Zakeeruddin, S. M.; Grätzel, M. Porphyrin-Sensitized Solar Cells with Cobalt (II/III)–Based Redox Electrolyte Exceed 12 Percent Efficiency. *Science* **2011**, *334*, 629–634.

(2) Fabregat-Santiago, F.; Bisquert, J.; Palomares, E.; Otero, L.; Kuang, D. B.; Zakeeruddin, S. M.; Gratzel, M. Correlation between Photovoltaic Performance and Impedance Spectroscopy of Dye-Sensitized Solar Cells Based on Ionic Liquids. *J. Phys. Chem. C* **2007**, *111*, 6550–6560.

(3) Shi, D.; Pootrakulchote, N.; Li, R. Z.; Guo, J.; Wang, Y.; Zakeeruddin, S. M.; Gratzel, M.; Wang, P. New Efficiency Records for Stable Dye-Sensitized Solar Cells with Low-Volatility and Ionic Liquid Electrolytes. *J. Phys. Chem. C* **2008**, *112*, 17046–17050.

(4) Idígoras, J.; Pellejà, L.; Palomares, E.; Anta, J. A. The Redox Pair Chemical Environment Influence on the Recombination Loss in Dye-Sensitized Solar Cells. *J. Phys. Chem. C* **2014**, *118*, 3878–3889.

(5) Bisquert, J.; Fabregat-Santiago, F.; Mora-Seró, I.; Garcia-Belmonte, G.; Giménez, S. Electron Lifetime in Dye-Sensitized Solar Cells: Theory and Interpretation of Measurements. *J. Phys. Chem. C* **2009**, *113*, 17278–17290.

(6) Gonzalez-Vazquez, J. P.; Oskam, G.; Anta, J. A. Origin of Nonlinear Recombination in Dye-Sensitized Solar Cells: Interplay between Charge Transport and Charge Transfer. *J. Phys. Chem. C* **2012**.

(7) Bisquert, J.; Marcus, R. A. Device Modeling of Dye-Sensitized Solar Cells. In; Topics in Current Chemistry; Springer Berlin Heidelberg, 2013; pp. 1–71.

(8) Ondersma, J. W.; Hamann, T. W. Measurements and Modeling of Recombination from Nanoparticle TiO2 Electrodes. *J. Am. Chem. Soc.* **2011**, *133*, 8264–8271.

(9) Liu, Y.; Hagfeldt, A.; Xiao, X.-R.; Lindquist, S.-E. Investigation of Influence of Redox Species on the Interfacial Energetics of a Dye-Sensitized Nanoporous TiO2 Solar Cell. *Sol. Energy Mater. Sol. Cells* **1998**, *55*, 267–281.

(10) Kelly, C. A.; Farzad, F.; Thompson, D. W.; Stipkala, J. M.; Meyer, G. J. Cation-Controlled Interfacial Charge Injection in Sensitized Nanocrystalline TiO2. *Langmuir* **1999**, *15*, 7047–7054.

(11) Nakade, S.; Kanzaki, T.; Kubo, W.; Kitamura, T.; Wada, Y.; Yanagida, S. Role of Electrolytes on Charge Recombination in Dye-Sensitized TiO2 Solar Cell (1): The Case of Solar Cells Using the I-/I3⊖ Redox Couple. *J. Phys. Chem. B* **2005**, *109*, 3480–3487.

(12) Pelet, S.; Moser, J.-E.; Grätzel, M. Cooperative Effect of Adsorbed Cations and Iodide on the Interception of Back Electron Transfer in the Dye Sensitization of Nanocrystalline TiO2. *J. Phys. Chem. B* **2000**, *104*, 1791–1795.

(13) Kambe, S.; Nakade, S.; Wada, Y.; Kitamura, T.; Yanagida, S. Effects of Crystal Structure, Size, Shape and Surface Structural Differences on Photo-Induced Electron Transport in TiO2 Mesoporous Electrodes. *J Mater Chem* **2002**, *12*, 723–728.

(14) Nakade, S.; Kambe, S.; Kitamura, T.; Wada, Y.; Yanagida, S. Effects of Lithium Ion Density on Electron Transport in Nanoporous TiO2 Electrodes. *J. Phys. Chem. B* **2001**, *105*, 9150–9152.

(15) Yu, Z.; Vlachopoulos, N.; Hagfeldt, A.; Kloo, L. Incompletely Solvated Ionic Liquid Mixtures as Electrolyte Solvents for Highly Stable Dye-Sensitized Solar Cells. *RSC Adv.* **2013**, *3*, 1896–1901.

(16) Reynal, A.; Forneli, A.; Palomares, E. Dye Structure–charge Transfer Process Relationship in Efficient Ruthenium-Dye Based Dye Sensitized Solar Cells. *Energy Env. Sci* **2010**, *3*, 805–812.

(17) Halme, J. Linking Optical and Electrical Small Amplitude Perturbation Techniques for Dynamic Performance Characterization of Dye Solar Cells. *Phys. Chem. Chem. Phys.* **2011**, *13*.

(18) Zaban, A.; Greenshtein, M.; Bisquert, J. Determination of the Electron Lifetime in Nanocrystalline Dye Solar Cells by Open-Circuit Voltage Decay Measurements. *Chemphyschem* **2003**, *4*, 859–864.

(19) Bisquert, J. Theory of the Impedance of Electron Diffusion and Recombination in a Thin Layer. *J. Phys. Chem. B* **2002**, *106*, 325–333.

(20) Fabregat-Santiago, F.; Bisquert, J.; Garcia-Belmonte, G.; Boschloo, G.; Hagfeldt, A. Influence of Electrolyte in Transport and Recombination in Dye-Sensitized Solar Cells Studied by Impedance Spectroscopy. *Sol. Energy Mater. Sol. Cells* **2005**, *87*, 117–131.

(21) Cameron, P. J.; Peter, L. M. How Does Back-Reaction at the Conducting Glass Substrate Influence the Dynamic Photovoltage Response of Nanocrystalline Dye-Sensitized Solar Cells? *J. Phys. Chem. B* **2005**, *109*, 7392–7398.

(22) Anta, J. A.; Idígoras, J.; Guillén, E.; Villanueva-Cab, J.; Mandujano-Ramírez, H. J.; Oskam, G.; Pellejà, L.; Palomares, E. A Continuity Equation for the Simulation of the Current–voltage Curve and the Time-Dependent Properties of Dye-Sensitized Solar Cells. *Phys. Chem. Chem. Phys.* **2012**, *14*, 10285–10299.

(23) Bisquert, J.; Mora-Seró, I. Simulation of Steady-State Characteristics of Dye-Sensitized Solar Cells and the Interpretation of the Diffusion Length. *J. Phys. Chem. Lett.* **2010**, *1*, 450–456.

(24) Kubo, W.; Kambe, S.; Nakade, S.; Kitamura, T.; Hanabusa, K.; Wada, Y.; Yanagida, S. Photocurrent-Determining Processes in Quasi-Solid-State Dye-Sensitized Solar Cells Using Ionic Gel Electrolytes. *J. Phys. Chem. B* **2003**, *107*, 4374–4381.

(25) Noda, A.; Hayamizu, K.; Watanabe, M. Pulsed-Gradient Spin−Echo 1H and 19F NMR Ionic Diffusion Coefficient, Viscosity, and Ionic Conductivity of Non-Chloroaluminate Room-Temperature Ionic Liquids. *J. Phys. Chem. B* **2001**, *105*, 4603–4610.

(26) Kuang, D. B.; Klein, C.; Ito, S.; Moser, J. E.; Humphry-Baker, R.; Evans, N.; Duriaux, F.; Graetzel, C.; Zakeeruddin, S. M.; Graetzel, M. High-Efficiency and Stable Mesoscopic Dye-Sensitized Solar Cells Based on a High Molar Extinction Coefficient Ruthenium Sensitizer and Nonvolatile Electrolyte. *Adv. Mater.* **2007**, *19*, 1133–1137.

(27) Ansari-Rad, M.; Abdi, Y.; Arzi, E. Reaction Order and Ideality Factor in Dye-Sensitized Nanocrystalline Solar Cells: A Theoretical Investigation. *J Phys Chem C* **2012**, *116*, 10867–10872.

(28) Boschloo, G.; Hagfeldt, A. Characteristics of the Iodide/Triiodide Redox Mediator in Dye-Sensitized Solar Cells. *Acc. Chem. Res.* **2009**, *42*, 1819–1826.

(29) Rowley, J.; Meyer, G. J. Reduction of I2/I3− by Titanium Dioxide. *J. Phys. Chem. C* **2009**, *113*, 18444–18447.

(30) ZHOU, Y.; LIN, Z.; WU, K.; XU, G.; HE, C. A Group Contribution Method for the Correlation of Static Dielectric Constant of Ionic Liquids. *Chin. J. Chem. Eng.* **2014**, *22*, 79–88.

(31) Castner, E. W.; Wishart, J. F.; Shirota, H. Intermolecular Dynamics, Interactions, and Solvation in Ionic Liquids. *Acc. Chem. Res.* **2007**, *40*, 1217–1227.

(32) Jennings, J. R.; Li, F.; Wang, Q. Reliable Determination of Electron Diffusion Length and Charge Separation Efficiency in Dye-Sensitized Solar Cells. *J. Phys. Chem. C* **2010**, *114*, 14665–14674.

(33) Jennings, J. R.; Wang, Q. Influence of Lithium Ion Concentration on Electron Injection, Transport, and Recombination in Dye-Sensitized Solar Cells. *J. Phys. Chem. C* **2010**, *114*, 1715–1724.

(34) Ansari-Rad, M.; Abdi, Y.; Arzi, E. Simulation of Non-Linear Recombination of Charge Carriers in Sensitized Nanocrystalline Solar Cells. *J. Appl. Phys.* **2012**, *112*, 074319–074319 – 7.

(35) Boschloo, G.; Gibson, E. A.; Hagfeldt, A. Photomodulated Voltammetry of Iodide/Triiodide Redox Electrolytes and Its Relevance to Dye-Sensitized Solar Cells. *J Phys Chem Lett* **2011**, 3016–3020.

(36) Peter, L. M. Characterization and Modeling of Dye-Sensitized Solar Cells. *J. Phys. Chem. C* **2007**, *111*, 6601–6612.

(37) Gonzalez-Vazquez, J.; Anta, J. A.; Bisquert, J. Determination of the Electron Diffusion Length in Dye-Sensitized Solar Cells by Random Walk Simulation: Compensation Effects and Voltage Dependence. *J. Phys. Chem. C* **2010**, *114*, 8552–8558.

(38) Wang, Q.; Ito, S.; Gratzel, M.; Fabregat-Santiago, F.; Mora-Sero, I.; Bisquert, J.; Bessho, T.; Imai, H. Characteristics of High Efficiency Dye-Sensitized Solar Cells. *J. Phys. Chem. B* **2006**, *110*, 25210–25221.

(39) Peter, L. M.; Wijayantha, K. G. U. Electron Transport and Back Reaction in Dye Sensitised Nanocrystalline Photovoltaic Cells. *Electrochimica Acta* **2000**, *45*, 4543–4551.

(40) Anta, J. A.; Mora-Sero, I.; Dittrich, T.; Bisquert, J. Interpretation of Diffusion Coefficients in Nanostructured Materials from Random Walk Numerical Simulation. *Phys. Chem. Chem. Phys.* **2008**, *10*, 4478–4485.

(41) Bisquert, J. Chemical Diffusion Coefficient of Electrons in Nanostructured Semiconductor Electrodes and Dye-Sensitized Solar Cells. *J. Phys. Chem. B* **2004**, *108*, 2323–2332.

(42) Sivaram, V.; Kirkpatrick, J.; Snaith, H. Critique of Charge Collection Efficiencies Calculated through Small Perturbation Measurements of Dye Sensitized Solar Cells. *J. Appl. Phys.* **2013**, *113*, 063709–063709 – 6.

(43) Liu, Y.; Jennings, J. R.; Huang, Y.; Wang, Q.; Zakeeruddin, S. M.; Grätzel, M. Cobalt Redox Mediators for Ruthenium-Based Dye-Sensitized Solar Cells: A Combined Impedance Spectroscopy and Near-IR Transmittance Study. *J Phys Chem C* **2011**, *115*, 18847–18855.

Chapter 9:

Global analysis of Dye-Sensitized Solar Cells: Influence of the electrical nature of the metal-oxide

1. Introduction.

The development of new types of dyes, electrolytes and alternative semiconductors for DSSC is a subject that it is still widely investigated. Furthermore, the advent of new technologies like perovskite solar cells makes it very interesting to gain fundamental knowledge of the capability of metal oxides to act as efficient photoanodes in solar cells in general. In this chapter a fundamental study of the influence of the electrolyte composition in contact with two semiconductors has been carried out taking into account *all* processes that control charge separation at the semiconductor surface.

One of the commonly used approaches to optimize the efficiency of DSSC is to use certain additives in the electrolyte that shift the electrochemical potential of the conduction band of TiO_2 nanoparticles. These *potential-determining* additives can improve the open circuit voltage (V_{OC}) of the cell at the expense of a slight decrease of the short circuit current density (J_{SC}) or with the opposite effect.[1] Despite known effects on the global parameters, detailed studies on the microscopic action of these additives at the interfaces in DSSC still brings new findings.[2] On the other hand, photoanodes prepared with ZnO have been studied as an alternative to TiO_2, being the second most used semiconductor. Although in many aspects the properties of ZnO are advantageous with respect to those of TiO_2 (better transport properties in the bulk and easy fabrication of different nanostructures), the best efficiencies of ZnO-based cells are far behind those of TiO_2-based cells.[3,4]

All these issues will be studied in this chapter. Bearing in mind the importance on DSSC functioning of semiconductor/electrolyte, the aim of this chapter is to compare the effect of different electrolyte additives on the properties of DSSCs with TiO_2 and ZnO as photoanodes using the standard ruthenium dye N719 (*cis-diisothiocyanato-bis(2,2'-bipyridyl-4,4'-dicarboxylato) ruthenium(II) bis (tetrabutylammonium).* In contrast to many previous reports, time-resolved spectroscopy techniques and electrochemical measurements have been combined. Therefore, the kinetics of injection and dye regeneration on the short-time scale and information on the oxide/electrolyte interface (like the chemical capacitance or the electron lifetime) has been obtained. Time-resolved spectroscopic studies in real, functioning solar cells, has been performed making it possible to correlate the data with cell performance. Time-resolved laser spectroscopy has been widely applied to study the primary steps in charge separation in DSSCs, especially for those based on Ru compounds.[5–8] Recent reports point out the importance of the measurements of complete devices rather than isolated systems to obtain the relevant information for cells under working conditions.[9–15]

The obtained results for conventional DSSCs are very important for one hot topic related to the semiconductor/dye/electrolyte interface: the recently proposed coordinated shifts of interfacial energy levels of the semiconductor as well as those of the dye in DSSC in the presence of typical additives.[16] This issue drastically changes the typical understanding of the working principles of this kind of solar cells, and our findings bring a novel and deeper look into the fundamental processes behind the operation of the DSSC. In addition, based on the novel insights here obtained, a molecular interpretation of the reasons why ZnO solar cells perform poorly compared to TiO_2 cells is proposed.

2. Experimental Section.

2.1. Fabrication of Dye-Sensitized Solar cells.

Solar cell devices were fabricated using films consisting of a layer of 20 nm TiO_2 nanoparticles (*Dyesol© paste*) or 40 - 100 nm ZnO nanoparticles prepared by a forced hydrolysis method by the group of Professor Gerko Oskam (**Appendix**, Figure A-9.1).[17] Prior to the deposition of the different films, the substrates (Pilkington-TEC 15) were carefully cleaned in an ultrasonic bath using detergents, deionized water, isopropanol and ethanol successively, and secondly, heated to 500ºC. Films were deposited onto the conducting glass substrates with the screen printing method. The active area of the films was 0.16 cm^2 with a thickness of 5μm and 3.5 μm for TiO_2 and ZnO electrodes, respectively. The films were gradually heated under airflow until 500°C for TiO_2 electrodes and 450°C for ZnO electrodes. Only for TiO_2 electrodes, after cleaning the substrates and sintering the films, an immersion step in a solution of $TiCl_4$ (40 mM) at 70°C for 30 min was carried out. Finally, TiO_2 electrodes were heated again at 500°C for 30 min and cooled before dye adsorption.

The counter-electrode (Pilkington-TEC 8) was prepared by spreading *Platisol* (Solaronix) onto the conducting glass substrate followed by heating at 390°C for 15 minutes. A small hole was perforated in the counter electrode to allow for the introduction of the liquid electrolyte into the cell.

TiO_2 electrodes were immersed overnight in a solution containing the ruthenium dye coded N719, whereas ZnO electrodes were only immersed for 1 hour. This solution was composed of 0.3 mM N719 and 0.3 mM chenodeoxycholic acid in ethanol. The sensitized electrodes were washed with ethanol and dried in air. Finally, the working and counter-electrodes were sandwiched together using a thin thermoplastic frame (*Surlyn*, Solaronix). The cells were filled with the electrolyte by vacuum through the hole previously perforated in the platinized counter-electrode, which was sealed with the thermoplastic polymer and a cover-glass slide.

The composition of the electrolytes studied in this chapter is shown in **Table 9.1**. Only Acetonitrile (99.9%, Panreac) as solvent is kept in all studied devices, whereas the redox pair and the additives are varied.

Series (Redox Pair)	Electrolyte	Additives
Series 1: I_2/LiI	Reference	**0.03M I_2 + 0.5M LiI**
	Pyr	0.03M I_2 + 0.5M LiI +**0.5M Pyr**
	Tbp	0.03M I_2 + 0.5M LiI + **0.5M Tbp**
	TP	0.03M I_2 + 0.5M LiI + **0.5M Tbp + 0.5M Pyr**
Series 2: I_2/BMII	Reference	**0.03M I_2 + 1M BMII**
	Li	0.03M I_2 + 1M BMII + **0.05M LiI**
	Tbp	0.03M I_2 + 1M BMII + **0.5M Tbp**

Series 3: I_2/DMPII	Reference	**0.03M I_2 + 1M DMPII**
	Li(x1)	0.03M I_2 + 1M DMPII + **0.05M LiI**
	Li(x2)	0.03M I_2 + 1M DMPII + **0.10M LiI**
	Li(x3)	0.03M I_2 + 1M DMPII + **0.15M LiI**
	Tbp	0.03M I_2 + 1M DMPII + **0.5M Tbp**

Table 9.1: Composition of the electrolytes studied in this work. I_2: Iodine (99.5%,Fluka), LiI: Lithium iodide (99%,Aldrich), Tbp: 4-tert-butylpiridine (96%,Aldrich), Pyr: 1-Buthyl-1-Methylpyrrolidinium bis(trifluoromethanesulfonyl)imide (99.9%, Solvionic), BMII: 1-butyl-3-methylimidalozlium iodide (99%,Aldrich), DMPII: 1,2-Dimethyl-3-propylimidazolium iodide (>98%, Iolitec).

2.2. Characterization of solar devices.

The devices were characterized using a solar simulator equipped with an AM1.5G filter (*ABET*). The light intensity was calibrated to the standard value of 1 sun (100 mW/cm^2) using a reference solar cell with temperature output (*Oriel,* 91150). The current-voltage characteristics were determined by applying an external potential bias to the cell and measuring the photocurrent using an *Autolab/PGSTAT302N* potentiostat.

Electrochemical impedance spectroscopy (EIS) was utilized to study the chemical capacitance in order to monitor the shift of the band system of the oxide in the presence of different additives in the electrolyte. The illumination for this small perturbation (frequency response) technique was provided by a 530 nm light emitting diode (*LUXEON*) over a wide range of DC light intensities. This allows for probing the devices at different positions of the Fermi level in the semiconductor. A response analyzer module (*PGSTAT302N/FRA2, AutoLab*) was utilized to analyze the frequency response of the devices. To avoid voltage drop due to series resistance, EIS measurements were performed at the open circuit potential, the Fermi level (related to the open-circuit voltage) being fixed by the DC illumination intensity. A 10 mV perturbation in the 10^{-5} to 10^{-2} Hz range was utilized to obtain the spectra. Zview equivalent circuit modelling software (*Scribner*) was used to fit the EIS spectra, including the distributed element DX11 (transmission line model).

The nanosecond flash photolysis setup is based on a *Q-switched Nd:YAG laser* (excitation wavelength 532 nm) and a 150 W xenon arc lamp (probing light source).[18] The time-resolved emission measurements in the picosecond time window were performed using a time-correlated single photon counting technique (TCSPC).[19] TCSPC measurements were carried out at the magic angle with the excitation wavelength of 425 nm. The same setup was used to measure steady-state emission spectra. The steady-state UV-visible absorption spectra were measured with a *UV-VIS-550* (*Jasco*) spectrophotometer.

For ultrafast transient absorption experiments a commercial femtosecond broadband transient absorption spectrometer (*Helios, Ultrafast Systems*) was used in a single-beam configuration, with an all reflective white light continuum generator and depolarizer in the pump beam to avoid influence of rotational dynamics. The femtosecond pulses were provided by a Spectra Physics setup consisting of a MaiTai SP oscillator, a Spitfire Ace amplifier (pumped by an Empower laser) and a Topas Prime wavelength converter (optical parametric amplifier). The pump pulses were set at 535 nm. Typical IRF (pump-probe cross correlation function) was 250-300 fs. In most experiments, the pump pulse energy was 500 nJ, corresponding to an energy density of about 1 mJ/cm^2. In some experiments 160 nJ and 1.8 μJ pulses were also used. The probe light continuum was generated in a sapphire or YAG-type crystal. All spectra analysed were corrected for chirp of white light continuum. The transient absorption measurements were performed in the spectral ranges of 450-800 nm (VIS) and 800-1400 nm (NIR) and in the time range of up to 3 ns. The global analysis of the transient absorption data was performed using Surface Explorer software (Ultrafast Systems), which fits a multi-exponential function (convoluted with IRF) to the kinetic vectors of a selected number of singular values and reproduces the spectra of the amplitudes associated with the time components. As a result of the analysis the characteristic time constants were obtained as well as the wavelength-dependent amplitudes associated with them (also called decay associated difference spectra).

3. Results and Discussion.

3.1. Current-voltage characteristics of solar cells and electrochemical impedance studies.

Figure 9.1 shows the current-voltage characteristics under 1-*sun* AM1.5G illumination of the best TiO_2 and ZnO solar cells employing N719 as sensitizer and with an electrolyte based on the I_2/DMPII redox pair and different *potential-determining* additives. Higher photocurrents and photovoltages were found in TiO_2 cells (6.30 mA/cm^2 and 720 mV) with respect to ZnO cells (3.35 mA/cm^2 and 650 mV) when the Reference electrolyte composition was used. For TiO_2 cells, Li^+ and Tbp were found to produce the well-known effects in photovoltage and photocurrent, which is commonly explained by positive and negative band-shifts in the semiconductor metal oxide band edge. In contrast, no significant changes were found between the different electrolytes in ZnO cells. Similar behaviour was found in *Series 2* (**Appendix**, Figure A-9.2B).

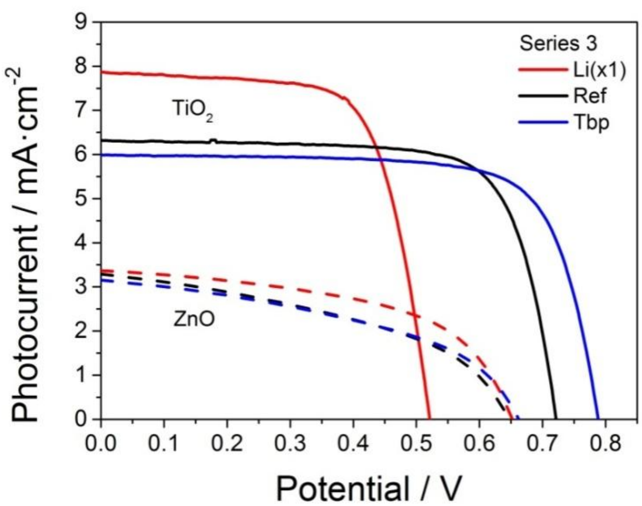

Figure 9.1: Current-voltage curves under 1-sun AM1.5G illumination for DSSC based on TiO_2 and ZnO electrodes with different electrolytes.

To analyze the shifts in the semiconductor band edges, the chemical capacitance (C_{μ}) was determined by EIS. In **Figure 9.2**, the chemical capacitance extracted from EIS analysis at different potentials is shown for *Series 3*. The EIS results show that the capacitance is not altered in ZnO cells in the presence of different *potential-determining* additives. Similar results have been recorded for *Series 2* (**Appendix**, Figure A-9.2A). Thus, it is possible to infer from these results that no significant shifts of the photoanode electronic levels are taking place for ZnO solar cells, in striking contrast to TiO_2.

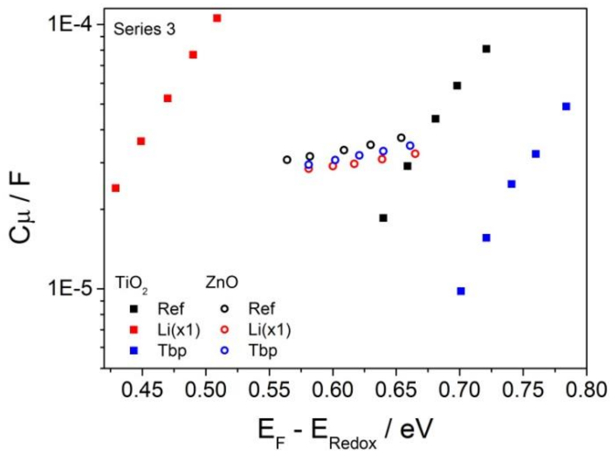

Figure 9.2: Chemical capacitance data as extracted from EIS measurement for TiO_2-cells and ZnO-cells using different potential-determining additives as Li and Tbp.

As mentioned in **Chapter 3**, for TiO_2 it is known that conduction band edge (E_{CB}) shifts towards lower energy under the presence of Li^+ in the electrolyte due to surface adsorption and the formation of negative dipoles, whereas E_{CB} shifts towards higher energy upon the addition of Tbp in the electrolyte.[20–22] In the latter case, in response to the electron-rich nitrogen in Tbp, a positive dipole appears. In general, it can be stated that Lewis acids (like metal cations) tend to shift the band towards positive potentials, whereas Lewis bases (like electron-rich nitrogen compounds) produce the opposite effect. In this context, we can expect that the dielectric constant of the oxide plays a determining role. Thus, due to its lower dielectric constant, the formation of surface dipoles across the ZnO surface is more difficult and, probably, this could explain why the capacitance and E_{CB} in ZnO cells are less sensitive to the presence of these additives.

Finally, it is important to mark the difference of the trap distribution parameter α (0.48 for TiO_2 and 0.055 for ZnO), related to the energy of the exponential distribution of localized states in the oxide (see **Equation 1.20**). This is a very typical result in ZnO-based solar cells that points to a relatively higher density of deep traps states and doping level in the ZnO electrodes.[23,24] In this respect, it is pertinent to mention here that ZnO nanostructured materials obtained via wet chemical methods tend to be highly doped.[23,25,26] The relatively high carrier concentration may also contribute to the small voltage dependence of the capacitance and its small shift in the presence of additives.

3.2. Steady-state absorption and emission studies.

Figure A-9.3 in the **Appendix** presents the steady-state spectra of the TiO_2 and ZnO nanoparticle films sensitized with N719 (after correction for the background due to scattering and absorption of the metal oxide), which were used for the preparation of all solar cells. The differences in the N719 absorbance at the maximum (0.65 for TiO_2 and 0.35 for ZnO) are mainly related to the measured different thickness of the metal oxide films (5 µm for TiO_2 and 3.5 µm for ZnO), and the lower surface area for the ZnO films related to the larger particle size as compared to TiO_2. Knowing the steady-state spectra it is possible to calculate the number of absorbed photons under AM 1.5G illumination (N_{ph}), which are 6×10^{16} $s^{-1}cm^{-2}$ for TiO_2 cells and 3.5×10^{16} $s^{-1}cm^{-2}$ for ZnO cells. Therefore, these values are used for the calculation of the relative photocurrent of each cell (J_{SC}/N_{ph}), which has to be used to compare the charge separation quantum yields of the cells with different light absorption. The J_{SC}/N_{ph} values, together with V_{OC} and J_{SC} of all solar cells studied in this chapter are presented in **Appendix** (Table A-9.1). In general, larger J_{SC}/N_{ph} ratios are found for TiO_2 cells, which points to a better charge separation in this semiconductor/dye system in comparison to ZnO. This is consistent with previous reports.[27]

Figure A-9.3 in the **Appendix** also presents emission spectra of the triplet state for *Series 1* of electrolytes. Within each series of metal oxide and electrolyte, the phosphorescence maxima are similar for different electrolytes. For all TiO_2 cells the maxima are at 700 ± 10 nm, while for ZnO cells they are red shifted: at 760 ± 10 nm for *Series 1* and *Series 3* of electrolytes and at 720 ± 10 nm for *Series 2* of electrolytes. This indicates that the energy gap between T_1 and S_0 states is constant within ± 0.02-0.03 eV for different additives in each series of electrolytes.

3.3. Flash photolysis studies.

A representative probe wavelength (700 nm) was selected to monitor the dynamics of dye regeneration as a function of electrolyte additives (LiI and Tbp) for TiO_2 and ZnO cells. The kinetics at 700 nm for cells of the *Series 2* is shown in **Figure 9.3** with the corresponding rate constants of the decays. There is a clear dependence on the observed rate constants on the electrolyte additives: regeneration is the fastest for samples with LiI, while it is the slowest when Tbp is used. This result clearly supports a recently proposed shift of HOMO levels of the ruthenium dyes in the presence of different additives.[16] When LiI is added, the HOMO level of N719 shifts towards more positive potential (lower energy),[16] increasing the driving force (ΔG_{reg}) for dye regeneration. The opposite situation (with respect to the reference cells) occurs upon addition of Tbp, which causes the shift of HOMO level towards more negative potentials and the reduction of energy gap ΔG_{reg}. Since the concentration of the redox couple is the same for Li, Reference and Tbp electrolytes, the regeneration rate should not change between electrolytes if there is no shift in relative position between redox and HOMO potentials. It should be noted that in principle steric factors and local field created by additive ions can also influence the regeneration rate.[28] However, the changes in the regeneration rate upon addition of Tbp were not observed in the cells with organic dye[29] for which the HOMO level shift is not expected.[16] Thus, the shift in HOMO level upon addition of Tbp is probable the main factor modifying the regeneration rate.

Moreover, the regeneration is slower for ZnO samples than that for corresponding TiO_2 cells (about 2 times for Reference and Tbp cells and about 4 times for Li cells). A recently report[27] observed similar differences for the solar cells sensitized with the indoline dye D149. The present results obtained for a completely different dye suggests that the differences between regeneration rates on both metal oxides depend mainly on the physicochemical nature of the metal oxide. Furthermore, the electrolyte effect in the case of ZnO is much smaller than in TiO_2: for instance the rate constant remains almost the same when Li^+ ions are added to the electrolyte in the case of ZnO cells, whereas for TiO_2 cells, the regeneration rate constant become doubled. This insensitivity of the regeneration kinetics upon variation of electrolyte compositions in the case of ZnO is likely connected to the small shift of band edges mentioned above.

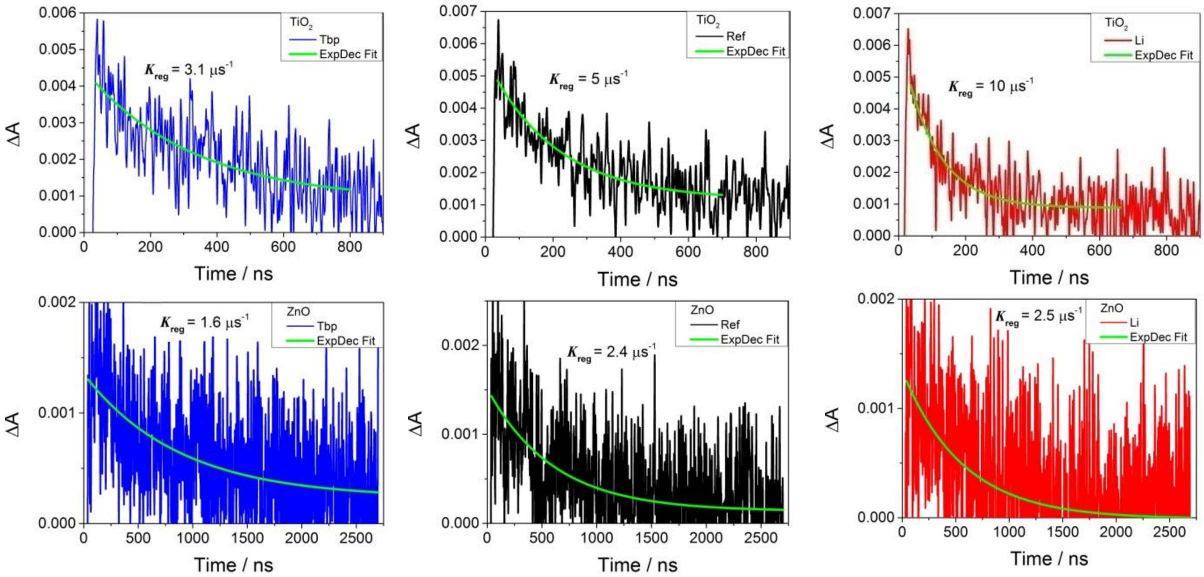

Figure 9.3: Kinetics at 700 nm obtained in flash photolysis experiments for the cells of *Series 2* using a pump pulse fluence of 1.3mJ/cm^2. The green solid lines represent one-exponential fits.

As described in **Chapter 4**, the decay of the oxidized dye absorption band observed in flash photolysis experiments can be due to dye regeneration and/or electron recombination (back electron transfer from the semiconductor to the dye). Recently, a precise procedure to obtain the electron recombination rate in functioning solar cells with electrolytes was proposed.[14] In this chapter, its determination is beyond the scope of the work, but it is important to check that the rates presented above are not influenced by electron recombination processes. To do so, control experiments were developed with pump pulse fluences of different energy (5.2 mJ/cm^2, 1.3 mJ/cm^2 and 0.25 mJ/cm^2) (**Appendix**, Figure A-9.4). Unlike dye regeneration, electron recombination dynamics depend on the concentration of electrons in the oxide film, being faster for higher pump pulse fluence.[30–32] Therefore, if recombination contributes to the measured decay of the oxidized dye, some increase in the decay rates with pump fluence should be observed.

Figure A-9.4 of the **Appendix** shows the results obtained for TiO_2/S2/Tbp cell. It is observed that for higher pump fluence (5.2 mJ/cm^2) the decay becomes faster, which indicates that electron recombination starts to compete with dye regeneration. However, for lower energy densities (1.3 mJ/cm^2 and 0.25 mJ/cm^2) the time constants are the same. This means that the pump fluence used in flash photolysis (1.3 mJ/cm^2) is safe enough to observe only the regeneration process, at least for TiO_2 cells. For ZnO cells it was not possible to measure the kinetics for lower pump fluence due to too weak signal intensities.

3.4. Emission decays studies.

Emission decays were measured in the maximum of phosphorescence spectrum and upon excitation at 425 nm for all series of cells in ps-ns time scale. **Figure 9.4** shows representative emission decay traces for TiO_2, ZnO and Al_2O_3 cells.

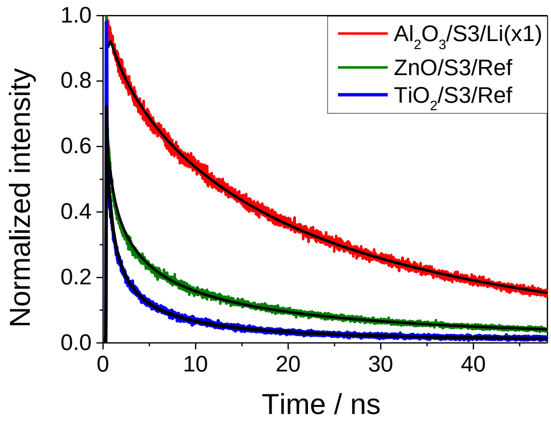

Figure 9.4: Representative emission decay traces for the indicated cells. The black solid lines represent best fits to Equation 4.22.

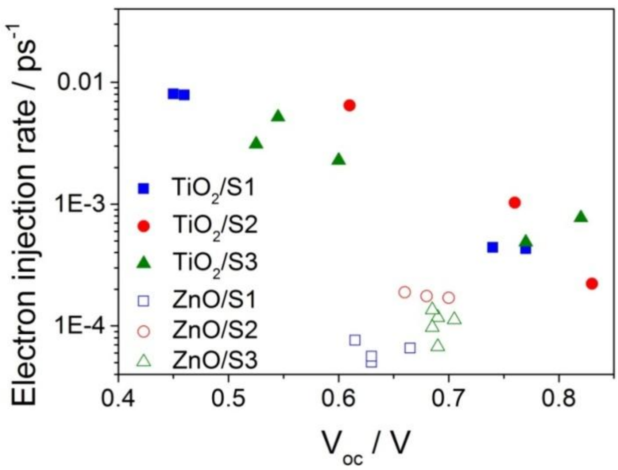

Figure 9.5: Electron injection rate constants from triplet state obtained from time-resolved emission experiments (phosphorescence) as a function of V_{OC} of the cells.

The fitted parameters and averaged decay rate constants (k_{AVG}) (see **Equation 4.22** and **4.23**) are presented in **Figure 9.5** and in the **Appendix** (Table A-9.2). The obtained lifetimes of the triplet state are generally long, in the nanosecond range. However, the fastest part of the decay could not be resolved in these studies because the scattered light partially influenced the measured phosphorescence decays. Therefore, the first 50 ps after the maximum were excluded from the fit.

For TiO_2 and ZnO cells the observed phosphorescence decays are due to electron injection and internal radiative and non-radiative decay of the N719 triplet state, while for Al_2O_3 cells electron injection is not possible due to the high energy of the conduction band edge.[33–35] Thus, the additional measurements for the reference Al_2O_3 system enable the determination of the electron injection quantum yield (of the triplet state) from the following equation

$$\eta_{ei\,(Triplet\,)} = \frac{k_{AVG\,(sample\,)} - k_{AVG\,(Al_2O_3)}}{k_{AVG\,(sample\,)}} \qquad (4.24)$$

where *sample* is either TiO_2 or ZnO. For these calculations an average rate constant of $4.15 \cdot 10^{-5}$ ps^{-1} was assumed for alumina cells based on the similar values obtained for Al_2O_3/S3/Tbp and Al_2O_3/S3/Li(x1) samples (Appendix Table A-9.2). The electron injection quantum yields from triplet state are collected in **Table 9.2**, together with the relative photocurrents of the cells (J_{SC}/N_{ph}).

A few important observations should be pointed out based on the emission studies. As can be seen from **Figure 9.5**, the phosphorescence decay rates for titania samples correlate in an approximately exponential way with respect to the V_{OC} of the cells. These decays can almost be directly related to triplet electron injection rates since quantum yields of this process are very high (Table 9.2). A similar dependence of electron injection rate on V_{OC} has been reported for Ru-based DSSC.[9]

Electrolytes		TiO_2		ZnO	
		J_{sc}/N_{ph} (10^{-19}C)	$\eta_{ei(Triplet)}$	J_{sc}/N_{ph} (10^{-19}C)	$\eta_{ei(Triplet)}$
Series 1 **I2/LiI**	**Ref**	1.60	0.99	1.30	0.17
	Pyr	1.55	0.99	1.35	0.45
	Tbp	1.55	0.90	1.42	0.37
	TP	1.50	0.90	1.51	0.27
Series 2 **I2/BMII**	**Ref**	2.30	0.95	1.85	0.78
	Li	2.45	0.99	1.83	0.76
	Tbp	2.20	0.81	1.84	0.75
Series 3 **I2/DMPII**	**Ref**	1.90	0.91	1.80	0.64
	Li(x1)	1.93	0.98	1.80	0.69
	Li(x1)	1.83	0.99	1.80	0.57
	Li(x3)	2.10	0.98	1.75	0.40
	Tbp	1.80	0.94	1.70	0.63

Table 9.2: Relative photocurrent of each cell (J_{sc}/N_{ph}) and the efficiency of electron injection from the triplet state (η_{ei}).

For ZnO cells the phosphorescence decay rates are significantly smaller (roughly 1 order of magnitude) than those of TiO_2 samples for the corresponding V_{OC} (Table 9.2 and Figure 9.5). Slower electron injection in ZnO as compared to TiO_2 has been observed several times.[5,27,36,37] Most probably, slower rates are due to the smaller effective mass of electrons in ZnO, which decreases the density of acceptor states.[5,36] This effect is probably accentuated by the afore-mentioned lower dielectric constant of ZnO that makes charge separation at the oxide/dye interface more difficult. Moreover, in contrast to TiO_2 cells, there is almost no dependence of the decay rates on the electrolyte additives for ZnO cells (Figure 9.5). This correlates quite well with the small changes in V_{OC} for these cells, pointed out in the first section.

The data collected in **Table 9.2** indicate that the electron injection quantum yield from the triplet state (hence also the electron injection rate) correlates well with the relative photocurrent of the solar cells. First, higher quantum yields occur for samples with higher J_{SC} (and smaller V_{OC}) for TiO_2 cells. Nevertheless, for all TiO_2 cells the quantum yields are larger than 90%. Second, the lower quantum yields for ZnO cells with respect to TiO_2 cells for the corresponding *Series* agree with the lower J_{SC}/N_{ph} ratio. In addition, for both TiO_2 and ZnO cells the highest photocurrents occur for the *Series 2* of electrolytes, and for this series electron injection is slightly faster than for the other two. All this indicates that the primary charge separation process determines the global parameters (V_{OC}, J_{SC}) of the N719 cells. Finally, it should be pointed out that the true electron injection quantum yields might be higher than those based on phosphorescence data in Table 9.2, because the fastest components of electron injection (from the singlet state and from the triplet states for time shorter than 50 ps) are not resolved in the emission experiment. To observe these processes transient absorption studies in fs-ps domain were utilized, for which the results will be presented in the next section.

3.5. Femtosecond transient absorption studies.

Transient absorption measurements with 200 fs resolution in 3 ns time window enable observation of the fast part of electron injection process. In contrast to emission, not only excited states of N719 are probed, but also the products of electron injection: the oxidized dyes and electrons in the conduction band of metal oxides. Transient absorption was carried out in a very broad spectral range from 450 to 1400 nm, joining both the visible (VIS) and near-infrared (NIR). To the best of my knowledge, the combined transient spectra in such a broad range have not been reported so far for Ru-based DSSC systems, not only for complete solar cells, but even for films. The used pump wavelength was set at 535 nm with an energy density of ≈1 mJ/cm^2.

Figure 9.6 presents the representative transient absorption spectra for selected time delays between pump and probe pulses for TiO_2/S2/Ref and ZnO/S2/Ref in both the VIS and NIR range. Due to the IRF of the setup the initial spectra (time zero) should be assigned to the triplet state and, possibly, a partial contribution from the oxidized dye formed by ultrafast electron injection from the singlet state. The decay of the singlet state occurs within the first 100 fs for ruthenium dyes and cannot be observed in the setup employed.[38,39] Even any spectral evolution on the rising part of IRF is hard to recognize because the artefacts from the FTO glass plates (two photon absorption and cross phase modulation)[40] are present during pump-probe overlap. Thus, the changes observed of the transient spectra are due to the decrease of the population of the triplet state and to the increase of the population of electrons and oxidized dyes in the process of electron injection from the triplet state. As a consequence of the different absorption coefficients of the triplet state and resultant absorption coefficient of oxidized dye and electrons in the semiconductor, a clear decrease of the signal can be observed in the 450-500 nm, 550-700 nm and 850-1400 nm ranges, and a signal increase in the 700-850 range (Figure 9.6). The latter increase is not observed for all ZnO cells, a crucial feature that will be discussed below. The negative signal below 600 nm is due to the dominant contribution of the bleach (ground state depopulation signal is higher than absorption from the transient species). Therefore, the clearly defined isobestic points recognized in both the VIS and NIR range confirm that the observed evolution of the transient spectra is mainly due to one process: electron injection from the triplet state. Electrons in the semiconductor contribute to the transient absorption signal as the trapped (absorption between 500 and 1100 nm)[41] and free electrons (absorption increasing towards longer wavelength, especially in NIR range).[41,42]

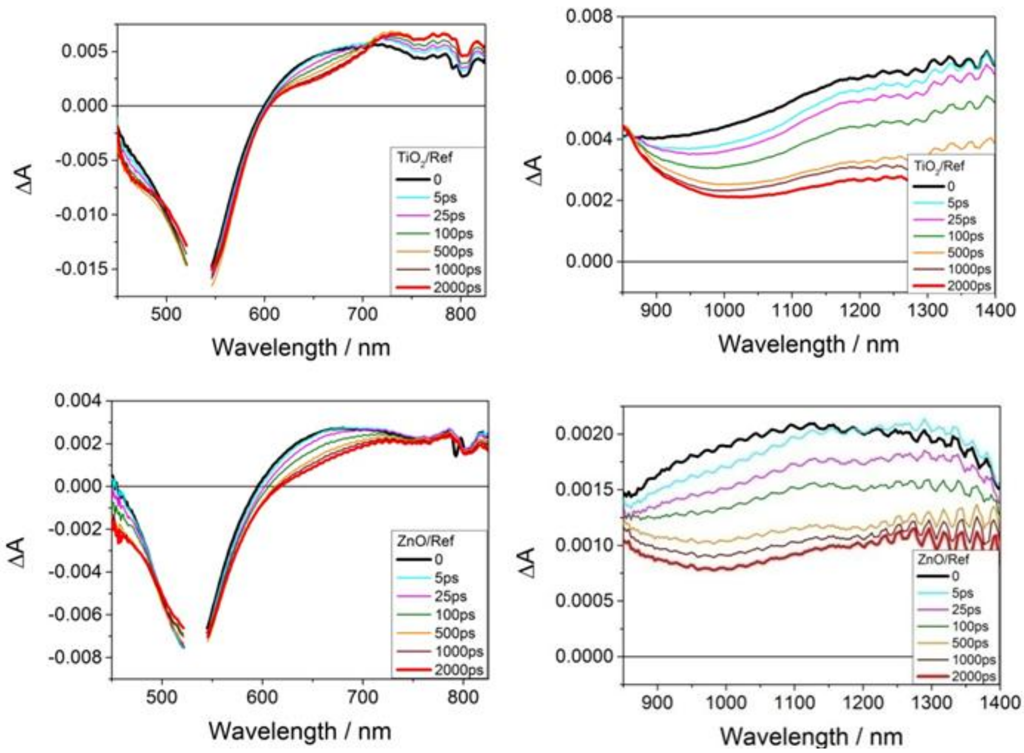

Figure 9.6: Representative transient absorption spectra for selected time delays between pump and probe pulses for TiO_2/S2 and ZnO/S2 reference cells in both the VIS and NIR range.

The representative kinetics for selected wavelengths is shown in the **Appendix** (Figure A-9.5) for different electrolytes of *Series 3*. By qualitative inspection, as expected, the decays (or rises) are significantly faster with LiI additive and much slower for Tbp additive for TiO_2 cells, while for ZnO samples the kinetics for different electrolytes are more or less similar. This is in line with what it has been discussed so far regarding the afore-mentioned insensitivity of the electronic properties of the ZnO photoanodes with respect to the electrolyte composition.

The following explanation is proposed for the lack of rise in the 700-850 nm range of transient absorption signal for all ZnO cells. Oxidized dyes show absorption in the 700-850 nm region, which is present in TiO_2 cells but absent in ZnO cells. It should be noted that in other spectral ranges the transient absorption changes due to the decay of the triplet state are present in ZnO cells (Figure 9.6). Therefore, the existence of an intermediate state is considered, which occurs after the decay of the triplet state (due to electron injection) and before full charge separation into a oxidized dye and a free electron. The low dielectric constant of ZnO (with respect to TiO_2) supports the possibility of the presence of such bound complex between oxidized dye and electrons in the conduction band, as proposed in several reports before.[43–45] Since the nature of this intermediate in ZnO cells is different from that of the free oxidized dye, the intermediate probably does not have such a pronounced absorption in 700-850 nm as the free oxidized dye, and, unlike for TiO_2 cells, a flat kinetics for ZnO cells in this spectral region is observed at this time scale (1-3 ns). Further confirmation of this hypothesis is brought by comparison of the final transient absorption spectra measured with the fs-ps setup at 2 ns and the initial spectra measured with the flash photolysis equipment at 60 ns (**Appendix**, Figure A-9.6).

In a very recent contribution the presence of an ultrafast (ps time scale) first step of dye regeneration by I^- was postulated for N3 and N719 dyes.[15] It was based on a very small rise of the transient absorption signal in the 700-850 nm range for TiO_2 cells. However, in Figure 9.6 a clear and pronounced rise in TiO_2 cells is shown, especially for those electrolytes with faster electron injection (low V_{OC}). Therefore, it is possible to think that a small rise of the signal in the visible range can exclusively be explained by slow (occurring mainly on the ns time scale) electron injection process from the triplet state in efficiency-optimized electrolyte. Hence, dye regeneration is not necessary to explain the observed feature.

In many reported studies so far of Ru-based DSSC the kinetics at only one wavelength was probed (very often at 820 nm) and considered representative for oxidized dye population. This assumption often led to conclusions about the dominant role of ultrafast (<100 fs) electron injection.[46–48] However, such supposition was recently questioned in NIR studies of complete cells and a significant contribution of the triplet state absorption at this wavelength was postulated.[10] The results presented in this chapter clearly support this assumption and show that measuring transient absorption in a broad spectrum is advantageous for the correct assignment of the signals. Moreover, the probe wavelength of 820 nm is quite close to the isobestic point at around 850 nm where the absorption coefficients of oxidized dye and triplet state are equal.

A global multi-exponential analysis of the transient absorption data has been performed (**Figure 9.7**). The electron injection for longer times than the temporal window (3 ns) and the contribution of electron recombination and the vibrational relaxation in the triplet state makes it difficult to determine pure electron injection dynamics. Therefore, the following procedure to calculate average electron injection rate constants for all solar cells with different electrolytes has been used. The amplitudes and time constants of the short (fitted) and long (fixed at 2 ns) components obtained in the global multi-exponential analysis (**Appendix**, Table A-9.3) are used to reproduce the kinetics at 820 nm for TiO_2 samples. Then, the reciprocals of the half decay times for such simulated kinetics were taken as electron injection rate constant. For ZnO cells the wavelength at 470 nm instead of at 820 nm was chosen because there is almost no rise at 820 nm for ZnO samples as observed in **Figure 9.6** and discussed above (it was checked that for TiO_2 cells, the results obtained at 470 nm are similar to those at 820 nm, but the signal to noise ratio is worse). In principle, this procedure is similar to taking the half decays directly from the experimental kinetics at a chosen wavelength. However, the advantage of the global fit (better signal to noise ratio) and the extension of the analyzed time window (with τ_2=2 ns) a little bit further than the experimental window (3 ns) are taken into account. The results are shown in **Figure 9.8**.

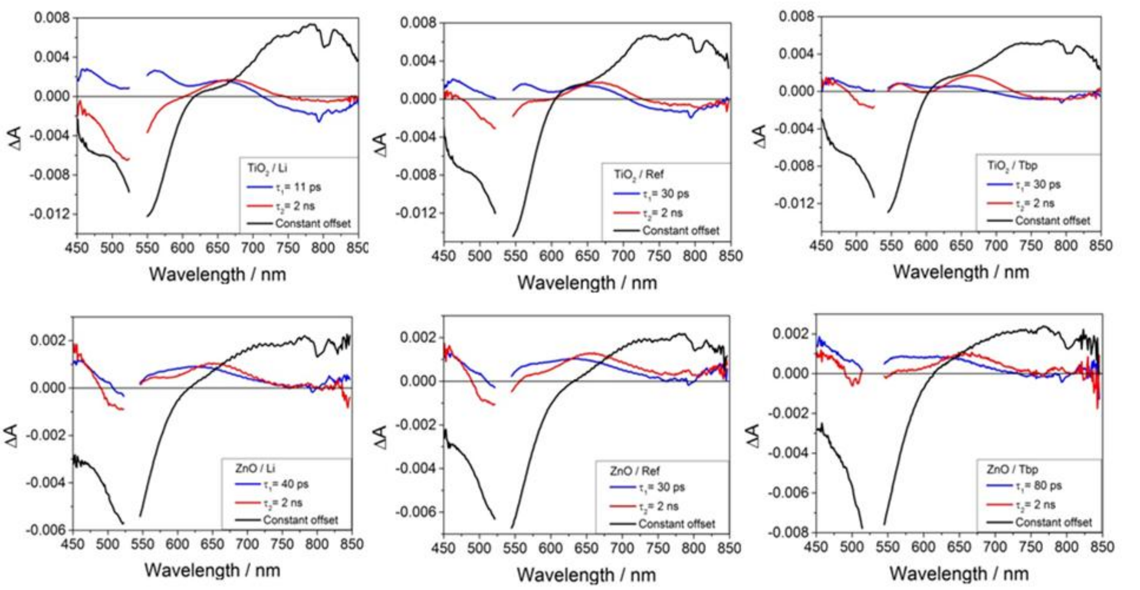

Figure 9.7: Wavelength dependent amplitudes of the indicated time constants obtained from global analysis of transient absorption spectra in VIS range of TiO_2 and ZnO cells for the *Series 2* of electrolytes.

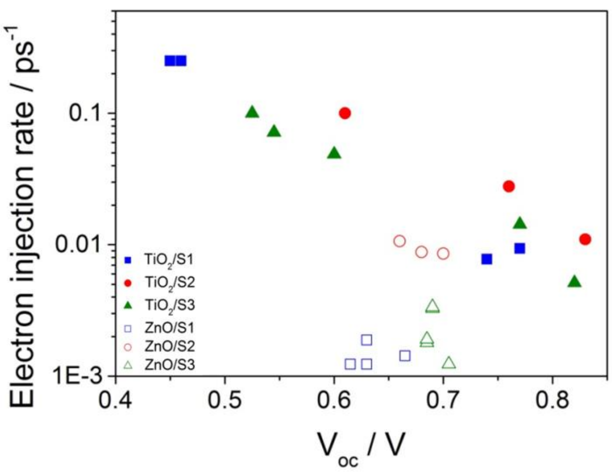

Figure 9.8: Electron injection rate constants obtained in femtosecond transient absorption experiments as a function of V_{OC} of the cells.

Figure 9.8 should be compared with analogous **Figure 9.5** obtained from the phosphorescence decays. The electron injection rate constants from transient absorption experiments are always higher than those from the phosphorescence decays because the former technique probes shorter times while the latter one probes longer times. This cannot be avoided due to the nature of electron injection process in DSSC, with time constants spreading over many orders of magnitude. However, as can be seen in Figure 9.8, the conclusions from transient absorption dynamics of different cells agree very well with those observed in emission studies. Electron injection is faster for TiO_2 cells than for ZnO cells. Furthermore, the rate of injection changes in an exponential way with respect to V_{OC} in TiO_2 cells, whereas for ZnO cells the electron injection rate is rather independent of the open circuit voltage of the cell and electrolyte composition. Finally, for all cells the highest injection rates are those for the *Series 2* of electrolytes and the lowest for the *Series 1*. The reasons for this behaviour are likely related to the bulkier nature of the BMII cation as compared to DMPII, however, why this leads to faster injection is not clear at this point.

4. General discussion.

In this section the results of this chapter are discussed in the view of (1) the recent report[16] about the coordinated shifts of ground state (S_0) and excited states (S_1 or T_1) levels of ruthenium dyes and, connected to this, (2) the comparison of TiO_2 and ZnO as photoanode materials for primary charge separation. In the conventional understanding of DSSC functioning the potentials of S_0 and T_1 levels do not change when Lewis acids or Lewis bases are added to electrolyte, which is schematically shown as *Model 1* in **Figure 9.10**. According to the new findings, the potentials of both S_0 and T_1 levels of N719 dye attached to TiO_2 particles are found to shift by a certain amount in accordance to *Model 2* in Figure 9.10.[16] Interestingly, the indication of not fixed potential of the sensitizing dye has been reported also much earlier,[49] but that contribution seems to be forgotten. For some ruthenium dyes the shift in HOMO level was estimated to be smaller than the shift of the titania conduction band.[50,51]However, for dyes like N719, having many COOX groups, the shift was shown to be large.[16]

As discussed in the flash photolysis section, the results support the shift of S_0 potential according to *Model 2*, since faster regeneration is observed for Lewis acid and slower for Lewis base additives, which implies differences in energy gaps and driving forces for this process (larger energy gaps implies faster regeneration in normal Marcus region). It should be noted that the regeneration rate has also been observed to be dependent on the cation size and charge.[28] This latter parameters also determine the conduction band edge shift, so those findings can be similarly explained by *Model 2*. Flash photolysis studies reveal also that dye regeneration is 2-4 times faster for TiO_2 cells than for ZnO cells, in agreement with previous results for different sensitizing dyes, which suggests that this is a general feature of ZnO nanostructured electrodes. Most probably, the lower dielectric constant of ZnO and, possibly, its high degree of doping, softens the dipole effect of the additives in the displacement of all electronic levels (both bands and dye S_0-T_1 levels), hence reducing the driving force for regeneration in the case of ZnO with respect to TiO_2. This effect remains in the absence of additives, as regeneration is also faster for TiO_2

reference cells. This indicates that the electronic properties of the oxide also affects this part of the primary charge separation process.

Although no direct evidence has been shown, the findings also support the shift of the triplet state potential of the dye according to *Model 2*. The steady-state emission results show that the energy gap between the T_1 and S_0 states is rather insensitive to the electrolyte additives, therefore, if there is a shift in S_0/S^+ potential, a similar displacement should then occur for the T_1 state.

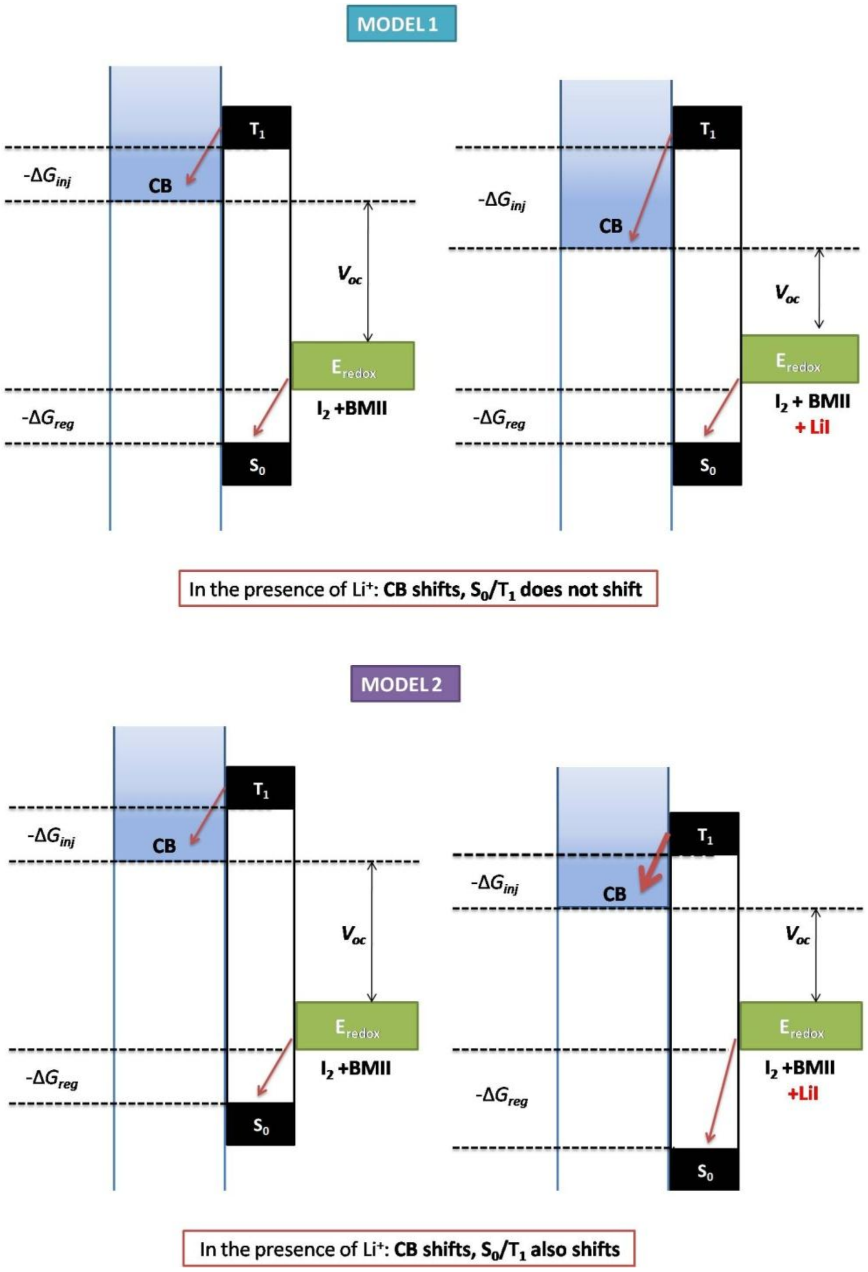

Figure 9.10: Two models based on conventional understanding of operation of DSSC (*Model 1*) and recently discovered shifts (*Model 2*).

Emission decay measurements for N719 solar cells allowed the determination of slower (>50 ps) part of electron injection. For TiO_2 cells of different open circuit voltage, the electron injection rate constant (from 1×10^{-2} to 2×10^{-4} ps^{-1}) correlates well with the composition of the electrolyte (rate increases upon addition of LiI and decreases upon addition of Tbp). So far, the standard interpretation was that the injection becomes faster for lower V_{OC} because the density of acceptor states in titania corresponding to the T_1 level of the dye increases accordingly to the shifts in the potential of the conduction band edge (*Model 1* in Figure 9.10). However, according to coordinated shift of S_0 and T_1 levels (*Model 2* in Figure 9.10) the density of acceptor states do not change for different electrolyte additives.[16] Therefore, the exponential dependence of electron injection rate on V_{OC} has to be explained by the changes in electronic coupling between the semiconductor and anchored dyes when different additives are added (higher coupling for Li^+ cations, lower coupling for Tbp, *Model 2* in Figure 9.10).[16]

Smaller relative photocurrents for ZnO cells with respect to TiO_2 ones are explained by lower injection yields and slower regeneration. The observed weak dependence of open circuit voltage and short circuit current on the presence of electrolyte additives in ZnO cells agrees with the observed similar electron injection rate constants for all ZnO cells (about 1×10^{-4} ps^{-1}) as well as similar regeneration kinetics for all electrolyte compositions (Figure 9.3). Therefore, it confirms that the interface of ZnO nanoparticles is significantly less affected by electrolyte additives due to its lower dielectric constant and likely high degree of doping (when compared to TiO_2): the additives not only hardly shift the conduction band potential but they also do not influence the electronic coupling between the dye and the semiconductor.

The insensitivity of the ZnO surface upon addition of *potential-determining* additives in the electrolyte is confirmed by the constancy of the electrochemical capacitance as extracted from impedance measurements (Figure 9.2). In contrast to TiO_2, ZnO capacitance data, while remaining exponential, which is indicative of a chemical capacitance, do not shift when either Li^+ or Tbp are added to the electrolyte. This effect can simply be explained by the difficulty to create surface dipoles in the case of ZnO, due to its lower dielectric constant and the effect of higher carrier concentration (doping), which is likely present in the material. However, that those additives do not adsorb to the ZnO surface cannot be ruled out as an alternative explanation. In any other case, the absence of surface dipoles explains the lower quantum yield of injection, which highlights the importance of the charge asymmetries to favour primary charge separation in dye solar cells. Furthermore, our results show that the surface dipole effect goes beyond a change in the oxide electronic levels, as it also affects the S_0 and T_1 levels of the dye, in accordance to *Model 2.*

In a very recent contribution the presence of an ultrafast (ps time scale) first step of dye regeneration by I^- was postulated for N3 and N719 dyes.[15] It was based on a very small rise of the transient absorption signal in the 700-850 nm range for TiO_2 cells. However, in Figure 9.6 a clear and pronounced rise in TiO_2 cells is observed, especially for those electrolytes with faster electron injection (low V_{OC}). Therefore, the small rise of the signal in the visible range could exclusively be explained by slow (occurring mainly on the ns time scale) electron injection process from the triplet state in efficiency-optimized electrolyte. Hence, it is possible that dye regeneration is not necessary to explain the observed feature.

In many reported studies so far of Ru-based DSSC the kinetics at only one wavelength was probed (very often at 820 nm) and considered as representative for oxidized dye population, which often led to conclusions about the dominant role of ultrafast (<100 fs) electron injection.[46–48] Such supposition was recently questioned in NIR studies of complete cells and a significant contribution of the triplet state absorption at this wavelength was postulated.[11] The result presented in this chapter clearly support this assumption and show that measuring transient absorption in a broad spectrum is advantageous for the correct assignment of the signals. Moreover, the probe wavelength of 820 nm is quite close to the isobestic point at around 850 nm where the absorption coefficients of oxidized dye and triplet state are equal.

5. Conclusions.

The present chapter provides new important data that helps to understand why a metal-oxide such as ZnO bears a critical limitation to perform efficiently in a DSSC. This limitation is likely connected to the smaller value of the dielectric constant. These results bring a revision or a more detailed look at several paradigms concerning important aspects of the primary charge separation in Ru-dye based DSSC:

- The insensitivity of primary charge separation ZnO solar cells upon electrolyte composition as inferred from time-resolved spectroscopy experiments is correlated with the insensitivity of the electrochemical capacitance extracted from impedance measurements. This finding suggests that the dielectric properties of ZnO and its doping level (carrier concentration) are crucial with regards to the ability of this oxide to sustain efficient charge separation in dye solar cells.
- A shift of the metal oxide conduction band potential upon different additives in the electrolyte (that change both V_{OC} and J_{SC} of the cell) is not a general property of DSSCs because it is almost not present for ZnO-based cells.
- For ZnO cells any influence of additives on electron injection has been observed, while for TiO_2 the electron injection rate changes significantly. In addition, injection rate constants vary exponentially for TiO_2 with respect to the open-circuit voltage of the cell.
- The potential changes of the ground state level of the N719 dye upon adding Tbp and Li^+ can explain the influence of the additives on the dye regeneration rate. Steady-state emission data indicate that a similar shift occurs for the triplet state of N719. Interestingly, a smaller influence of the electrolyte composition on dye regeneration is observed in ZnO devices.
- Lower photocurrents, and thus worse performance, of ZnO-based solar cells with respect to that of TiO_2 originate either from lower rate of electron injection, slower dye regeneration and/or the presence of an intermediate state with efficient back recombination.

6. References.

(1) Hagfeldt, A.; Boschloo, G.; Sun, L.; Kloo, L.; Pettersson, H. Dye-Sensitized Solar Cells. *Chem. Rev.* **2010**, *110*, 6595–6663.

(2) Friedrich, D.; Valldecabres, L.; Kunst, M.; Moehl, T.; Zakeeruddin, S. M.; Grätzel, M. Dye Regeneration Dynamics by Electron Donors on Mesoscopic TiO2 Films. *J. Phys. Chem. C* **2014**, *118*, 3420–3425.

(3) Memarian, N.; Concina, I.; Braga, A.; Rozati, S. M.; Vomiero, A.; Sberveglieri, G. Hierarchically Assembled ZnO Nanocrystallites for High-Efficiency Dye-Sensitized Solar Cells. *Angew. Chem. Int. Ed.* **2011**, *50*, 12321–12325.

(4) Saito, M.; Fujihara, S. Large Photocurrent Generation in Dye-Sensitized ZnO Solar Cells. *Energy Environ. Sci.* **2008**, *1*, 280–283.

(5) Anderson, N. A.; Lian, T. ULTRAFAST ELECTRON TRANSFER AT THE MOLECULE-SEMICONDUCTOR NANOPARTICLE INTERFACE. *Annu. Rev. Phys. Chem.* **2004**, *56*, 491–519.

(6) Ardo, S.; Meyer, G. J. Photodriven Heterogeneous Charge Transfer with Transition-Metal Compounds Anchored to TiO2 Semiconductor Surfaces. *Chem. Soc. Rev.* **2009**, *38*, 115–164.

(7) Ramakrishna, G.; Jose, D. A.; Kumar, D. K.; Das, A.; Palit, D. K.; Ghosh, H. N. Strongly Coupled Ruthenium−Polypyridyl Complexes for Efficient Electron Injection in Dye-Sensitized Semiconductor Nanoparticles. *J. Phys. Chem. B* **2005**, *109*, 15445–15453.

(8) Katoh, R.; Furube, A. Electron Injection Efficiency in Dye-Sensitized Solar Cells. *J. Photochem. Photobiol. C Photochem. Rev.* **2014**, *20*, 1–16.

(9) Koops, S. E.; O'Regan, B. C.; Barnes, P. R. F.; Durrant, J. R. Parameters Influencing the Efficiency of Electron Injection in Dye-Sensitized Solar Cells. *J. Am. Chem. Soc.* **2009**, *131*, 4808–4818.

(10) Juozapavicius, M.; Kaucikas, M.; van Thor, J. J.; O'Regan, B. C. Observation of Multiexponential Pico- to Subnanosecond Electron Injection in Optimized Dye-Sensitized Solar Cells with Visible-Pump Mid-Infrared-Probe Transient Absorption Spectroscopy. *J. Phys. Chem. C* **2012**, *117*, 116–123.

(11) Juozapavicius, M.; Kaucikas, M.; Dimitrov, S. D.; Barnes, P. R. F.; van Thor, J. J.; O'Regan, B. C. Evidence for "Slow" Electron Injection in Commercially Relevant Dye-Sensitized Solar Cells by vis–NIR and IR Pump–Probe Spectroscopy. *J. Phys. Chem. C* **2013**, *117*, 25317–25324.

(12) Anderson, A. Y.; Barnes, P. R. F.; Durrant, J. R.; O'Regan, B. C. Simultaneous Transient Absorption and Transient Electrical Measurements on Operating Dye-Sensitized Solar Cells: Elucidating the Intermediates in Iodide Oxidation. *J. Phys. Chem. C* **2010**, *114*, 1953–1958.

(13) Anderson, A. Y.; Barnes, P. R. F.; Durrant, J. R.; O'Regan, B. C. Quantifying Regeneration in Dye-Sensitized Solar Cells. *J. Phys. Chem. C* **2011**, *115*, 2439–2447.

(14) Li, F.; Jennings, J. R.; Wang, Q. Determination of Sensitizer Regeneration Efficiency in Dye-Sensitized Solar Cells. *ACS Nano* **2013**, *7*, 8233–8242.

(15) Antila, L. J.; Myllyperkiö, P.; Mustalahti, S.; Lehtivuori, H.; Korppi-Tommola, J. Injection and Ultrafast Regeneration in Dye-Sensitized Solar Cells. *J. Phys. Chem. C* **2014**, *118*, 7772–7780.

(16) Yang, X.; Zhang, S.; Zhang, K.; Liu, J.; Qin, C.; Chen, H.; Islam, A.; Han, L. Coordinated Shifts of Interfacial Energy Levels: Insight into Electron Injection in Highly Efficient Dye-Sensitized Solar Cells. *Energy Env. Sci* **2013**, *6*, 3637–3645.

(17) Vega-Poot, A. G.; Macías-Montero, M.; Idígoras, J.; Borrás, A.; Barranco, A.; Gonzalez-Elipe, A. R.; Lizama-Tzec, F. I.; Oskam, G.; Anta, J. A. Mechanisms of Electron Transport and Recombination in ZnO Nanostructures for Dye-Sensitized Solar Cells. *ChemPhysChem* **2014**, *15*, 1088–1097.

(18) Burdzinski, G.; Karolczak, J.; Ziolek, M. Dynamics of Local Stark Effect Observed for a Complete D149 Dye-Sensitized Solar Cell. *Phys Chem Chem Phys* **2013**, *15*, 3889–3896.
(19) Wróżowa, T.; Ciesielska, B.; Komar, D.; Karolczak, J.; Maciejewski, A.; Kubicki, J. Measurements of Picosecond Lifetimes by Time Correlated Single Photon Counting Method: The Effect of the Refraction Index of the Solvent on the Instrument Response Function. *Rev. Sci. Instrum.* **2004**, *75*, 3107–3121.
(20) Redmond, G.; Fitzmaurice, D. Spectroscopic Determination of Flatband Potentials for Polycrystalline Titania Electrodes in Nonaqueous Solvents. *J. Phys. Chem.* **1993**, *97*, 1426–1430.
(21) Liu, Y.; Hagfeldt, A.; Xiao, X.-R.; Lindquist, S.-E. Investigation of Influence of Redox Species on the Interfacial Energetics of a Dye-Sensitized Nanoporous TiO2 Solar Cell. *Sol. Energy Mater. Sol. Cells* **1998**, *55*, 267–281.
(22) Raga, S. R.; Barea, E. M.; Fabregat-Santiago, F. Analysis of the Origin of Open Circuit Voltage in Dye Solar Cells. *J. Phys. Chem. Lett.* **2012**, *3*, 1629–1634.
(23) Anta, J. A.; Guillén, E.; Tena-Zaera, R. ZnO-Based Dye-Sensitized Solar Cells. *J. Phys. Chem. C* **2012**, *116*, 11413–11425.
(24) Guillén, E.; Peter, L. M.; Anta, J. Electron Transport and Recombination in ZnO-Based Dye-Sensitized Solar Cells. *J. Phys. Chem. C* **2011**, *115*, 22622–22632.
(25) Tena-Zaera, R.; Elias, J.; Lévy-Clément, C.; Bekeny, C.; Voss, T.; Mora-Seró, I.; Bisquert, J. Influence of the Potassium Chloride Concentration on the Physical Properties of Electrodeposited ZnO Nanowire Arrays. *J. Phys. Chem. C* **2008**, *112*, 16318–16323.
(26) Mora-Sero, I.; Fabregat-Santiago, F.; Denier, B.; Bisquert, J.; Tena-Zaera, R.; Elias, J.; Levy-Clement, C. Determination of Carrier Density of ZnO Nanowires by Electrochemical Techniques. *Appl. Phys. Lett.* **2006**, *89*, 203117–203120.
(27) Sobuś, J.; Burdziński, G.; Karolczak, J.; Idígoras, J.; Anta, J. A.; Ziółek, M. Comparison of TiO2 and ZnO Solar Cells Sensitized with an Indoline Dye: Time-Resolved Laser Spectroscopy Studies of Partial Charge Separation Processes. *Langmuir* **2014**, *30*, 2505–2512.
(28) Pelet, S.; Moser, J.-E.; Grätzel, M. Cooperative Effect of Adsorbed Cations and Iodide on the Interception of Back Electron Transfer in the Dye Sensitization of Nanocrystalline TiO2. *J. Phys. Chem. B* **2000**, *104*, 1791–1795.
(29) Ziółek, M.; Martín, C.; Sun, L.; Douhal, A. Effect of Electrolyte Composition on Electron Injection and Dye Regeneration Dynamics in Complete Organic Dye Sensitized Solar Cells Probed by Time-Resolved Laser Spectroscopy. *J. Phys. Chem. C* **2012**, *116*, 26227–26238.
(30) Haque, S. A.; Tachibana, Y.; Willis, R. L.; Moser, J. E.; Gratzel, M.; Klug, D. R.; Durrant, J. R. Parameters Influencing Charge Recombination Kinetics in Dye-Sensitized Nanocrystalline Titanium Dioxide Films. *J. Phys. Chem. B* **2000**, *104*, 538–547.
(31) Nelson, J.; Haque, S. A.; Klug, D. R.; Durrant, J. R. Trap-Limited Recombination in Dye-Sensitized Nanocrystalline Metal Oxide Electrodes. *Phys. Rev. B* **2001**, *6320*.
(32) Barzykin, A. V.; Tachiya, M. Mechanism of Charge Recombination in Dye-Sensitized Nanocrystalline Semiconductors: Random Flight Model. *J. Phys. Chem. B* **2002**, *106*, 4356–4363.
(33) Palomares, E.; Clifford, J. N.; Haque, S. A.; Lutz, T.; Durrant, J. R. Control of Charge Recombination Dynamics in Dye Sensitized Solar Cells by the Use of Conformally Deposited Metal Oxide Blocking Layers. *J. Am. Chem. Soc.* **2002**, *125*, 475–482.
(34) Dworak, L.; Matylitsky, V. V.; Wachtveitl, J. Ultrafast Photoinduced Processes in Alizarin-Sensitized Metal Oxide Mesoporous Films. *ChemPhysChem* **2009**, *10*, 384–391.
(35) Luo, L.; Lin, C.-J.; Tsai, C.-Y.; Wu, H.-P.; Li, L.-L.; Lo, C.-F.; Lin, C.-Y.; Diau, E. W.-G. Effects of Aggregation and Electron Injection on Photovoltaic Performance of Porphyrin-Based Solar Cells with Oligo(phenylethynyl) Links inside TiO2 and Al2O3 Nanotube Arrays. *Phys Chem Chem Phys* **2010**, *12*, 1064–1071.

(36) Tiwana, P.; Docampo, P.; Johnston, M. B.; Snaith, H. J.; Herz, L. M. Electron Mobility and Injection Dynamics in Mesoporous ZnO, SnO2, and TiO2 Films Used in Dye-Sensitized Solar Cells. *ACS Nano* **2011**, *5*, 5158–5166.
(37) Martín, C.; Ziółek, M.; Marchena, M.; Douhal, A. Interfacial Electron Transfer Dynamics in a Solar Cell Organic Dye Anchored to Semiconductor Particle and Aluminum-Doped Mesoporous Materials. *J. Phys. Chem. C* **2011**, *115*, 23183–23191.
(38) Benkö, G.; Kallioinen, J.; Korppi-Tommola, J. E. I.; Yartsev, A. P.; Sundström, V. Photoinduced Ultrafast Dye-to-Semiconductor Electron Injection from Nonthermalized and Thermalized Donor States. *J. Am. Chem. Soc.* **2001**, *124*, 489–493.
(39) Bram, O.; Cannizzo, A.; Chergui, M. Ultrafast Fluorescence Studies of Dye Sensitized Solar Cells. *Phys Chem Chem Phys* **2012**, *14*, 7934–7937.
(40) Lorenc, M.; Ziolek, M.; Naskrecki, R.; Karolczak, J.; Kubicki, J.; Maciejewski, A. Artifacts in Femtosecond Transient Absorption Spectroscopy. *Appl. Phys. B* **2002**, *74*, 19–27.
(41) Yoshihara, T.; Katoh, R.; Furube, A.; Tamaki, Y.; Murai, M.; Hara, K.; Murata, S.; Arakawa, H.; Tachiya, M. Identification of Reactive Species in Photoexcited Nanocrystalline TiO2 Films by Wide-Wavelength-Range (400−2500 Nm) Transient Absorption Spectroscopy. *J. Phys. Chem. B* **2004**, *108*, 3817–3823.
(42) Berger, T.; Anta, J. A.; Morales-Flórez, V. Electrons in the Band Gap: Spectroscopic Characterization of Anatase TiO2 Nanocrystal Electrodes under Fermi Level Control. *J. Phys. Chem. C* **2012**, *116*, 11444–11455.
(43) Furube, A.; Katoh, R.; Yoshihara, T.; Hara, K.; Murata, S.; Arakawa, H.; Tachiya, M. Ultrafast Direct and Indirect Electron-Injection Processes in a Photoexcited Dye-Sensitized Nanocrystalline Zinc Oxide Film: The Importance of Exciplex Intermediates at the Surface. *J Phys Chem B* **2004**, *108*, 12583–12592.
(44) Stockwell, D.; Yang, Y.; Huang, J.; Anfuso, C.; Huang, Z.; Lian, T. Comparison of Electron-Transfer Dynamics from Coumarin 343 to TiO2, SnO2, and ZnO Nanocrystalline Thin Films: Role of Interface-Bound Charge-Separated Pairs. *J Phys Chem C* **2010**, *114*, 6560–6566.
(45) Katoh, R.; Furube, A.; Barzykin, A. V.; Arakawa, H.; Tachiya, M. Kinetics and Mechanism of Electron Injection and Charge Recombination in Dye-Sensitized Nanocrystalline Semiconductors. *Coord. Chem. Rev.* **2004**, *248*, 1195–1213.
(46) Teuscher, J.; Décoppet, J.-D.; Punzi, A.; Zakeeruddin, S. M.; Moser, J.-E.; Grätzel, M. Photoinduced Interfacial Electron Injection Dynamics in Dye-Sensitized Solar Cells under Photovoltaic Operating Conditions. *J. Phys. Chem. Lett.* **2012**, *3*, 3786–3790.
(47) Kuang, D.; Ito, S.; Wenger, B.; Klein, C.; Moser, J.-E.; Humphry-Baker, R.; Zakeeruddin, S. M.; Grätzel, M. High Molar Extinction Coefficient Heteroleptic Ruthenium Complexes for Thin Film Dye-Sensitized Solar Cells. *J. Am. Chem. Soc.* **2006**, *128*, 4146–4154.
(48) Wenger, B.; Grätzel, M.; Moser, J.-E. Rationale for Kinetic Heterogeneity of Ultrafast Light-Induced Electron Transfer from Ru(II) Complex Sensitizers to Nanocrystalline TiO2. *J. Am. Chem. Soc.* **2005**, *127*, 12150–12151.
(49) Zaban, A.; Ferrere, S.; Gregg, B. A. Relative Energetics at the Semiconductor/Sensitizing Dye/Electrolyte Interface. *J. Phys. Chem. B* **1998**, *102*, 452–460.
(50) Qu, P.; Meyer, G. J. Proton-Controlled Electron Injection from Molecular Excited States to the Empty States in Nanocrystalline TiO2. *Langmuir* **2001**, *17*, 6720–6728.
(51) She, C.; Anderson, N. A.; Guo, J.; Liu, F.; Goh, W.-H.; Chen, D.-T.; Mohler, D. L.; Tian, Z.-Q.; Hupp, J. T.; Lian, T. pH-Dependent Electron Transfer from Re-Bipyridyl Complexes to Metal Oxide Nanocrystalline Thin Films. *J. Phys. Chem. B* **2005**, *109*, 19345–19355.

Chapter 10:

Photovoltaic performance of ZnO photoanodes with novel purely organic D-π-A dyes

1. Introduction.

As described in **Chapter 3**, among all components of a Dye-Sensitized Solar Cell (DSSC),[1,2] the function of light absorption and charge separation by means of electron injection in the electronic states of the semiconductor is carried out by the sensitizer dye molecules attached to its surface. However, not only the generation of an electric current depends on the properties of the dye, but also the electron recombination with the oxidized species present in the electrolyte, which determines the photovoltage of solar devices.[3] Therefore, bearing in mind the importance of dyes in the global performance of DSSC, the study and development of new sensitizers have received much interest. A clear example has been the discovery of perovskite solar cells.[4–6]

Since the origins of DSSCs, the most employed dyes have been complexes of ruthenium, which have demonstrated high efficiencies when used as sensitizers. These dye molecules are characterized by the presence of a Metal-to-Ligand Charge Transfer (MLCT) feature with a wide absorption spectrum and a moderate absorption coefficient (ε < 18000 M^{-1} cm^{-1}).[7] This latter characteristic influences negatively the use of these dyes in solar cells with ionic liquids or hole solid conductors as electrolytes, where the mass transfer limitation and the rapid recombination requires very thin films as photoanodes. Nevertheless, they show a long excited-state lifetime, a good electrochemical stability under illumination and appropriate energy levels (LUMO and HOMO) for an efficient electron injection and for a rapid dye regeneration with TiO_2. As an additional drawback, the main element in these dyes is a precious metal (Ru), which is not very common on the Earth and it is associated with high costs of fabrication due to the high purity degree required.

In the search and development of new sensitizers, fully organic dyes, which are characterized by a high absorption coefficient,[8] have extensively been studied. Up to date, numerous papers show efficiencies comparable to ruthenium dyes. For instance, efficiencies of 10.1% (*C219*)[9] and 12.3% (co-sensitization between the porphyrin dye *YD2-o-C8* and other organic dye)[10] have been achieved under simulated 1 sun AM 1.5 global sunlight. The advantage of these dyes is not only their absorption coefficients, but also the low production costs and the possibility of modifying the route of synthesis and of incorporating new groups altering its absorption spectrum or other properties.[11]

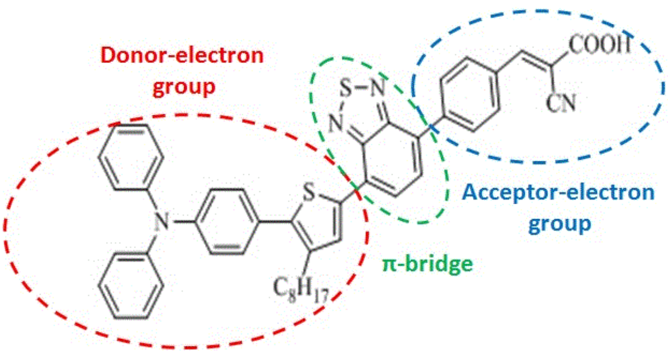

Figure 10.1: Structure of a typical donor-π-acceptor (D-π-A) dye.

Among organic dyes, the family of *Donor-π-Acceptor* (*D-π-A*) dyes has received much attention due to its facility to modify their structure (**Figure 10.1**) and then their properties.[9,12,13] These dyes result from the combination of two units linked covalently through a spacer (*π-bridge*). One of them is an *electron-donor* group, whose aim is the light absorption, whereas the other unit is an *electron-acceptor* group, which carries out the electron injection in the semiconductor after the intramolecular charge transfer from electron-donor group. Thanks to this architecture it is possible to design new dyes modifying the structure of each unit.

In this chapter, a comparative study of the photovoltaic performance of nanostructured ZnO photoanodes sensitized with different organic D-π-A dyes with respect to the most common ruthenium dye (N719) is developed. All the organic dyes employed in this chapter (**Figure 10.2**) are derived from the same dye (RK1), whose structure has been modified. The main difference between these organic dyes is related to the number and nature of their anchoring groups. To the best of our knowledge, this is the first report where the photovoltaic performance of ZnO with this kind of dyes has been studied

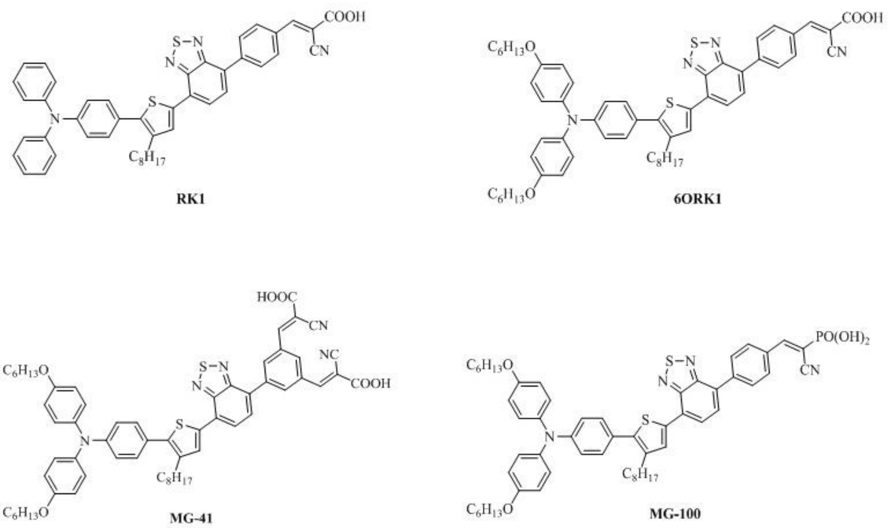

Figure 10.2: Structure of dyes employed in this work.

At this point it is important to remember the limitations of ZnO electrodes as photoanode in DSSC. As discussed in the previous chapter, ZnO-based solar cells show worse performance with respect to TiO_2-based solar cells as a consequence of its lower rate of electron injection, slower dye regeneration and/or the presence of an intermediate state of the dye with strong back recombination. In addition, ZnO electrodes show a high instability under the presence of ruthenium dyes, like N719, u other acidic dyes.[14] A partial dissolution of the semiconductor and the formation of dye-ZnO aggregates have been found after immersion in acidic dye solution.[15,16] In this chapter, a special attention has been paid to the number and nature of the anchoring group of dyes. Nevertheless, the record of efficiency for ZnO-based solar cell (7.5%) has been achieved using N719 as sensitizer.[17] However, in this chapter, using the same architecture of solar devices, the efficiency of a DSSC with ruthenium dye has been doubled by using a fully organic dye.

2. Experimental section.

2.1. Fabrication of Dye-Sensitized Solar Cells.

The working-electrodes were made using films consisting of layers of different thicknesses of 40 - 100 nm ZnO nanoparticles prepared by a forced hydrolysis method (**Appendix**, Figure A-9.1) by the group of Professor Gerko Oskam in CINVESTAV (Mexico).[18] Prior to the deposition of the ZnO paste the conducting glass substrates (Pilkington - TEC15) were heated to 500°C. The ZnO nanoparticle paste was deposited onto a conducting glass substrate using the screen printing technique. The DSSC active area was 0.16 cm^2. The ZnO electrodes were gradually heated under airflow at 225°C for 5 min, 275°C for 5 min, 400°C for 15 min and 450°C for 15 min. Finally, before dye adsorption the electrodes were heated again at 450°C for 30 min and cooled.

The counter-electrodes were made by spreading a *Platisol solution* (Solaronix) onto a conducting glass substrate (Pilkington - TEC8) with a small hole to allow the introduction of the liquid electrolyte using vacuum, followed by heating at 390°C for 15 minutes.

The electrodes were immersed in a solution containing the different dyes employed in this chapter. These solutions were composed of 0.5 mM dye and 5 mM chenodeoxycholic acid in ethanol. The sensitized electrodes were washed with ethanol and dried in air. Finally, the working- and counter-electrodes were sandwiched together using a thin thermoplastic frame (*Surlyn*, Solaronix) that melts at 100°C. The cells were filled with the electrolyte through a hole previously made in the back of a platinized counter-electrode. Then, the hole was sealed with a thermoplastic polymer and a cover-slide glass.

The dyes employed in this chapter have been kindly provided by the group of Professor Renaud Demadrille from CEA (France) except RK1, which was purchased from Solaronix.

2.2. Characterization of solar devices.

The devices were characterized using a solar simulator with AM 1.5G filter (*ABET*). The light intensity was calibrated to the standard value of 1 sun (100 mW/cm^2) using a reference solar cell with temperature output (*Oriel,* 91150). The current-voltage characteristics were determined by applying an external potential bias to the cell and measuring the photocurrent using an *Autolab/PGSTAT302N* potentiostat. Open-circuit Voltage Decay (OCVD) measurements were made by keeping the solar cell at open-circuit at 1-sun and recording the voltage decay after interrupting the illumination.

Electrochemical Impedance Spectroscopy (EIS) and Open-Circuit Voltage Decay (OCVD) were utilized to study electron recombination, chemical capacitance and to extract electron lifetimes. The illumination for the small perturbation (frequency response) technique was provided by a 530 nm light emitting diode (*LUXEON*) over a wide range of DC light intensities. This allows for probing the devices at different positions of the Fermi level in the semiconductor. A response analyzer module (*PGSTAT302N/FRA2, AutoLab*) was utilized to analyze the frequency response of the devices. To avoid voltage drop due to series resistance, EIS measurements were performed at the open circuit potential, the Fermi level (related to the open-circuit voltage) being fixed by the DC illumination intensity. A 10 mV perturbation in the 10^{-5} to 10^{-2} Hz range was utilized to obtain the spectra. Zview equivalent circuit modelling software (*Scribner*) was used to fit the EIS spectra, including the distributed element DX11 (transmission line model). In all cases the samples were illuminated from the dye-coated TiO_2 electrode side.

Incident photon-to-electron conversion efficiencies (IPCE) were measured by means of an Oriel Xenon lamp coupled to a 0.2 m monochromator (McPherson). The light intensity was determined as a function of the wavelength using a calibrated silicon photodiode (PH-100 Si, GENTECE).

UV-Vis absorption spectra were recorded in solution on a Perkin-Elmer Lambda 2 spectrometer (wavelength range: 180-820 nm; resolution: 2 nm). Electrochemical studies of the synthesized dyes were carried out in a one compartment, three-electrode electrochemical cell equipped with a flat platinum working electrode (7 mm^2), a Pt wire counter electrode, and a Ag wire pseudo-reference electrode, whose potential was checked using the Fc/Fc^+ couple as an internal standard. The electrolyte consisted of 0.2 M tetrabutylammonium hexafluorophosphate (Bu_4NPF_6) solution in dichloromethane containing 2 x 10^{-3} M of the dye. These characterization measurements were performed in the group of Professor Renaud Demadrille.

3. Results and Discussion.

3.1. Optical and electrochemical characterization.

The UV-Vis spectra in dichloromethane of the synthesized dyes are shown in **Figure 10.3A**. The spectra of these organic dyes are characterized by the presence of two absorption bands. One of them, the most intensity band located in the UV region, is associated with the high-energy π-π* orbital transition. On the other hand, the band located in the visible region is associated with the intramolecular charge transfer from the electron-donor group to the electron acceptor-group. This latter absorption band exhibits absorption maxima at 481, 503, 492 and 492 nm with a molar absorption coefficient of 29810, 20000, 11200 and 12300 $M^{-1}cm^{-1}$ for RK1, 6ORK1, MG-41 and MG-100, respectively (**Table 10.1**).

Assuming the same surface area as a consequence of employing the same thickness for all photoanodes, higher molar absorption coefficient should be connected to higher absorption signal as it is shown in **Figure 10.3B** for RK1-, 6ORK1- and MG-41-ZnO photoanodes. Nevertheless, the MG-100-ZnO photoanode shows an absorption maximum very similar to the RK1-ZnO photoanode (0.05 and 0.044, respectively) in spite of showing the second smaller molar absorption coefficient. Therefore, a higher concentration of dye molecules on ZnO surface seems to be inferred from the results in the case of MG-100-ZnO. Thus, we can infer that $–PO_3H_2$ group tend to favour dye adsorption with respect to the -COOH group.

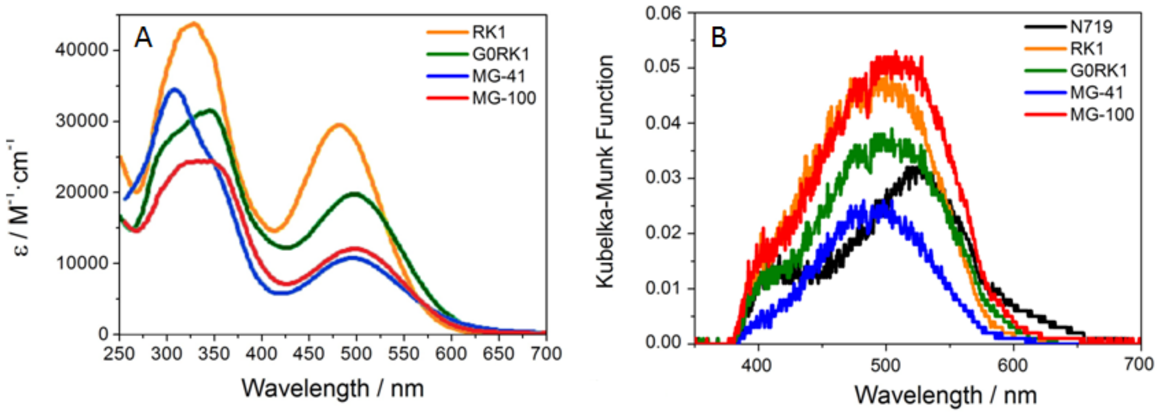

Figure 10.3: (A) UV-Vis spectra of synthesized dyes studied in dichloromethane and (B) onto the ZnO surface.

In order to determine the position of the LUMO and HOMO levels of the dyes an electrochemical study was performed by means of cyclic voltammetry (**Table 10.1**). Both energy levels were determined from the oxidation and reduction onset with respect to NHE, respectively. The band-gap energy was determined by the energy difference between both levels. Although, as pointed out in the previous chapter, the HOMO-LUMO difference does not necessarily corresponds to the energy absorption onset, it is still a good approximation for the energy difference between ground and excited state. A band-gap of around 1.6-1.7 eV confirms that the studied dyes absorb strongly in the visible range.

	λ_{abs} $^{(a)}$ / nm	ε $^{(a)}$ / $M^{-1}cm^{-1}$	HOMO$^{(b)}$ / V	LUMO$^{(b)}$ / V	$Eg^{(c)}$ / eV
RK1	**481**	**29810**	**0.93**	**-0.72**	**1.65**
6ORK1	**503**	**20000**	**0.82**	**---**	**---**
MG-41	**492**	**11200**	**0.81**	**-0.93**	**1.74**
MG-100	**492**	**12300**	**0.77**	**-0.95**	**1.72**

Table 10.1: Photophysical data: (a) Measured in CH_2Cl_2, (b) determined from the onset of the first oxidation and reduction and (c) calculated *Eg*= HOMO – LUMO. All potentials were obtained during cyclic voltammetric investigations in 0.2 M Bu_4NPF_6 in CH_2Cl_2. Potentials measured vs Fc^+/Fc were converted to NHE by addition of +0.69 V Platinum electrode diameter 1 mm, sweep rate: 200 mV s^{-1}

As mentioned in **Chapter 3**, the energy levels of the LUMO (considered an approximation to the excited state energy) and the HOMO with respect to the conduction band edge of the semiconductor and redox potential of the electrolyte determine the electron injection in the electronic states of the semiconductor and the dye regeneration, respectively (see **Chapter 9**). As a consequence of the position of conduction band edge of ZnO (-0.4V versus NHE, see Figure 3.3) and redox pair of I^-/I_3^- (0.35V versus NHE) an efficient electron injection and dye regeneration is expected.

3.2. Photovoltaic performance: Dye-Sensitized Solar Cells.

In order to analyze the photovoltaic properties of the synthesized dyes employed in this chapter, the overall light conversion efficiency of ZnO-based DSSC has been determined by means of IV curve measurements.

As reported many times in the literature, due to the low chemical stability of ZnO, the concentration of the dye solution and the sensitization time are key factors for an optimal dye adsorption when working with ZnO photoanodes.[14,15] In particular, the dissolution of the ZnO surface by the acidic carboxylic groups of dyes produces the formation of Zn^{2+}-dye complexes, which can affect to electron injection.[16] For this reason, the sensitization time for a given concentration of dye solution has been optimized prior to the characterization study (**Appendix**, Figure A-10.1). No significant differences were found in the first 3 hours for RK1-DSSC. Nevertheless, for the rest of organic dyes a clear deterioration of fill factor and even short-circuit photocurrent are observed. For this reason, only 1 hour sensitization time was employed in the preparation of the photoanodes for DSSCs characterized here.

Figure 10.4A shows current-voltage characteristics of DSSCs employing a thin film (≈4 μm) of ZnO as photoanode sensitized with the dyes. Bearing in mind the insensitivity of ZnO under the presence of *potential-determining additives* showed in **Chapter 9**, the employed electrolyte in this chapter consists of a purely redox pair (0.05M I_2 + 0.5M BMII) in acetonitrile as solvent electrolyte. The most common ruthenium dye (N719) has been used as reference.

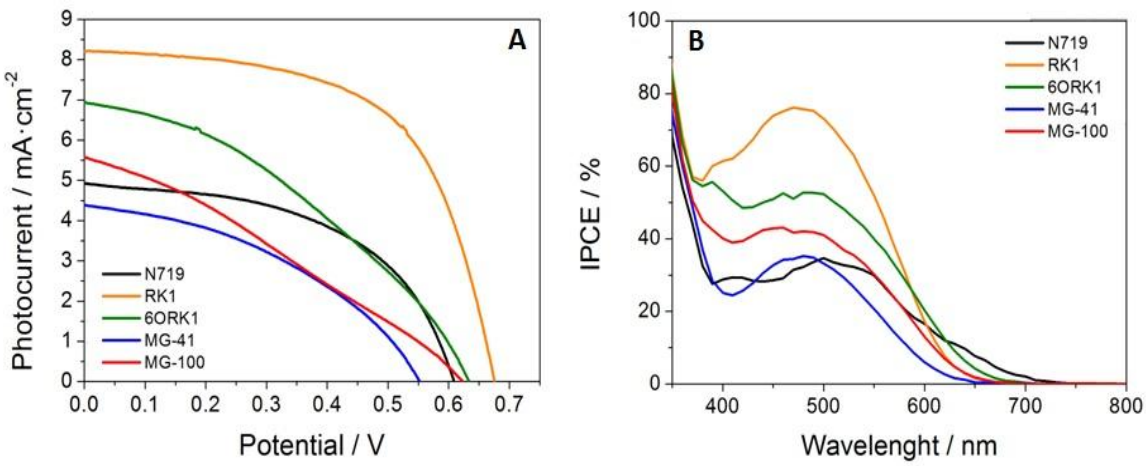

Figure 10.4: (A) Current-voltage curves of the best performing device under 1-sun AM 1.5 illumination and (B) corresponding IPCE spectra as a function of monochromatic wavelength for the dyes studied.

	J_{sc} (mA/cm^{-2})	V_{oc} (mV)	Fill Factor (%)	Efficiency (%)
N719	4.9	610	52	1.6
RK1	8.2	675	60	3.3
6ORK1	6.9	630	39	1.7
MG-41	4.4	555	41	1
MG-100	5.6	620	30	1

Table 10.2: Photovoltaics parameters of the best performing device for each dye for a non-optimized architecture obtained under simulated AM 1.5 illumination.

As it is shown in **Table 10.2**, the maximum efficiency (3.3%) was found for the RK1-DSSC. This efficiency is achieved by the combination of the highest photocurrent (8.2 mA/cm^2) and photovoltage (675 mV). In addition, a good fill factor is obtained for RK1-DSSC, especially when it is compared with the rest of the organic dyes. As a consequence of the low fill factor of 6ORK1-DSSC, this dye shows a similar efficiency to N719-DSSC (1.7% and 1.6%, respectively) in spite of the higher photocurrent and photovoltage. On the other hand, MG-41-DSSC and MG-100-DSSC show a comparable photocurrent to N719-DSSC. Nevertheless, due to their low fill factor, these DSSCs show the worst efficiencies (1%). Previous studies[19–21] have shown that higher rates of electron recombination lead to poor fill factors, which suggests that 6ORK1-, MG-41- and MG-100-DSSC suffer a faster recombination. However, as it is shown in **Appendix** (Figure A-10.2), once corrected for band-shifts of the semiconductor using chemical capacitance data, RK1-DSSC shows the smallest electron recombination resistance for a given value of the electron density.

As described in **Chapter 3**, the short circuit photocurrent can also be determined via **Equation 3.15**. As it is shown in **Figure 10.4**, the difference of short-circuit photocurrents is consistent with the differences of the incident photon-to-current conversion efficiency. RK1-DSSC, which shows the higher photocurrent, shows an IPCE closer to 80% at the maximum absorption wavelength, whereas in N719-DSSC an IPCE lower than 40% has been recorded.

According to **Equation 3.16**, the IPCE depends on the light-harvesting efficiency, the electron generation efficiency and the electron collection efficiency. As it is shown in **Figure 10.3B**, MG-100-DSSC shows the highest light-harvesting efficiency. Nevertheless, RK1-DSSC, whose light-harvesting efficiency is approximately similar to MG-100-DSSC, produces the maximum photocurrent and IPCE. If a good electron collection efficiency is assumed at short-circuit conditions,[8,22,23] two possible explanations can be established: (1) MG-100 shows the higher light harvesting efficiency but a poor electron injection in the semiconductor or (2) the dissolution of Zn^{2+} during the dye sensitization is more intense for MG-100. Under this assumption, a higher concentration of Zn^{2+}-dye complexes is accumulated in the pores of semiconductor. If it is assumed that the electron injection is only carried out by dye molecules directly attached to the ZnO surface, these complexes can only contribute to the light-harvesting efficiency but not to the electron injection.[24] Nevertheless, bearing in mind the poor photocurrent and the low fill factor, a combination of these two effects is most likely: A high light-absorption due to the formation of Zn^{2+}-dye complexes and poor electron injection from MG-100 molecules to the oxide. This latter effect is probably related to the chemical nature of the phosphonic group that links this dye to the oxide, which may hinder the electronic overlap between the excited state of the dye and acceptor states in the oxide.

3.3. Optimization of architecture of Dye-Sensitized Solar Cell.

To optimize the energy conversion efficiency achieved in the previous section using RK1 dye as sensitizer, different thicknesses of ZnO films have been tested. As shown in **Figure 10.5**, the longer the thickness the higher the photocurrent, due to the larger surface area available for the attachment of dye molecules. However, for the same reason, a decrease of the photovoltage is also expected as a consequence of the electron recombination at the semiconductor/electrolyte interface. The results confirm this expectation.

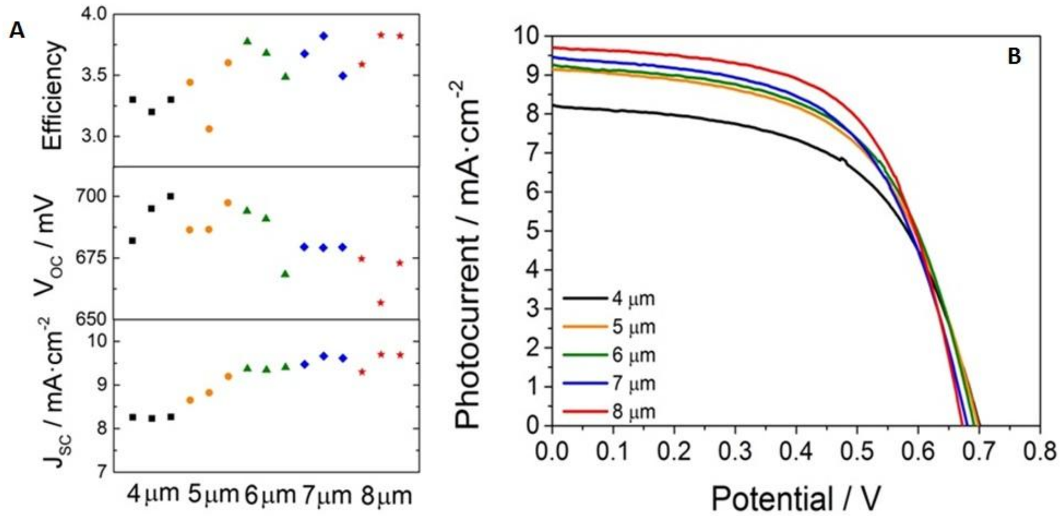

Figure 10.5: (A) Photovoltaic parameter (efficiency, open-circuit photovoltage and short-circuit photocurrent) for RK1-DSSCs using different thickness of photoanode. 3 samples have been measured. (B) Current-voltage for the best cell of each configuration. All DSSCs were characterized under 1-sun AM 1.5 illumination.

Bearing in mind the high absorption coefficient of RK1 dye (**Figure 10.3A**), the thinnest film shows just a difference of 1.5 mA/cm^{-2} with respect to the thickest film in spite of this being two times longer (4 μm and 8 μm, respectively). Therefore, longer thickness only contributes to an insignificant increase of the photocurrent and an important efficiency loss as a consequence of the electron recombination. In contrast to the previous section, to guarantee the penetration of dye solution along the whole thickness of photoanodes and to make sure that the entire surface in the thickest films is covered, a sensitization time of 90 min was applied in the preparation of the photoanodes.

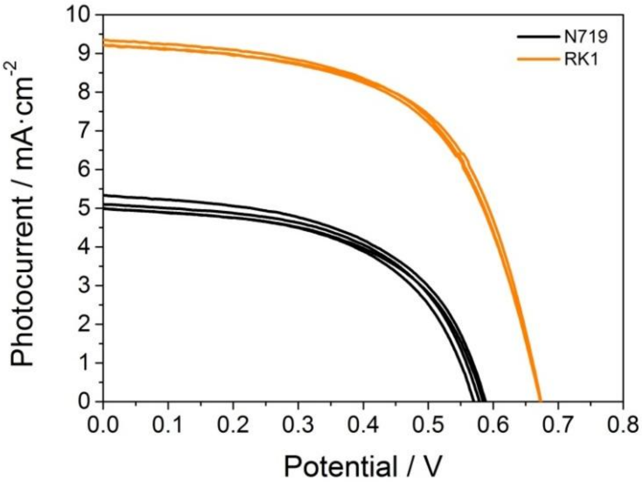

Figure 10.6: Current-voltage curves under 1-sun AM 1.5 illumination for RK1 and N719 using a 8μm ZnO film as photoanode.

Figure 10.6 shows current-voltage characteristics of the optimal architecture for DSSCs employing a thin film (8 μm) of ZnO as photoanode sensitized with the organic dye RK1 and the ruthenium dye N719. In contrast to a previous report,[25] where the energy conversion efficiencies are approximately similar when TiO_2 is employed as photoanode, RK1-DSSCs double the efficiency recorded for N719-DSSCs (3.7% and 1.7%, respectively).

In **Figure 10.6**, RK1-DSSCs show a short-circuit photocurrent of 9.3 mA/cm^{-2} whereas in N719-DSSCs a values of 5.2 mA/cm^{-2} has been found. This difference is consistent with the IPCE showed in **Figure 10.4B** where values approximately two times higher were obtained. However, the open-circuit photovoltage is also greatly increased when RK1 is used as sensitizer. To cast light on this remarkable effect, an electrochemical impedance spectroscopy study has been performed.[26,27] By means of impedance spectroscopy the two factors that determine the open-circuit photovoltage are analyzed: (1) the position of the conduction band edge and (2) the electron recombination rate.

In **Figure 10.7**, the electron recombination resistance and chemical capacitance extracted from the EIS spectra at different illumination intensities are reported.

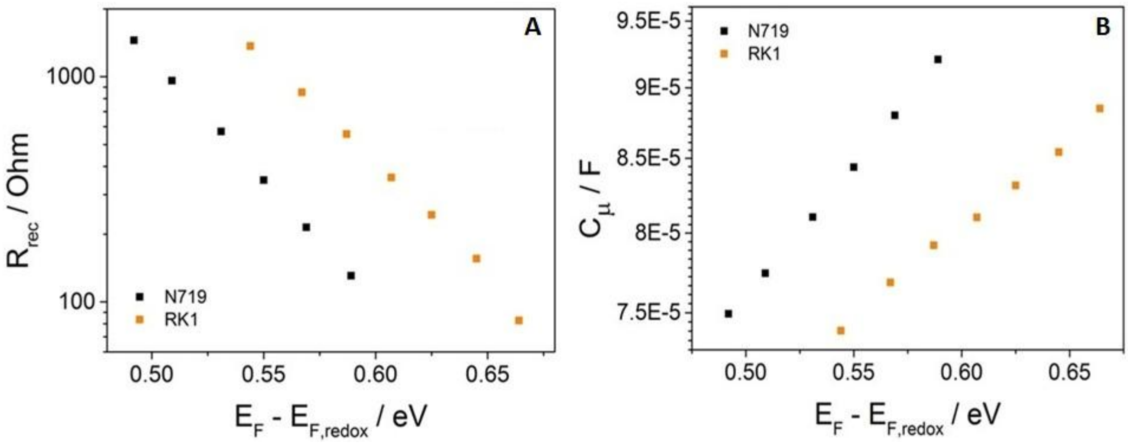

Figure10.7: (A) Electron recombination resistance and (B) chemical capacitance data as extracted from EIS measurements in RK1-DSSC and N719-DSSC.

Figure 10.7A shows a higher electron recombination resistance for RK1-DSSC than for N719-DSSC at a given value of Fermi level. However, the chemical capacitance data (**Figure 10.7B**) evidences a clear difference between RK1-DSSC and N719-DSSC. This means that the adsorption of these dyes on the surface of the ZnO semiconductor produces a shift in the position of the conduction band edge with respect to E_{redox} of the electrolyte. In particular, a negative band-shift in the semiconductor oxide band edge has been found for RK1-DSSC with respect to N719-DSSC. Therefore, the energy difference between the conduction band edge and E_{redox} of electrolyte, which is the other factor that determine the open-circuit photovoltage, is higher for RK1-DSSCs. Using **Equation 4.17**, the electron lifetime can be extracted from electron recombination resistance and chemical capacitance data (**Figure 10.8**).

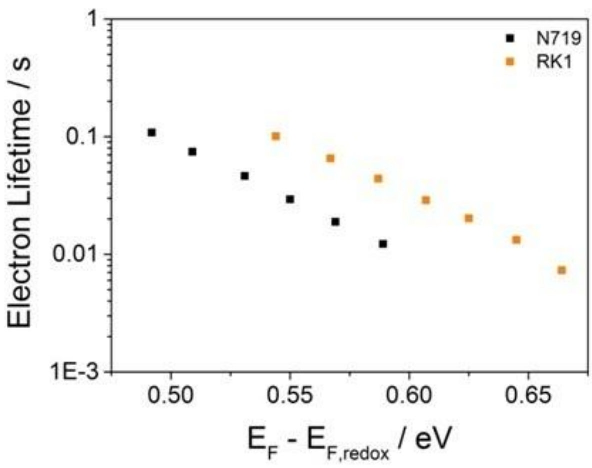

Figure10.8: Electron lifetime data is extracted from EIS measurements in RK1-DSSC and N719-DSSC.

It is observed that the electron lifetime is longer for RK1-DSSC than for N719-DSSC, as it can be inferred from the chemical capacitance and the electron recombination data. A similar result is obtained when electron lifetime is extracted from OCVD measurements (**Appendix**, Figure A-10.3).[28,29] Consequently, RK1-DSSC shows a higher open-circuit photovoltage. Nevertheless, to determine the origin of the longer electron lifetime it is neccesary to separate out the thermodynamic and kinetics effects (see **Chapter 7** for details). Once corrected for band-shift according to chemical capacitances, a slightly lower electron recombination resistance is found for RK1-DSSC than for N719-DSSC (**Appendix**, Figure A-10.4). We can then conclude that the kinetics of the electron recombination at the same value of electron density is very similar for both dyes. Therefore the band-shift of the semiconductor oxide is the main factor responsible for the different open-circuit photovoltage in both DSSCs.

4. Conclusions.

In this chapter, the photovoltaic performances of different donor-π-acceptor organic dyes have been studied with respect to the most common ruthenium dye (N719). These organic dyes have been obtained modifying the synthesis route of one of the most promising organic dyes (RK1). The main structural differences reside in the number and nature of anchoring groups. However, the different photovoltaic performances have been attributed to their light-harvesting efficiencies. In relation to the interaction between the dyes and ZnO surface, it seems that the use of $-PO_3H_2$ radical as anchoring group lead to a more intense dissolution of the semiconductor than the –COOH groups and/or a poorer electron injection rate.

After the optimization of the architecture of DSSCs, using as sensitizer the RK1 organic dye an overall light conversion efficiency of 3.7% has been achieved. In spite of showing a similar electron recombination kinetics to N719, due to its high absorption coefficient and the induced negative band-shift of the conduction band edge of the ZnO semiconductor, a higher photocurrent and photovoltage is achieved. In particular, the efficiency becomes doubled with respect to N719 when using ZnO as photoanode.

5. References.

(1) O'Regan, B.; Gratzel, M. A Low-Cost, High-Efficiency Solar-Cell Based on Dye-Sensitized Colloidal Tio2 Films. *Nature* **1991**, *353*, 737–740.

(2) Grätzel, M. Recent Advances in Sensitized Mesoscopic Solar Cells. *Acc. Chem. Res.* **2009**, *42*, 1788–1798.

(3) Liu, Y.; Jennings, J. R.; Huang, Y.; Wang, Q.; Zakeeruddin, S. M.; Grätzel, M. Cobalt Redox Mediators for Ruthenium-Based Dye-Sensitized Solar Cells: A Combined Impedance Spectroscopy and Near-IR Transmittance Study. *J Phys Chem C* **2011**, *115*, 18847–18855.

(4) Hardin, B. E.; Snaith, H. J.; McGehee, M. D. The Renaissance of Dye-Sensitized Solar Cells. *Nat. Photonics* **2012**, *6*, 162–169.

(5) Snaith, H. J. Perovskites: The Emergence of a New Era for Low-Cost, High-Efficiency Solar Cells. *J. Phys. Chem. Lett.* **2013**, *4*, 3623–3630.

(6) Im, J.-H.; Lee, C.-R.; Lee, J.-W.; Park, S.-W.; Park, N.-G. 6.5% Efficient Perovskite Quantum-Dot-Sensitized Solar Cell. *Nanoscale* **2011**, *3*, 4088–4093.

(7) Gao, F.; Wang, Y.; Shi, D.; Zhang, J.; Wang, M. K.; Jing, X. Y.; Humphry-Baker, R.; Wang, P.; Zakeeruddin, S. M.; Gratzel, M. Enhance the Optical Absorptivity of Nanocrystalline TiO2 Film with High Molar Extinction Coefficient Ruthenium Sensitizers for High Performance Dye-Sensitized Solar Cells. *J. Am. Chem. Soc.* **2008**, *130*, 10720–10728.

(8) Hagfeldt, A.; Boschloo, G.; Sun, L.; Kloo, L.; Pettersson, H. Dye-Sensitized Solar Cells. *Chem. Rev.* **2010**, *110*, 6595–6663.

(9) Zeng, W. D.; Cao, Y. M.; Bai, Y.; Wang, Y. H.; Shi, Y. S.; Zhang, M.; Wang, F. F.; Pan, C. Y.; Wang, P. Efficient Dye-Sensitized Solar Cells with an Organic Photosensitizer Featuring Orderly Conjugated Ethylenedioxythiophene and Dithienosilole Blocks. *Chem. Mater.* **2010**, *22*, 1915–1925.

(10) Yella, A.; Lee, H.-W.; Tsao, H. N.; Yi, C.; Chandiran, A. K.; Nazeeruddin, M. K.; Diau, E. W.-G.; Yeh, C.-Y.; Zakeeruddin, S. M.; Grätzel, M. Porphyrin-Sensitized Solar Cells with Cobalt (II/III)–Based Redox Electrolyte Exceed 12 Percent Efficiency. *Science* **2011**, *334*, 629–634.

(11) Mishra, A.; Fischer, M. K. R.; Bäuerle, P. Metal-Free Organic Dyes for Dye-Sensitized Solar Cells: From Structure: Property Relationships to Design Rules. *Angew. Chem. Int. Ed.* **2009**, *48*, 2474–2499.

(12) Ito, S.; Miura, H.; Uchida, S.; Takata, M.; Sumioka, K.; Liska, P.; Comte, P.; Pechy, P.; Graetzel, M. High-Conversion-Efficiency Organic Dye-Sensitized Solar Cells with a Novel Indoline Dye. *Chem. Commun.* **2008**, 5194–5196.

(13) Dualeh, A.; De Angelis, F.; Fantacci, S.; Moehl, T.; Yi, C.; Kessler, F.; Baranoff, E.; Nazeeruddin, M. K.; Grätzel, M. Influence of Donor Groups of Organic D–π–A Dyes on Open-Circuit Voltage in Solid-State Dye-Sensitized Solar Cells. *J. Phys. Chem. C* **2012**, *116*, 1572–1578.

(14) Guillen, E.; Casanueva, F.; Anta, J. A.; Vega-Poot, A.; Oskam, G.; Alcantara, R.; Fernandez-Lorenzo, C.; Martin-Calleja, J. Photovoltaic Performance of Nanostructured Zinc Oxide Sensitised with Xanthene Dyes. *J. Photochem. Photobiol. - Chem.* **2008**, *200*, 364–370.

(15) Chou, T. P.; Zhang, Q.; Cao, G. Effects of Dye Loading Conditions on the Energy Conversion Efficiency of ZnO and TiO2 Dye-Sensitized Solar Cells. *J. Phys. Chem. C* **2007**, *111*, 18804–18811.

(16) Katoh, R.; Furube, A.; Tamaki, Y.; Yoshihara, T.; Murai, M.; Hara, K.; Murata, S.; Arakawa, H.; Tachiya, M. Microscopic Imaging of the Efficiency of Electron Injection from Excited Sensitizer Dye into Nanocrystalline ZnO Film. *Sixth AIST Int. Symp. Photoreact. Control Photoreact. Mater.* **2004**, *166*, 69–74.

(17) Memarian, N.; Concina, I.; Braga, A.; Rozati, S. M.; Vomiero, A.; Sberveglieri, G. Hierarchically Assembled ZnO Nanocrystallites for High-Efficiency Dye-Sensitized Solar Cells. *Angew. Chem. Int. Ed.* **2011**, *50*, 12321–12325.

(18) Vega-Poot, A. G.; Macías-Montero, M.; Idígoras, J.; Borrás, A.; Barranco, A.; Gonzalez-Elipe, A. R.; Lizama-Tzec, F. I.; Oskam, G.; Anta, J. A. Mechanisms of Electron Transport and Recombination in ZnO Nanostructures for Dye-Sensitized Solar Cells. *ChemPhysChem* **2014**, *15*, 1088–1097.

(19) O'Regan, B. C.; Lenzmann, F. Charge Transport and Recombination in a Nanoscale Interpenetrating Network of N-Type and P-Type Semiconductors: Transient Photocurrent and Photovoltage Studies of TiO2/Dye/CuSCN Photovoltaic Cells. *J. Phys. Chem. B* **2004**, *108*, 4342–4350.

(20) Bisquert, J.; Mora-Seró, I. Simulation of Steady-State Characteristics of Dye-Sensitized Solar Cells and the Interpretation of the Diffusion Length. *J. Phys. Chem. Lett.* **2010**, *1*, 450–456.

(21) Anta, J. A.; Idígoras, J.; Guillén, E.; Villanueva-Cab, J.; Mandujano-Ramírez, H. J.; Oskam, G.; Pellejà, L.; Palomares, E. A Continuity Equation for the Simulation of the Current–voltage Curve and the Time-Dependent Properties of Dye-Sensitized Solar Cells. *Phys. Chem. Chem. Phys.* **2012**, *14*, 10285–10299.

(22) Peter, L. M. Characterization and Modeling of Dye-Sensitized Solar Cells. *J. Phys. Chem. C* **2007**, *111*, 6601–6612.

(23) Anta, J. A.; Guillén, E.; Tena-Zaera, R. ZnO-Based Dye-Sensitized Solar Cells. *J. Phys. Chem. C* **2012**, *116*, 11413–11425.

(24) Horiuchi, H.; Katoh, R.; Hara, K.; Yanagida, M.; Murata, S.; Arakawa, H.; Tachiya, M. Electron Injection Efficiency from Excited N3 into Nanocrystalline ZnO Films: Effect of (N3–Zn2+) Aggregate Formation. *J. Phys. Chem. B* **2003**, *107*, 2570–2574.

(25) Joly, D.; Pellejà, L.; Narbey, S.; Oswald, F.; Chiron, J.; Clifford, J. N.; Palomares, E.; Demadrille, R. A Robust Organic Dye for Dye Sensitized Solar Cells Based on Iodine/Iodide Electrolytes Combining High Efficiency and Outstanding Stability. *Sci Rep* **2014**, *4*.

(26) Fabregat-Santiago, F.; Bisquert, J.; Garcia-Belmonte, G.; Boschloo, G.; Hagfeldt, A. Influence of Electrolyte in Transport and Recombination in Dye-Sensitized Solar Cells Studied by Impedance Spectroscopy. *Sol. Energy Mater. Sol. Cells* **2005**, *87*, 117–131.

(27) Bisquert, J. Theory of the Impedance of Electron Diffusion and Recombination in a Thin Layer. *J. Phys. Chem. B* **2002**, *106*, 325–333.

(28) Zaban, A.; Greenshtein, M.; Bisquert, J. Determination of the Electron Lifetime in Nanocrystalline Dye Solar Cells by Open-Circuit Voltage Decay Measurements. *Chemphyschem* **2003**, *4*, 859–864.

(29) Ansari-Rad, M.; Abdi, Y.; Arzi, E. Reaction Order and Ideality Factor in Dye-Sensitized Nanocrystalline Solar Cells: A Theoretical Investigation. *J Phys Chem C* **2012**, *116*, 10867–10872.

General conclusions

In this thesis nanocrystalline semiconductor metal-oxide (TiO_2, ZnO) photoanodes in contact with liquid electrolytes have been studied at a fundamental level in connection with their photoelectrocatalysis and photovoltaic performance. All results presented and discussed in this work show the crucial effect of the electrolyte composition on the electronic structure of the oxide and its impact on the charge transfer processes between semiconductor and electrochemically active species in the electrolyte. These processes are the ones that ultimately limit the efficiency of energy conversion.

In **Chapter 5** and **6** it was shown that a simple electrochemical treatment can improve the photoelectrocatalytic activity of mesoporous TiO_2 electrodes. The photocurrent enhancement in photooxidation reactions was attributed to reduced electron recombination and improved electron transport in the semiconductor. It has been shown that the origin of this beneficial effect is the accumulation of charge carriers in the semiconductor and the formation of a depletion layer at the semiconductor/electrolyte interface. This electrochemical doping relies on electron accumulation upon cathodic polarization and the concomitant insertion of protons in the subsurface region of the semiconductor. The kinetics of the doping and undoping processes depends on the position of the Fermi level during the treatment, which can be shifted by an external cathodic polarization or by band gap excitation at open-circuit. In addition, it has been shown that the doping persistence depends critically on the morphological properties of the thin film electrode such as the particle size. The fact that doping can take place even at open circuit conditions upon band gap excitation highlights the relevance of these findings for photocatalytic applications.

In **Chapter 7** and **8** the effect of the chemical environment of the redox couple on the recombination rate in Dye-Sensitised Solar Cells was analyzed. It has been shown that the polarity of the electrolyte solvent critically influences the recombination kinetics. Two behaviours of the electron lifetime as the applied potential is varied were observed. As the reorganization energy strongly depends on the chemical environment and the interaction of the components of the redox couple with solvent molecules, this magnitude has been proposed as a key factor that controls recombination. This is explained by the availability of extra routes for electron recombination for relatively large values of the reorganization energy. This is for instance the case of dye-sensitized solar cells with an ionic liquid-based electrolyte. A fundamental study that consisted in controlling the recombination rate by means of the modification of the polarity of the electrolyte was carried out. In this connection, a mixture of an ionic liquid with an organic solvent as electrolyte has been presented as a possible strategy to obtain long-life devices with larger electron lifetime. This knowledge can be of major interest for Building Integrated Photovoltaics (BIPV) applications.

In **Chapter 9** a global analysis of all processes that determine charge separation in dye-sensitized solar cells was performed. One of the main objectives of this chapter has been to identify the processes that limit the efficiency of solar cells based on ZnO as photoanode (as compared with TiO_2). A poor electron injection and dye regeneration rate have been identified as the main drawback of ZnO photoanodes. This difference with respect to solar cells based on TiO_2 can be explained by the higher density of deep traps states in ZnO as electron acceptors. In addition, as a consequence of its lower dielectric constant, charge separation at the oxide/dye interface can critically be hindered. The lower dielectric constant does also explain the insensitivity of the chemical capacitance and injection rate under the presence of potential-determining additives. Due to its difficulty to form surface dipoles, the presence of additives like Li^+ or Tbp does not alter the solar cell performance and hence it does not offer a strategy to improve the efficiency of devices based on ZnO.

In **Chapter 10**, a more application-oriented study based on the characterization of state-of-the-art dyes for ZnO solar cells has been performed. Bearing in mind that the optimization of electrolyte composition by means of the addition of potential-determining additives does not represent a way to improve the efficiency of ZnO-DSSC, the search of new dyes with a high light-harvesting efficiency can be considered an alternative strategy in these systems characterized by a low electron injection rate. In particular, we have shown that the purely organic dye coded RK1 is a recommended sensitizer for ZnO photoanodes. Thanks to this organic dye, the energy conversion efficiency has been doubled with respect to the efficiency achieved with the most common ruthenium dye.

As a general conclusion, this fundamental thesis has shown the importance of understanding the microscopic processes taking place at the semiconductor/electrolyte interface. A profound knowledge of these interfacial processes constitutes undoubtedly a prerequisite for future systematic optimizations of materials' properties in applications such as photocatalysis or photovoltaics.

Appendix

Chapter 4:

Experimental: Characterization techniques and preparation of devices.

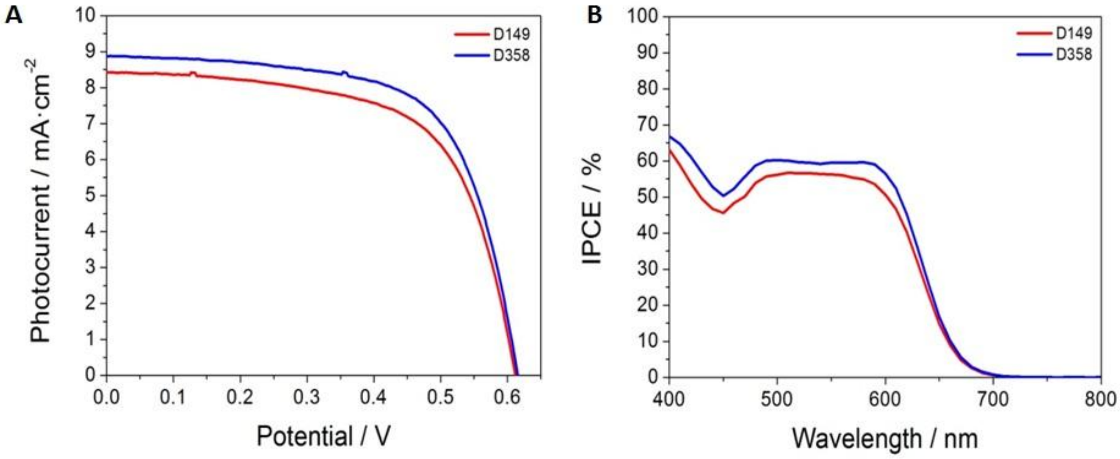

	J_{sc} / mA·cm^{-2}		
Dye	**Curve IV**	**IPCE**	**Error**
D149	**8.4**	**8.2**	**1.2%**
D358	**8.9**	**8.6**	**1.7%**

Figure A-4.1: (A) Current-voltage curves under 1-sun AM1.5 + UV filter (<400nm) and (B) IPCE measured in the range of 400-800nm for DSSCs with different dye: *D149* and *D358*. In the table is shown the short-circuit photocurrent (J_{sc}) extracted from Curve IV and IPCE (**Equation 3.15**) and the error associated with these two techniques.

Chapter 5:

In situ self-doping of mesoporous titanium dioxide films.

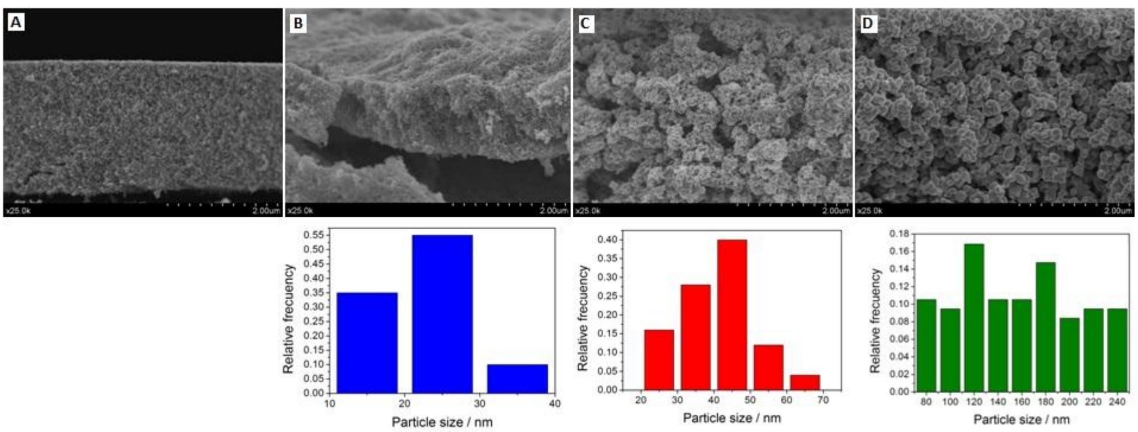

Figure A-5.1: Scanning electron micrographs (SEM) and the distributions of nanoparticles for (A) Solaronix, (B) Sachtleben, (C) PI-KEM and (D) Sigma films.

	Solaronix		Sachtleben		PI-KEM		Sigma	
Doping type	Light	Bias	Light	Bias	Light	Bias	Light	Bias
Doping potential	-0.425V		-0.36V		-0.35V		-0.40V	
PCEF	1.3	1.25	1.3	1.25	2.7	2.4	3.5	3.3

Table A-5.1: Photocurrent enhancement factors determined for all electrodes upon voltage-induced and light-induced doping in of hole scavenger. Electrolyte: N_2-purged 0.1 M $HClO_4$.

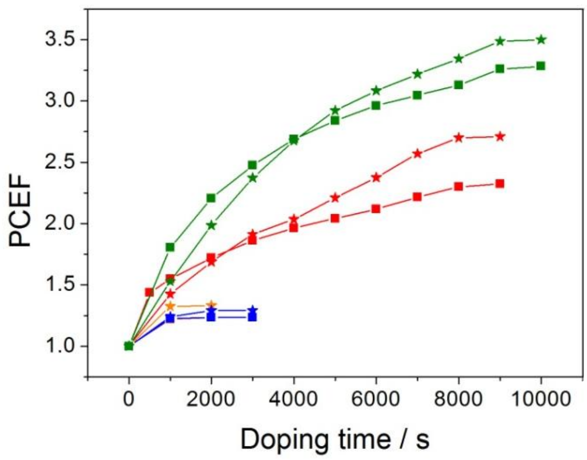

Figure A-5.2: Photocurrent enhancement factors determined for Solaronix (orange), Sachtleben (blue), PI-KEM (red) and Sigma (green) electrodes under cumulative cycles of voltage-induced (square) and light-induced doping (star). The electrode potentials during doping are indicated in Table 6.1. Electrolyte: N_2-purged 0.1 M $HClO_4$.

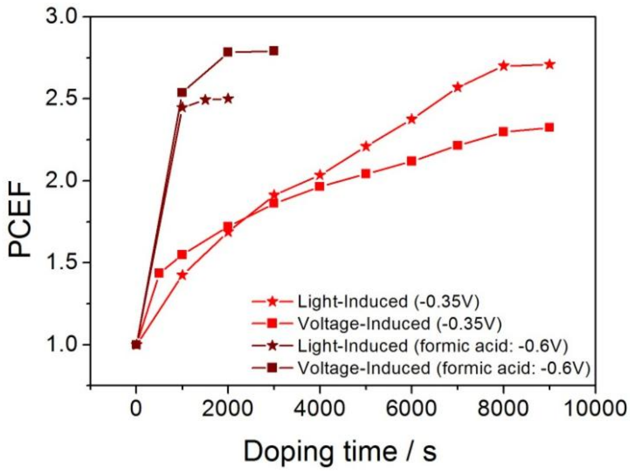

Figure A-5.3: Photocurrent enhancement factors determined for PI-KEM electrodes at different stages of voltage-induced (square) and light-induced doping (star) in absence (red) and presence (brown) of hole scavenger. The electrode potentials during doping (voltage-induced doping: externally applied bias; light-induced doping: open circuit photopotential) are indicated in the brackets. Electrolyte: Electrolyte: N_2-purged 0.1 M $HClO_4$ or 1 M HCOOH/0.1 M $HClO_4$ aqueous solution

Doping type	Solaronix		Sachtleben		PI-KEM		Sigma	
	Undoped	Doped	Undoped	Doped	Undoped	Doped	Undoped	Doped
Voltage-Induced	0.25	0.28	0.46	0.15	0.36	0.37	0.41	0.34
Light-Induced	0.25	0.29	0.45	0.19	0.26	0.20	0.37	0.23

Table A-5.2: α parameter extracted from the semilogarithmic plot of $C\mu = j_C/v$ before and after voltage- and light-induced electrochemical doping.

Chapter 6:

Electrochemical hydrogen-doping: Impact on photoelectrocatalytic and photovoltaic applications.

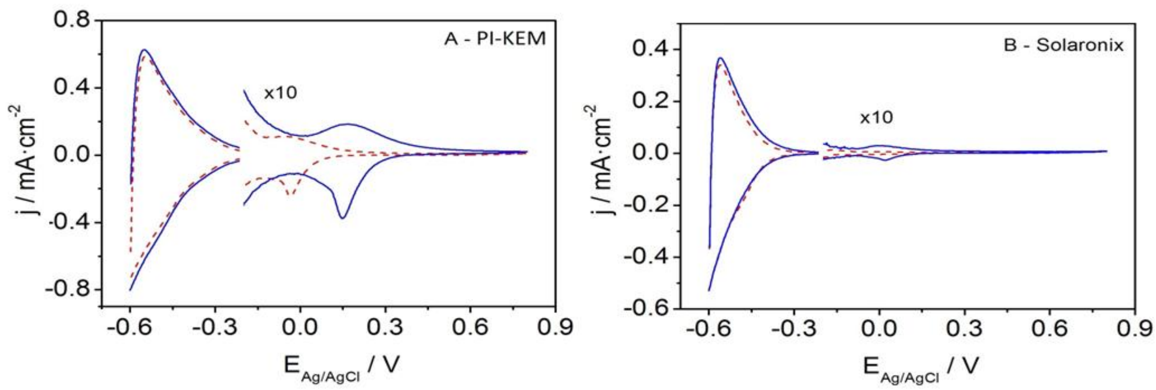

Figure A-6.1: CVs in the dark for undoped (dashed red lines) and doped (solid blue lines) (A) PI-KEM and (B) Solaronix electrodes. Electrolyte: N_2-purged 0.1 M $HClO_4$ aqueous solution.

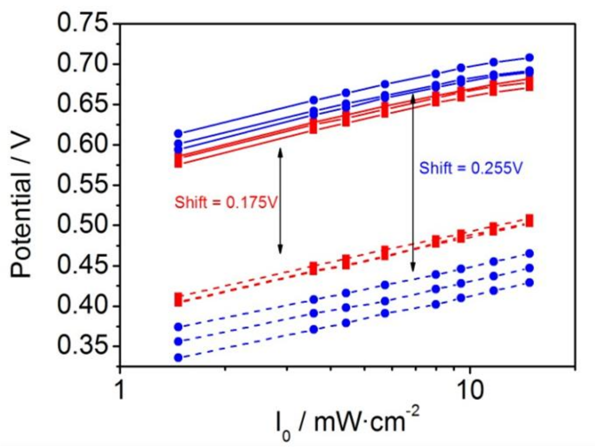

Figure A-6.2: Open-circuit (solid-lines) and short-circuit (dashed lines) potentials as a function of light intensity for doped (squares) and undoped (electrodes). The Fermi-level shifts between open-circuit and short-circuit conditions, obtained for both kinds of electrodes, are indicated in the graph.

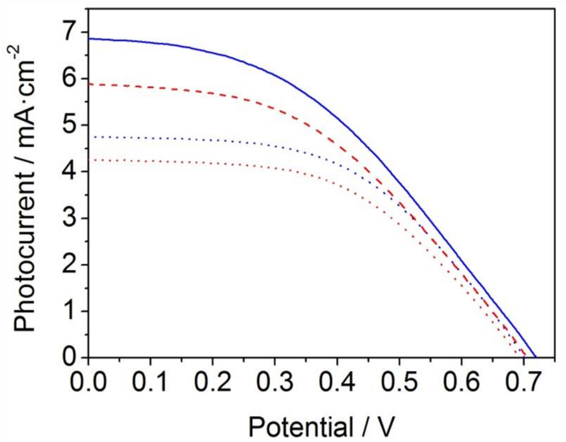

Figure A-6.3: Current-voltage characteristics under AM 1.5 (100 mW·cm^{-2}) illumination of DSC test devices (PI-KEM, electrolyte A) based on doped (solid blue lines) and undoped (dashed red lines) electrodes for illumination through the working electrode (front illumination) or through the counter-electrode (back illumination). Electrochemical doping in 0.1 M $HClO_4$ aqueous solution: $E_{Ag/AgCl}$ = -0.6 V; t_{dop} = 750 s.

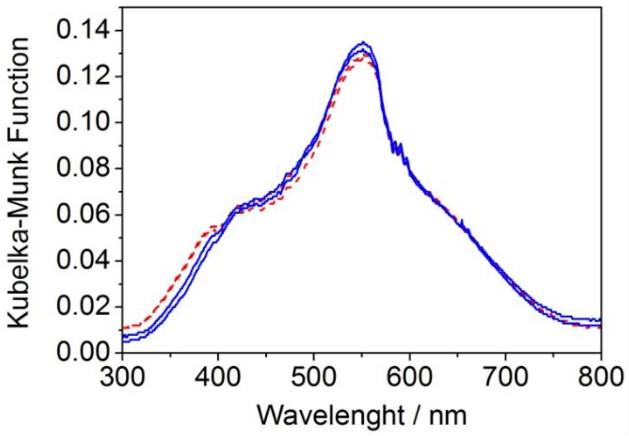

Figure A-6.4: Vis-spectrum of dye-sensitized undoped (dashed red lines) and doped (solid blue lines) PI-KEM electrodes. Electrochemical doping in 0.1 M $HClO_4$ aqueous solution: $E_{Ag/AgCl}$ = -0.6 V; t_{dop} = 750 s.

Configuration		J_{sc} (mA·cm^{-2})	V_{oc} (mV)	Fill Factor (%)	Efficiency (%)
Electrolyte A	PI-KEM Undoped	5.9	683	52	2.2
	PI-KEM Doped	7.2	714	52	2.7
	PI-KEM Doped+24h storage at OCP	6.3	709	54	2.4

Table A-6.1: Photovoltaic parameters under 1-sun AM 1.5 for DSSC test devices based on PI-KEM electrodes.

Chapter 7:

The influence of the chemical environment of the redox pair on the recombination loss in Dye-Sensitized Solar Cells.

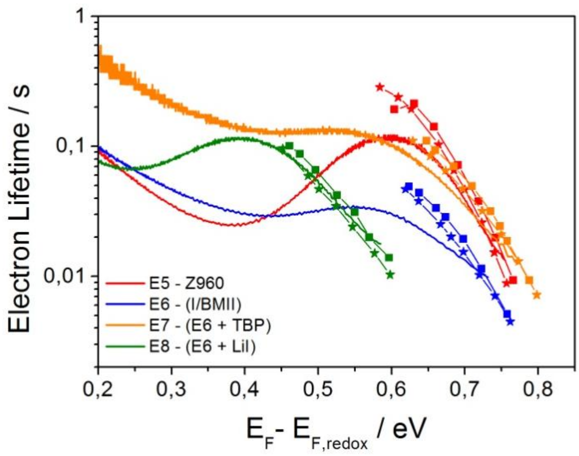

Figure A-7.1: Electron lifetimes as extracted from the three techniques utilized in this chapter: EIS (squares), IMVS (stars) and OCVD (lines) for electrolytes E5 to E8.

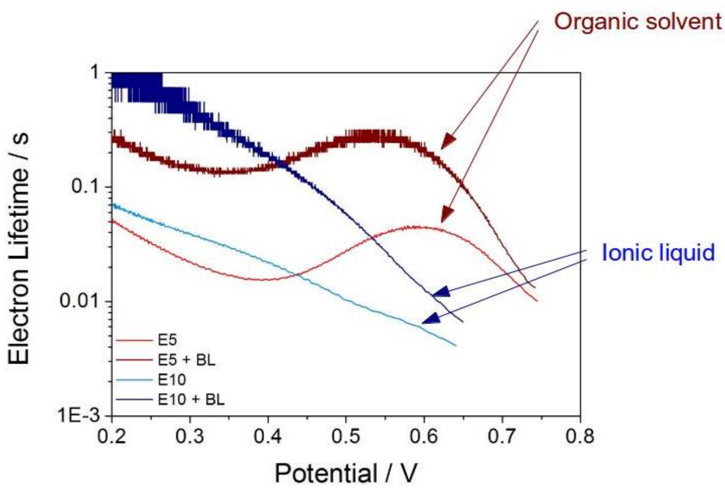

Figure A-7.2: Electron lifetime as extracted from OCVD for cells with and without blocking layer (BL). Results are presented for electrolyte E5 (organic solvent) and E10 (ionic liquid based).

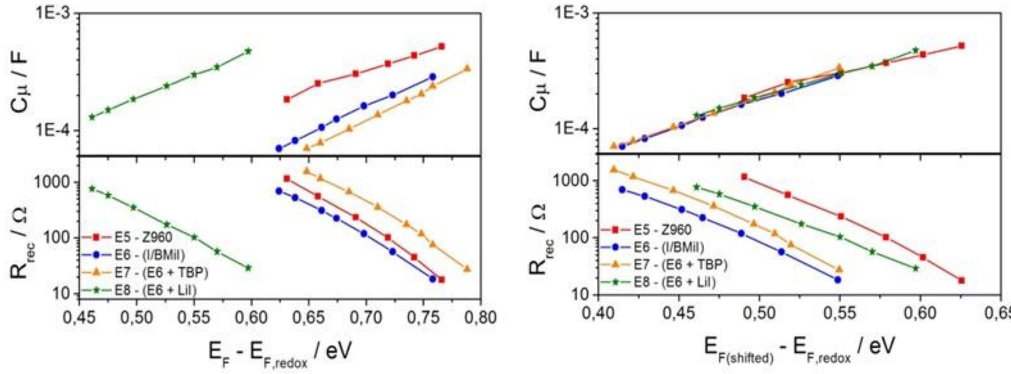

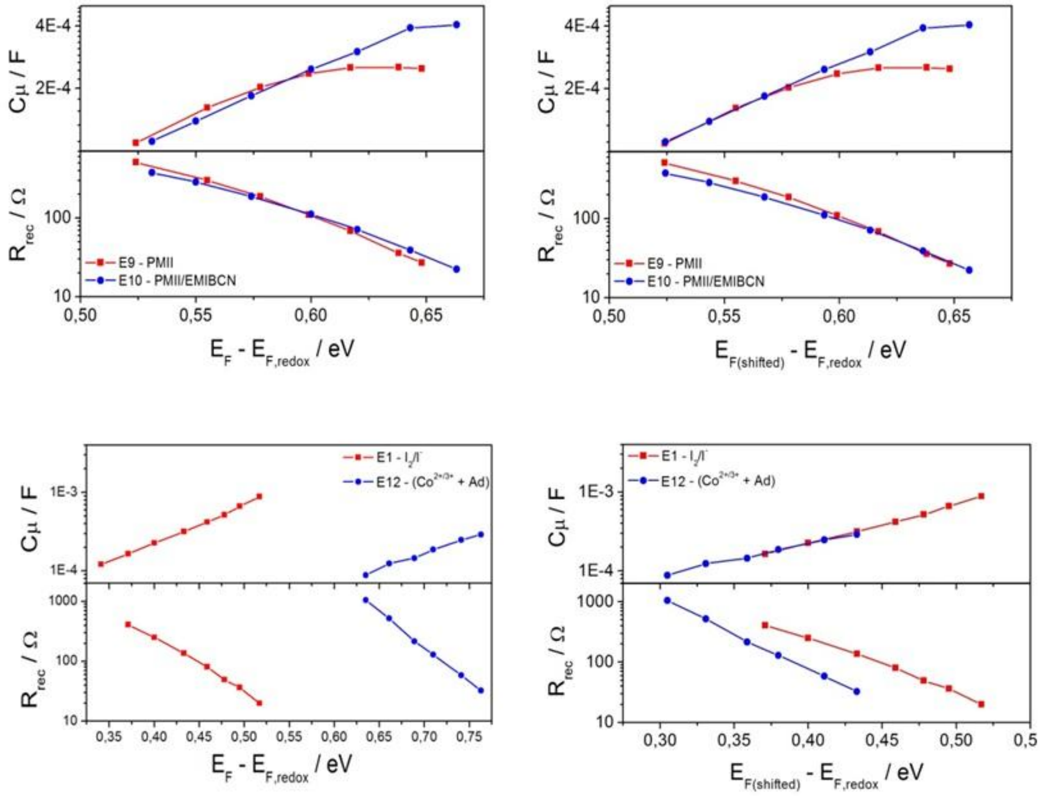

Figure A-7.3: Chemical capacitance and recombination resistances for electrolytes 5 to 13. In the left column absolute values are plotted. In the right column, the voltage scale is shifted to account for band displacements, as described in the main text.

Chapter 8:

Control of recombination rate by changing the polarity of the electrolyte in Dye-Sensitized Solar Cells.

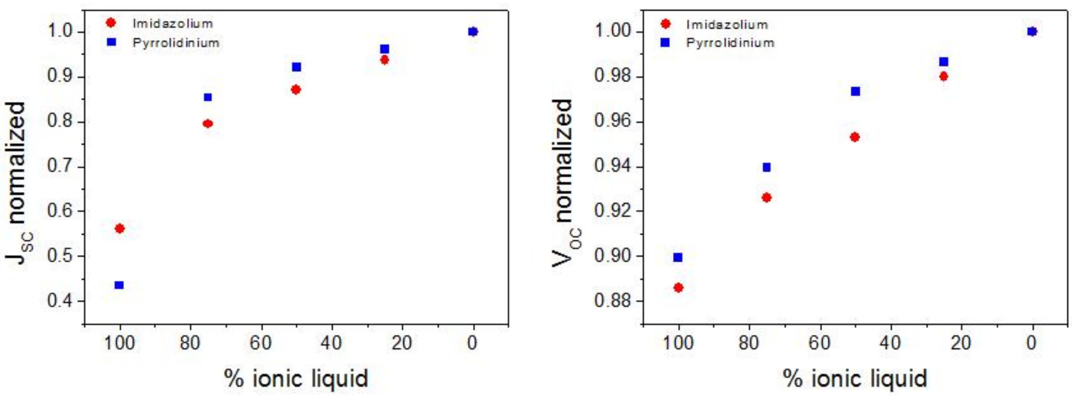

Figure A-8.1: J_{sc} and V_{oc} for all electrolytes normalized by the J_{sc} and V_{oc} obtain in pure acetonitrile-based electrolyte in N719-cells.

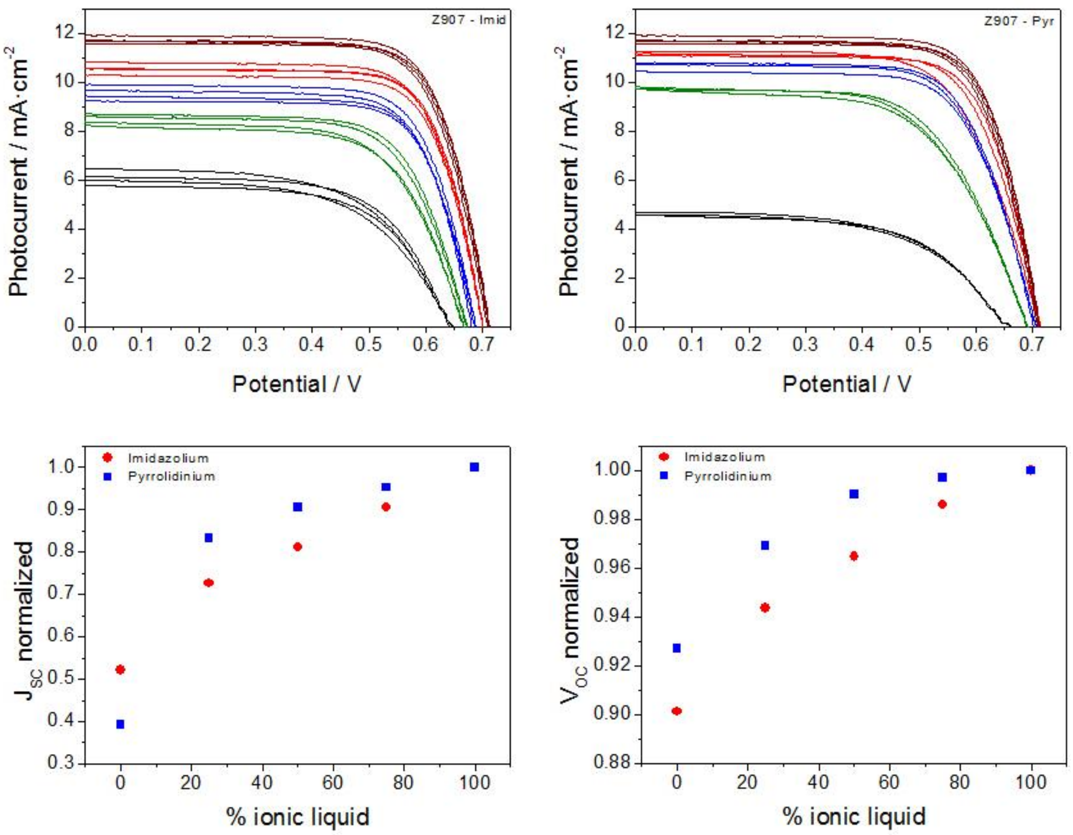

Figure A-8.2: (Top) Current-voltage curves under 1-sun AM 1.5 for all RTIL/Can mixing ratios for Imidazolium and Pyrrolidinium. (Bottom) J_{sc} and V_{oc} for all electrolytes normalized by the J_{sc} and V_{oc} obtain in pure acetonitrile-based electrolyte in N719-cells.

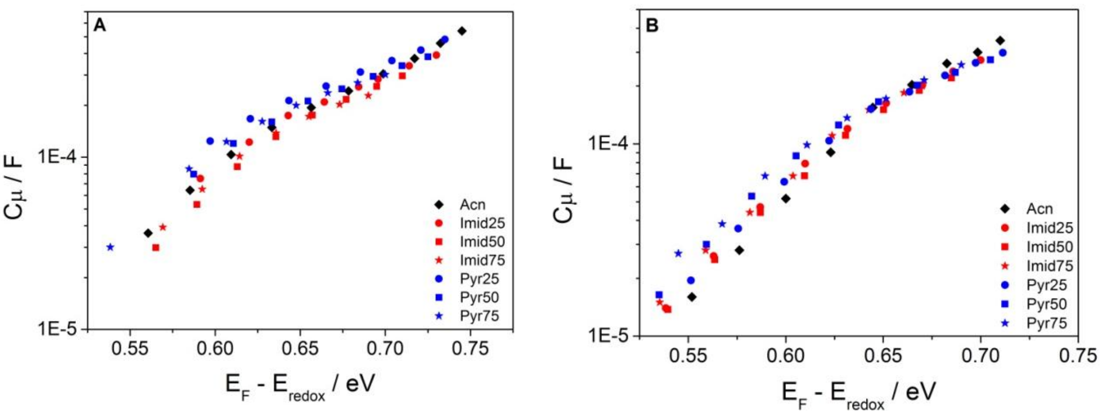

Figure A-8.3: Chemical capacitance data as extracted from EIS measurements: (A) N719-cells and (B) Z907-cells.

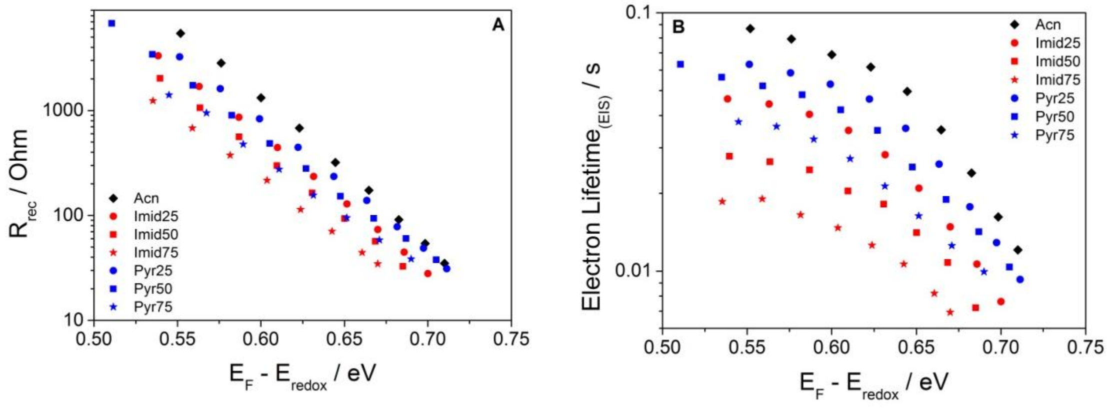

Figure A-8.4: (A) Electron recombination resistance and (B) electron lifetime data are extracted from EIS measurement in Z907-cells.

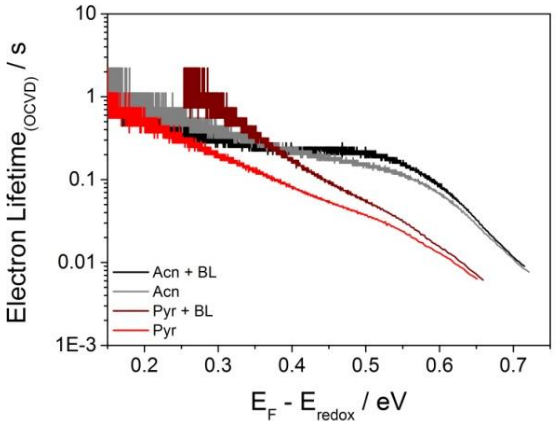

Figure A-8.5: Electron lifetime as extracted from OCVD for Z907-cells with and without blocking layer (BL).

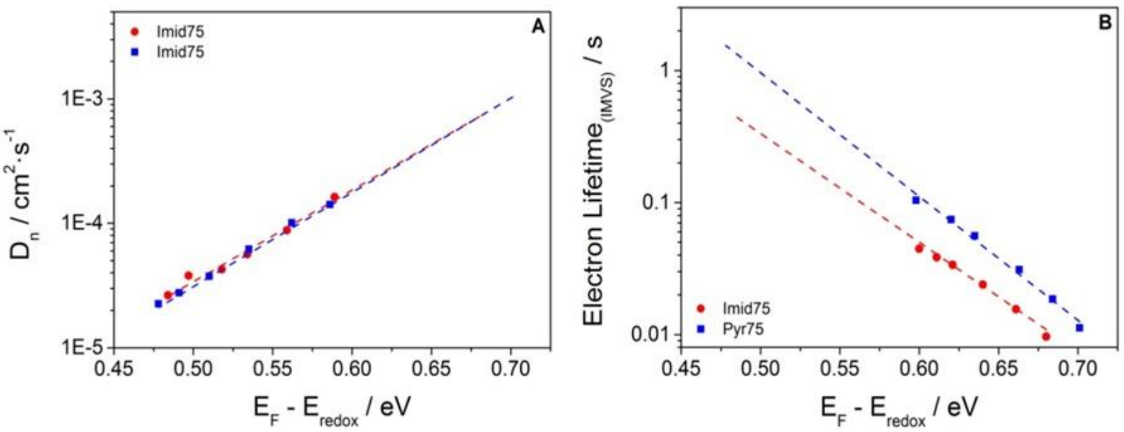

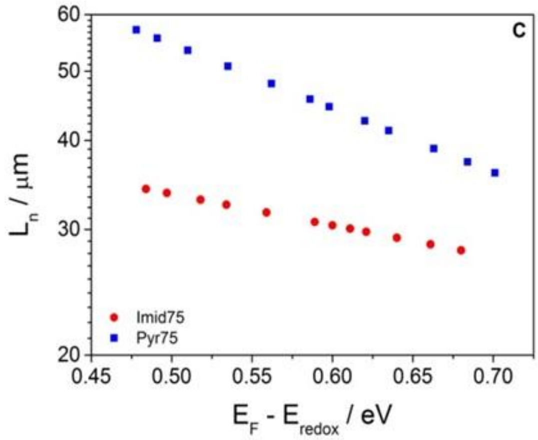

Figure A-8.6: (A) Electron diffusion coefficient obtained from IMPS, (B) electron lifetime obtained from IMVS and (C) electron diffusion length for Imid75 and Pyr75 in N719-cells.

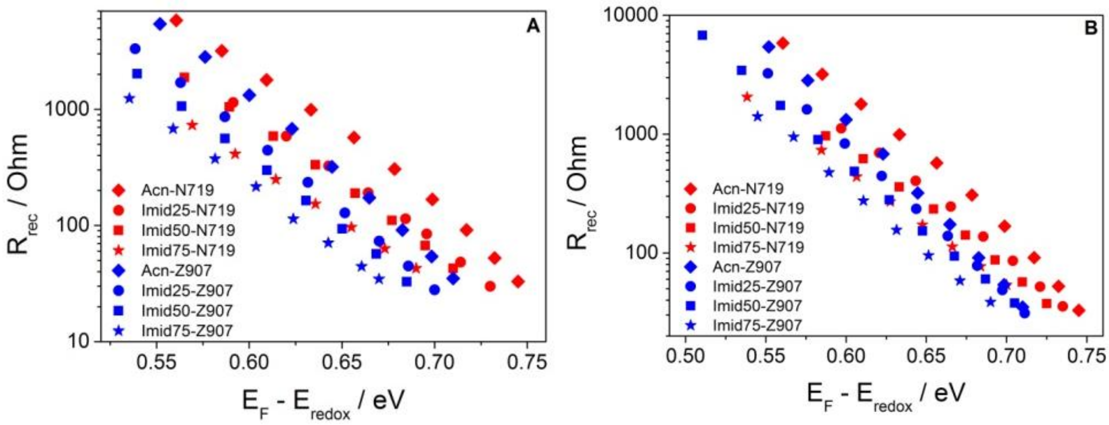

Figure A-8.7: Electron recombination resistance data extracted from EIS measurement in (A) Imid/Acn and (B) Pry/Acn in N719-cells and Z907-cells.

Chapter 9:

Global analysis of Dye-Sensitized Solar Cells: Influence of the electrical nature of the metal-oxide.

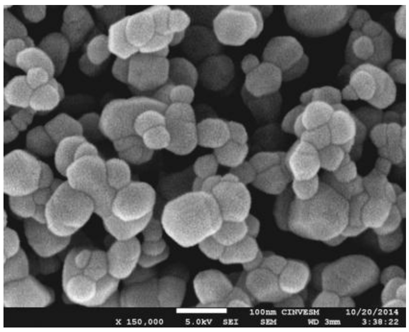

Figure A-9.1: SEM picture of a sintered ZnO nanostructured film used as photoanode

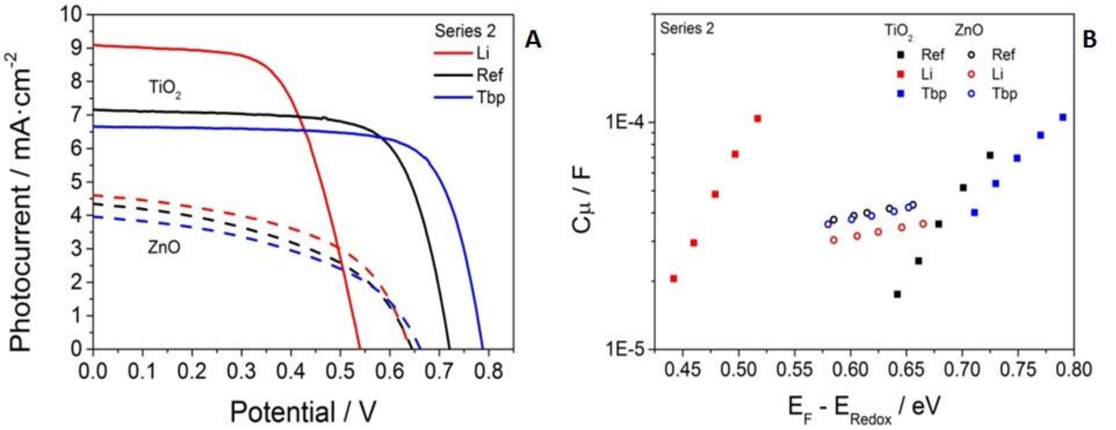

Figure A-9.2: (A) Current-voltage curves under 1-sun AM1.5 illumination and (B) Chemical capacitance data as extracted from EIS measurement for DSSC based on TiO_2 and ZnO as electrodes with electrolyte of Series 2.

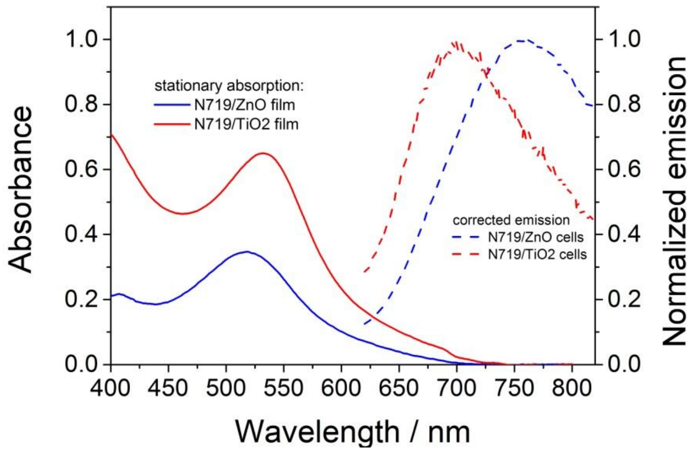

Figure A-9.3: Steady-state absorption spectra of TiO_2 and ZnO films sensitized with N719 and corrected steady-state emission spectra of complete solar cells.

Electrolyte		**TiO_2**			**ZnO**		
		J_{sc} (mA/cm^{-2})	**V_{oc} (mV)**	**J_{sc}/N_{ph} (10^{-19}C)**	**J_{sc} (mA/cm^{-2})**	**V_{oc} (mV)**	**J_{sc}/N_{ph} (10^{-19}C)**
***Series 1*: I_2/LiI**	**Reference**	**9.7**	**460**	**1.60**	**4.5**	**630**	**1.30**
	Pyr	**9.4**	**450**	**1.55**	**4.7**	**615**	**1.35**
	Tbp	**9.4**	**770**	**1.55**	**5.0**	**665**	**1.42**
	TP	**9.1**	**740**	**1.50**	**5.3**	**630**	**1.51**
***Series 2*: I_2/BMII**	**Reference**	**13.75**	**760**	**2.30**	**6.55**	**660**	**1.85**
	Li	**14.70**	**610**	**2.45**	**6.4**	**680**	**1.83**
	Tbp	**13.12**	**830**	**2.20**	**6.45**	**700**	**1.84**

Series 3: I_2/DMPII	Reference	11.25	770	1.90	6.25	690	1.80
	Li(x1)	11.55	600	1.93	6.25	685	1.80
	Li(x2)	11.0	545	1.83	6.25	685	1.80
	Li(x3)	12.5	525	2.10	6.15	690	1.75
	Tbp	10.60	820	1.80	5.95	705	1.70

Table A-9.1: Parameters of the cell used for time-resolved laser spectroscopy studies under LED illumination (slightly higher photocurrents than for 1 sun AM 1.5) are shown. The abbreviation used for electrolyte additives of each series of cells is indicated in Table 1. N_{ph} is the number of absorbed photons.

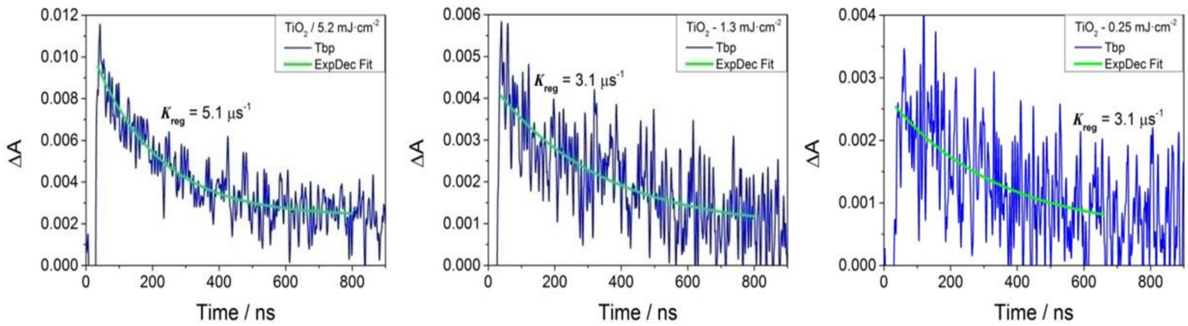

Figure A-9.4: Kinetics at 700 nm obtained in flash photolysis experiment for TiO_2/S2/Tbp cell under different pump pulse fluence. Green solid line presents one-exponential fit.

Electrolyte		τ		β		$k_{AVG(Triplet)}$ / ps^{-1}		Lifetime / ns	
		TiO_2	ZnO	TiO_2	ZnO	TiO_2	ZnO	TiO_2	ZnO
S1	Ref	9.9	7632	0.28	0.44	$8\cdot10^{-3}$	$5\cdot10^{-5}$	0.12	20
	Pyr	9.7	4355	0.28	0.39	$7.8\cdot10^{-3}$	$7.6\cdot10^{-5}$	0.13	13
	Tbp	577	3542	0.37	0.38	$4.4\cdot10^{-4}$	$6.6\cdot10^{-5}$	2.3	15
	TP	653	5704	0.37	0.41	$4.3\cdot10^{-4}$	$5.6\cdot10^{-5}$	2.2	17
S2	Ref	75.6	171	0.28	0.24	$1\cdot10^{-3}$	$1.9\cdot10^{-4}$	0.97	5.3
	Li	12	101	0.28	0.22	$6\cdot10^{-3}$	$1.8\cdot10^{-4}$	0.15	5.7
	Tbp	1050	190	0.36	0.24	$2.2\cdot10^{-4}$	$1.7\cdot10^{-4}$	4.5	5.9
S3	Ref	251.9	1530	0.31	0.34	$4.9\cdot10^{-4}$	$1.2\cdot10^{-4}$	2.05	8.5
	Li(x1)	34	574	0.28	0.28	$2.3\cdot10^{-3}$	$1.4\cdot10^{-4}$	0.43	7.4
	Li(x2)	15	1212	0.28	0.31	$5.2\cdot10^{-3}$	$9.7\cdot10^{-5}$	0.19	10
	Li(x3)	25	5488	0.28	0.43	$3.1\cdot10^{-3}$	$6.7\cdot10^{-5}$	0.32	15
	Tbp	95.3	1593	0.27	0.34	$7.7\cdot10^{-4}$	$1.1\cdot10^{-4}$	1.3	9
Al_2O_3/Li		18597		0.68		$4.17\cdot10^{-5}$		23.95	
Al_2O_3/Tbp		19189		0.7		$4.13\cdot10^{-5}$		24.25	

Table A-9.2: Fitted parameters of phosphorescence decay and calculated averaged rate constants.

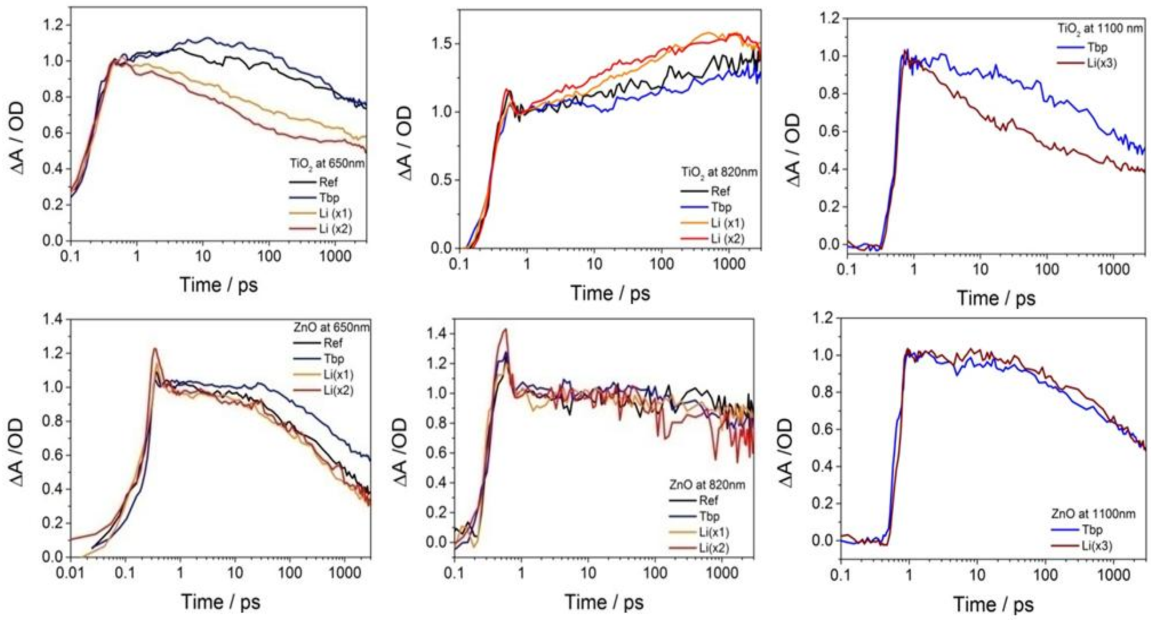

Figure A-9.5: Transient absorption kinetics at indicated probe wavelength for TiO_2/S3 and ZnO/S3 cells.

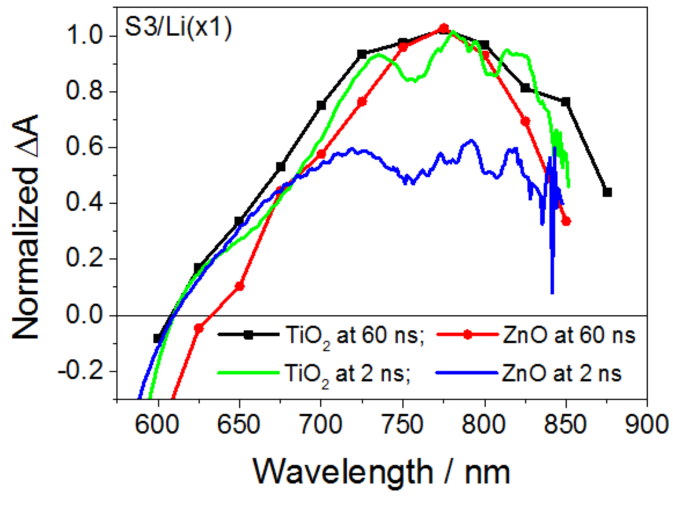

Figure A-9.6: Comparison of transient absorption spectra measured with the fs-ps setup at 2 ns and the initial spectra measured with the flash photolysis equipment at 60 ns (shorter times are disturbed by the presence of spontaneous emission signals). The figure shows that the absorption spectra at 60 ns for both TiO_2 and ZnO cells have a clear maximum between 750 and 800 nm, similar as that at 2 ns for TiO_2, pointing out the presence of free radical cation. On the contrary, the spectrum of ZnO cell at 2 ns is flat in 700-850 region, which means that the formation of free radical cation occurs slower than in TiO_2, between 2 and 60 ns.

Electrolyte		TiO$_2$ τ_1 (ps)	TiO$_2$ Contrib (%)	TiO$_2$ τ_2 (ns)	TiO$_2$ Contrib (%)	ZnO τ_1 (ps)	ZnO Contrib (%)	ZnO τ_2 (ns)	ZnO Contrib (%)
S1: I$_2$/LiI	Ref	5.1	88	2	12	23.8	25	2	75
	Pyr	4.8	85	2	15	31.3	25	2	75
	Tbp	36.4	50	2	50	79.4	30	2	70
	TP	46.7	50	2	50	101.7	35	2	65
S2: I$_2$/BMII	Ref	30.3	71	2	29	30.4	50	2	50
	Li	11	80	2	20	39.7	50	2	50
	Tbp	29.6	50	2	50	79.6	60	2	40
S3: I$_2$/DMPII	Ref	16.8	50	2	50	57.6	50	2	50
	Li(x1)	17.7	74	2	26	23.5	25	2	75
	Li(x2)	17	88	2	12	30.9	31	2	69
	Li(x3)	14.8	100	2	-	124.1	25	2	75
	Tbp	33.1	45	2	55	35.6	41	2	59

Table A-9.3: Time constant and contributions extracted from global multi-exponential analysis on the transient absorption data.

Chapter 10:

Photovoltaic performance of ZnO photoanodes with a novel purely organic D-π-A dyes.

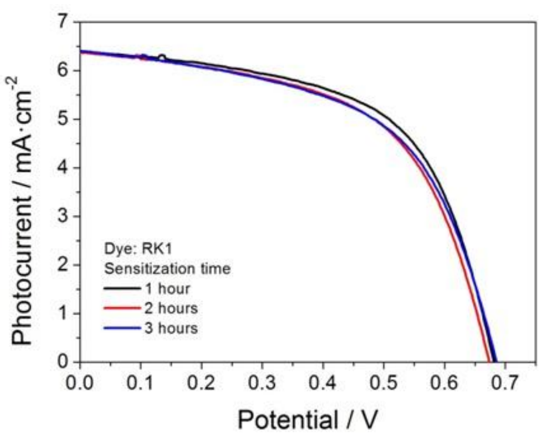

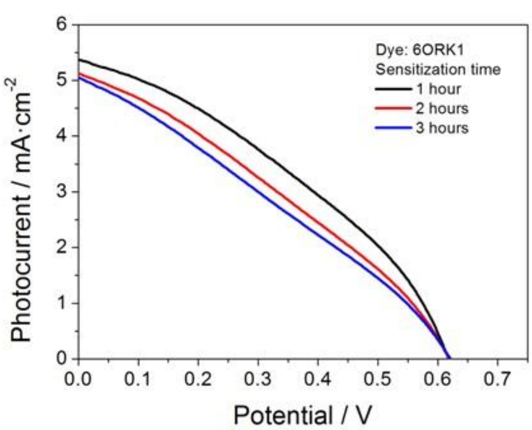

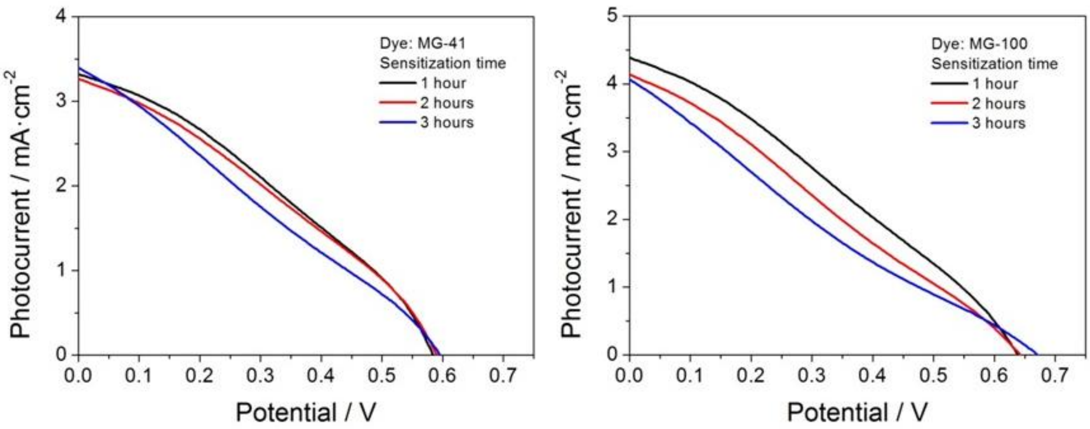

Figure A-10.1: Current-voltage characteristics under 1-sun AM1.5 illumination for all the organic dyes using different sensitization times.

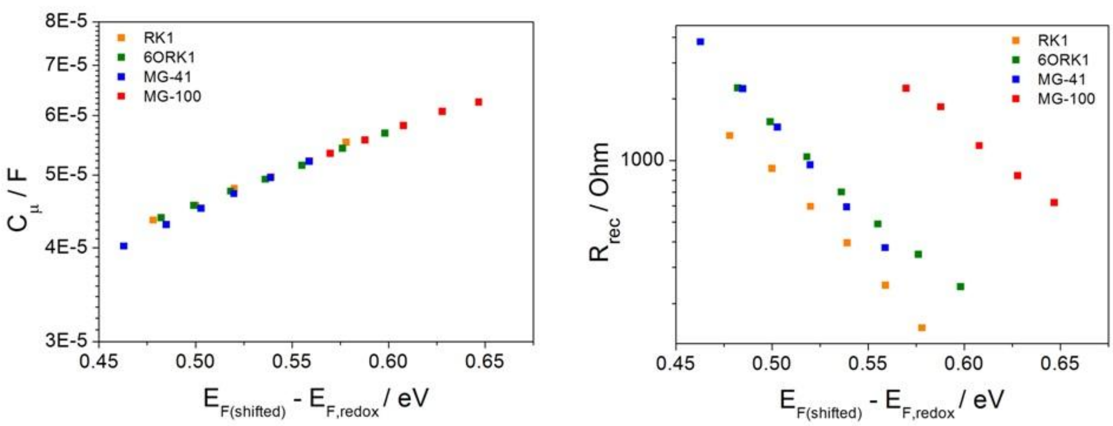

Figure A-10.2: (A) Chemical capacitance and (B) electron recombination resistance data as extracted from EIS measurements for organic dyes employed.

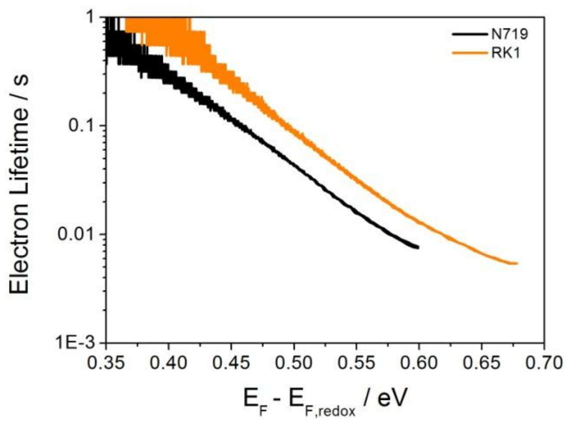

Figure A-10.3: Electron lifetime as extracted from OCVD for N719-DSSC and RK1-DSSC.

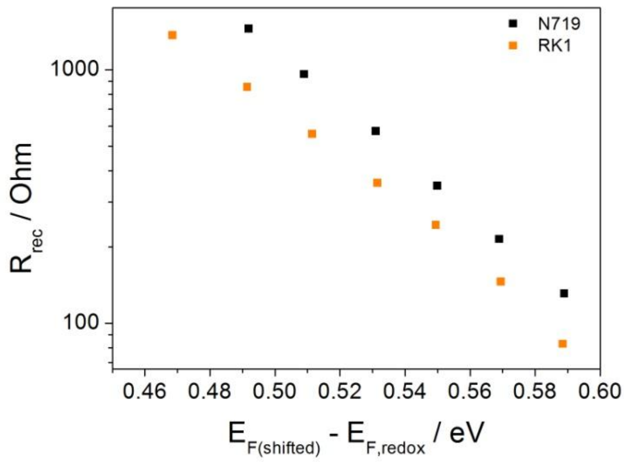

Figure A-10.5: Electron recombination resistance data as extracted from EIS measurements for N719-DSSC and RK1-DSSC after applying a shift on the Fermi level (both sample show the same capacitance at the same electron density).

Resumen (Español)

Como consecuencia de la demanda energética a nivel mundial y los impactos medioambientales derivados del uso de los combustibles fósiles, la búsqueda de nuevas fuentes de energía se ha visto fomentada en las últimas décadas. Desde que se tomó consciencia de la problemática ambiental, la comunidad científica ha centrado sus esfuerzos en explotar y maximizar el rendimiento de los dispositivos capaces de aprovechar las energías renovables, como es el caso de la luz solar. Desde que se descubrió la posibilidad de explotar los procesos fotoinducidos que tienen lugar en la interface semiconductor/electrolito para la conversión de la energía solar en otras formas de energía, estos sistemas han sido ampliamente estudiados por químicos, físicos y por miembros de otras ramas científicas. Actualmente, el uso de estructuras basadas en nanomateriales está recibiendo un gran interés al ser considerados como sistemas de bajo coste capaces de capturar, almacenar y convertir la energía solar en energía química y electricidad.

Un claro ejemplo de estas estructuras ampliamente estudiadas son los electrodos mesoporosos basados en óxidos semiconductores. En concreto, se trata de sistemas complejos cuyas propiedades fisicoquímicas no solo dependen de la naturaleza de los nanocristales, sino también de la interacción entre las unidades cristalinas que forman la película semiconductora. Además, como consecuencia de su elevada área superficial derivada de su condición mesoporosa, la complejidad de estos sistemas se incrementa cuando son puestos en contacto con algún electrolito, como puede ser un gas o un liquido. De este modo, el estudio y la comprensión de cómo manipular sistemáticamente la interface semiconductor/electrolito y de cómo controlar los procesos interfaciales que tiene lugar son un requisito necesario para la optimización de estas tecnologías y sus posibles aplicaciones como baterías, sensores y células solares entre otros.

En relación a las aplicaciones fotocatalíticas y fotovoltaicas de estos sistemas, se ha prestado una especial atención a la relación entre las propiedades microscópicas de la película semiconductora (propiedades electrónicas, estructura cristalina, tamaño y forma de la nanopartícula) y el rendimiento macroscópico de un fotocatalizador o una celda solar, respectivamente. Por esta razón, en esta tesis se ha desarrollado un estudio fundamental de las propiedades fotocatalíticas y fotovoltaicas de semiconductores como el TiO_2 y ZnO. El objetivo de este trabajo ha sido analizar el impacto de la interface semiconductor/electrolito en los procesos de transferencia de carga interfaciales y la recombinación de los portadores de cargas.

En las aplicaciones fotocatalíticas y fotovoltaicas la recombinación ocurre de diferentes maneras. En el primer caso, la recombinación tiene lugar entre los electrones y huecos, los cuales han sido generados en el semiconductor bajo la absorción de luz. Por otro lado, en las celdas solares basadas en la interacción semiconductor-electrolito (como es el caso de las celdas Grätzel o DSSC, del inglés: *Dye-Sensitized Solar Cell*), la recombinación tiene lugar entre las electrones fotoinyectados en el semiconductor y la especie oxidada del par redox presente en el electrolito. Esta transferencia de carga representa la principal ruta de pérdida de eficiencia y constituyen un factor determinante para el voltaje a circuito abierto en tales dispositivos.

En relación a los procesos de recombinación, dos líneas de investigación han sido desarrolladas en esta tesis:

- Se ha mostrado un procedimiento electroquímico basado en la acumulación de electrones en la película semiconductora como una estrategia para reducir la recombinación en procesos fotocatalíticos y fotovoltaicos. Este tratamiento (dopaje reductivo) se ha realizado *in situ* por medio de la polarización catódica del electrodo en una disolución ácida. El desplazamiento del nivel de Fermi durante la polarización del sistema hacia valores negativos ha sido llevado a cabo mediante la aplicación de un potencial externo o, alternativamente, por la acumulación de los electrones fotogenerados bajo la exposición a luz UV. En ambos casos, los cambios mostrados en el rendimiento global son muy similares. Además, la influencia de las propiedades estructurales y morfológicas de la película semiconductora sobre la cinética del dopado electroquímico también ha sido analizado.

- Para aplicaciones fotovoltaicas un estudio de la recombinación electrónica basado en la influencia de la naturaleza química del electrolito ha sido desarrollado. Los efectos sobre la cinética de recombinación empleando diferentes composiciones electrolíticas y moléculas de colorantes han sido discutidos. En concreto, se ha analizado como influye propiedades como la polaridad del electrolito y la presencia de ciertos aditivos en la tasa de recombinación. A partir de las conclusiones derivadas de tal estudio, ha sido presentada una estrategia para lograr sistemas caracterizados por una larga estabilidad y una baja recombinación mediante el uso de electrolitos basados en la mezcla de solventes orgánicos y líquidos iónicos a temperatura ambiente.

Los procesos de recombinación electrónica en las celdas DSSC tienes lugar en una escala de tiempo específica, en el orden de 0.001 -1 segundos. Sin embargo, hay otros procesos que limitan la eficiencia de los dispositivos fotovoltaicos y que ocurren en un rango de tiempo más corta (fs-ns). Es el caso de la inyección electrónica y la regeneración de las moléculas de colorantes. En esta tesis, se presenta un análisis global de todos estos procesos mediante la combinación de técnicas experimentales que incluyen decaimientos de fluorescencia, espectroscopia de transitorios de absorbancia, flash fotolisis y técnicas electroquímicas como la espectroscopia de impedancia. Este análisis global ha sido utilizado para mostrar por primera vez las limitaciones fundamentales que están asociadas al ZnO cuando es utilizado como fotoánodo para la separación de carga en la interface semiconductor/electrolito.

Agradecimientos

Y a la segunda llego la vencida. Hace ya más de cuatro años de aquel día en el que acabe consiguiendo una de aquellas becas que me permitieron comenzar mi carrera como investigador. Una carrera de obstáculos superada con esfuerzo y dedicación gracias al apoyo de muchas personas con las que he tenido el placer de compartir numerosas experiencias dentro y fuera del ámbito laboral. Todas aquellas personas han conseguido contribuir de alguna manera especial al desarrollo tanto de mi trabajo, como de mi persona. Por ello, me es imposible no dedicarles algunos renglones.

En primer lugar, y de manera incuestionable, quiero darles las gracias a mis directores de tesis Juan A. Anta y Thomas Berger. Gracias por darme la posibilidad de enfrentarme a este reto y de crecer como lo he hecho. Gracias por vuestro tiempo y dedicación, por vuestra confianza y apoyo, como por hacerme ver vuestra manera de vivir la ciencia. Gracias a todo ello nunca he tenido la sensación de estar acudiendo a un puesto de trabajo, sino más bien a un lugar de superación personal y desarrollo intelectual.

Agradecer los buenos ratos compartidos dentro y fuera del laboratorio a todos mis compañeros y miembros del departamento, con especial mención a Elena Guillén y Pablo González por ser con quienes compartí laboratorio inicialmente y de quienes trate de aprender lo máximo posible.

A Emilio Palomares por permitirme la oportunidad de trabajar en su grupo en el Instituto Catalán de Investigación Química (ICIQ) de Tarragona. Gracias por hacerme sentir parte de un grupo tan numeroso de jóvenes y entusiastas investigadores, como Iván Castello, J. Manuel Beloqui y Alba Matas, con quienes mantuve una especial relación. Y por último, y no por ello menos importante, Laia Pelleja, mi tutora durante mi corta estancia.

A Marcin Ziolek de la Universidad Adam Mickiewicz (Poznan, Polonia) por todo su tiempo y amabilidad mostrada durante mi estancia en el extranjero. Gracias por acogerme bajo su tutela y transportarme al mundo de los picosegundos. Gracias por abrirme las puertas de su casa haciéndome sentir como un miembro más de su encantadora familia.

A mi familia, novia y amigos, quienes me han sufrido cuando las cosas no salían y han conseguido distraerme y aconsejarme como tomarme la vida. Gracias a todos vosotros soy lo que soy.

Finalmente, también me gustaría hacer una especial mención a aquellos grupos de investigación con los que a través de diferentes colaboraciones han contribuido de alguna manera al desarrollo de este trabajo:

- Al grupo de Gerko Oskam del Centro de Investigación y de Estudios Avanzados del Instituto Politécnico Nacional (CINVESTAV) (México).
- Al grupo de Ramón Tena-Zaera del IK4-CIDETEC (San Sebastián, España).
- Al grupo de Renaud Demadrille del CEA (Francia).
- Al grupo de Shahzada Ahmad, de ABENGOA Research (España)
- Al Departamento de Química Física de la Universidad de Cádiz (España).
- Al grupo de A. R. González-Elipe del Instituto de Ciencia de Materiales de Sevilla (España)